UNIVERSITAT POLITÈCNICA DE VALÈNCIA

DEPARTAMENTO DE INGENIERÍA ELÉCTRICA

PhD Thesis

CURRENT-BASED TECHNIQUES FOR CONDITION MONITORING OF PUMPS

Author: Vincent Becker

Director: Jose Alfonso Antonino Daviu

Valencia, November 2022

Acknowledgments

I would like to express my great gratitude to everyone who has supported me in the preparation of my doctoral thesis.

My special thanks go to Prof. Jose Antonino-Daviu for the excellent supervision and the tremendous support during the execution of the entire thesis.

Likewise, I would like to thank Prof. Sven Urschel from Kaiserslautern University of Applied Sciences, Germany, who was instrumental in helping me come up with ideas for the doctoral thesis in the beginning and who was always available with advice and support in all aspects during the work.

Furthermore, I would like to thank Sebastian Bold, Vicente Biot-Monterde, Daniel Dieterich, Juri Dolgirev, Marco Garbe, Angela Navarro Navarro, Dr. Jose Enrique Ruiz Sarrio, Thilo Schwamm, and Israel Zamudio-Ramírez, who accompanied me during my studies with suggestions and productive conversations. I would especially like to thank Dr. Jose Enrique Ruiz Sarrio, who helped me with the translation of the thesis summary. I have Thilo Schwamm to thank for his active support in numerous measurements.

I would also like to express my sincere thanks to Dr. Martin Eckl, Dr. Benedikt Müller, Dr. Stefan Laue, Dr. Jochen Schaab, and Michael Schneider from the KSB company, who were always there to help and advise me.

To my parents and friends: I thank you all for your support during my work on this doctoral thesis.

Contents

Acronyms

ATCSA	Advanced Transient Current Signature Analysis
ARFT	Adapted Reference Frame Theory
BEP	Best Efficiency Point
BPF	Blade pass frequency
BBH	Broken bar harmonics
DC	Direct current
DFT	Discrete Fourier Transform
DWT	Discrete Wavelet Transform
DTFA	Disturbance Transfer Function Approach
DUT	Device Under Test
ESP	Electric submersible pumps
EEI	Energy Efficiency Index
ErP	Energy-related Products
EU	European Union
FFT	Fast Fourier Transform
FOC	Field Oriented Control
FC	Fundamental component
IM	Induction motors
LoPoFIA	Load Point Depending Fault Indicator Analysis
MMF	Magnetomotive force
MPU	Microprocessor unit

MCSA	Motor Current Signature Analysis
NPSH	Net positive suction head
PVA	Parks Vector Approach
PMSM	Permanent-magnet synchronous motor
PSH	Principal slot harmonics
RFT	Reference frame theory
STFT	Short-time Fourier transform
SVAF	Space Vector Angle Fluctuation
VSD	Variable speed drive
WH	Winding harmonics

Thesis Summary

Pumps are the heart of many processes in industry and service sector. Electric motors are responsible for 69% of electric energy consumption in industry, with 22% of them being used for the operation of pumps. Pump faults can lead to process breakdowns and are thus related to high costs for the plant operator. Furthermore, faulty operation of pumps reduces the energy efficiency of the plant. In many cases, a time-based maintenance strategy is applied, which means that typical wear parts are replaced within defined time cycles, which comes with some drawbacks such as poor resource efficiency and high costs. Condition-based maintenance strategies – meaning that the replacement of parts is planned based on the condition of the pump – are often based on the evaluation of sensor signals like vibration or noise. However, the use of sensors also has some drawbacks, such as additional investment costs, frequent problems with the sensor mounting, and possible sensor faults. There is no widespread use of the current signal to make statements about the pump condition, although current sensors are installed in many applications anyway. As for motor fault diagnosis, different current-based techniques have demonstrated their function. Today, motor current signature analysis is used in industry, especially for the diagnosis of induction motors.

In this thesis, the current-based diagnosis of typical pump-related faults in different applications is evaluated. In total, three different pump types are investigated: a wet-rotor pump, a dry-runner inline pump, and a submersible pump. The techniques used for motor fault detection are adapted for the diagnosis of pump-related faults. The results indicate that the faults clogging, impeller crack, and bearing wear, in particular, influence two frequencies in the current spectrum, which can be used as a basis for a condition-based maintenance strategy. Especially in wet-rotor pumps, these two fault indicators strongly vary depending on the hydraulic load point of the pump. With the help of a feature extraction method based on the adapted reference frame theory, this work demonstrates that the two frequencies can be analyzed in real time in a field environment. Furthermore, a concept for cloud monitoring is presented and validated with the help of a laboratory test. Additionally, it is demonstrated that the faults are visible if the starting current is evaluated in a time-frequency map, which has not been considered before in the literature on pump-related faults. In summary, the findings of this work indicate that current-based diagnosis methods

can successfully detect typical faults in pumps, a fact that is of high interest for companies using these assets in their industrial processes.

The results of the investigation carried out in the thesis have led to three different publications in international indexed journals, four publications in prestigious international conferences and one book chapter. These outcomes show the novelty of the developed work as well as the interest that it has drawn among the scientific and industrial communities.

Resumen de la tesis doctoral

Las bombas hidráulicas son el núcleo de muchos procesos en la industria y el sector servicios. Conviene tener en cuenta que los motores eléctricos son responsables del 69% del consumo de energía eléctrica en la industria, siendo en torno a un 22% de motores utilizados para el accionamiento de bombas. Los fallos de estas bombas pueden provocar averías en el proceso y, por lo tanto, implican altos costes económicos para el operador de la planta. Además, un funcionamiento defectuoso de las bombas conlleva una reducción de la eficiencia energética de la planta. De forma habitual, se utilizan principalmente dos tipos de estrategias orientadas al mantenimiento de maquinaria. Una estrategia de mantenimiento (mantenimiento preventivo) consiste en la sustitución de las piezas desgastadas en un intervalo de tiempo fijo. Este tipo de estrategia presenta muchas desventajas asociadas a la escasa optimización en el uso de los recursos y al consiguiente impacto económico. Por otro lado, la estrategia basada en la condición del equipo (mantenimiento basado en la condición) liga el reemplazo de las piezas desgastadas al estado del equipo, el cual es monitorizado a través de señales adquiridas mediante sensores. Sin embargo, el uso de sensores tiene algunos inconvenientes, como costes de inversión adicionales, posibles problemas en el montaje del sensor y posibles fallos del mismo. El análisis de la señal de corriente no se ha utilizado de forma habitual en la práctica para evaluar el estado de la bomba, aunque en muchas aplicaciones se dispone de sensores de corriente ya instalados que se podrían utilizar a tal fin. Se ha demostrado que técnicas basadas en el análisis de la corriente resultan de gran utilidad para diagnosticar varios tipos de fallos en motores eléctricos. De hecho, el análisis de la firma de corriente del motor se utiliza hoy en día ampliamente en la industria, especialmente para el diagnóstico de fallos en motores de inducción.

En la presente tesis, se evalúa la utilización de la técnica de análisis de corrientes para el diagnóstico de fallos típicos relacionados con las bombas en diferentes aplicaciones. Se investigan tres tipos de bombas diferentes: bombas en línea de rotor húmedo, bombas de rotor seco y bombas sumergibles. En la tesis se han adaptado diversas técnicas, previamente empleadas para la detección de fallos en motores, al diagnóstico de fallos en la propia bomba. Los resultados indican que fallos como obstrucción de la bomba, fisura del impulsor y desgaste de los cojinetes influyen especialmente en dos frecuencias del espectro de corriente, las cuales pueden utilizarse como base de estrategias de mantenimiento basadas en la condición. En concreto, en las bombas de rotor

húmedo, estos dos indicadores de fallo varían sensiblemente en función del punto de carga hidráulica de la bomba. Con la ayuda de un método de extracción de características basado en la motor reference frame theory, se demuestra que las mencionadas frecuencias pueden analizarse en tiempo real en un entorno industrial. Además, se presentan directrices para la monitorización en la nube y se valida con la ayuda de ensayos de laboratorio. Adicionalmente, se demuestra que los fallos son también detectables al analizar la corriente de arranque mediante herramientas de descomposición tiempo-frecuencia. Este hito no se había abordado anteriormente en la literatura técnica del área en lo referente a la detección de fallos en bombas. En conclusión, los resultados de este trabajo demuestran que los métodos de diagnóstico basados en la corriente pueden detectar con éxito diversos tipos de fallo en bombas, lo cual constituye un punto de gran interés para las industrias que utilicen estos activos en sus procesos.

Los resultados de la investigación realizada en la tesis han dado lugar a tres publicaciones diferentes en revistas internacionales indexadas y cinco publicaciones en congresos internacionales de prestigio. Estos resultados muestran la novedad del trabajo desarrollado, así como el interés que ha suscitado en las comunidades científica e industrial.

Resum de la tesi doctoral

Les bombes hidràuliques són el nucli de molts processos en la indústria i en el sector dels serveis. Cal mencionar que els motors elèctrics són responsables del 69% del consum de la energia elèctrica en la indústria, sent al voltant del 22% dels motors utilitzats per l'accionament de bombes. Les fallades d'aquestes bombes poden causar avaries en els processos, i per tant, representen un alt cost econòmic per a l'operador de la planta. A més a més, un funcionament defectuós en les bombes representa una reducció de l'eficiència energètica de la planta. De manera habitual, s'utilitzen principalment dos tipus d'estratègies orientades al manteniment de la maquinària. Una estratègia de manteniment (manteniment preventiu) consisteix en la canvi de les peces desgastades en un interval fixe de temps. Aquest tipus d'estratègia presenta molts desavantatges associats a la reduïda optimització en el ús dels recursos i el seu impacte econòmic. D'altra banda, la estratègia basada en la condició dels equipaments (manteniment basat en la condició) enllaça la substitució de les peces desgastades al estat de l'equip, el qual es monitoritzat per mig de senyals adquirides per sensors. No obstant això, el ús de sensors té alguns inconvenients com costos d'inversió addicionals, possibles problemes al muntatge i possibles fallades. L'anàlisi dels senyals de corrent no s'utilitzen de manera habitual en la pràctica per avaluar l'estat de la bomba, encara que en moltes aplicacions, estos sensors es troben instal·lats i es podrien fer servir per a aquesta finalitat. Ha estat demostrat que les tècniques basades en l'anàlisi de la corrent són de gran utilitat per el diagnosi de diversos tipus de fallades en motors elèctrics. De fet, l'anàlisi de la firma de la corrent del motor s'utilitza àmpliament en l'indústria, especialment per el diagnosi de fallades en motors d'inducció.

En la present tesi, s'avalua l'utilització de la tècnica d'anàlisi de corrents per el diagnosi de fallades típiques relacionades en bombes per a diferents aplicacions. Se investiguen tres tipus de bombes diferents: bombes en línia de rotor humit, bombes de rotor sec i bombes submergibles. En aquesta tesi se han adaptat diverses tècniques, prèviament utilitzades en el diagnosi de màquines elèctriques, per al diagnosi de la pròpia bomba. Els resultat indiquen que les fallades com obstrucció de la bomba, la fissura de l'impulsor i el desgast dels coixinets influeixen especialment en dos freqüències de l'espectre de la corrent, les quals es poden utilitzar com a base per a una estratègia de manteniment basada en la condició. Particularment, en les bombes de rotor humit, aquestos dos indicadors de fallada varíen sensiblement en funció del punt de càrrega hidràulica de

la bomba. En l'ajuda de un mètode d'extracció de característiques basat en la "motor reference frame theory", es demostra que les mencionades freqüències es poden analitzar en temps real en un entorn industrial. A més a més, es presenten directrius per la monitorització en el núvol i es valida en l'ajuda de assajos en el laboratori. Addicionalment, es demostra que les fallades són també detectables quan s'analitza la corrent d'arrancada mitjançant ferramentes de descomposició temps-freqüència. Aquest fet no ha estat analitzat prèviament en cap tipus de literatura tècnica dins del camp de detecció de fallades en bombes. En conclusió, els resultats d'aquest treball demostren que els mètodes de diagnosi basats en la corrent poden detectar en èxit diversos tipus de fallades en bombes, el qual constitueix un punt d'interés per a l'indústria que utilitzen aquest tipus de actiu en els seus processos.

Els resultats de l'investigació realitzada en aquesta tesi han produït tres publicacions diferents en revistes internacionals indexades i cinc publicacions en congressos internacionals de prestigi. Aquestos resultats demostren la novetat del treball desenvolupat, aixina com l'interés que ha suscitat en les comunitats científica e industrial.

1 Introduction

In this first section, the background of this thesis is introduced first, followed by the definition of the objective and sub-objectives and a discussion of the methodology used in this thesis.

1.1 Background

Pumps used to transport liquids are among the biggest electric energy consumers in the European Union (EU). The maintenance of pumps is still a challenge in industry, since there are no known automated solutions for the condition monitoring of pumps. Faulty operation can lead to a reduction of energy efficiency, but also to plant shutdown, and is thus related to high costs for plant operators.

Most existing condition monitoring approaches for pumps that are not based on time-based replacement of certain machine parts rely on the evaluation of the vibration or acoustic signals of a pump. However, the use of additional sensors often implies additional costs for the company. Furthermore, it is not possible to mount a sensor in every type of application. The current signal of the motor that is used to drive a pump is easier to access in most cases. In many applications where variable speed drives (VSD) are used, current sensors are installed anyway, since they are often used for control or safety purposes. In these cases, there is an easy access to the current signal and a platform for current-based monitoring is provided in addition. The number of VSD-driven pump systems in industry is increasing dramatically. Even in applications where no VSD is used, there is usually a relatively easy access to the power lines.

Condition monitoring of electric motors based on the use of the current signal is already being applied in industry, with the analysis being mainly focused on the detection of faults in induction motors (IM). However, there are also approaches for detecting faults in synchronous motors. Conventional techniques are based on evaluating the motor current in stationary operation. The best-known approach is the Motor Current Signature Analysis (MCSA), which is based on the evaluation of certain frequencies in the amplitude spectrum of the current of one of the motor’s supply phases. Other known approaches are based on the application of space vector techniques and other methods. Recent developments in motor current analysis also consider transient signals, for example during the startup of a motor.

The detection of faults in the load driven by a motor via current analysis, however, has been barely used in industry. The number of contributions in this research topic is still very reduced. Using a VSD as a platform for the implementation of algorithms provides an opportunity for more efficient and reliable operation of pumps.

1.2 Objectives of the Thesis

1.2.1 Final Objective

The main objective of this work is to examine different condition monitoring methods for pumps that are based on the evaluation of the current signal. The focus of this work will be on pump-specific faults, which have been barely investigated in state of the art research. Several techniques (both classical and more recent) that have already been successfully applied for the detection of motor faults are implemented and adapted here for the detection of pump-specific faults. This includes the stationary analysis of signals, but also the transient analysis of startup signals of pumps. The main objective also includes demonstrating that such a method can be successfully implemented online in a target hardware to detect pump faults.

1.2.2 Sub-Objectives

This ultimate objective can be divided into a set of sub-objectives to be achieved throughout the development of this thesis in the corresponding sections indicated below:

1) Review of the state of the art related to the diagnosis of the condition of rotating machines based on the analysis of the motor current. The aim is to review the bibliographical references that have dealt with the topic under investigation and to review the fundamentals of the considered methods (Section 3 and 4). From the state of the art, different research questions can be derived, some of which are discussed in the context of this thesis.
2) Development of a method that relates torque oscillations introduced by the faults with certain harmonic amplitudes of a VSD-fed synchronous motor. This consideration helps to better understand the transfer behavior of a motor for the detection of faults in its driven load. If such mathematical model was available, it would be possible to assess in advance whether a particular method can be successful with a specific pump. If, for example, there is a high damping at a certain frequency that is influenced by the fault, then the current signal could only be influenced so slightly that it is lost in the noise. (Section 4)

3) The first part of the analysis of the experimental data focuses on steady-state parameters, including power input, efficiency, and current consumption. The aim is to evaluate what the implications are for the operator regarding the operation of pumps with faults. In addition, it is to be considered whether the steady-state parameters reveal any information about the condition of the pump. As a secondary aspect, it is investigated how the clogging error affects the estimation of the flow and head parameters for a wet rotor pump. (Section 6)
4) After the evaluation of the steady-state parameters, another sub-goal is to investigate which frequencies in the current signal are influenced by pump-related faults. Spectra of both healthy and faulty variants of the different pumps are analyzed using the MCSA approach. (Section 6)
5) The thesis is also aimed to analyze the fault indicators found in MCSA in terms of whether they have a dependence on the hydraulic load point. The goal is to validate whether this novel method helps to distinguish the investigated faults. (Section 6)
6) Based on the results, another goal is to develop a method that implements the MCSA on a pump's controller in real time. The aim is to find out whether such an algorithm can be implemented in a field environment, in this case on the microprocessor unit (MPU) of a pump. (Section 6)
7) In addition, another objective is to propose a method for monitoring a large number of pumps, in particular circulators, using a cloud. This method is validated in a laboratory experiment. (Section 6)
8) Finally, another goal is to answer the question of whether transient analysis of the stator current is suitable for the detection of pump faults. (Section 7)

1.3 Structure of the Thesis

The content of this thesis has been structured into a series of sections, which are briefly described below:

1.3.1 Section 2: State of the Art

After introducing the topic, the function and basics of pumps and their corresponding drives are explained in Section 2. In addition, the design and construction of the pumps that will be examined in more detail in this thesis are explained. This is followed by a presentation of the current state of the art in the area of rotating machines maintenance, with the typical faults of pumps being also considered. How the monitoring of these pump faults is currently implemented is discussed in another subsection. The section is rounded off with a presentation of the current state of the art in current-based fault detection of electric motors and pumps.

1.3.2 Section 3: Theoretical Background

Section 3 lays the groundwork needed to apply the methods and analyze the results. First, the basic relationships are explained to understand how a pump fault affects the stator current. Here, the motor is considered as a kind of sensor with specific transfer behavior. In the following, basic relationships are presented that are important for the spectral analysis of signals. This is followed by a presentation of the most important relationships for the investigation of specific amplitudes in the amplitude spectrum, which is particularly suitable for multiphase motors. Finally, the fundamental equations needed for the transient analysis of a current signal are presented.

1.3.3 Section 4: Methods

In Section 4, all methods implemented to achieve the goals of this work are illustrated. As a first step, the test objects to be analyzed are presented. In the following section, it is discussed which faults were provoked and how the test objects were manipulated in the thesis. After a discussion of the test benches and the measurement setup, the analysis methods are presented.

1.3.4 Section 5: Experiment Results: Stationary Analysis

In Section 5, the experiment results are discussed. However, in this section, only results corresponding to the tested assets operating at stationary condition (meaning that the load and the supply remained constant when the measurement values were obtained) are presented. First, the stationary values, especially the rms value of the current, but also the input power or overall efficiency are considered. The analysis of these values allows drawing conclusions regarding the operation of a faulty pump, e.g., additional energy losses, and also for fault detection. It is analyzed whether the caption of the stationary values is sufficient to detect a fault in the pump. In the next section, the current signal of different pump configurations is investigated with the help of the MCSA. Next, the influence of the hydraulic load point on the two typical frequencies of the stator current that are especially influenced in MCSA is investigated. Finally, the results of the Adapted Reference Frame Theory (ARFT), which was developed to investigate certain amplitudes in the current spectrum to detect faults of a pump, are discussed.

1.3.5 Section 6: Experiment Results: Transient Analysis

In Section 6, the current signals of different test objects are investigated in transient regimes. As test objects, a wet-rotor and a submersible pump are investigated. The method implemented for the analysis of the current signal is Advanced Transient Current Signature Analysis (ATCSA).

1.3.6 Section 7: Conclusion and Future Work

Finally, Section 7 presents the overall conclusions of this thesis, as well as future work on the subject. The main goal of the conclusion is to summarize the findings of this work. Based on the findings and the unanswered research questions, future work is derived.

The final part of the document presents a list of the articles that support the present work, including three publications in indexed international journals (IEEE and MDPI) and four publications at international conferences of great relevance in the area (IEEE ICEM20, IEEE SDEMPED21, EEMODS22, IEEE ICEM22) and one book chapter.

2 State of the Art

In the Energy Roadmap 2050, the European Union has committed to reducing its greenhouse gas emissions in 2050 by 80 to 95% below the level of 1990 (European Commission, 2012). Since the energy sector accounts for a large share of man-made greenhouse gas emissions, a radical reduction in greenhouse gas emissions is only possible through targeted measures and structural changes in this sector. 70% of the worldwide electrical energy used in industry is fed into processes via electrical drives (Shankar, 2016), resulting in 46% of the total electrical energy consumption in the world (Waide, 2011). Of these 70%, energy is mostly used for the operation of pumps (22%), air compressors (18%), and fans (16%); see Figure 2.1 (de Almeida, 2003). Electric drives for medium transport thus represent an outstanding segment within the energy sector and can have a correspondingly large leverage effect in the implementation of efforts to increase energy efficiency.

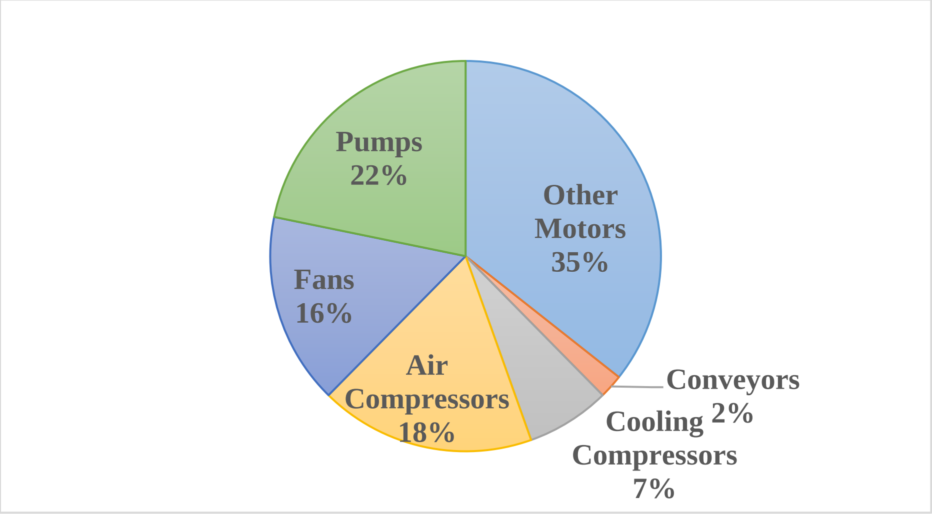

Figure 2.1: Electromotive energy consumption for different applications (de Almeida, 2003)

In recent years, the focus has been on optimizing the design and control of rotating machinery, as shown, e.g., by the Energy-Related Products Directive, which defines a minimum efficiency of electrical equipment. An effect that is less in focus is the reduction of energy efficiency due to incorrect or faulty operation of rotating machines. Rotating machines show a high degree of wear due to their principle. All rotating parts, e.g., a rotor or the impeller, are under the influence of static and dynamic forces, which are one cause of wear in the machine. In many processes, ensuring performance is the top priority, which can lead to over-dimensioned components. Furthermore, it is possible that the system designer does not have enough information about the process parameters, which can also lead to over- or under-dimensioning of the machine. For a rotating machine, this means that it often operates in part loads and thus with worse efficiency compared to the nominal point, for example in pumps (Glover, 2005). However, not only the efficiency of the machine is reduced, but wear processes can also be accelerated due to the fact that the machine is designed for the rated operation point. Examples of these evoked effects are insufficient lubrication of the bearings or cavitation in pumps (Barringer, 2003). For pumps, these wear processes can lead to an efficiency decrease of 10 to 25% before they are replaced (Sustainability Victoria, 2009). The additional energy consumption usually goes completely unnoticed by the plant operators and is accepted due to the lack of indicators.

However, there is already a technical solution for the detection of faults of rotating machines: The condition of a rotating machine can be monitored based on the evaluation of sensor signals. Suitable sensor signals include vibration, sound, or stray flux, but also the current. Low-cost current sensors are well suited in that in many cases, they are installed for monitoring anyway. This means that no additional costs for the hardware arise. Although experience has shown that the initial costs for such sensor systems are lower than the energy costs that can be saved, these systems have not yet become established.

In recent years, different methods have emerged. Of all the techniques mentioned in the literature, MCSA is one of the best possible options today: It can be used during normal operation (online) and non-invasively. Under favorable conditions, motor faults such as bearing damages or eccentricities can be detected. A disadvantage of MCSA is the fact that it was developed solely for the diagnosis of electric motors. One of the reasons for this is that the manufacturers of the driving electrical machines do not know in which application their motor will be used. The driven working machine is therefore not considered, which means that no statements can be made about the condition of the load machine.

2.1 Pumps and their Drives

Mechatronic pump systems are the driving force in almost all production plants in the process engineering industry. Pumps generate flow and increase fluid pressure to route the fluid through the piping systems. In many applications, a large part of the energy used in the system is consumed for pumping. For example, in drinking water systems, 80% of the energy is used for pumping (Sperlich, 2018). The different requirements in terms of flow and head or pressure difference are covered by different types of pumps. They can be divided into two main groups according to their functional principle: rotodynamic and positive-displacement pumps. In industry, 73% of the pumps used are rotodynamic pumps, whereas about 27% are positive-displacement pumps (Dutta, 2018). The most frequently used rotodynamic pump is the centrifugal pump (Bachus, 2003). Both in the design and in the coupling of the motor and pump, there is wide variety in the design of pumps. Standard pumps are usually connected to the motor via mechanical coupling. With integrated pumps, the impeller sits on the shaft of the motor. In all cases, a bladed impeller rotates at high speed in a housing adapted to the shape of the impeller. The liquid between the blades is accelerated by centrifugal force and ejected from the impeller. The pumped medium leaves the impeller at high velocity flows through the screw surrounding the impeller and is deflected into the piping system.

Pumps are used in many different applications, for example in water management, general process engineering, chemical industry, cooling, heating and drinking water systems, or to transport liquid foodstuffs. The hydraulic system, which can be designed as an open or closed circuit, consists of a large number of components, such as tanks or basins, pipelines, fittings, elbows, measurement and control equipment, and internals such as heat exchangers and filters.

The impeller of a pump is driven in nearly all cases by an electric motor. Electric motors are mainly classified into Direct Current (DC) motors, synchronous motors, and IM, which are also called asynchronous motors. IMs have the property that the rotor of the motor runs slower than the force-generating rotating field of the stator. The slip s of an IM is calculated based on equation (2.1), taking into account the stator magnetic field speed n_s and the rotor speed n_r.

$$s = \frac{n_s - n_r}{n_s} \tag{2.1}$$

IMs are the most widespread electric motors in industry, as they account for more than 90% of the rotating electrical machines in industry (Antonino-Daviu, 2019). The biggest advantage of DC motors is their easy speed regulation. However, in most cases significant disadvantages, e.g., delicate maintenance (commutator, brushes), outweigh the advantages. Therefore, their utilization has been progressively decreasing in industry in recent decades. Synchronous motors have some drawbacks, such as the need for auxiliary systems for their startup, possible stability problems, and construction complexity. The three-phase line-fed IM has established itself as the standard drive for pump systems. If the pumping process does not require a continuous change in flow or head, this is currently the best choice, especially thanks to its robustness and simple maintenance, low-cost manufacture, and ability to start on the mains.

In many applications, it is necessary to adjust the duty point of the pump during operation. If flow or head need to be varied in order to supply the process, different variants are suitable for adjusting the operation point.

a) Use of a throttle valve: In this case, a throttle valve is used to increase the flow resistance of the piping system. The addition of the flow resistances of the piping system and the throttle valve results in a steeper overall system curve. The point of intersection of the overall system curve and the pump curve serves as the new operating point of the pump, which should not be confused with the operating point of the system.
b) Use of a bypass valve: By connecting a valve in parallel, the opposite effect to throttling is achieved and the overall system resistance is reduced. The reason for this is that the medium can now flow both through the bypass and through the pressure system to the suction port of the pump.
c) Parallel operation of two or more pumps: Parallel operation can be achieved by either connecting several pumps in parallel or by using twin pumps. This allows the nominal flow and head of the system to be increased. (Viholainen, 2013)
d) Impeller trimming: Impeller trimming means reducing the impeller diameter of a pump and thus reducing the rotating speed at the impeller outlet of a centrifugal pump. Although trimming leads to lower pump efficiency compared to the use of a valve, this method results in higher system efficiency (Schaab, 2019).
e) Speed control: The use of a VSD to drive the motor enables setting an individual speed. This speed can be higher or lower than the rated speed of the motor, within certain limits. The position of the pump curve at the changed speed can be predicted with the aid of affinity laws. The operating point desired by the customer can thus be easily achieved by adjusting the speed (Vodovozov, 2013)

Despite additional losses due to VSD, it is generally accepted that in nearly all cases, speed control is the most energy-efficient method for adjusting operating points (Saidur, 2012), (Schaab, 2019). The VSD-fed IM is currently the most common drive solution for variable-speed pump drives. However, due to its principle, the losses in the rotor are high, which has a negative effect on the efficiency of the motor. A decisive improvement in energy efficiency can only be achieved by switching to a permanent-magnet synchronous motor (PMSM). In some applications, such PMSMs have already become completely established. One example are controlled heating circulation pumps, where all known suppliers use a PMSM as a drive (Rasmussen, 2002). The use of reluctance motors is also becoming more and more interesting, as they do not require rare earth magnets.

The pump impeller converts the mechanical power of the shaft into hydraulic power. The power output P_Q (hydraulic power) of a pump is calculated in dependence of the head H, specified in m, and the flow Q. Since H is given in m, the density of the transported fluid ρ and the gravity constant g also have to be considered; see equation (2.2).

$$P_Q = \rho g Q H \tag{2.2}$$

The efficiency of a pump η_{Pump} is calculated based on P_Q and the input power, which equals the shaft power P_{Mech}; see equation (2.3).

$$\eta_{Pump} = \frac{P_Q}{P_{Mech}} \tag{2.3}$$

In many cases, the overall efficiency of a pump unit η_{Sys}, which includes the pump and the motor, is also of interest. η_{Sys} is calculated using equation (2.4), based on the electric power P_{El} and P_Q.

$$\eta_{Sys} = \frac{P_Q}{P_{El}} \tag{2.4}$$

There are two curves that are typically used to describe the behavior of a pump: the flow-head curve and the flow-power curve; see Figure 2.2. The pump curves indicate the behavior of the pump when the operating conditions change. The two curves describe the dependence of the head and the power input (P_{Mech}) on the flow in a process at constant speed. If the process is closed, and thus no flow is available in the piping system, the head of the pump is at the highest point, and thus referred to as the zero head of the pump, and the power input is at its lowest point. At this point, the power input only includes electrical, mechanical, and hydraulic losses. With increasing flow, the head of the pump starts to drop, and the input power increases. If the head drops to zero, again the power input only contains the mentioned losses, since the pump efficiency η_{Pump} drops to zero. The point where η_{Pump} is the highest is called the Best Efficiency Point (BEP) of the pump. Most manufacturers recommend operating a pump close to its BEP. The shape of the two characteristic curves varies depending on the design and shape of the pump impeller used.

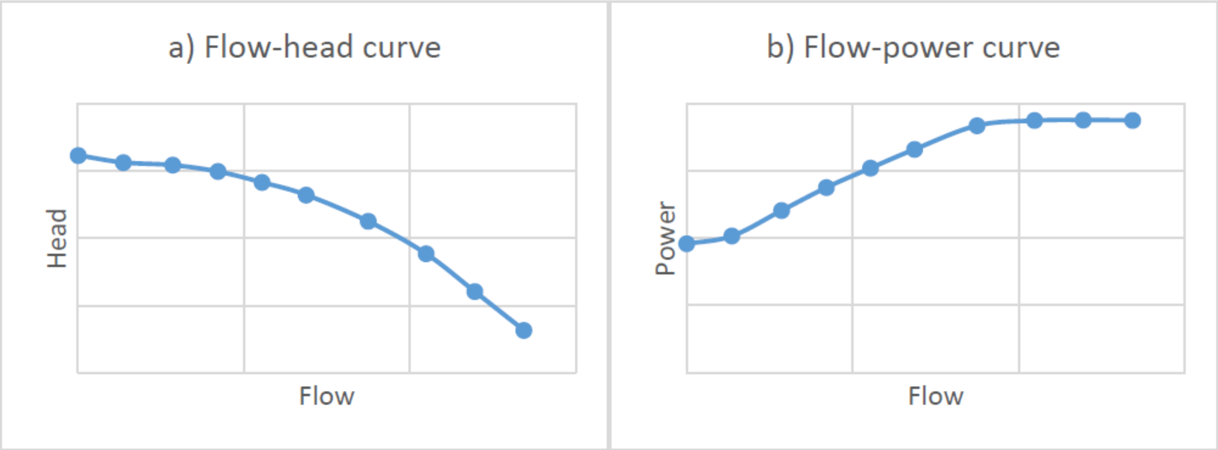

Figure 2.2: Characteristic curves of a pump: a) flow-head curve; b) flow-power curve

The head to be overcome by the pump consists of a geodetic component that is independent of the flow and the head loss, which increases quadratically with increasing flow. The head loss is determined by the dimensions of the pipe (diameter, length), the type of pipeline fittings, and the materials used. Due to changes in the plant, but also due to deposits in the pipeline, the pressure drop can change over time. If the piping circuit is a closed system, as is the case with heating circuits, for example, the geodetic head that the pump has to overcome is zero. The resulting curve, a parabola with y-intercept, is called the system curve. An operating point is set automatically from the intersection of the pump curve with the system curve.

If a VSD is used to drive the pump, the characteristic curves of the pump change. The affinity laws – see equations (2.5) with the flow Q, speed n, pump head H, and shaft power P_{Mech}, which are also used for other rotating machines – are used describe the changed characteristics of a pump. The affinity laws are used for nearly all rotodynamic pump types, including centrifugal (Gevorkov, 2016) and submersible pumps (Sperlich, 2018).

$$Q = Q_1 \frac{n}{n_1};\ H = H_1 \left(\frac{n}{n_1}\right)^2;\ P_{Mech} = P_{Mech1} \left(\frac{n}{n_1}\right)^3 \tag{2.5}$$

In order to adapt to real-world conditions, values from 2.8 to 2.95, instead of 3, are also used as the exponent in the power equation (Schaab, 2019). The effect of decreasing the speed on the two characteristic curves is depicted in Figure 2.3. If the speed is lowered, for example, by 50%, the flow is decreased by 50%, the head by 75%, and the input power by 87.5%.

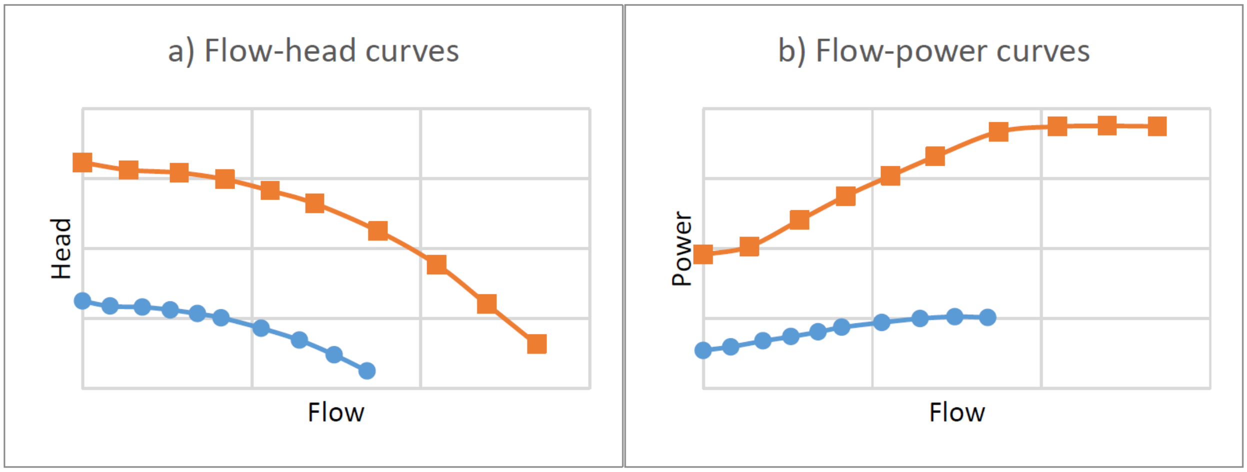

Figure 2.3: Characteristic curves of a pump when speed conditions change (orange: nominal speed; blue: lowered speed): a) flow-head curves; b) flow-power curves

To implement the affinity laws, it is assumed that the efficiency of the pump remains constant under changed speed conditions. The change in efficiency can be captured using scale-up formulas. An example to capture the efficiency change is given by the Ackeret equation; see equation (2.6) (Hess, 2009).

$$\frac{1-\eta}{1-\eta_1} = 0.5 \cdot \left[1 + \left(\frac{n_1}{n}\right)^{0.2}\right] \tag{2.6}$$

An important parameter for pumps is the net positive suction head (NPSH) value, which defines the difference between the total head in the inlet nozzle and the vapor head. If the pressure in the inlet nozzle of the pump is too low, cavitation can form in the impeller of the pump. Cavitation implies the partial evaporation of liquid in a flow process, which is created when the static pressure locally drops to the vapor pressure of the liquid. After the liquid is transported to an area of static pressure, the vapor condenses and implodes. Depending on the size of the cavitating zone, the head and efficiency of a pump decrease, noise and vibrations increase, and components of the pump are damaged. $NPSH$ is calculated using equation (2.7), based on the inlet pressure p_S, the vapor pressure p_V, the density ρ, and the flow velocity in the suction nozzle c_S. (Gülich, 2014)

$$NPSH = \frac{p_S - p_V}{\rho g} + \frac{{c_s}^2}{2g} \tag{2.7}$$

Pump manufacturers specify a minimum value for $NPSH$ in the pump data sheet, the $NPSH$ required ($NPSH_r$). The specification of the $NPSH_r$ value means a cavitation-induced head drop of 3%. Therefore, the data sheets often contain the $NPSH_3$. (KSB, 2022a)

If the speed of a pump is changed, $NPSH_r$ is calculated on the basis of the affinity laws; see equation (2.8) (Gülich, 2014).

$$NPSH_r = NPSH_{r,1} \left(\frac{n}{n_1}\right)^2 \tag{2.8}$$

Within the scope of this work, the three pump types, namely, wet-rotor pumps, dry-runner pumps, and submersible pumps were analyzed, with a special focus on wet-rotor pumps. Because of this, these three pump types will be described in more detail in the following sections.

2.1.1 Wet-Rotor Pumps

In wet-rotor pumps, the motor is flanged to the liquid-carrying pump housing and sealed off from the environment. They are characterized by the rotor of the motor being surrounded by the pumped liquid. The pump impeller and the rotor are mounted on a common shaft. A permanent seal must be provided against the flow-carrying components of the motor.

One famous representative of the wet-rotor pump is the canned motor pump; see Figure 2.4. Here, the wet rotor space is hermetically sealed by a can to the dry stator space (Urschel, 2017). In order to improve motor efficiency, the can should be as thin as possible. At the same time, the can must withstand the inner liquid pressure. Most of the medium flows from the inlet of the pump via the impellers to the outlet. However, a part of the medium enters the rotor space through special bores, flows around the rotor, and flows back into the pump housing through a bore in a hollow shaft. The outlet is an opening in the shaft and is located in the low-pressure area. The force for the circulation is provided by the pressure difference between inlet and outlet. The medium in the rotor space additionally cools the can and the motor.

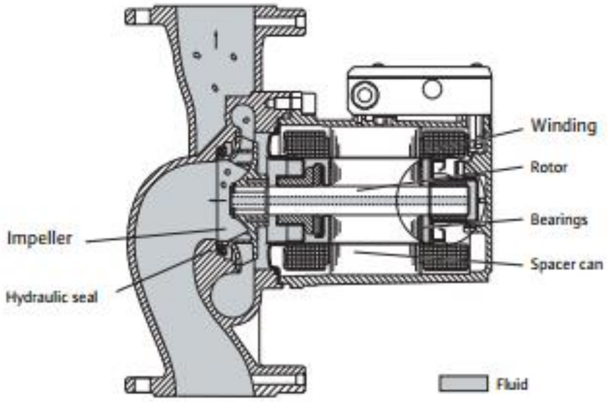

Figure 2.4: Scheme of a canned motor pump (Wikimedia, 2013)

Compared to dry-runner centrifugal pumps, no shaft sealing is needed. This is one advantage of wet-rotor pumps, as a defect of the shaft sealing is a common fault in dry-runner pumps. Furthermore, the risk of leakage is minimized, which can be interesting for applications in chemical plants.

Since ball bearings cannot be used in many liquids, journal bearings are used in wet-rotor pumps. Journal bearings are used for the rotor bearings, with the lubrication of the journal bearings and the cooling of the motor being taken over by the pumped medium. The pumped medium must therefore meet specified viscosity and purity requirements. The load capacity of the journal bearings is based on the formation of a lubrication film in the bearing gap. This gap has to be small in order to be able to provide the load capacity. The lubrication film is formed with increasing speed of the motor. Without a lubrication film, the shaft and the bearing shell are damaged. Consequently, every startup of a wet-rotor pump can increase the risk of bearing wear. In an asymmetrically worn bearing, no lubrication film can be formed. If no liquid enters the rotor space, the bearing will be destroyed within a short period of time. The use of wet-rotor pumps is limited to liquids with good lubricating properties.

Figure 2.5: Picture of two wet-rotor pumps installed in a heating system

The circulation pump is a prominent representative of wet-rotor pumps. Circulation pumps have a wide range of applications in heating, cooling, and photovoltaic systems. Circulation pumps alone are responsible for about 2 to 3% of the total electric energy consumption in the EU, caused by over 100 million circulation pumps (Barthel, 2006). Figure 2.5 depicts two circulation pumps installed in a single-house heating system. Today's pumps are mostly designed as integrated wet-rotor pumps. Circulation pumps are available in the power range from 5 W to 1.1 kW. Based on (Bidstrup, 2001), a circulation pump with a power of 50 W is normally sufficient to supply one household.

The first circulation pump was developed and patented by Wilhelm Opländer in 1929. It was called a “circulation accelerator”. It was the first step from gravitational hot water heating, which was based on the principle that hot water has lower density than cold water, to the hot-water circulating heating in use today. Circulation accelerators based on the patent of Opländer were used until approximately 1955 (Wilo, 2005). In 1987, the first pump with continuous variable speed and differential pressure control was developed (Bidstrup, 2001). There, the differential pressure was estimated based on sensing the slip of the IM. Further developments were based on the usage of more advanced electronics and the application of PMSM.

In the early 2000s, first products were available based on PMSM (Bidstrup, 2002). Compared to IMs, PMSMs had their advantage especially at partial load – and a circulation pump runs in partial load for approximately 80% of the operation time (Rasmussen, 2002). Even in the smallest power range, from 5 to 10 W, PMSMs had an efficiency of over 80% (Staubli, 1996).

The European Union has recognized that increasing efficiency can lead to major energy savings and thus CO_2 reduction. For this reason, the EU has adopted the ErP Directive (Energy-related Products Directive), which specifies minimum efficiency levels, the so-called Energy Efficiency Index (EEI), for circulation pumps; see (European Parliament, 2009). The developments of the last 20 years have focused on improving control and motor design. In addition, new concepts based on the principle of synchronous reluctance have been proposed in the literature (Urschel, 2017). In 2002, the first product with an automatic set point control was presented (Bidstrup, 2002). The basis of the development of new control approaches is the fact that flow and head can be estimated using soft sensors (Eckl, 2019a). In some cases, pressure sensors are also installed; however, this induces higher costs for the pump (Kallesøe, 2014). The variable manipulated to control the head is the speed of the motor. For speed control of the PMSM, vector control is used in circulation pumps (Eser, 2019). Conventionally, there are three types of operation modes to control a circulation pump (Bidstrup, 2002) (Eckl, 2019b). With the simplest type, an uncontrolled pump, the speed is kept constant over the entire flow range. The pump continues to run unchanged at its set speed and the differential pressure generated increases since the flow is limited by the valve. With constant pressure control, on the other hand, the differential pressure generated is kept constant over the entire range by determining the instantaneous pressure from the motor data and adjusting it by changing the speed. This ensures the same flow at a lower differential pressure. The most common way to control circulation pumps is proportional pressure control (Bidstrup, 2002) (Eckl, 2019b). Here, the head of the pump is set in linear dependence of the flow. The biggest disadvantage of the three mentioned control modes is that the heating technician who installs the pump has to set the control parameters. To overcome this problem and further improve efficiency, there have been further developments in recent years. The basis of the new control types is differential pressure control. In (Eckl, 2019a), the author states that the aim of pump control is to provide the smallest possible head. In other words, an attempt is made to open the thermostatic valves as widely as possible in order to minimize pressure losses. In (Kallesøe, 2009), the aim is formulated as controlling the pump in such way that the thermostatic valves are kept in the middle position. The background of this approach is that the thermostatic valves in the middle position have the best control behavior. (Eckl, 2019a) and (Tamminen, 2014) used ramped speed reduction, where the flow of the pump is observed and used as an abort criterion for speed reduction. Compared to differential pressure control, (Eckl, 2019a) notes an energy saving potential of 21%.

2.1.2 Dry-Runner Pumps

Dry-runner pumps are driven by motors mounted on roller bearings and separated from the pumped liquid by mechanical seals. As with wet-rotor pumps, the impeller is mounted directly on the motor shaft. Figure 2.6 depicts an example of a typical dry-runner pump. For larger drive capacities, standard motors are also used, which means that the impeller has to be mounted on a separate shaft, which is flanged to the motor via a coupling.

Figure 2.6: Illustration of a dry-runner pump

In many cases, the mechanical seal is considered one of the most vulnerable components, making this a distinct disadvantage compared to wet-rotor pumps. The mechanical seal is usually replaced after a set period of time depending on the running time of the pump. Fan impeller and roller bearings can be the source of noise, which can make the pumps too loud in certain applications (such as residential use). Compared to wet-rotor pumps, where a stainless steel can is used, dry-runner pumps have the advantage of higher electrical efficiency. This is especially true for higher power classes of motors. This is why they are used especially in applications where high flow is needed. Dry-runner pumps are used, in particular, for transporting aggressive fluids, as the motor is not in contact with the transported fluid, which is why they are often used in the chemical industry.

2.1.3 Submersible Pumps

Submersible pumps are centrifugal pumps whose hydraulic components are flooded by the handled fluid. Usually, this type of pump is not fitted with a suction line (KSB, 2022b). A submersible pump is most commonly driven by an electric motor. Electric submersible pumps (ESP) are used in many applications, for example in drainage, wastewater and slurry pumping, but also in water extraction, water and oil wells.

Figure 2.7: Illustration of an electric submersible pump (Dergreg, 2004)

Submersible pumps play a special role especially in wastewater systems. Wastewater pumps, also known as sewage pumps, are used to pump coarsely contaminated water, often containing solids of various organic, inorganic, or mineral origins. Wastewater pumps are preferably single-stage and are generally not self-priming. The use of impeller shapes depends on the pumped liquid. Channel impellers are often used as impellers, especially in the form of a single, double, or triple channel impeller, each closed or open. However, there are also designs with open single-channel and diagonal impellers as well as vortex impellers.

2.2 Maintenance of Rotating Machines and Pumps

Maintenance must use suitable strategies and measures to meet the high expectations that are put on the systems and minimize unplanned system downtimes and the resulting costs of production downtime. The choice of maintenance strategy (see Figure 2.8) is of great importance for the efficient and cost-optimized operation of a rotating machine system. As an example, in the petrochemical sector, maintenance costs account for 15-40% of the total cost of production (Wowk, 1991). The high costs associated with the downtime resulting from a failure could be avoided if the degradation is diagnosed in due time (McInroy, 2001).

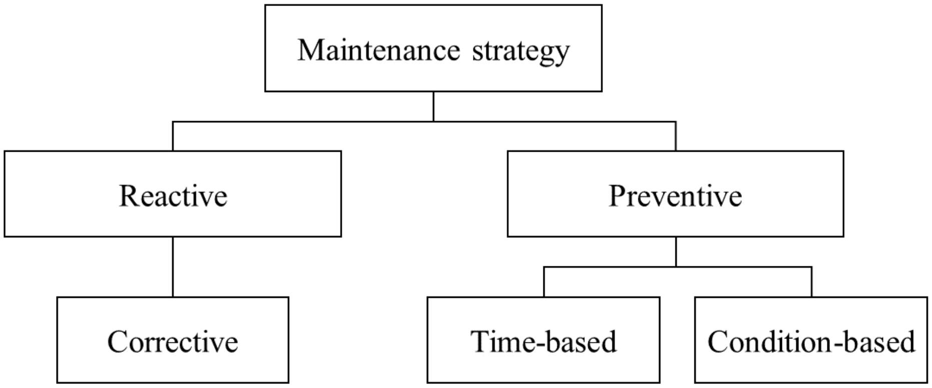

Figure 2.8: Strategies for maintaining a rotating equipment system

Maintenance strategies are divided into two categories, reactive and preventive approaches. Reactive maintenance means that no diagnostic method is applied during operation and the plant operator does not respond to a fault until there is a failure in the plant. Corrective maintenance can be useful for systems whose unplanned shutdown is not so cost-intensive or for rotating machines that are designed with redundancy. This strategy has the advantage that the wear reserve of the machine or of individual components can be fully utilized. Preventive maintenance means that the plant operator reacts to any changes before the plant fails. It is divided into two sub-categories, time-based and condition-based maintenance. With time-based maintenance, the components that are susceptible to faults are replaced at regular intervals. To ensure high operational reliability, components are often replaced early to minimize the risk of failure. Condition-based maintenance means that the condition of the system is evaluated during maintenance. This evaluation can be based on sensor signals or the experience of human beings. However, this approach to condition assessment is often not totally reliable, and unplanned shutdowns and thus also unplanned maintenance measures cannot be prevented completely. The majority of pump operators and maintainers practice corrective and time-based maintenance strategies, even though these strategies often do not achieve the desired availability.

A poor maintenance system can have various consequences, some of them serious. These include (Thomson, 2017):

- Unplanned downtime and loss of production and income
- Catastrophic failures
- Dangerous operating conditions that can lead to serious accidents

A large proportion of faults in rotating machinery can be attributed to the electric motor. Since IMs are typically used, most faults are due to the motor type. Among others, these include (Thomson, 2017):

- Bearing failures
- Stator winding failures
- Broken rotor bars or end rings in cage IM
- High airgap eccentricity and unbalanced magnetic pull

In addition to the motor, its driven load can also be a source of faults. With pumps, it is not possible to make a general statement about which fault is the most likely, since this strongly depends on the pump type and the application. In general, pumps are used to transport fluids, which can be the source of faults, as the machine can corrode or form deposits on its surface due to contact with the pumped medium. Furthermore, a significant source of problems in pumps occurs when they operate away from their BEP (Casada, 1994). According to (Schöb, 2002), 80% of the pump faults in the chemical industry are related to problems with the mechanical seal. (Dutta, 2018) assumes that cavitation and sludge are the most probable reasons for pump faults.

On the one hand, cavitation itself causes a loss of hydraulic power and therefore affects the system parameters. On the other hand, cavitation can be the cause of other faults, including, above all, damage to the impeller; see Figure 2.9.

Figure 2.9: Damage to an impeller due to cavitation (Milan, 2004)

Solids in the transport medium can also be the cause of damage to the impeller. In addition, solids can cause the impeller to clog partially or completely. In wastewater applications, clogging of ESPs is the most common problem; it can cause increased energy consumption and additional maintenance and emergency call-outs (Flygt, 2017). The solids settle in the pump's hydraulic unit and slowly adhere to the pump's impeller and to the inside of the pump casing. In the worst case, the impeller is completely blocked, so that further rotation is no longer possible. If the drive is not switched off in such a case, the pump hydraulics may be mechanically damaged or the electric drive motor may be overloaded. 26% of the lifecycle costs of a wastewater pump are caused by its maintenance and 4% are due to downtimes (Flygt, 2015). The most used maintenance approach is the reactive approach, which means having an employee cleaning the pump while the plant is out of service. Even with circulating pumps, for example, a blockage can be caused by solids or contaminants in the piping system, as can be seen in Figure 2.10.

Figure 2.10: Circulation pump blocked by contaminants (Janlepkowski, 2014)

Another fault that can occur is dry running of the impeller, which occurs when gas is carried along or created in the suction line, or even when there is no liquid in the suction line (Dias, 2021). The reasons for dry running can be turbulences in the system or incorrect NPSH (Tiwari, 2020). A dry-running impeller can also cause overheating, abrasion, and vibration in the pump system (Dias, 2021).

Other typical pump faults are mentioned in (Dister, 2003). Among others, the most important faults are listed below:

- Seal leakage: A defect of the mechanical seal followed by a seal leakage is especially likely in standard chemical pumps, designed as dry-runner pumps (e.g., wet-rotor pumps do not have mechanical seals).
- Water hammering: This effect occurs when a valve suddenly closes at the end of a piping system and a wave propagates in the piping system.
- Cracked housing or mounting foot: This rare fault can be caused by extensive vibrations.

In order to evaluate the quality of a diagnostic system, the state of the art mainly uses two parameters: the false negative rate and the false positive rate. The false positive rate FPR is calculated as the ratio between the number of negative events falsely classified as positive (false positives) FP and the total number of actual negative events, which equals the sum of FP and the number of true negatives TN; see equation (2.9).

$$FPR = \frac{FP}{FP + TN} \tag{2.9}$$

The false negative rate FNR, on the other hand, equals the number of false negatives FN divided by the total number of actual positive events, which equals the sum of FN and the total number of positives TP; see equation (2.10).

$$FNR = \frac{FN}{FN + TP} \tag{2.10}$$

2.3 Condition Monitoring of Pumps

Depending on the area of application, very different methods based on different sensors are used for condition-based pump maintenance. Therefore, it is impossible to make a general statement that a certain method can work for all types of pumps. The choice of method must always be adapted to the situation. Note that additional sensor technology is associated with extra costs in most cases. In addition, it depends on the application whether an installation of additional sensors is possible at all.

Different authors have proved that certain faults affecting the impeller of a pump have an influence on the head of the pump (Beebe, 2004) (Jahangiri, 2018) (Thomson, 2017). In uncontrolled systems, a decreasing head is followed by a decrease of flow. Consequently, the monitoring of head and flow can be used to detect problems of the pump. However, the pump curve must always be considered, since a system change can also result in a change of the pump operating point. In addition, it must be assumed that such sensors are available in the first place, and that they can permanently provide accurate results (keywords sensor drift and calibration). In many applications, such sensors are not available.

Probably the most common method for pumps is the evaluation of the vibration signal. The evaluation of rolling bearings on the basis of vibration analysis is already state of the art and can be found in standards such as VDI 3832. However, if the vibration is measured with the help of an accelerometer at the casing of a pump, the signal additionally depends on the casing geometry and material (Gülich, 2014). Bearing faults belong to a type of faults that do not strongly affect the hydraulic quantities of the pump (Beebe, 2004). (Muralidharan, 2014) analyzed the vibration signal of a monoblock centrifugal pump with support vector machine to detect the faults cavitation, impeller, and bearing fault. (Mohanty, 2012) proposed a method for detecting a broken impeller using the vibration signal. In (Ebrahimi, 2017), the signals of accelerometers are used for diagnosis, especially of mechanical faults. Inlet and exit tip faults of an impeller were detected using vibration in (Hamomd, 2014). Also, a damaged impeller was detected by evaluating the vibration signal using linear discriminant analysis (Ahmad, 2020).

The first indicator of the fault cavitation, as a consequence of a low NPSH, is noise, which is detectable with a hydrophone. (Čdina, 2003) proved that the evaluation of the acoustic signal of the pump enables the detection of cavitation. Further decreasing NPSH is detectable with an accelerometer at the surface of the pump casing. Vibration-based monitoring of pumps using a neural network was proposed by (Nasiri, 2011). (Kotb, 2015) showed that the consideration of the vibration spectrum is useful for detecting cavitation in a pump. Only with a further drop of the NPSH does the abrasion of the impeller increase and the effective head of the pump starts to drop. The occurrence of cavitation causes the pressure of the pump to drop, hence the degree of cavitation is defined by the head drop (Gülich, 2014). The sooner cavitation is detected, the better it is for the service life of the pump, even if efficiency is not affected at first. It was shown that the evaluation of the signal of the pressure sensor enables detection of cavitation (Werner, 2009).

Especially in applications where no head or flow sensors are available, methods are proposed that are based on the evaluation of input values, like power or current consumption. In (Jahangiri, 2018), a clogged impeller was examined and a decrease in the RMS value of the motor current was detected. In wastewater applications, clogging of the motor pump is a common problem. There are two options for reducing the probability of pump clogging: The first option is to design the impeller in a special way (Flygt, 2017). The second option is to apply a maintenance strategy specific to wastewater pumps. It was shown that changing the direction of rotation of the motor helps to loosen debris or clogging (World pumps, 2019). The procedure of changing the direction of rotation is called deragging. This measure requires an extra electrical circuit or a VSD. Two approaches are proposed for triggering deragging. The first option, which can be classified as a time-based maintenance strategy, is to trigger deragging at defined time intervals (World pumps, 2019). The second option, classified as a condition-based maintenance strategy, is to trigger deragging based on the evaluation of a condition variable. As condition variables, especially the RMS current (Fullemann, 2013), but also the power factor (World pumps, 2019) are used. In this application, the placement of additional sensors, such as vibration sensors, is a major problem, and this explains why only electrical variables are currently used. It has been shown in field tests that this approach can be successfully applied and can reduce the number of clogging occurrences by 70% (World pumps, 2019). However, the detection of clogging is only successful if the power consumption is strongly increased. If clogging is present, this does not automatically mean that the power consumption of the pump is significantly incremented.

In the field of circulation pumps, an important factor is to avoid additional costs for sensor technology. For this application, few methods are known for diagnosing the faults of circulation pumps. In the German-speaking region, an approach was presented that can detect the journal bearings used by means of sound analysis (Deckers, 2001). However, as mentioned, no sound sensors are installed in circulation pumps. (Albers, 2006) showed for a different application that sound analysis is a useful tool for diagnosing journal bearing faults. (Eckl, 2019b) presents an approach for circulation pumps that is based on the evaluation of the estimated mechanical power in different speed conditions. However, the validity of the method was not proven with experimental data. Circulation pumps that are driven by modern VSDs can be monitored for the faults dry-running and hydraulic blockage (KSB, n.d.).

The current signal or electrical signals in general are also used to monitor the condition of pumps. These methodologies will be considered in section 2.4.5.

2.4 Current-based Fault Detection of Rotating Machines

For the diagnosis of rotating machines, a distinction is made between model-based and signal-based techniques (Harihara, 2012). However, signal-based techniques have become more widespread. The main advantage of signal-based techniques is their lower complexity, which allows easier implementation in practice (Harihara, 2003). As a basis for signal-based diagnosis, a wide spectrum of signals (voltages, currents, vibrations, partial discharges, fluxes, sound…) are available. Electrical monitoring, in particular, has some advantages compared to the other options, which are summarized by (Antonino-Daviu, 2019) as follows:

- Possibility of remote monitoring (from Motor Control Center, substation, inverter…)
- Non-invasive
- Low implementation cost (simple equipment and possibility of using available sensors)
- Continuous, on-line monitoring capability
- Broad coverage of faults.

For electric motors, many papers and industrial implementations have shown successful application of electric-signal-based diagnosis.

The current signals contain information about the condition of a motor. A simple, rough method is to consider the waveform of the three current signals of a motor. For example, an imbalance between the currents can indicate an electrical problem in the electrical circuit. However, a problem in the supply system can also cause an imbalance in the current signals. Then again, the modulation of the RMS value of the continuous current may be an indication of the presence of rotor damages, although it may also be due to other causes such as oscillations in the driven load.

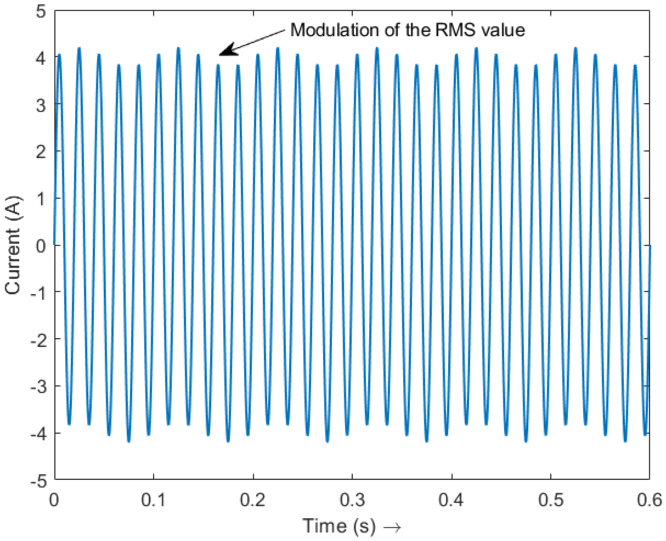

Figure 2.11: Example of a rough analysis of the current analysis of a motor (Antonino-Daviu, 2019)

In recent years, different procedures have been presented for analyzing current signals based on more sophisticated signal processing and analysis tools. The basis of current analysis is that certain faults in the motor or in the load can cause harmonics in the stator current. For the analysis of such harmonics, different methods have been developed in the last decades, which have advantages and disadvantages depending on the application.

Although the current analysis technique has been used for decades, it has become increasingly important in the industrial sector, especially in recent years. The search for diagnostic techniques that are reliable, easy to use, and cost-effective for companies has led to the emergence of this technique as a very interesting alternative that can help diagnose certain faults that are not easily detected with other quantities. The basic idea of current analysis is very simple and is based on recording the waveform of the current demanded by the motor over a period of time and then analyzing this waveform to detect indicators of the presence of a fault.

Measurement of the current signal demanded by the motor is carried out non-invasively, i.e., without disturbing the motor itself. This is crucial in most industrial applications, where stopping the machine to install suitable sensors for measurement would not be feasible or would cause significant inconvenience to the company.

Depending on the analysis method, only the current signal of one or more phases of the motor is needed. To capture the current signal, different sensors are available: Depending on the current range and the application, one possibility is to measure the voltage that drops across a so-called shunt resistor. A second possibility is to evaluate the magnetic field around the conductor to measure the current (e.g., by using a clamp-on ammeter). So-called Hall sensors measure the voltage that is induced when a current crosses a magnetic field applied from the outside.

In the following, the most widespread techniques for current-based fault detection, such as MCSA, space-vector-based techniques, and ATCSA will be highlighted. Next, the typical harmonics in the stator current will be presented, which is necessary in order to finally present the current state of the art in current-based fault detection of pumps.

2.4.1 Motor Current Signature Analysis

MCSA is the most widespread method for the detection of faults in a motor based on the evaluation of the motor current. It was developed in the late 1970s to mid-1980s to detect faults in IMs

(Thomson, 1994). MCSA is based on the refined analysis of the one-phase current signal of a motor in the amplitude spectrum. Compared to the rough analysis of the current signal in the time domain, in MCSA, the current signal must be transformed into the frequency domain. This makes it possible to better evaluate the amplitudes of the components present in the current signal.

In most cases, MCSA is implemented as a kind of offline approach, which means that a current signal is first recorded and then processed. The sensor for capturing the current signal has to be connected to one phase of the motor supply line (often, it can be also installed in the secondary of current transformers that are located in the Motor Control Center for the measurement devices). The sensor signal is evaluated by a wave recorder, e.g., an oscilloscope, capable of measuring the current signal with a high enough sampling rate and the recording time. After recording, Discrete Fourier Transform (DFT) or Fast Fourier Transform (FFT) is used to transform the signal into the frequency domain. Since the frequency resolution (distance between the peaks in the amplitude spectrum) is the reciprocal of the recording time, a sufficiently long recording time is needed ($1s \triangleq 1\mathrm{Hz}$), with a recording time $> 30s$ being recommended. In addition to the recording time, the sampling rate also has to be sufficiently high, since the spectrum can only be evaluated to half the sample rate (Nyquist criterion). In most cases, a sampling rate of 2 kHz is sufficient to identify and assess the fault components under analysis. While the signal is being captured, the motor has to operate in a stationary condition. Consequently, both the supply frequency and the load must remain stable. The fundamental component (FC) is the main component of the current signal. Depending on the supply frequency of the grid, the FC mostly equals 50 or 60 Hz (in motors fed through a variable speed drive, the FC equals the frequency applied by the inverter). The amplitude of the FC is much higher than the amplitudes of the other components. Due to this reason, the frequency spectrum is usually displayed on a logarithmic scale (decibels, dB). In order to be able to compare current signals in different motor conditions, the FC is usually normalized to 0 dB. After the transform, typical frequency components associated with faults are analyzed. If the amplitude of these harmonics exceeds a certain threshold, the fault is considered to be present in the machine and action should be taken. Figure 2.12 depicts the MCSA with an implemented threshold system of a condensate pump motor.

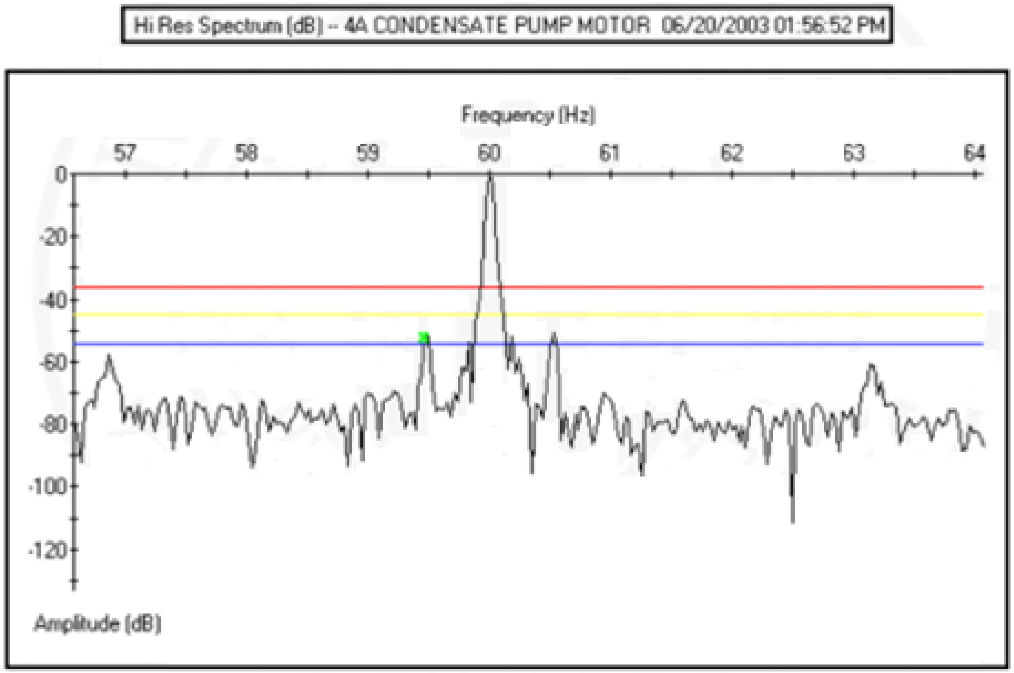

Figure 2.12: Example of an MCSA with implemented threshold systems in the frequency range from 56.5 to 64 Hz (Antonino-Daviu, 2019)

One of the first reports of industrial application of MCSA was in 1986, when an unacceptable level of airgap eccentricity was diagnosed (Thomson, 2017). In the late 1970s, the advances in digital signal processing made it possible to produce a more accurate spectrum of the current, followed by a better diagnosis of cage winding breaks and airgap eccentricities. (Thomson, 2000) presented three case histories where MCSA was successfully used to detect broken rotor bars of an IM in industry. In addition to faults that are typical for IMs, such as broken rotor bars, mechanical faults were detected; these occur in all motor types. These faults include, above all, bearing damages (Benbouzid, 2000) and eccentricities (Cameron, 1986). Later, the MCSA was also successfully applied to detect faults in PMSMs. It has been shown that both eccentricities (Rajagopalan, 2006) (Rosero, 2007) and broken magnets (le Roux. 2007) in PMSMs can be detected by means of MCSA. Moreover, MCSA is also suitable for the detection of faults outside a motor (e.g. in the coupling system). It was shown that faults of the gear can be detected through MCSA (Lo, 2018).

However, this technique also has drawbacks. Some of them have been discovered and reported in recent years. The use of MCSA is not suitable in applications where the frequency of the supply or load varies within the recording time. Under these conditions, application of the technique is at least difficult, if not infeasible. As a result of speed or supply frequency variations, harmonics spread across different frequencies in the FFT spectrum, instead of being represented by a single frequency peak. This complicates the evaluation of the actual amplitudes of the fault components in the FFT spectrum and may even lead to errors in the diagnosis (Antonino, 2014b). Furthermore, effects like load torque oscillations (Schoen, 1996) or blade pass frequency vibrations (Park, 2017), or design aspects like cooling axial ducts (Lee, 2013) or rotor core magnetic anisotropy (Antonino-Daviu, 2015) can lead to false positive alarms when MCSA is used. On the other hand, false negative alarms are caused by non-adjacent bar breakages (Riera-Guasp, 2010), outer bar breakages in double cage rotors (Antonino-Daviu, 2012), reduced slip condition of the IM (Antonino-Daviu, 2006), and problems in speed estimation (Antonino-Daviu, 2020).

To implement MCSA online, i.e., in real time, different methods are presented in the literature. In all cases, a transformation of the current signal into the frequency domain must be undertaken. For this purpose, DFT is normally applied, but its implementation requires large computing effort and storage capacity. For this reason, FFT is used, which represents a more efficient implementation of the DFT. However, there are also major hurdles associated with implementing an FFT on an MPU. Disadvantages of the FFT are the high frequency resolution required, the leakage effect, and the assumed stationary operation during the observation period (Spyropoulos, 2018). Several authors have shown methods for investigating the frequency spectrum of the current on a digital signal processor. One way to implement MCSA is to use the Goertzel algorithm, which is based on the application of an IIR filter. It has been shown that the Goertzel algorithm allows a more efficient implementation than FFT and is suitable for fault detection (Spyropoulos, 2018). Another approach that has been successfully implemented to detect faults in an IM is based on a Hilbert transform; it has shown good results in detecting faults under reduced slip conditions (Sapena-Bano, 2015). Another possibility is shown in (Serna, 2006), where the motor currents were transformed into the rotor coordinate system and the oscillation amplitudes of the fault frequencies were investigated. The approach that is most promising in terms of minimizing the storage effort and number of operations is based on multiple reference frame theory. The idea is – similar to what is done in Field Oriented Control (FOC) – to have a coordinate system rotate. Where the coordinate system rotates in the frequency of the rotor in FOC, it rotates in the frequency of a fault in the sense of fault detection. Approaches can be found in the literature, some of which differ slightly, but are based on the same basic idea. (Cruz, 2005) presented an application of the method for the detection of stator faults in IMs and (Odavic, 2010) showed its application to PMSMs.

2.4.2 Space-Vector-based Techniques

A different approach than MCSA is discussed in this section. The techniques described in this section need more than the current signal of one phase. This necessity of having than one signal is indeed one disadvantage of these approaches (Antonino-Daviu, 2019). The idea of space-vector-based techniques is to summarize the information of more than one current signal in one data vector. Consequently, the current signals are summarized in one space vector. This transform is also known as the Clarke transform and is a useful tool in motor control. To analyze this space vector, different approaches are proposed in the literature. In Space Vector Angle Fluctuation (SVAF), the difference of the angle of the current vector and an ideal reference vector in the frequency domain is investigated (Kostic-Perovic, 2000). It was shown that SVAF can be used to detect broken rotor bars (Kostic-Perovic, 2000) and bearing and misalignment faults in IMs (Arkan, 2005). The Parks Vector Approach (PVA) analyzes the pattern of the space vector current of the motor (Cardoso, 1997). It has been shown that the pattern of the space vector in PVA is influenced by broken rotor bars (Abitha, 2013) and inter-turn stator winding faults (Cardoso, 1997). A combination of PVA and a neural network for decision-making for IM fault detection was presented in (Nejjari, 2000).

2.4.3 Advanced Transient Current Signature Analysis

Despite its many advantages, classic MCSA has the major disadvantage that it can lead to false indications; see section 2.4.1. In recent years, intensive research has been carried out on methods that are able to extend the limits of MCSA. A promising method is to analyze the quantities of the motor regardless of the operating condition (steady-state or transient). Quantities for analysis can be vibrations or stray flux; however, in most cases, the one-phase current of a motor is a preferred option. Transient current analysis is known under the term ATCSA.

In most cases, ATCSA has been used to analyze the starting current of a motor. However, it can also be used to investigate plug stop or load oscillations. An oscillating load, in particular, can be a major issue when using MCSA, for example in belt conveyors, mills, and other applications with nonperiodic load fluctuation, which can account for a high number of motors in a production company (e.g., 10% of the medium-voltage motor fleet) (Lee, 2022). Startups can be analyzed whenever a motor is turned on. How often a motor is switched on and off is very plant-specific.

Unlike MCSA, where certain amplitudes are investigated in the Fourier spectrum, the idea of ATCSA is to identify time-frequency evolutions that are followed by fault-related components during a transient. In order to implement ATCSA, advanced signal processing tools are applied to perform the necessary time-frequency transforms.

The first documented cases of ATCSA used Discrete Wavelet Transform (DWT) (Riera-Guasp, 2005) (Antonino-Daviu, 2005). DWT was used to detect broken rotor bars of line-fed IMs (Riera-Guasp, 2005). To date, however, other types of transformations have stood out, such as the Gabor transform. In the first documented case, it was also used to detect broken rotor bars (Riera-Guasp, 2012). In this context, it should also be noted that ATCSA is only applicable to startups that take a certain amount of time. As a guideline, a time of at least 0.5 s is specified in (Antonino-Daviu, 2005). In (Riera-Guasp, 2005), it is argued that this is not a disadvantage, since broken rotor bars occur mainly in large motors, which have a long startup time anyway. But for laboratory studies, where smaller motors are usually evaluated, this may be a problem. Since the method is also used for other faults, the minimum time can be interpreted as a disadvantage of the method. It was shown with experimental data that dynamic eccentricities in line-fed IMs can also be detected with the help of DWT analysis (Antonino-Daviu, 2007). Additionally, it was shown that outer bearing race defects (Haddad, 2015) and misalignment problems (Antonino-Daviu, 2018) were detected using ATCSA. The method has shown its functionality to detect rotor faults in the petrochemical sector (Antonino-Daviu, 2014a) and in mining facilities (Antonino-Daviu, 2014b). On the other hand, with the advent of more and more VSDs, the disadvantage is again obsolete, since the startup time can usually be set more or less flexibly. There are several studies that proved the function of ATCSA for VSD-fed IMs to detect different kinds of faults. (Pons-Llinares, 2014a) showed that with the help of chirplet transform, broken rotor bars of VSD-fed were detected. Adaptive slope transform, which is an adapted implementation of the Gabor transform, proved its function for detecting broken rotor bars (Fernandez-Cavero, 2021) and mixed-eccentricity problems of VSD-fed IMs (Pons-Llinares, 2014b).

ATCSA was developed in order to overcome the disadvantages of MCSA. In addition to the prevention of false alarms, ATCSA is more reliable than MCSA, since the diagnosis is based on the identification of evolutions in the time-frequency plane, instead of on the consideration of one single frequency peak, as in MCSA (Antonino-Daviu, 2020). This reduces the probability that the frequency is masked by other phenomena. It must be also noted that the ATCSA approach has been employed to detect faults in other machines different than IM, such as for detecting damper cage damages in synchronous motors. This element carries current in the transient condition. This means that the condition of the damper cage can only be monitored in the transient condition. Especially in startups, the damper is operative and carries a significant amount of current (Antonino-Daviu, 2019).

2.4.4 Harmonics in Rotating Machines

The shape of the current signal of a three-phase motor never equals an ideal sine wave. Even in healthy conditions, so-called harmonics are visible in the current signal. However, the highest amplitude in the current spectrum is the FC, which is located at the supply frequency of the electric motor.

In this section, the typical harmonics in the supply phase current of an electric motor will be highlighted. These include harmonics that appear in healthy conditions (sections 2.4.4.1 – 2.4.4.4) and harmonics, whose amplitude is typically increased due to faults (sections 2.4.4.4 – 2.4.4.7). The highest amplitude in the current spectrum of a motor is always found at the FC, which equals the supply frequency of the motor. In a line-fed motor, the supply frequency equals mostly 50 or 60 Hz.

2.4.4.1 Winding Harmonics

The winding harmonics (WH) are caused by the presence of harmonics in the supply voltage and by the fact that the conductors in the stator are not continuously distributed along its circumference, but are installed in a finite number of slots, so that the resulting air gap field is not entirely sinusoidal (Popaleny, 2019). WH are usually visible in the odd multiples ν of the fundamental frequency f_s; see equation (2.11).

$$f_{WH} = \nu \cdot f_s \tag{2.11}$$

In many cases, the amplitudes at $\nu = 5$ and $\nu = 7$ have high values and WH with orders that are multiples of 3 often have lower amplitudes. Furthermore, the amplitudes decrease as the order increases. (Antonino-Daviu, 2019)

2.4.4.2 Principal Slot Harmonics

Principal slot harmonics (PSH) are caused by the slotting of the rotor and the subsequent inharmonic permeability, depending on the radial rotor position. The frequencies influenced depend on the constructive characteristics of the motor. PSH are calculated on the basis of equation (2.12), where k is a natural number; however, the amplitudes for $k > 1$ are low. R is the number of rotor slots, p the number of pole pairs, s the slip, and ν is the order of the considered harmonic of the supply voltage (Antonino-Daviu, 2019). Since rotor slots are only used in IMs, these frequencies only appear in the spectrum of IMs.

$$f_{PSH} = \left(k \cdot \frac{R}{p}(1-s) \pm \nu\right) \cdot f_s \tag{2.12}$$

Depending on the number of stator slots, the amplitudes at f_{PSH} can vary (Joksimović, 2013). Furthermore, not every predicted frequency appears in the motor, with PSH1($-$) ($\nu = -1$) often being one of the largest amplitudes.

Since PSH appear in the healthy condition of a motor, they are also interesting for a different purpose: speed estimation of IMs. Several frequencies that are related to faults in MCSA are calculated based on the slip of the motor, which depends on the speed of the motor. In many cases, the speed is not known, since the measurement of the speed is related to various design issues and additional costs. For $k = 1$, and with knowledge of the parameters $R, p,$ and f_s (mostly the largest amplitude in the amplitude spectrum if line-fed $f_s = 50/60Hz$), the slip can be calculated if f_{PSH} is found in the spectrum. However, it has to be known for which ν an amplitude at f_{PSH} is visible. Then, by detecting the peak at f_{PSH}, the slip can be calculated from equation (2.12) (Bonet-Jara, 2021).

2.4.4.3 Blade Pass Frequency Vibration

The shaft power of a rotating machine (pump, fan, compressor, …) is converted by means of an impeller. Every time an impeller blade is loaded, an impulse is produced dynamically. These evoked oscillations are called blade pass frequency (BPF) vibration and can cause pressure pulsations in the pump (Gülich, 2014) or in other rotating machines. Since an impeller has a finite number of blades, a periodic vibration can be produced depending on the speed of the impeller. If the amplitude is large, it can result in increased frequency sidebands in the stator current. BPF

(f_{BPF}) is calculated on the basis of equation (2.13), depending on s, the positive integer k_1, the number of blades of the impeller N_b, p and f_s (Park, 2017).

$$f_{BPF} = \left(1 \pm (1-s)\frac{k_1 N_b}{p}\right) \cdot f_s \tag{2.13}$$

Consequently, BPF is visible in the healthy condition of a rotating machine. Additionally, an increase of the BPF amplitude can indicate problems inside pumps and fans, such as vane deterioration (Bonaldi, 2012). Other examples where BPF is used as a fault indicator for pumps will be presented in section 2.4.5.

2.4.4.4 Load Oscillations and Wear

Oscillations of the breaking torque of the motor cause speed oscillations, which also influence the stator current of the motor. Torque oscillations can be due to a fault in the motor load, but can also occur in normal motor operation, for example in the cement industry (Mabrouk, 2013). In many cases, the oscillation has the same frequency as the rotor frequency f_R. In this case, the stator current is influenced at the sidebands $f_s \pm f_R$ and the two frequencies are calculated based on s, p, and f_s based on equation (2.14). As in the context of this work, pump faults are considered, the influenced frequency bands are called $f_{r,pump}$ following (Bonaldi, 2012).

$$f_{r,pump} = \left(1 \pm \frac{(1-s)}{p}\right) \cdot f_s \tag{2.14}$$

(Bonaldi, 2012) stated that problems of pumps and fans, such as imbalance or misalignment, can occur in sidebands of the stator frequency depending on the speed.

2.4.4.5 Broken Rotor Bars

A fault that is typical for IMs, especially for IMs with high power, are broken rotor bars. In other motor types, this fault does not play any role. There are two families of harmonics that are influenced by broken rotor bars. The first family of the broken bar harmonics (BBH) are calculated based on equation (2.15), where k is a natural number. The two sidebands for $k = 1$ “BB1” are called the main *sideband harmonics*. The *sideband harmonics* are commonly used for rotor fault detection.

$$f_{BB1} = (1 \pm 2 \cdot k \cdot s) \cdot f_s \tag{2.15}$$

The amplitudes at BB1 give an indication of the state of the rotor bars. If the amplitudes are below −60 dB, it can be assumed that the condition is *excellent*. Worsening of the condition ranges from *good* (−60 dB to −54 dB), *moderate* (−54 dB to −48 dB), *bar crack may be developing or high resistance joints* (−48 dB to −42 dB), *two bars may be cracked or high resistance joints likely* (−42 dB to −36 dB), *multiple cracked or open bars or end rings probable* (−36 dB to −30 dB) to *multiple broken bars and/or end rings very likely* (>−30 dB). (Thomson, 2017)

The second family of harmonics, which are normally not as strongly influenced as the first family, are calculated on the basis of equation (2.16), where $\frac{k}{p}$ is a natural odd number.

$$f_{BB2} = \left(\frac{k}{p}(1-s) \pm s\right) \cdot f_s \tag{2.16}$$

2.4.4.6 Eccentricities

For eccentricities, a distinction is made between static, dynamic, and mixed eccentricity; see Figure 2.13. Static eccentricity means that the rotor center is moved away from the stator center, but the position of the rotor center is fixed (Thomsen, 1994). In the case of dynamic eccentricity, the rotor changes its position depending on its angle, with the rotor rotating around the center of the stator center. Mixed eccentricity is a combination of static and dynamic eccentricity. It is the one that occurs most frequently in practice (Benbouzid, 2000).

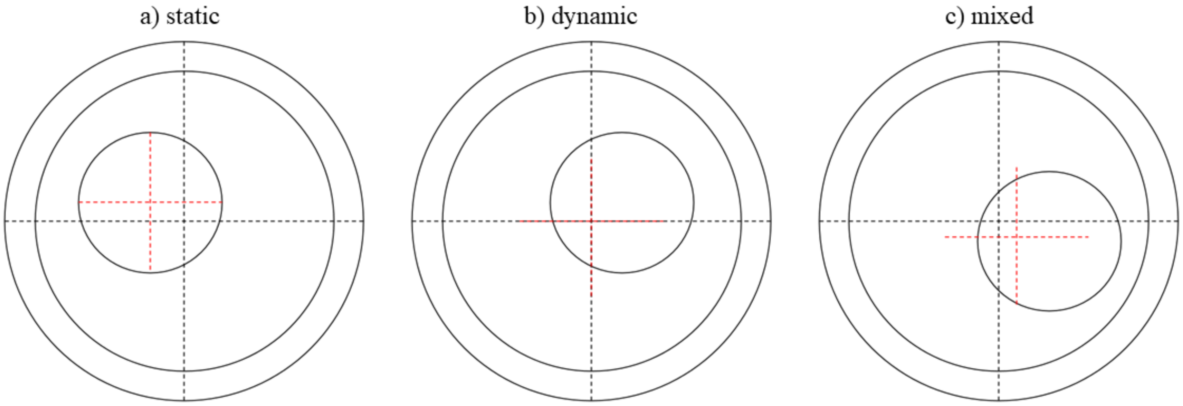

Figure 2.13: Different types of eccentricities in electric motors

Eccentricities cause amplitudes at certain frequencies of the current spectrum. Two families of frequency components are distinguished in the literature. Both families depend on the order of the stator harmonics v ($v = 1, 3, 5, \ldots$), the slip s, the eccentricity order n_d, the number of pole pairs

p, and the supply frequency of the stator current f_s. The eccentricity order contains information about the type of eccentricity. For static eccentricities $n_d = 0$, whereas for dynamic eccentricities it holds that $n_d = 1,2,3, \ldots$. The first family of eccentricities are calculated on the basis of equation (2.17).

$$f_{ecc1} = \left(v \pm (1-s)\frac{n_d}{p}\right) \cdot f_s \tag{2.17}$$

The frequency components around the FC ($v = 1$) "ECC1" are usually the most significant (Rajagopalan, 2007). The use of $v = 1$ in the general equation for the first family of eccentricities is also found in the literature (Antonino-Daviu, 2019). If static eccentricities ($n_d = 0$) of a synchronous motor are considered ($s = 0$), f_{ecc1} equals the frequencies of the WH. This makes it difficult to detect static eccentricities in synchronous motors (Rajagopalan, 2007). The same problem occurs when it comes to the detection of dynamic eccentricities ($n_d > 0$) of synchronous motors with $p = 1$.

If equation (2.17) is compared with equation (2.14), it can be noticed that if $v = 1$ and $n_d = 1$, f_{ecc1} is equal to $f_{r,pump}$. This makes it difficult to distinguish between eccentricity faults, especially dynamic eccentricities ($n_d = 1$), and load oscillations or wear of the load.

The second family of frequencies are also dependent on the number of rotor slots R,; see equation (2.18). The use of the second family of eccentricities is only suitable for IMs.

$$f_{ecc2} = \left((R \pm n_d)\frac{(1-s)}{p} \pm v\right) \cdot f_s \tag{2.18}$$

In the case of static eccentricity ($n_d = 0$), f_{ecc2} equals f_{PSH}. In the case of dynamic eccentricities ($n_d > 0$), f_{ecc2} appear in the sidebands of f_{PSH}.

2.4.4.7 Bearing Faults

Since the balls of ball bearings have a speed, which differs from the rotational speed of the rotor, certain frequencies in the stator current are also influenced if the bearings are damaged. A distinction is made between outer race damage f_O (2.19), inner race damage f_I (2.20), ball damage f_B (2.21), and cage damage f_C (2.22). N_{Be} is the number of rolling elements, D_b the ball diameter, D_p the pitch diameter, β the ball contact angle, and f_r the mechanical rotor frequency. (Antonino-Daviu, 2019)

$$f_o = \frac{N_{Be}}{2} f_r \cdot \left(1 - \frac{D_b}{D_p} cos\, \beta\right) \tag{2.19}$$

$$f_I = \frac{N_{Be}}{2} f_r \cdot \left(1 + \frac{D_b}{D_p} cos\, \beta\right) \tag{2.20}$$

$$f_B = \frac{D_b}{D_p} f_r \cdot \left(1 + \frac{{D_b}^2}{{D_p}^2} cos^2\, \beta\right) \tag{2.21}$$

$$f_C = \frac{1}{2} f_r \cdot \left(1 - \frac{D_b}{D_p} cos\, \beta\right) \tag{2.22}$$

In the current spectrum, these frequencies influence the harmonics in the sidebands of FC, see equation (2.23), with $m = 1,2,3$ ... (Antonino-Daviu, 2019).

$$f_{bf} = f_s \pm m \cdot f_{i,o} \tag{2.23}$$

2.4.5 Detection of Pump Faults

In this section, the current state of the art in the detection of pumps faults will be discussed. Only faults that occur outside the motor, i.e., those that affect the impeller or the hydraulics, are considered. The number of research publications based on the detection of faults in the pump (considered as motor load) is still low compared to the detection of motor faults.

The first documented case where MCSA was used to diagnose a fault on the impeller of an ESP in an oil well dates back to 1990. First, several amplitude increases at different frequencies in MCSA were observed and then a decrease in the hydraulic power of the motor pump. Therefore, it was decided to remove and check the motor pump. During the analysis, radial wear on the pump stage hubs and shaft was found, whereas the electric motor was still in healthy condition. (Thomson, 2017)

In an article published in 1995 it was shown that an eroded impeller of a sea water pump was detected by analyzing the current in the frequency spectrum (Siegler, 1995). In the same year, (Casada, 1995) investigated different motor faults, like broken rotor bars, bearing faults, as well as a clogged suction strainer of a pump. It was shown that the spectral analysis of the power spectrum was more beneficial than the vibration spectrum for detecting the clogged suction strainer. (Perovic, 2000) detected cavitation, hydraulic blockage, and a damaged impeller by relating the spectral features from MCSA to the individual faults. It was shown that cavitation and hydraulic blockage especially influenced the noise level at ±25 Hz around the FC in the current spectrum. The damaged impeller was the reason for an increase in amplitude at the frequency $f_{r,pump+}$. In (Schmalz, 2004), the spectral energy in the range from 5 to 25 Hz was analyzed to detect the presence of cavitation and low flow condition (hydraulic blockage) in centrifugal pumps. Impeller cracks have also been detected using MCSA, which was verified in (Harihara, 2008). In (Hernández-Solís, 2010), the current and power signatures of a motor at different operating conditions were analyzed to identify not only when cavitation is present in the pump, but also when it starts. In (Pradhan, 2012), an IM-driven centrifugal pump with a power of 0.75 kW and 24 blades was investigated. Due to manipulation of the impeller, the amplitudes at the BPF in the current spectrum increased from 13.3 dB (healthy) to 14.1 dB (1 missing blade) to 14.6 dB (2 missing blades) to finally 16.1 dB (3 missing blades). The authors of (Tian, 2014) showed that inlet and exit tip faults of an impeller caused a decrease in amplitude at the BPF in MCSA. The analysis should take into account that the error frequencies of the BPF can be equal to those of an eccentricity (Park, 2017). (Stopa, 2014) showed a successful detection of cavitation at the BPF component in the current using an adapted MCSA. Additionally, it was shown that a damaged pump impeller causes speed oscillations and could be detected by analyzing the current signal (Pradhan, 2019). (Irfan, 2019) showed a successful application of PVA to detect a damaged impeller and pipe blockage.

Several authors have used Artificial Intelligence to evaluate the current signal of a cavitating impeller or hydraulic blockage. (Dutta, 2018) showed first that cavitation can be detected using a Machine Learning algorithm. In (Dutta, 2020), the space vector machine and K-nearest neighbor were compared in order to detect cavitation. (Bold, 2020) presented a comparison of SVAF and MCSA for the faults hydraulic blockage cavitation and dry running. It was shown that Machine-Learning-based detection of cavitation and hydraulic blockage can be implemented in an industrial environment (Dias, 2021). Additionally, it was shown that the use of a big feature pool based on time and frequency domain features can be used by the implementation of Machine Learning in order to detect cavitation and seal leakage (Husna, 2021).

3 Theoretical Background

This section lays the theoretical foundations needed for current-based analysis for fault detection in rotating machinery. First, it will be shown how faults in the load of a motor can affect the stator current and how the transmission behavior of the "motor" sensor is in this case. Two methods will be presented, one based on harmonic field analysis and a second one based on the consideration of the disturbance transfer function. Next, the theoretical bases for the spectral analysis of time-based signals will be provided. This is followed by an explanation of the adapted reference frame theory, which is a memory-efficient implementation of spectral analysis for electric motors. Finally, the theoretical foundations for the time-frequency analysis of time-based signals will be laid.

3.1 Transfer Behavior of an Electric Motor as a Transducer

The references mentioned in section 2.4.5 proved that pump-related faults have an influence on the stator current of the motor. Thus, it has already been shown that the motor, consisting of the stator, the rotor, and the current sensor, can be considered as a sensor unit for detecting faults in the load. This sensor unit has a certain transfer behavior, which is mainly characterized by the motor parameters. The transfer behavior of the motor is the topic of this section.

In the literature, traditional approaches like the magnetomotive force (MMF) and the permeance wave approach have been used to investigate the theoretical behavior of IMs. These approaches, however, are not suitable for predicting the exact harmonic amplitudes of the airgap magnetic field. For a more detailed analysis, finite element simulations have been suggested. However, the drawbacks of computational burden and the fact that a model is only valid for one motor have to be considered. Additionally, it is not possible to obtain an analytical model for a fault from finite element simulation. (Blodt, 2006)

A different approach was shown in (Stopa, 2010), where the differential equation system of the IM was used as a basis for examining the transfer behavior. The references have in common that load-related oscillations can be modeled with torque oscillations that are added to a constant load torque (Salles, 2000) (Bonaldi, 2012) (Blodt, 2005). For the general assumption, see the equation of an oscillating load as described in (Trajin, 2010). T_0 is the constant load torque, T_n the torque amplitude of one oscillation at the frequency f_n; see equation (3.1).

$$T_{load} = T_0 + \sum_n T_n \cdot cos(2\pi f_n t) \tag{3.1}$$

In an ideal system, the value T_n would be equal to zero. However, it is to be expected that even with no faults, there will be some oscillations in the load torque. One example are the BPF vibrations that occur in rotating machines (fans, compressors, pumps), which occur at the frequency of $f_n = N_b \cdot f_R$. What is also typical in many applications is an oscillation in the frequency of the rotor ($f_n = f_R$), as demonstrated in the cement industry (Mabrouk, 2013).

In the following two sections, the theoretical background of two approaches that can be used to calculate the influence of torque oscillation on the stator current will be presented. The first one is harmonic field analysis, which was developed to understand the transfer behavior of line-fed IMs. The second one, the Disturbance Transfer Function Approach (DTFA), was developed in the framework of this work and is used to model the transfer behavior of a controlled PMSM.

3.1.1 Harmonic Field Analysis

In this section, harmonic field analysis is used to model the transfer behavior of a motor as a transducer in order to detect faults in the motor load. The requirement for the load-related fault is that it has an influence on the load torque of the motor; see equation (3.1). Other faults that cause eccentricity of the motor, for example, are treated separately in the literature (Cappelli, 2014) (Haddad, 2016). The following paragraphs are based in large parts on the explanations of (Blodt, 2006).

If the friction losses of a motor are neglected, the equation of motion – see equation (3.2), with the electromagnetic torque of the motor $T_{motor}(t)$, the load torque $T_{load}(t)$, the mass inertia of the motor and the impeller J, and the angular velocity of the rotor $\omega_R(t)$ – is valid.

$$T_{motor}(t) - T_{load}(t) = J \frac{d\omega_R(t)}{dt} \tag{3.2}$$

In the next step, equation (3.2) is converted to ω_R, resulting in equation (3.3).

$$\omega_R(t) = \frac{1}{J} \int \big(T_{motor}(t) - T_{load}(t)\big)\, dt \tag{3.3}$$

It is now assumed that in the steady-state condition, T_{motor} equals T_0 of equation (3.1); see equation (3.4) (Blodt, 2005). Thus, it is assumed that in the steady state, the torque is constant in time and space. This assumes, on the one hand, an ideal design of the motor and, on the other hand, the neglect of feedback, e.g., by controlling torque or speed.

$$T_{motor}(t) = T_0 \tag{3.4}$$

For the sake of simplification, it is now assumed that the torque – see equation (3.4) – is only superimposed by one oscillation ($n = 1$). By substituting equations (3.4) and (3.1) in equation (3.3), we obtain equation (3.5).

$$\omega_R(t) = -\frac{1}{J}\int (T_1\, cos(\omega_1 t))\, dt = -\frac{T_1}{J\omega_1} sin(\omega_1 t) + \omega_0 \tag{3.5}$$

Consequently, ω_R consists of a mean value ω_0 and an oscillation with the frequency of the load oscillation ω_1. The amplitude of the oscillation depends on the amplitude of the torque oscillation T_1, the mass inertia J of the rotor, and the angular velocity of the torque oscillation ω_1.

Further integration of ω_R is performed in order to obtain the angular rotor position Θ_R – see equation (3.6), where the integration constant is assumed to be zero.

$$\Theta_R(t) = \int \omega_R\, dt = \frac{T_1}{J{\omega_1}^2} cos(\omega_1 t) + \omega_0 t \tag{3.6}$$

How Θ_R interacts with the magnetomotive force and the airgap flux density is explained in detail in (Blodt, 2006). An important parameter that describes the transfer behavior of IMs is the modulation index β', which equals the product of the amplitude of the angle oscillation and the number of pole pairs p; see equation (3.7).

$$\beta' = p\frac{T_1}{J{\omega_1}^2} \tag{3.7}$$

To allow for further simplification, small load fluctuations are assumed so that $\beta' \ll 1$.

The phase-modulated stator current i_{to} is expressed with equation (3.8), with the unmodulated part $i_{st}(t)$, and the part $i_{rt}(t)$, which shows the modulation, depending on $\beta{\sim}\beta'$ and the amplitude I_{rt}.

$$i_{to}(t) = i_{st}(t) + i_{rt}(t) = I_{st}\, sin(\omega_s t) + I_{rt}\, sin\big(\omega_s t + \beta\, cos\big(\omega_C t - \varphi_\beta\big) - \varphi_r\big) \tag{3.8}$$

However, harmonic field analysis does not capture any coupling between ω_R and T_{motor}. Especially when the motor is controlled, the speed has an influence on the motor torque. PMSMs and reluctance motors are only used in combination with a VSD, with the exception of example line-start motors. Furthermore, more and more IMs are fed by VSD and controlled via FOC.

3.1.2 Disturbance Transfer Function Approach

The DTFA was developed as part of this thesis in order to solve the problem of harmonic field analysis, which is currently only suitable for line-fed motors. In DTFA, the coupling between the controlled value and the motor torque is considered. In detail, equation (3.2) only describes a part of the transfer behavior of the motor.

The motor torque depends on the transfer function of the controller, the electric transfer behavior G_{S1}, and the control deviation e,; see equation (3.9).

$$T_{motor}(s) = e \cdot G_{S1}(s) \tag{3.9}$$

The dynamic behavior of a motor depends on the motor type and design. There are different ways of describing the dynamic behavior of a motor. In most cases, a differential equation system is used to model the motor. In the following paragraphs, PMSMs will be considered in more detail.

Equations (3.10) to (3.12) contain the non-linear mathematical model of a PMSM in the dq frame, with the d and q-current i_d and i_q, stator inductance L_S, d and q-voltage u_d and u_q, stator resistance R_S, number of pole pairs p, angular velocity of the rotor ω_R, flux ψ_{PM} and mass inertia J. In these equations, it is assumed that L_S equals the inductance in the d and q direction, which is true in many cases, for example in surface-mounted PMSMs (Xu, 2012).

$$\frac{di_d}{dt} = \frac{1}{L_S} \cdot u_d - \frac{R_S}{L_S} \cdot i_d + p \cdot \omega_R \cdot i_q \tag{3.10}$$

$$\frac{di_q}{dt} = \frac{1}{L_S} \cdot u_q - \frac{R_S}{L_S} \cdot i_q - p \cdot \omega_R \cdot i_d + \frac{p}{L_S} \cdot \omega_R \cdot \psi_{PM} \tag{3.11}$$

$$\frac{d\omega_R}{dt} = \frac{3}{2} \cdot \frac{p}{J} \cdot \psi_{PM} \cdot i_q - \frac{p}{J} \cdot T_{load} \tag{3.12}$$

Equations (3.10) and (3.11) are nonlinear due to the cross-coupling of ω_R and i_q, respectively ω_R and i_d. Because of this nonlinearity, no transfer functions $T_{load} \rightarrow i_q$, $T_{load} \rightarrow i_d$ can be derived from the equation system, which is a known issue in the control design of such motors. To overcome this problem, the equation system is linearized and the coupling is canceled (Xu, 2012). However, if linearization is allowed in terms of DTFA, it has to be evaluated for each parameter set. It not only depends on the electrical and mechanical parameters, but also on the control structure and the control parameters. Furthermore, it is also assumed that the controllers have linear behavior. For a parameter set of the PMSM-fed wet-rotor pump investigated in this work, it has been shown that linearization is valid. To prove this, equations (3.10) to (3.12) were implemented in Matlab/Simulink, with a Proportional Integral (PI) controller for speed, q-current, and d-current control. Speed and q-current control were implemented in a cascade structure; see Figure 3.2. The transfer behavior of $T_{load} \rightarrow i_q$ and $T_{load} \rightarrow i_d$ was simulated with the help of a *model linearizer app* with a sine stream from 0.1 to 1000 Hz with 200 data tips.

Figure 3.1 depicts the amplitude responses of i_d and i_q on an excitation with T_{load}; see the blue curves. It becomes visible that the value of i_d over the entire frequency range is low, which means that the influence of T_{load} on i_d is negligibly small. However, the transfer behavior from T_{load} to i_q strongly resembles the behavior of a PT2 link.

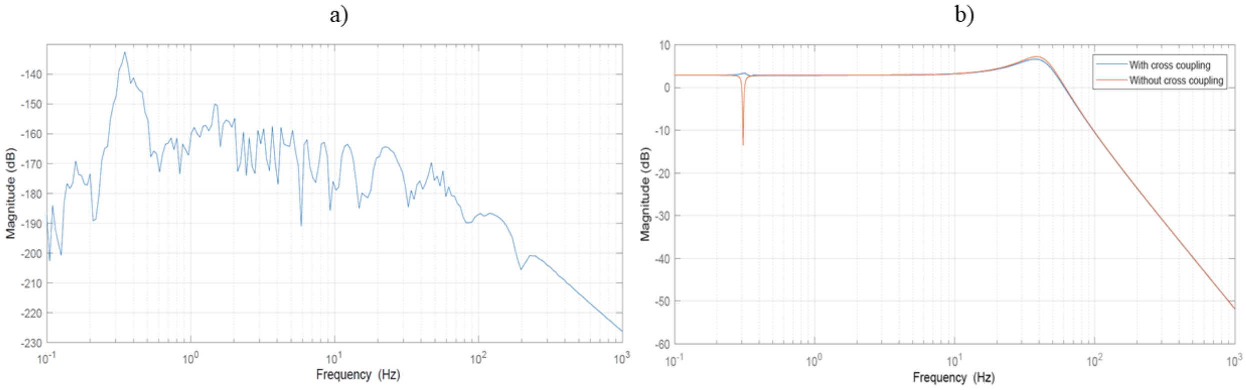

Figure 3.1: Disturbance transfer behavior of a PMSM with 800 W with nonlinear transfer behavior; a) $\boldsymbol{T_{load}} \rightarrow \boldsymbol{i_d}$; b) $\boldsymbol{T_{load}} \rightarrow \boldsymbol{i_q}$

For the parameter set and control design used, it was proven that the influence on i_d is negligible. This means that, as in control design (Xu, 2012), the next step, i.e., the decoupling of the model, can be taken. The transfer behavior of the decoupled PMSM is shown in the signal flow diagram in Figure 3.2, including the cascade structure for speed and current control, with the motor constant K_t (see equation (3.13)).

$$K_t = \frac{3}{2} p\psi_{PM} \tag{3.13}$$

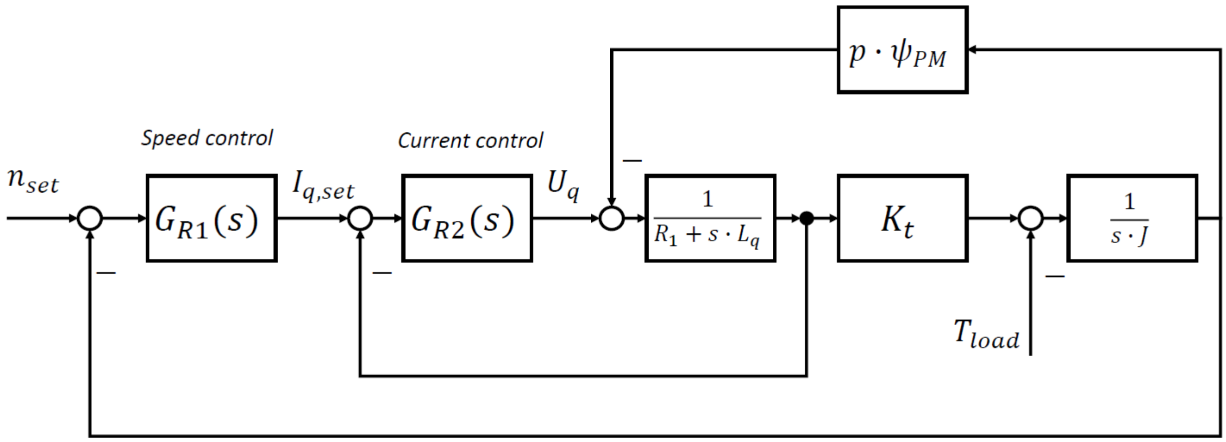

Figure 3.2: Structure of a PMSM with cascade control structure (Schröder, 2009)

Since the signal flow diagram represents a linear system, the disturbance transfer function $\frac{I_q}{T_{Load}}$ can be derived from it, as seen in equation (3.14), which depends on the transfer functions of speed $G_{R1}(s)$ and q-current control $G_{R2}(s)$. This is a general expression for the structure shown in Figure 3.2, but it is difficult to interpret without information about the controller structure.

$$\frac{I_q}{T_{Load}} = \frac{\frac{1}{Js} G_{R1}(s) G_{R2}(s) \frac{1}{R_1 + sL_q} + \frac{1}{Js} p\psi_{PM} \frac{1}{R_1 + sL_q}}{1 + K_t \frac{1}{Js} G_{R1}(s) G_{R2}(s) \frac{1}{R_1 + sL_q} + G_{R2}(s) \frac{1}{R_1 + sL_q} + K_t \frac{1}{Js} p\psi_{PM} \frac{1}{R_1 + sL_q}} \tag{3.14}$$

In many cases, PI controllers are used for speed and current control. The transfer function of a PI controller is given by equation (3.15), with the gain of the proportional component K_P and the gain of the integral component K_I.

$$G_R(s) = K_P + K_I \frac{1}{s} \tag{3.15}$$

For the design of the PI controller, the cutoff frequency $\omega_N = \frac{K_I}{K_P}$ is of interest. For low frequency signals $\omega < \omega_N$, the PI controller behaves like an integral controller ($K_P = 0$), and for higher frequency signals $\omega > \omega_N$, it behaves like a proportional controller ($K_I = 0$). This behavior is of interest when we try to simplify the disturbance transfer function $\frac{I_q}{M_L}$.

In general, without simplification, with the proportional gains $K_{P,R1}$ (speed control) and $K_{P,R2}$ (current control) and the integral gains $K_{I,R1}$ (speed control) and $K_{P,R2}$ (current control), we obtain a transfer function $\frac{I_q}{M_L}$ with a difference order of 2 from equation (3.14); see equation (3.16).

$$\frac{I_q}{T_{Load}} = \frac{a_1 s^3 + a_2 s^2 + a_3 s + a_4}{b_1 s^5 + b_2 s^4 + b_3 s^3 + b_4 s^2 + b_5 s + b_6} \tag{3.16}$$

The parameters a_1 to b_6 are written in equations (3.17) to (3.26).

$$a_1 = L_q\left(K_{P,R1} K_{P,R2} + p\psi_{PM}\right) \tag{3.17}$$

$$a_2 = K_{P,R1} K_{P,R2} R_1 + R_1 p\psi_{PM} + K_{I,R1} K_{P,R2} L_q + K_{P,R1} K_{I,R2} L_q \tag{3.18}$$

$$a_3 = K_{I,R1} K_{P,R2} R_1 + R_1 K_{P,R1} K_{I,R2} + K_{I,R2} K_{I,R1} L_q \tag{3.19}$$

$$a_4 = R_1 K_{I,R2} K_{I,R1} \tag{3.20}$$

$$b_1 = J{L_q}^2 \tag{3.21}$$

$$b_2 = JL_q\left(2R_1 + K_{P,R2}\right) \tag{3.22}$$

$$b_3 = {R_1}^2 J + JR_1 K_{P,R2} + L_q K_t K_{P,R1} K_{P,R2} + JL_q K_{I,R2} + L_q K_t p\psi_{PM} \tag{3.23}$$

$$b_4 = R_1 K_t K_{P,R1} K_{P,R2} + JR_1 K_{I,R2} + R_1 K_t p\psi_{PM} + L_q K_t K_{P,R1} K_{I,R2} + K_t L_q K_{I,R1} K_{P,R2} \tag{3.24}$$

$$b_5 = R_1 K_t K_{P,R1} K_{I,R2} + L_q K_t K_{I,R1} K_{I,R2} + R_1 K_t K_{I,R1} K_{P,R2} \tag{3.25}$$

$$b_6 = R_1 K_t K_{I,R1} K_{I,R2} \tag{3.26}$$

In order to verify the validity of equation (3.16), the amplitude response depicted in Figure 3.1 (orange curve in b) was compared to the amplitude response of equation system (3.10) to (3.12), including the controllers (blue curve in b). With the exception of two places, both curves lie on top of each other. One point is in the negligible low frequency range at 0.2 Hz and the other point is at the amplitude rise, although the difference here is small.

Further simplification of equation (3.16) is only possible if the parameters of the motor and the control are known. For the parameter set of our PMSM-fed wet-rotor pump (see section 4.1.1), the following assumptions hold; see equations (3.27) to (3.33).

$$\omega \gg \frac{K_{I,R1}K_{P,R2} + K_{P,R1}K_{I,R2}}{K_{P,R1}K_{P,R2} + p\psi_{PM}} \tag{3.27}$$

$$K_{P,R1}K_{P,R2} + p\psi_{PM} \gg K_{I,R2}K_{I,R1} \tag{3.28}$$

$$p\psi_{PM} \gg K_{P,R1}K_{P,R2} \tag{3.29}$$

$$R_1 \gg K_{P,R2} \tag{3.30}$$

$$K_t p\psi_{PM} \gg JK_{I,R2} \tag{3.31}$$

$$p\psi_{PM} \gg K_{P,R1}K_{I,R2} + K_{I,R1}K_{P,R2} \text{ and } p\psi_{PM} \gg K_{P,R1}K_{P,R2} \tag{3.32}$$

$$\omega \gg \sqrt{\frac{K_{I,R1}K_{I,R2}}{p\psi_{PM}}} \tag{3.33}$$

After implementation of the assumptions (3.27) to (3.33), the disturbance transfer function $\frac{I_q}{T_{Load}}$ can be simplified to a PT2 term, as shown in equation (3.34).

$$\frac{I_q}{T_{Load}} = \frac{p\psi_{PM}}{JL_q s^2 + JR_1 s + \frac{3}{2}p^2{\psi_{PM}}^2} \tag{3.34}$$

Consequently, the disturbance transfer function of the motor (only if the assumptions are valid) is the independent control parameter of speed control and current control. However, this does not mean that the control structure (see Figure 3.2) can be completely neglected. Nevertheless, this greatly simplifies the interpretation of the transmission behavior, since parameters can be calculated for PT2 links that mirror the transmission behavior. These include the gain factor K_γ, the time constant T_γ, the characteristic angular velocity ω_γ, and the degree of damping D_γ; see equation (3.35). In general, a decrease of −40 dB per decade is typical for a PT2 link, which means strong damping for higher frequency signals. Consequently, load oscillations $\omega \gg \omega_\gamma$ have no influence on I_q and are thus not visible in the stator current.

$$G(s) = \frac{K_\gamma}{{T_\gamma}^2 s^2 + 2D_\gamma T_\gamma s + 1} = \frac{K_\gamma}{\frac{1}{{\omega_\gamma}^2} s^2 + \frac{2D_\gamma}{\omega_\gamma} s + 1} \tag{3.35}$$

The gain factor K_γ is calculated from the reciprocal of K_t; see equation (3.36).

$$K_\gamma = \frac{2}{3p\psi_{PM}} = \frac{1}{K_t} \tag{3.36}$$

Where the time constant T_γ depends on J, L_q, p and ψ_{PM}; see equation (3.37).

$$T_\gamma = \sqrt{\frac{2JL_q}{3p^2{\psi_{PM}}^2}} \tag{3.37}$$

As the characteristic angular velocity ω_γ equals the reciprocal of T_γ, it depends on the same parameters; see equation (3.38). Consequently, high p and ψ_{PM} lead to high ω_γ, and low J and L_q to high ω_γ.

$$\omega_\gamma = \sqrt{\frac{3p^2{\psi_{PM}}^2}{2JL_q}} \tag{3.38}$$

The damping of the motor is calculated according to equation (3.39). Consequently, especially the parameters R_1, p and ψ_{PM} have an influence on D_γ. Negative values for D_γ, which would lead to instability of the transfer behavior, are not expected, since all parameters are positive and greater than zero. For values $D_\gamma > 1$, it is possible to split the PT2 link into two PT1 links. For values $0 < D_\gamma < \frac{1}{\sqrt{2}} \approx 0.7$, increases in the amplitude response are possible, which means that at frequencies around ω_γ, the load oscillation is amplified visibly in I_q and thus in the stator current.

$$D_\gamma = \frac{R_1 \cdot \sqrt{J}}{p \cdot \psi_{PM}\sqrt{6 \cdot L_q}} \tag{3.39}$$

The two important parameters ω_γ and D_γ are now calculated for two different PMSMs considered in this work. The motors have the same design, but differ in their parameters. Table 3.1 illustrates the two parameters of the two motors.

Table 3.1: Characteristic angular velocity $\boldsymbol{\omega_\gamma}$ and degree of damping $\boldsymbol{D_\gamma}$ for two PMSM-fed pumps with 800 and 150 W

	$\boldsymbol{\omega_\gamma}$	$\boldsymbol{D_\gamma}$
800 W motor	*43 Hz*	*0.3*
150 W motor	*36 Hz*	*1.2*

Both motors have ω_γ around a frequency of 40 Hz. The speed of both motors varies from 1000 to 3000 rpm, which means an f_R of 17 Hz to 50 Hz. Oscillations in the load torque with the rotational frequency are in the area of the characteristic frequency of the motors. BPF vibrations are expected with a frequency of 117 to 350 Hz and thus lie on the falling flank in the Bode diagram. The 800 W motor, however, has only a D_γ of 0.3, compared to the damping of the 150 W motor, which is four times higher. This leads to amplitude increases of the 800 W motor in the area of the characteristic frequency. The characteristics are confirmed by the consideration of the Bode diagram; see Figure 3.3. Especially in the higher speed range, the 800 W motor has a higher gain than the 150 W motor. This makes one motor more sensitive to the detection of torque variations above a certain frequency.

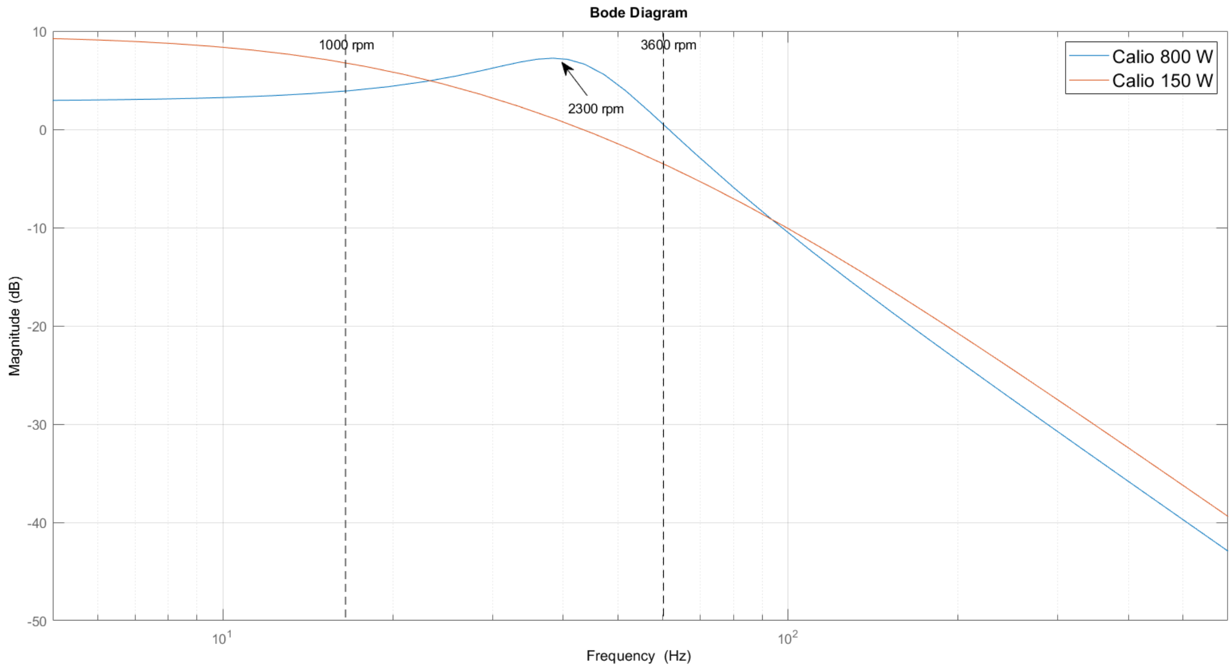

Figure 3.3: Theoretical amplitude responses of the q-current on a load torque oscillation of two PMSMs with 800 and 150 W

The curves of the respective motors in the Bode diagram are characteristic of the behavior of the motor as a sensor for detecting load oscillations or faults that cause load oscillations. Unlike sensors, such as temperature sensors, which usually output a value proportional to the temperature (voltage or current), the transmission behavior of the motor as a sensor varies depending on the frequency of the load oscillation. If the exact amplitude of the load oscillation is to be detected, precise knowledge of the transfer characteristic is necessary.

Based on the DTFA, one thus obtains for the q-current a constant quantity responsible for the torque formation $i_{q,dc}$ and an oscillation with frequency f_1 and amplitude i_1; see equation (3.40).

$$i_q = i_{q,dc} + i_1 \cos(2\pi f_1 t) \tag{3.40}$$

The amplitude i_1 depends on the transfer function $\frac{I_q}{T_{Load}}(s) = G_\gamma(s)$; see equation (3.34). If the frequency f_1 is known, i_1 is calculated based on equation (3.34). The Bode diagram, as shown in Figure 3.3, also allows graphical determination of $\left|G_\gamma(j2\pi f_1)\right|$ by reading the value for the gain at the location f_1.

$$i_1 = \left|G_\gamma(j2\pi f_1)\right| \cdot T_{Load} \tag{3.41}$$

In order to show the effect of the oscillating q-current on the stator current, a back transformation to the stator fixed alpha, beta system is performed first – see equations (3.42) and (3.43) – with the frequency of the rotating frame f_{dq}, which equals f_s, as shown in equation (3.44).

$$i_\alpha = i_d \cos\left(2\pi f_{dq} t\right) - i_q \sin\left(2\pi f_{dq} t\right) \tag{3.42}$$

$$i_\beta = i_d \sin\left(2\pi f_{dq} t\right) + i_q \cos\left(2\pi f_{dq} t\right) \tag{3.43}$$

$$f_{dq} = f_s \tag{3.44}$$

For further simplification, it is further assumed that $i_d = 0$. Equation (3.40) is now substituted in equations (3.42) and (3.43). As a result, we obtain equations (3.45) and (3.46).

$$i_\alpha = -i_{q,dc} \sin(2\pi f_s t) - i_F \cos(2\pi f_1 t) \sin(2\pi f_s t) \tag{3.45}$$

$$i_\beta = i_{q,dc} \cos(2\pi f_s t) + i_F \cos(2\pi f_1 t) \cos(2\pi f_s t) \tag{3.46}$$

Finally, i_α and i_β are then transformed into the stator currents i_1, i_2, i_3. In the following, only one phase i_{S1}, which equals i_α, is considered; see equation (3.47).

$$i_{S1} = i_\alpha = -i_{q,dc} \sin(2\pi f_s t) - i_F \cos(2\pi f_1 t) \sin(2\pi f_s t) \tag{3.47}$$

For even further simplification, the product rule for trigonometric functions is considered; see equation (3.48).

$$\cos(b) \sin(a) = \frac{1}{2}(\sin(a - b) + \sin(a + b)) \tag{3.48}$$

After application of equation (3.48), we finally obtain equation (3.49) for the stator current i_{S1}.

$$i_{S1} = -i_{q,dc} \sin(2\pi f_1 t) - \frac{i_F}{2} \sin\left(2\pi t(f_s - f_1)\right) - \frac{i_F}{2} \sin\left(2\pi t(f_s + f_1)\right) \tag{3.49}$$

Thus, the amplitude of the oscillation in the q-current i_F is divided 50:50 into two amplitudes with the frequencies $f_s - f_1$ and $f_s + f_1$. Any load oscillation therefore causes at least two harmonics in the stator current.

3.2 Spectral Analysis of Stationary Signals

The basis of MCSA is the spectral analysis of a current signal of a motor. For stationary signals, the mathematical tool for analyzing the spectrum is the Fourier transformation.

Aiming to simplify a mathematical problem, Joseph Fourier first used the approach to approximate a periodic function with a summation of trigonometric functions (Grattan-Guinness, 2005). A periodic signal course repeats itself in the same temporally regular sequence. The period T is the time of a complete oscillation, which is necessary for complete signal representation. Before using the Fourier series, it has to be verified that periodicity is given, by evaluating equation (3.50), with n being any integer.

$$g(t) \ = g(t + nT) \tag{3.50}$$

The signal $g(t)$ can then be approximated using the Fourier series, as shown in equation (3.51), where ω_0 equals the angular velocity.

$$g(t) \ = \frac{a_0}{2} + \sum_{k=1}^{\infty} a_k \, cos(k\omega_0 t) + \sum_{k=1}^{\infty} b_k \, sin(k\omega_0 t) \tag{3.51}$$

Based on the idea of minimizing a cost function, the coefficients a_0, a_k and b_k of the Fourier series can be obtained. These allow a perfect approximation of the original signal, unless the output signal has discontinuities. At discontinuity points, overshoots can occur, which are called Gibbs phenomenon. Alternatively to equation (3.51), the Fourier series can also be formulated as a sum of rotating vectors; see equation (3.52), with the complex coefficients A_k.

$$g(t) \ = \sum_{-\infty}^{\infty} A_k e^{-j\omega_k t} \tag{3.52}$$

The coefficients A_k are calculated based on equation (3.53).

$$A_k \ = \int_{-\frac{T}{2}}^{\frac{T}{2}} g(t) e^{-j\omega_k t} dt \tag{3.53}$$

If equation (3.53) is physically interpreted, we can obtain that the multiplication by $e^{-j\omega_k t}$ (which equals division by $e^{j\omega_k t}$) subtracts ω_k from each oscillation component of $g(t)$. If there is an oscillation in $g(t)$ with the frequency ω_k, the rotating vector is stopped in the position at $t = 0s$ while the components $\neq \omega_k$ are still rotating, and due to periodicity, the signal $g(t)$ and the integration in equation (3.53) equal zero.

The same idea is now applied to signals that are not periodic, by allowing the periodic time to tend to infinity. Given a time signal $f(t)$ in the time domain, its Fourier transform $F(\omega)$ is calculated based on the time t and the angular velocity ω; see equation (3.54).

$$F(\omega) = \int_{-\infty}^{\infty} f(t)e^{-j\omega t}\,dt \tag{3.54}$$

Since in reality only finite numbers occur in discrete distances, the discrete Fourier transform $F[n]$, with $n = 0{:}\,N-1$, is used to calculate the spectrum of a sequence $f[k]$, with the number of samples N calculated as in equation (3.55).

$$F[n] = \frac{1}{N}\sum_{k=0}^{N-1} e^{\frac{-j2\pi nk}{N}} f[k] \tag{3.55}$$

The number of matrix multiplications is directly related to N^2, which results in high computation burdens. Because of this fact, the FFT was introduced; it relies on the fact that standard DFT involves a lot of redundant calculations, so that FFT represents a more efficient approach to calculating the Fourier spectrum.

Before the use of DFT or FFT, attention has to be paid to correct signal acquisition. An effect that can appear while capturing the signal can give rise to so-called *aliasing*. The effect of aliasing appears if the sample time is greater than the period of the signal to be captured. Figure 3.4 illustrates an example of this effect, where the blue curve shows the original signal, the circles represent the samples, and the orange curve is derived from the samples. Consequently, in this situation a signal with a different period is obtained, which can lead to wrong conclusions in the analysis. To avoid aliasing, analog low-pass filters can be used during measurement acquisition (Song, 1996). In high-quality oscilloscopes, for example, such filters are already provided.

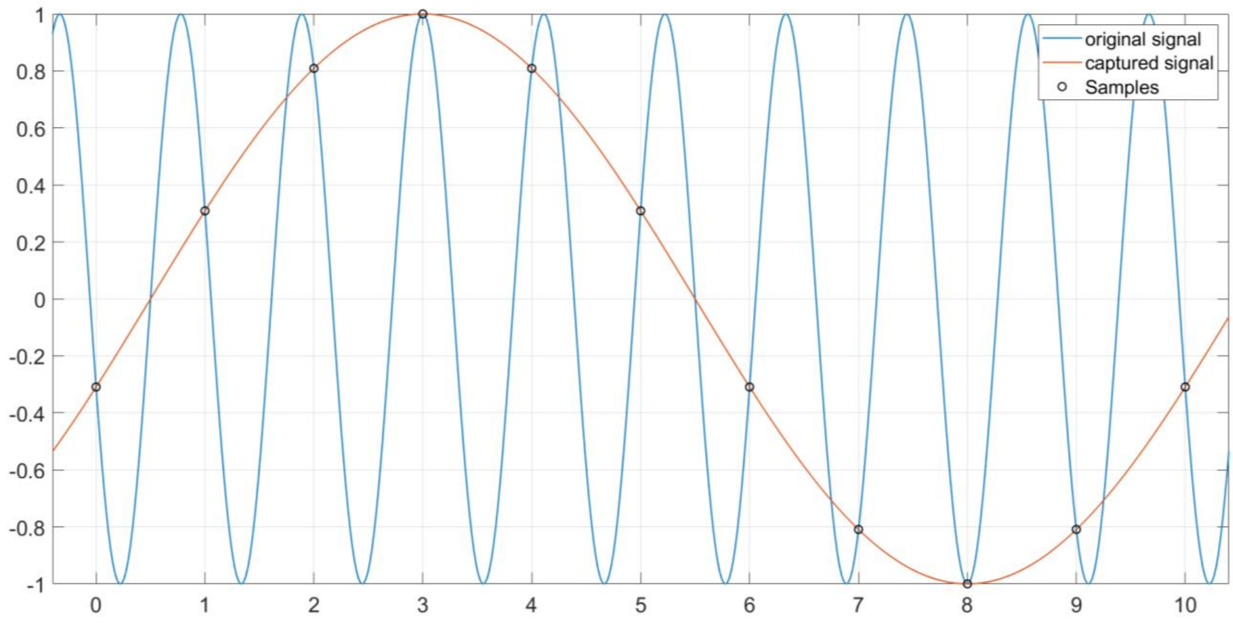

Figure 3.4: Demonstration of the effect aliasing of a signal

Furthermore, it must already be clear before the measured value is recorded up to which frequency the signal is to be examined in the frequency domain. The sampling frequency f_s, which equals the number of samples per second, determines the maximum frequency that can be detected with the Fourier spectrum. Considering the Nyquist criterion, we can obtain a spectrum where we can only visualize harmonics with frequencies up to $\frac{f_s}{2}$.

The total registered time T directly determines the frequency resolution of the resulting FFT spectrum. The higher the spectrum resolution, the better we can distinguish between very close frequency components. When the frequency resolution is low (poor resolution), each component is spread over a wider range of frequencies. The frequency resolution is the minimum separation between two consecutive distinguishable peaks in the FFT spectrum. If the registered time is T seconds, the frequency resolution will be $\frac{1}{T}$.

Compared to the continuous Fourier transform, as shown in equation (3.54), DFT is not always completed over an integer number of cycles of the input signal. This results in corruption of the signal in the frequency spectrum. A solution is the use of window functions, for example the Hamming or Hanning window. These window functions taper the samples toward zero at the beginning and at the end of the signal in order to minimize discontinuity with a possible next period. This reduces the side lobes around the FC in the amplitude response. Especially when frequencies around the FC are to be investigated, as for example in MCSA with broken rotor bars (see equation (2.15)), this is of high relevance, particularly when only a short recording time can be enabled.

3.3 Adapted Reference Frame Theory

The reference frame theory (RFT) is a method for multi-phase motors where the multi-phase values are represented as a space vector in the complex plane. In most cases, the number of considered phases equals three. The premise for the application of the RFT is that the sum of all phases is equal to zero. In this case, when two quantities are known, the third can be concluded, which allows a perfect description of three quantities by only two quantities. The RFT is mainly used in order to control motors, as DC values are very interesting for the control of motors. RFT makes it possible to calculate the amplitude of three-phase signals, for example of voltage, flux, or current signals, that are used for the control of the motor. The same idea can be adapted in the sense of fault detection in a motor. Here, however, it is not the amplitude at the fundamental frequency that is of interest, but the amplitude at typical fault frequencies. The approach becomes interesting if memory and computing power are low in an application, since only the frequencies that are influenced by a fault are calculated.

First, equation (3.56) is used to establish the zero-sequence condition for the stator currents i_a, i_b and i_c of a three-phase motor. The validity of this condition is a prerequisite for the further steps.

$$i_a(t) + i_b(t) + i_c(t) = 0 \tag{3.56}$$

Considering a real motor, the phase current and thus the current space vector is overlaid with oscillations. Especially in faulty operation of a motor, further oscillations occur, which is the premise for using MCSA for fault detection. In order to explain how ARFT can be used for fault detection, we now assume that the motor current is the sum of the torque-forming current with the amplitude $\hat{\imath}_T$ and the speed ω_S and one oscillation with the amplitude $\hat{\imath}_F$, the speed ω_F, and the angle θ; see equation (3.57). In this case, $\hat{\imath}_F$ contains information about the condition of the pump and about the fault severity. The curves of equation (3.57) are depicted in Figure 3.6 (left) for the values $\hat{\imath}_T = 2A$, $\omega_S = 2\pi \cdot 50Hz$, $\hat{\imath}_F = 0.1A$, $\omega_F = 2\pi \cdot 75Hz$, and $\theta = 0°$.

$$
\begin{aligned}
i_a(t) &= \hat{\imath}_T cos(\omega_S t) + \hat{\imath}_F cos(\omega_F t + \theta) \\
i_b(t) &= \hat{\imath}_T cos\left(\omega_S t - \frac{2\pi}{3}\right) + \hat{\imath}_F cos\left(\omega_F t + \theta - \frac{2\pi}{3}\right) \\
i_c(t) &= \hat{\imath}_T cos\left(\omega_S t - \frac{4\pi}{3}\right) + \hat{\imath}_F cos\left(\omega_F t + \theta - \frac{4\pi}{3}\right)
\end{aligned}
\qquad (3.57)
$$

As a first step, equation (3.56) is revised, resulting in equation (3.57), and it is found that equation (3.56) fulfills the zero-sequence condition.

As a next step, the space vector $\underline{\vec{\imath}}_{\alpha\beta}$ is created based on equation (3.58). What is important here is the factor 2/3, which is necessary so that the amplitudes of the oscillations remain the same.

$$
\underline{\vec{\imath}}_{\alpha\beta} = \frac{2}{3}\left(i_a(t) + i_b(t) \cdot e^{i\frac{2\pi}{3}} + i_c(t) \cdot e^{i\frac{4\pi}{3}}\right) \qquad (3.58)
$$

The real part of the space vector is denoted by α-current, while the imaginary part is denoted by β-current. The α-β coordinate system is denoted by a stator fixed coordinate system. The transformation from the three-phase stator currents to two-phase α-β current is called Clarke transformation. For later implementation, the context for the Clarke transform in the time domain is of interest; see equation (3.59).

$$
\begin{bmatrix} i_\alpha \\ i_\beta \end{bmatrix} = \begin{bmatrix} 1 & 0 & 0 \\ \frac{1}{\sqrt{3}} & \frac{2}{\sqrt{3}} & 0 \end{bmatrix} \begin{bmatrix} i_a \\ i_b \\ i_c \end{bmatrix} \qquad (3.59)
$$

As depicted in Figure 3.5, the current space vector $\underline{\vec{\imath}}_{\alpha\beta}$ in the stator coordinate system equals the sum of the torque-forming component $\underline{\vec{\imath}}_{T|\alpha\beta}$ rotating with the speed ω_S and the fault component $\underline{\vec{\imath}}_{F|\alpha\beta}$ rotating with the speed ω_F; see equation (3.60).

$$
\underline{\vec{\imath}}_{\alpha\beta} = \underline{\vec{\imath}}_{T|\alpha\beta} + \underline{\vec{\imath}}_{F|\alpha\beta} = \hat{\imath}_T \cdot e^{i(\omega_S \cdot t)} + \hat{\imath}_f \cdot e^{i(\omega_F \cdot t + \theta)} \qquad (3.60)
$$

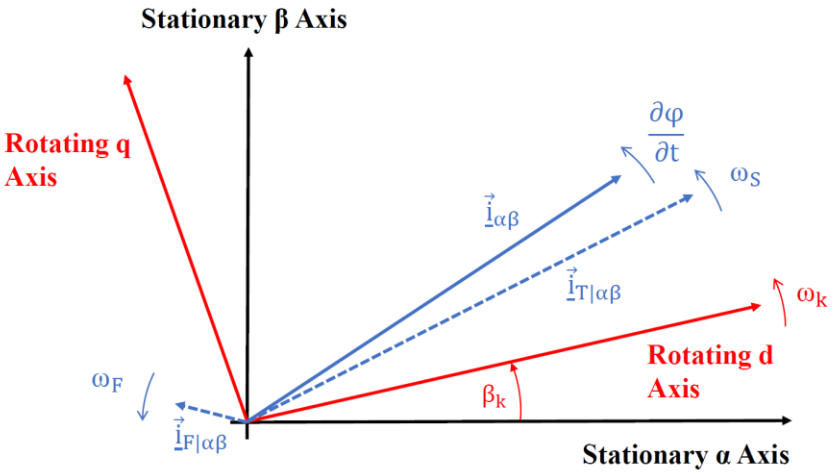

Figure 3.5: Current space vector in stator coordinate system and visualization of the rotating reference frame

The α-current in the time domain equals the part of $\underline{\vec{\imath}}_{\alpha\beta}$ at the stationary α-axis and the β-current of the stationary β-axis. Consequently, in the time domain, two oscillations with a phase shift of 90° remain, which is illustrated in Figure 3.6.

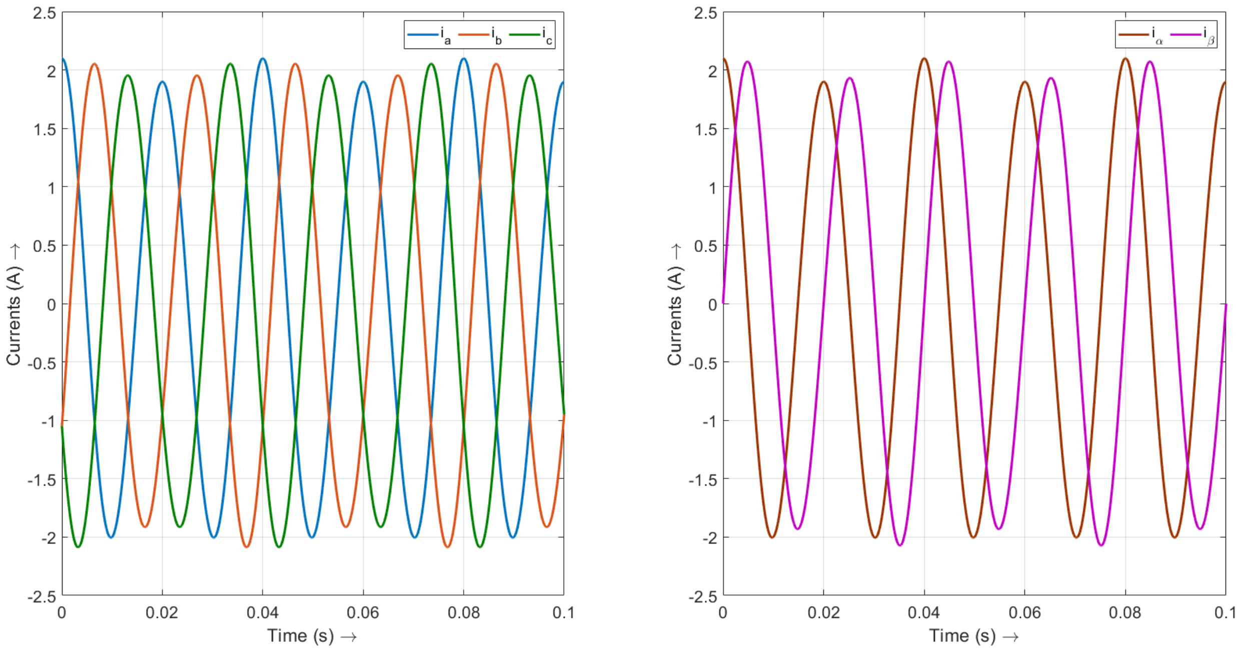

Figure 3.6: 3-phase current (left) and 2-phase α- and β-current after Clarke transform (right)

For fault detection, the length of the vector $\vec{\underline{\imath}}_{F|\alpha\beta}$ is of interest. There are two approaches for determining the length of $\vec{\underline{\imath}}_{F|\alpha\beta}$. Both approaches are based on the Park transform, in which the stator fixed α-β current $\vec{\underline{\imath}}_{\alpha\beta}$ is transformed to the rotor fixed d-q current $\vec{\underline{\imath}}_{dq}$. This is implemented by multiplying $\vec{\underline{\imath}}_{\alpha\beta}$ by the phase rotator $e^{-i\beta_k}$, which is rotating with the speed ω_k; see equation (3.61).

$$\vec{\underline{\imath}}_{dq} = \vec{\underline{\imath}}_{\alpha\beta} \cdot e^{-i\beta_k} \tag{3.61}$$

For the Park transform, the time-based context is also important for the later implementation; see equation (3.62).

$$\begin{bmatrix} i_d \\ i_q \end{bmatrix} = \begin{bmatrix} \cos\beta_k & \sin\beta_k \\ -\sin\beta_k & \cos\beta_k \end{bmatrix} \begin{bmatrix} i_\alpha \\ i_\beta \end{bmatrix} \tag{3.62}$$

In most cases where the Park transform is implemented for motor control, ω_k equals the speed of the FC ω_S. However, as in our application $\vec{\underline{\imath}}_{F|\alpha\beta}$ is of interest, there are two ways to adapt the Park transform, which will be presented in the next two sections. The final step of both approaches is the normalization of the result, by calculating the severity factor SF, see equation (3.61).

$$SF = \frac{\hat{\imath}_F}{\hat{\imath}_T} \cdot 100\% \tag{3.63}$$

3.3.1 Approach A: Adapted Frame Speed

The first option for obtaining $\vec{\underline{\imath}}_{F|\alpha\beta}$ is to rotate the d-q coordinate system with the speed of the oscillation frequency ($\omega_k = \omega_F$). To calculate the current vector in d-q coordinates, the standard equation for the Park transform is used; see equation (3.64).

$$\vec{\underline{\imath}}_{dq} = \vec{\underline{\imath}}_{\alpha\beta} \cdot e^{-i(\omega_F \cdot t)} \tag{3.64}$$

If equation (3.60) is inserted into equation (3.64), equation (3.65) results for the current vector $\vec{\underline{\imath}}_{dq}$ in the d-q coordinate system.

$$\vec{\underline{\imath}}_{dq} = \hat{\imath}_f \cdot e^{i\theta} + \hat{\imath}_T \cdot e^{i[(\omega_S - \omega_F)\cdot t]} \tag{3.65}$$

The rotating current vector $\vec{\underline{i}}_{dq}$ equals the sum of the vectors $\vec{\underline{i}}_{T|dq}$, rotating at the speed $\omega_S - \omega_F$ and the stationary vector $\vec{\underline{i}}_{F|dq}$; see Figure 3.7. If ω_F is greater than ω_S, both $\vec{\underline{i}}_{dq}$ and $\vec{\underline{i}}_{T|dq}$ will rotate in the other direction.

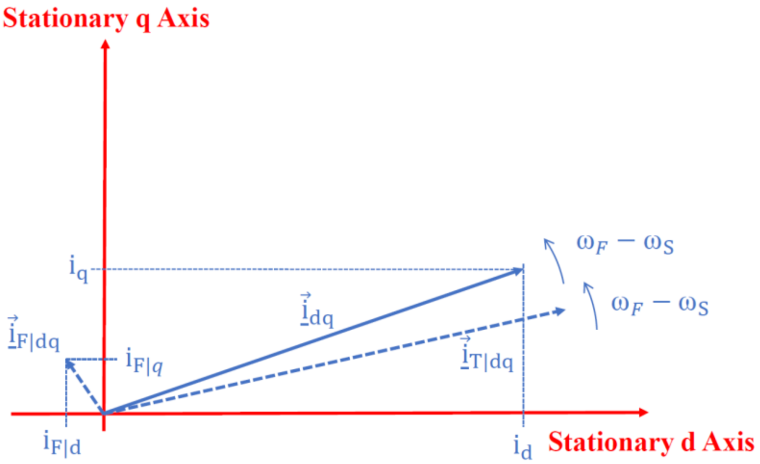

Figure 3.7: Current space vector in the d-q coordinate system.

If the time-dependent quantities are considered, i_d and i_q consist of a DC component and an alternating current component, as can be seen in equation (3.66).

$$\begin{aligned} i_d &= i_{F|d} + i_{T|d} \cdot cos\big((\omega_S - \omega_F)t\big) \\ i_q &= i_{F|q} + i_{T|q} \cdot sin\big((\omega_S - \omega_F)t\big) \end{aligned} \tag{3.66}$$

The curves of equation (3.66) are depicted in Figure 3.9. What stands out is the changed frequency of the main oscillation due to the use of the Park transform. The frequency of the oscillations now equals $\omega_S - \omega_F = 2\pi \cdot 25Hz$. The second and most important fact is that the DC offsets $i_{F|d}$ and $i_{T|q}$ are visible in the signal.

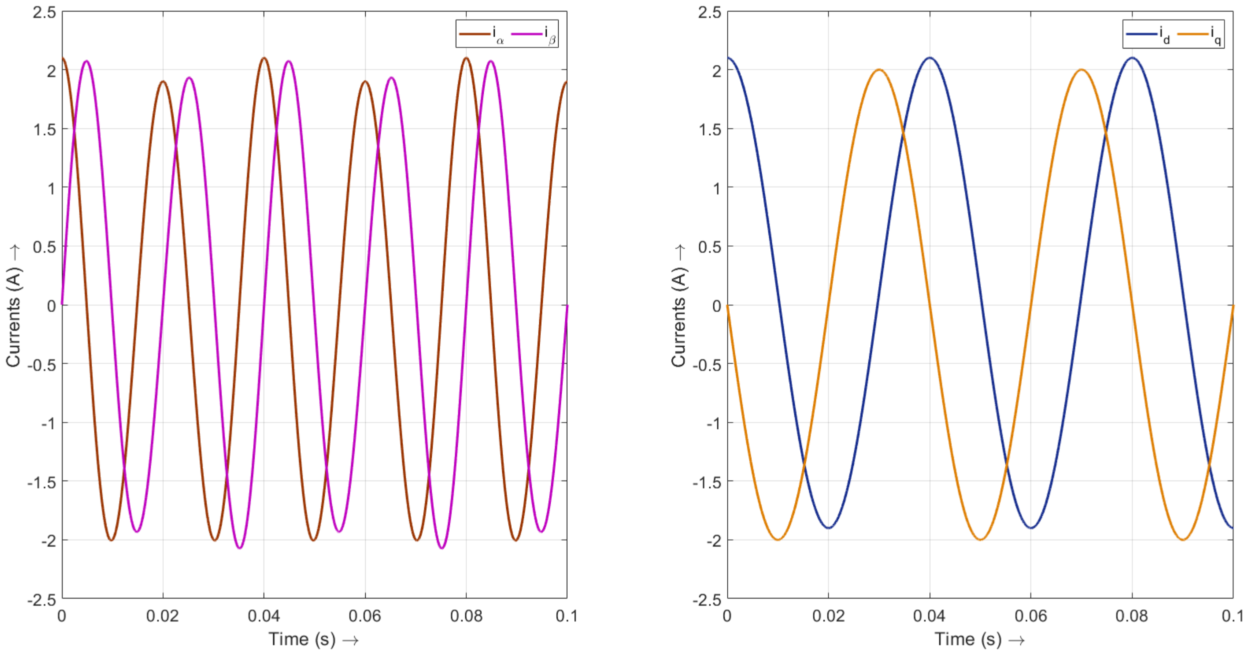

Figure 3.8: α- and β-current (left) and curves of d- and q-current after use of Park transform on the basis of equation (3.64)

The amplitude $\hat{\imath}_f$ can be calculated from the geometric sum of $i_{F|d}$ and $i_{F|q}$; see equation (3.67).

$$\hat{\imath}_f = \sqrt{{i_{F|d}}^2 + {i_{F|q}}^2} \tag{3.67}$$

If the DC parts of i_d and i_q are calculated, the amplitude $\hat{\imath}_\mathrm{f}$ can be calculated from this. After applying the Park transform with $\omega_k = \omega_F$, only the DC part of the two oscillations of i_d and i_q has to be calculated.

3.3.2 Approach B: Additional Phase Rotator

In the second option, the speed of the d-q coordinate system is first equated with the fundamental frequency, as is common in the control of motors ($\omega_k = \omega_S$); see equation (3.68).

$$\underline{\vec{\imath}}_{dq} = \underline{\vec{\imath}}_{\alpha\beta} \cdot e^{-i(\omega_S \cdot t)} \tag{3.68}$$

Equation (3.69) results for $\underline{\vec{\imath}}_{dq}$ if equation (3.60) is inserted into equation (3.68).

$$\underline{\vec{\imath}}_{dq} = \hat{\imath}_T + \hat{\imath}_F \cdot e^{i[(\omega_F - \omega_S) \cdot t + \theta]} \tag{3.69}$$

As is known from the control of motors, $\vec{\underline{i}}_{dq}$ equals the amplitude of the torque-forming component $\hat{\imath}_{\mathrm{T}}$, that is used as a control variable, with the addition of an oscillation with the speed $\omega_F - \omega_S$. This becomes visible when the curves of i_d and i_q are considered; see Figure 3.9.

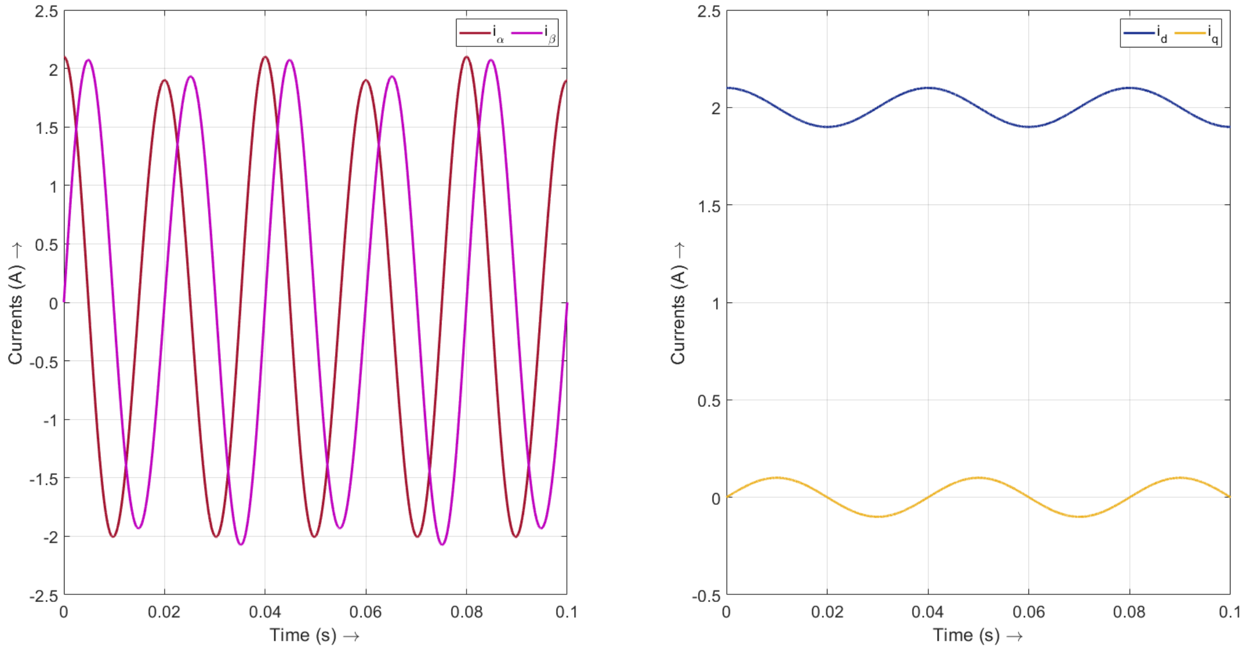

Figure 3.9: α- and β-current (left) and curves of d- and q-current after use of Park transform on the basis of equation (3.68)

As the next step, $\hat{\imath}_{\mathrm{T}}$ is subtracted from $\vec{\underline{i}}_{dq}$ in equation (3.69), with the consequence that only the oscillation remains in the signal; see equation (3.70).

$$\vec{\underline{i}}_{dq,osc} = \hat{\imath}_F \cdot e^{i[(\omega_F - \omega_S)\cdot t + \theta]} \tag{3.70}$$

In order to calculate the amplitude $\hat{\imath}_F$ of $\vec{\underline{i}}_{dq,osc}$, a second Park transform at the speed of the oscillation $\omega_F - \omega_S$ is applied on $\vec{\underline{i}}_{dq,osc}$; see equation (3.71).

$$\vec{\underline{i}}_{dq2} = \vec{\underline{i}}_{dq,\mathrm{osc}} \cdot e^{-i((\omega_F - \omega_S)\cdot t)} \tag{3.71}$$

As a result, we obtain equation (3.72), which equals a stationary value with the amplitude $\hat{\imath}_{\mathrm{F}}$ and the angle θ.

$$\vec{\underline{i}}_{dq2} = \hat{\imath}_F \cdot e^{\theta} \tag{3.72}$$

If equation (3.72) is compared with the stationary part of equation (3.65), the same result is obtained. Consequently, both approaches deliver the same result.

3.3.3 Filter Design

In both presented variants for the calculation of the amplitude $\hat{\imath}_{\mathrm{F}}$, one filter each is required. In approach A, it is needed to filter the oscillation $\hat{\imath}_T \cdot e^{i[(\omega_S-\omega_F)\cdot t]}$ of equation (3.65), and in approach B, it is needed to calculate the mean value of $\vec{\underline{\imath}}_{dq}$; see equation (3.69). To implement such filters, the most efficient way is to use low-pass filters. In the framework of this work, the focus is on the use of a first-order Butterworth filter, whose transfer function can be calculated using equation (3.73), where T equals the sample time of the MPU. The filter makes the implementation easy. However, the cut-off frequency ω_c has to be chosen relatively small in order to remove the oscillation to the greatest extent possible. This causes the time constant of the filter T_F to become relatively high, which makes the system slow, which can be a problem in dynamic systems. But in the application as a circulation pump, for example, no rapid load changes are to be expected (Eckl, 2019b).

$$H(z) = \frac{1-e^{\omega_c T}}{z-e^{\omega_c T}} = \frac{1-e^{\frac{T}{T_F}}}{z-e^{\frac{T}{T_F}}} \tag{3.73}$$

The larger T_F is selected, the lower the proportion of oscillations at the output of the filter. Depending on the application, however, there is a certain requirement for the speed of the algorithm, which is influenced exclusively by the time constant of the filter. The relation for the gain $|F|$ of a continuous T1 link, as shown in equation (3.74), indicates that full damping ($|F| = 0$) of a frequency ω (if $\omega > \omega_c$) is only possible with infinite T_F.

$$|F| = \frac{1}{\omega \cdot T_F} \tag{3.74}$$

In practice, however, complete removal of the oscillation is not necessary either, since the resolution of the MPU is finite. Oscillations at the output of the filter with an amplitude $\hat{\imath}_{filtered}$ smaller than the resolution of the MPU Δi can therefore not be displayed. An upper limit for T_F can be determined using equation (3.75).

$$\hat{\imath}_{filtered} \geq 0.5 \cdot \Delta i \tag{3.75}$$

For $\omega > \omega_c$, $\hat{\imath}_{filtered}$ is calculated based on the multiplication of $|F|$ with the input amplitude $\hat{\imath}_{\text{input}}$ at the frequency ω; see equation (3.76).

$$\hat{\imath}_{filtered} = \frac{1}{\omega \cdot T_F} \hat{\imath}_{input} \tag{3.76}$$

After consideration of equations (3.75) and (3.76), we obtain equation (3.77).

$$T_F \leq \frac{2\hat{\imath}_{input}}{\omega \cdot \Delta i} \tag{3.77}$$

Consequently, T_F depends on the amplitude of the oscillation at the input of the filter, the frequency of the oscillation to be filtered, and the resolution of the MPU. $\hat{\imath}_{input}$ and ω depend on the approach (approach A or approach B) that is used for feature extraction. If approach A is used, higher values for $\hat{\imath}_{input}$ are expected since $\hat{\imath}_{input}$ equals the torque-forming component $\hat{\imath}_T$. In this case, ω equals $|\omega_S - \omega_F|$; see equation (3.65).

For example, if approach A is used to investigate the frequency bands $f_{r,pump}$ of a PMSM ($s = 0$) based on equation (2.14), we obtain the relationship (3.78).

$$T_F \leq \frac{p}{\pi \cdot \Delta i} \frac{\hat{\imath}_T}{f_s} \tag{3.78}$$

T_F depends on the two variable parameters $\hat{\imath}_T$ and f_s and the constant $\frac{p}{\pi \cdot \Delta i}$. It can be seen here that it is quite possible to adjust the time constant variable to the current operating point of the motor, provided that $\hat{\imath}_T$ and f_s are known. For example, an eight-pole motor with a current measuring range from -4.5 to 4.5 A at 12-bit resolution and a current consumption of $\hat{\imath}_T = 2.9$ A at a speed of 2500 rpm leads to a filter time constant of $T_F = 10.1s$.

3.3.4 Comparison of the Approaches

Finally, in this section the two approaches presented in sections 3.3.1 and 3.3.2 for feature extraction based on ARFT will be compared with each other. Figure 3.10 depicts the different steps of the two approaches. The values shown with arrows are vectors, whose number of rows equals the number of investigated frequency bands.

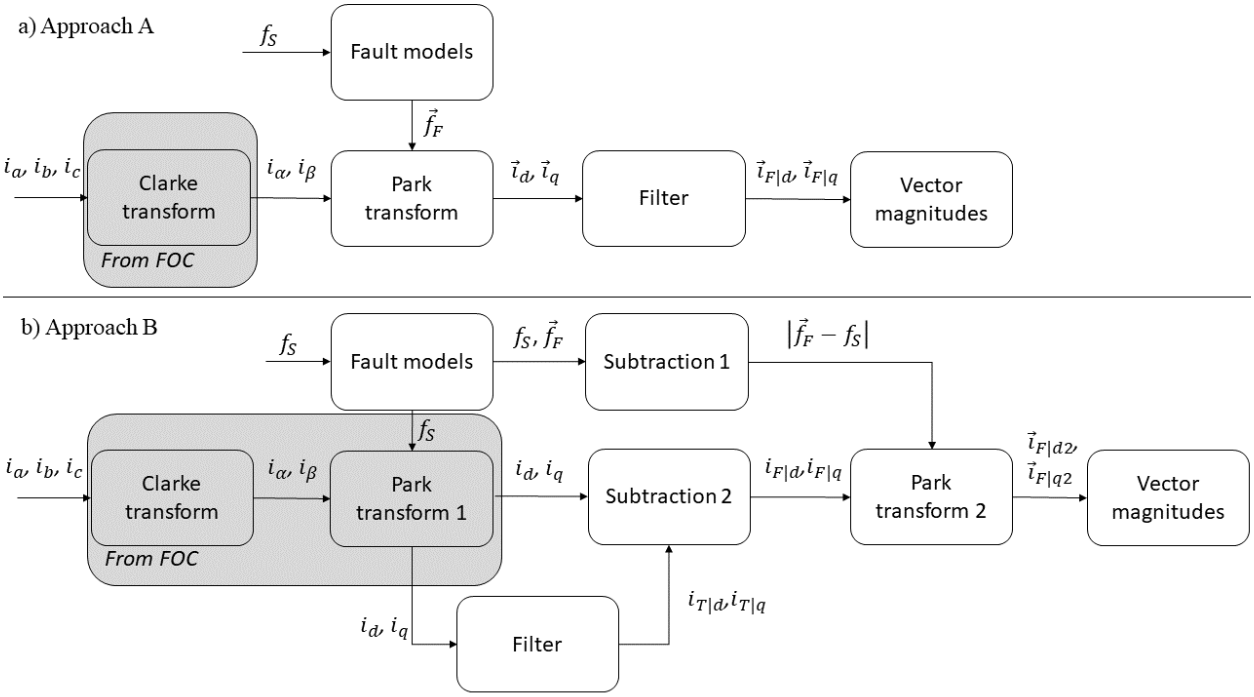

Figure 3.10: Schemes of the two approaches to determine the amplitude of the current oscillation

Approach A uses a total of 5 blocks, while approach B requires the use of a total of 8 blocks. For approach B, two extra subtraction blocks are needed, as well as one additional block for the second Park transform. However, in approach B, the block “Park transform 1” is only needed if there is no implementation of an FOC on the control board of the motor. The two additional subtraction blocks are needed to adjust the speed of the coordinate system for Park transform 2 (“subtraction 1”) and to eliminate the offset in the signal after the use of Park transform 1 (“subtraction 2”). Consequently, from the general design, approach A is a more efficient implementation method compared to approach B.

However, approach A also has one major drawback compared to approach B: the higher time constant of the filter, as described in section 3.3.3. This can be critical, especially in applications where dynamic load changes are possible. Also, a more thorough view at the required mathematical equations enables the consideration of another aspect. If $f_S > f_F$, which is true for all frequency bands that are investigated left of the fundamental frequency, then the absolute value of $f_F - f_S$ equals $f_F + f_S$. In this case, one less transform is needed in the block “Park transform 2”. On the other hand, it has to be considered that information can be lost, since the two amplitudes of the stator current ($f_s \pm f_F$) are combined into one amplitude in the block “Park transform 1”. Also, in approach B, only the two signals i_d and i_q, have to be filtered, compared to the vectors $\vec{\imath}_d$ and $\vec{\imath}_q$ of approach A, which can lead to reduced computational costs. Table 3.2 gives an overview of the advantages and disadvantages of the two presented feature extraction approaches for ARFT.

Table 3.2: Advantages and disadvantages of the two presented feature extraction approaches for ARFT

Approach A: Adapted Frame Speed	Approach B: Additional Phase Rotator
+ Fewer elements	− More elements
+ No information loss for frequencies left of the fundamental component	− Information loss for frequencies left of the fundamental component
− Only Clarke transform can be used from FOC	+ Clarke transform and Park transform can be used from FOC
− Slower algorithm due to high filter time constants	+ Fast computation

3.4 Time-Frequency Transformation

A variety of mathematical tools are available for time-frequency transformation, which are implemented depending on the application. In the field of technical diagnosis of motors, time-frequency transforms have been used in current-based analysis, although they have been also employed for the analysis of other quantities (vibrations, stray-fluxes, torques, etc.). Depending on the startup time of a motor, the motor current completes only a few complete oscillations, which requires an optimized analysis in the time-frequency domain. Two methods, in particular, are considered here, wavelet transform (continuous and discrete) and Short-time Fourier transform (STFT), despite there are also other time-frequency transforms that have been employed in the technical literature of the area (Hilbert-Huang transforms, Wigner-Ville or Choi-Williams Distributions, etc.). In recent years, STFT utilizing a Gaussian function for windowing, called Gabor transform, has demonstrated great performance in terms of high computation speed and resolution.

In general, the STFT of a function $f(t)$ is calculated on the basis of equation (3.79), where $g(t-\tau)$ is the window function, an even function with positive real values, centered at τ.

$$STFT(\tau,\omega) = \int_{-\infty}^{\infty} f(t)g(t-\tau)e^{-j\omega t}dt \tag{3.79}$$

The choice of the window function $g(t)$ has an influence on concentration and resolution in the expansion (Jones, 1990). On the other hand, measuring the performance of the selected window remains an issue (Riera-Guasp, 2012). The normalized Gaussian function $g(t)$ is calculated on the basis of equation (3.80) with respect to the deviation parameter α (Fernandez-Cavero, 2021).

$$g(t) = \sqrt[4]{\frac{\alpha}{\pi}} \cdot e^{-\frac{\alpha \cdot t^2}{2}} \tag{3.80}$$

The standard deviation σ_t is given by equation (3.81).

$$\sigma_t = \frac{1}{2\alpha} \tag{3.81}$$

The high resolution of the Gabor transform is justified by the theoretical fact that the Fourier transform of the Gaussian function equals a Gaussian function; see equation (3.82).

$$g(f) = \sqrt[4]{\frac{1}{\pi\alpha}} \cdot e^{-\frac{(2\pi f)^2}{2\alpha}} \tag{3.82}$$

With the standard deviation σ_f, which is interpreted as the bandwidth of the Gaussian function in the frequency domain, we obtain equation (3.83).

$$\sigma_f = \frac{\alpha}{8\pi^2} \tag{3.83}$$

This has the consequence that the product of time and frequency resolution is minimized compared to the use of other windowing functions (Heisenberg uncertainty); see equation (3.84).

$$\sigma_t \sigma_f = \frac{1}{4\pi} \tag{3.84}$$

Equation (3.84) describes the Heisenberg uncertainty principle applied to time-based signals. Equality of the function is only given if a Gaussian function is applied for $g(t)$. If other windows are used in equation (3.79), the product of $\sigma_t\sigma_f$ will be bigger than the constant $\frac{1}{4\pi}$; see equation (3.85) (Riera-Guasp, 2012).

$$\sigma_t \sigma_f > \frac{1}{4\pi} \tag{3.85}$$

In order to make a choice for the value α, the slope P, which is the ratio of σ_f and σ_t, as shown in equation (3.86), was introduced. If knowledge about the trajectory of the frequency of a fault in the time-frequency domain is available, P can be selected based on the slope in Hz/s (Pons-Llinares, 2013).

$$P = \frac{\sigma_f}{\sigma_t} \tag{3.86}$$

The trajectories of fault frequencies during the startup of a motor ($f_S = const.$) depend on the motor supply. In the case of line-start IMs, the components that are independent of the slip are constant (i.e. horizontal straight lines) in the time-frequency map. Slip dependency evolves in a very convenient way. For example, broken rotor bars lead to a significant V-shape in the time-frequency map. In the case of VSD-fed motors, the supply frequency changes during the startup of the motor from 0 Hz to the final operating frequency. Consequently, all frequencies show a certain pattern. If the stator frequency is changed, the frequency component of the eccentricity also changes. The theoretical evolutions at the ramped startup of the dynamic eccentricity components ($v = 1$ and $n_d = 1$) of an eight-pole PMSM are illustrated in Figure 3.11. If there is dynamic eccentricity in a motor, the evaluation of the ATCSA should show increased amplitudes at the location of the red lines. The same characteristic pattern is expected for load oscillations and pump faults, which influence the frequency $f_{r,pump}$.

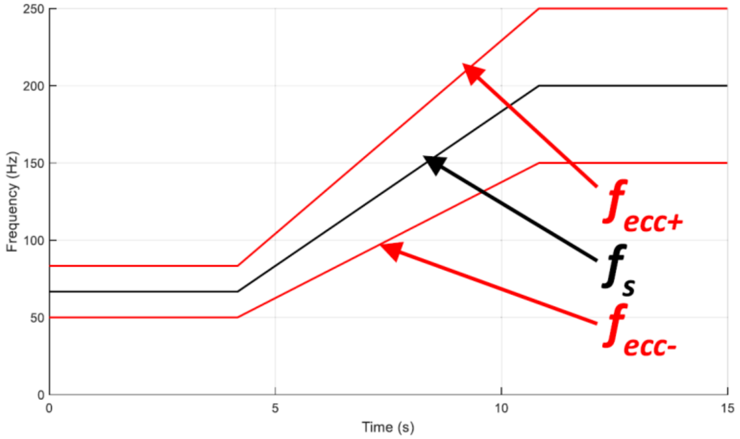

Figure 3.11: Theoretical curves of the dynamic eccentricity components given by equation (2.17) with $\boldsymbol{v = 1}$ and $\boldsymbol{n_d = 1}$, for the start of an eight-pole PMSM ($\boldsymbol{n_{Start} = 1000 rpm}$ and $\boldsymbol{n_{End} = 3000\ rpm}$)

4 Methods

In this section, all the methods that were needed for the analysis in the framework of this thesis will be described in detail. In total, three different kinds of pumps were measured, and their design and parameters will be discussed first. Next, it will be discussed how certain faults were implemented in these tested elements. After that, the test benches used to develop the experiments will be described. The section will be rounded off by the presentation of the analysis methods and parameters used in the analyses.

4.1 Test Objects

In summary, three different types of pumps were measured in order to validate the proposed methodologies: a wet-rotor pump, a dry-runner pump, and a submersible pump. More details about the individual test objects are described below.

4.1.1 Wet-Rotor Pump

Two different wet-rotor pumps with the same design, but different sizes, were measured in several measurement campaigns. This pump type is applied in one-pipe and two-pipe systems, underfloor heating systems, boiler or primary circuits, storage tank circuits, solar power systems, and heat pumps. The motor power of the first pump was 800 W and that of the second one 150 W. Note that the power rating is based on the rated mechanical power of the motor. The maximum power consumption (typical specification for these pumps) indicated on the pump type plates is higher than the indicated values in both cases. Figure 4.1 shows a picture of the 800 W pump installed in a test bench.

Figure 4.1: Picture of the measured wet-rotor pump with 800 W

As motor technology, a PMSM with a concentrated stator winding (tooth coil winding) was used. The rotor was built with surface-mounted permanent magnets. To control the motor, sensorless field-oriented control was applied. The motor currents were measured on the low side of the insulated gate bipolar transistors utilizing three shunt resistors. The current signals are resolved in 12 bit. The pump was constructed as a wet-rotor pump, and the rotor was sealed against the stator with a can. The rotor of the pump ran in a can filled with water. The rotor shaft was mounted in hydrodynamic journal bearings. In order to cool the stainless steel can, the water circulated in the can. This was achieved by channels in the journal bearings and a hollow shaft. For the impeller, a radial impeller was used.

Regarding the MPU, two STM32F405 of the Cortex-M4 family were used on the pump. One MPU was used as a control board (sample time of 0.3 s) and the other one for motor control (sample time of 100 µs); see Figure 4.2. Both MCUs shared parameters, e.g., for control, over an internal bus. The pump was connected to the test bench computer via a 3-phase signal cable with a USB-Nano-485 signal converter. The current values of flow, head, speed, and power can be captured via Modbus, among others. Furthermore, set values, such as the set speed or the set head, can be set from the test bench computer. Depending on the measurement, signal exchange was realized via the software LabVIEW or Pactware. Pactware also ensured the implementation of a modified firmware, which was needed for the field test of ARFT.

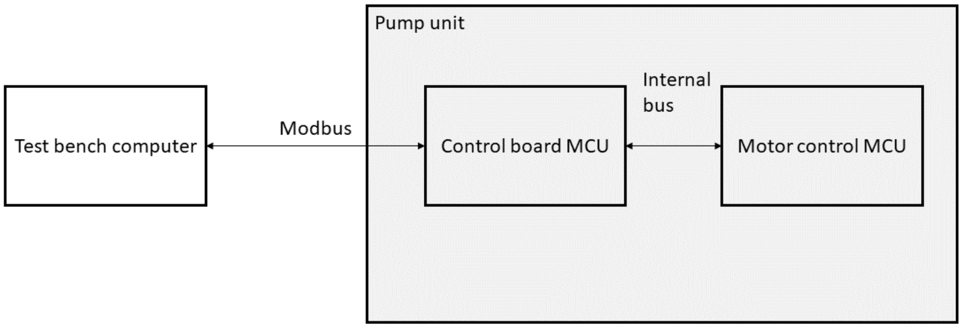

Figure 4.2: Schema of the hardware setup of the two wet-rotor pumps

The parameters of the two Devices Under Test (DUTs) are listed in Table 4.1. Two design variants of DUT1 were measured in different measurement campaigns. The difference was that the cans of the standard variant of DUT1 were welded, which allows no dismounting of the rotor and thus no possibility to manipulate the bearings. To solve this problem, special cans were used where screws can be used to dismount the rotor from the can.

Table 4.1: Parameters of the measured wet-rotor pumps

	DUT1	**DUT2**
Rated power	800 W	150 W
Nominal head	18 m	6 m
Nominal diameter of pipe connection	50 mm	25 mm
Speed	1000 – 3400 rpm	1000 – 3600 rpm
Number of impeller blades	7	7
Number of pole pairs	4	3

4.1.2 Dry-Runner Pump

As a second test object, a dry-runner in-line single-stage pump with a power of 180 W was investigated; see Figure 4.3 a). The pump design is characterized by a rigid connection between pump and motor. Application examples of this pump type are service water supply systems, heating systems, industrial recirculation systems, air conditioning systems, cooling circuits, swimming pools, and water supply systems. It is typical for this pump design that a mechanical seal is used to seal the shaft. As a motor, a surface-cooled squirrel-cage IM with an efficiency class of IE3 was used to drive the pump. The impeller of the pump was designed as a closed radial impeller with eight impeller channels and a diameter of 125 mm. The flanges were of the size DN50. As bearings, radial ball bearings were used in the motor. The windings of the stator were connected in star form in all measurements. The motor can be powered from the mains or from a VSD. The commercial VSD "Pumpdrive" with a maximum power of 370 W was used for the experiments; see Figure 4.3 b).

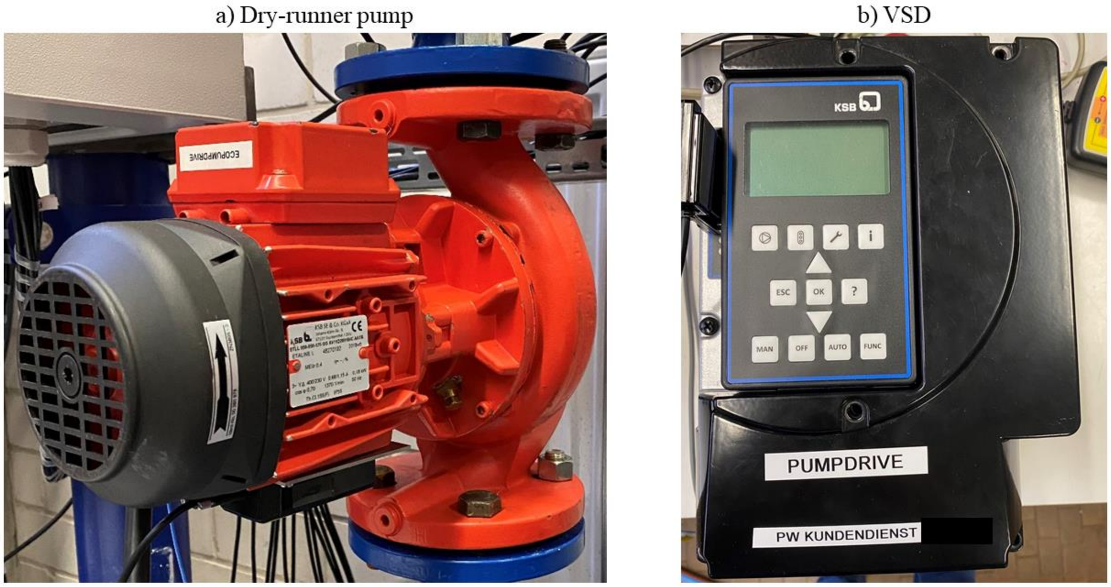
a) Dry-runner pump

b) VSD

Figure 4.3: Picture of the measured a) dry-runner pump; b) VSD

Further important parameters of the pump are summarized in Table 4.2.

Table 4.2: Parameters of the measured dry-runner pump

	DUT3
Rated power	180 W
Rated speed	1370 rpm
cos φ	0.7
Number of impeller blades	8
Number of pole pairs	2

4.1.3 Submersible Pump

The measured ESP is used in different applications, for example wastewater transport, management and treatment plants, drainage systems, stormwater transport, recirculation, and sludge treatment. It was designed as a fully floodable submersible motor pump, where the motor was directly fitted to the pump via a flange. For the impeller, an open two-vane impeller was used. A squirrel cage IM with a nominal power of 7.7 kW was used to drive the pump. The motor had a nominal current of 15.9/9.2 A at 400/690 V and a nominal speed of 1403 rpm. The guaranteed head of the pump was 9 m at a flow of 100 m^3/h and 1403 rpm. The most relevant parameters are summarized in Table 4.3. The motor was fed by a VSD with the option to change the operation direction of the ESP via the control panel.

Table 4.3: Parameters of the submersible pump

	DUT4
Rated power	7.7 kW
Nominal head	9 m
Nominal flow	100 m^3/h
Rated speed	1403 rpm
Nominal voltage	400/690 V
Number of impeller vanes	2
Number of pole pairs	2

4.2 Fault Implementation

During the tests, the different DUTs were examined with different faults. Their implementation of will be described in the following sections. However, not all DUTs were examined with all faults. Table 4.4 gives an overview of which DUT was measured with which fault.

Table 4.4: Combination of test objects and implemented faults in the measurements

	DUT1	**DUT2**	**DUT3**	**DUT4**
Clogging	✓	✓	✓	✓
Hydraulic blockage	✓	✓	✓	x
Cracked impeller	✓	x	x	x
Bearing damage	✓	x	x	x
Dry-running rotor	✓	x	x	x
Dry running	✓	x	x	x

4.2.1 Clogging

The *clogging* fault was implemented in all DUTs. Both the design of the impeller and the type of application where the DUTs are used in the field differed. For this reason, there were also two different ways of implementing the *clogging* fault. First, it will be described how the fault was implemented in the wet-rotor and the dry-runner pump, which both used a closed radial impeller. After that, the procedure of clogging the submersible pump, in which an open impeller was used, will be illustrated.

4.2.1.1 Wet-Rotor and Dry-Runner Pump

Two different materials were used to implement the *clogging* fault in the wet-rotor and the dry-runner pump. Both materials have been successfully used to prevent flow through a particular channel. One option was to use foam with armor tape, which is depicted in Figure 4.4a). However, with this approach, there was a risk of friction of the armor tape at the housing of the pump. In order to prevent the risk of additional friction, a second approach was applied. Here, polystyrene was used to clog the channel of the impeller, as depicted in Figure 4.4b). With the help of these two approaches, it was possible to clog a variable number of channels, depending on the total number of channels of the pump. In order to minimize the measurement effort, only adjacent channels were clogged in the case of multiple channel clogging. It is possible, especially if the flow is high, that the clogging is solved. Based on the experience of several experiments, this procedure causes a noticeable sound and an increase of flow and head after releasing the clogging. After this happened, the experiment was repeated. After measuring the manipulated pump, we checked whether the impeller was still clogged. The first step was to remove the impeller including the drive from the pump casing, which was easily accomplished by loosening four screws. After the appropriate number of channels were clogged, the impeller including the drive was reinstalled in the pump housing.

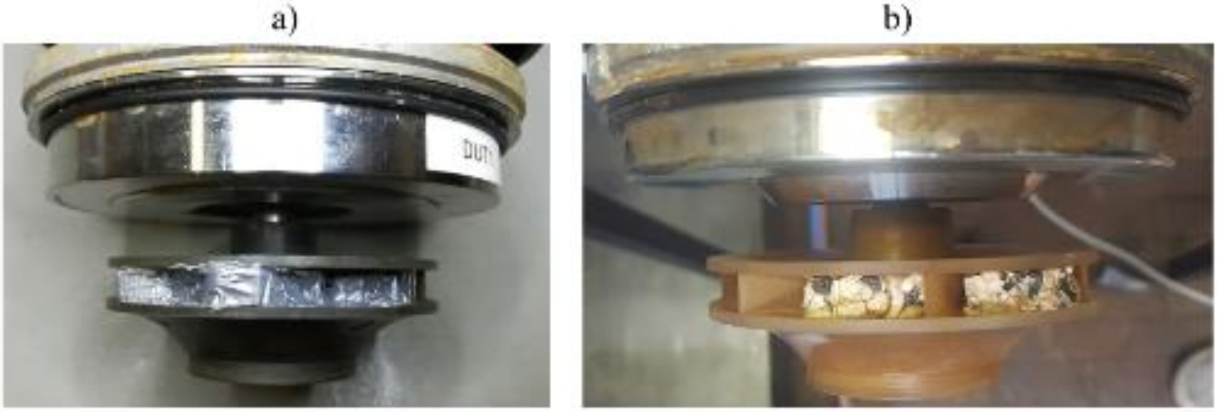

Figure 4.4: Examples of the implementation of the fault *two clogged impeller channels*; (a) foam and armor tape; (b) polystyrene

4.2.1.2 Submersible Pump

In the case of the submersible pump, the *clogging* fault was implemented with the help of a rag. This rag was inserted into the pump sump by means of a special filling device and was then pulled into the impeller of the pump. Figure 4.5 depicts the measured ESP in healthy condition before it was started (a) and in the condition of clogging (b). Despite the fact that it looks like a complete clogging here, the pump continued to provide some flow and head.

Figure 4.5: Standstill ESP impeller in healthy condition (a) and running with clogging (b)

4.2.2 Cracked Impeller

To implement the fault *cracked impeller channel*, part of one impeller blade was damaged, as shown in Figure 4.6. With the help of a file, a cut with a depth of 5 mm and a width of 4 mm was sawn into the impeller. First, as with the clogging fault, the impeller and the drive were removed from the pump casing. In addition, the impeller was pulled off the shaft with a special pull-off adapter. After the manipulation, the impeller was re-attached to the shaft.

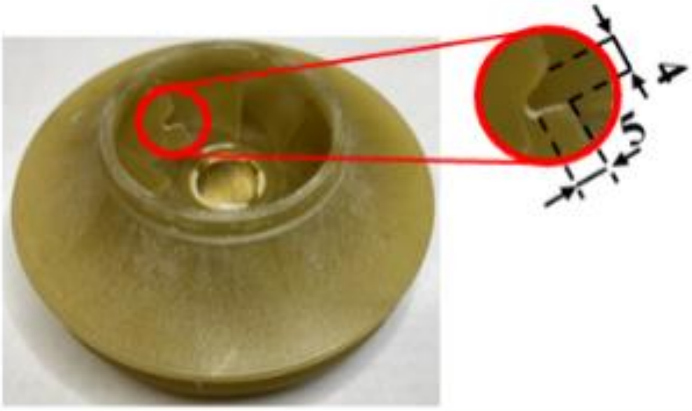

Figure 4.6: Implementation of the fault *impeller crack*

4.2.3 Hydraulic Blockage

A hydraulic blockage means that the pipe on the pressure side of the pump does not allow any flow through the piping system. In the field, this fault can be provoked, e.g., by deposits in the piping system or faulty control of throttle valves. In the measurements in the framework of this work, the fault *hydraulic blockage* was provoked by closing the valve on the pressure side of the measured pump. To avoid air formation and other turbulences, the respective valves on the suction side of the pump remained open.

4.2.4 Bearing Damage

For wet-rotor pumps, the use of journal bearings is recommended. Materials for such bearings include rubber, carbon graphite, plastic, and wood. Over the lifetime of a pump, the journal bearings can wear out. The wear process is influenced by many factors, such as speed, load, or contamination of the lubricant.

The implementation of this fault was only possible with the prototype of the glandless pump; see section 4.1.1. After removing the impeller and the drive from the pump casing and pulling the impeller off the shaft, the can was disassembled into its individual parts to access the A- and B-bearings, as illustrated in Figure 4.7. The fault was provoked by grinding down the bushing of the journal bearing with the help of a lathe.

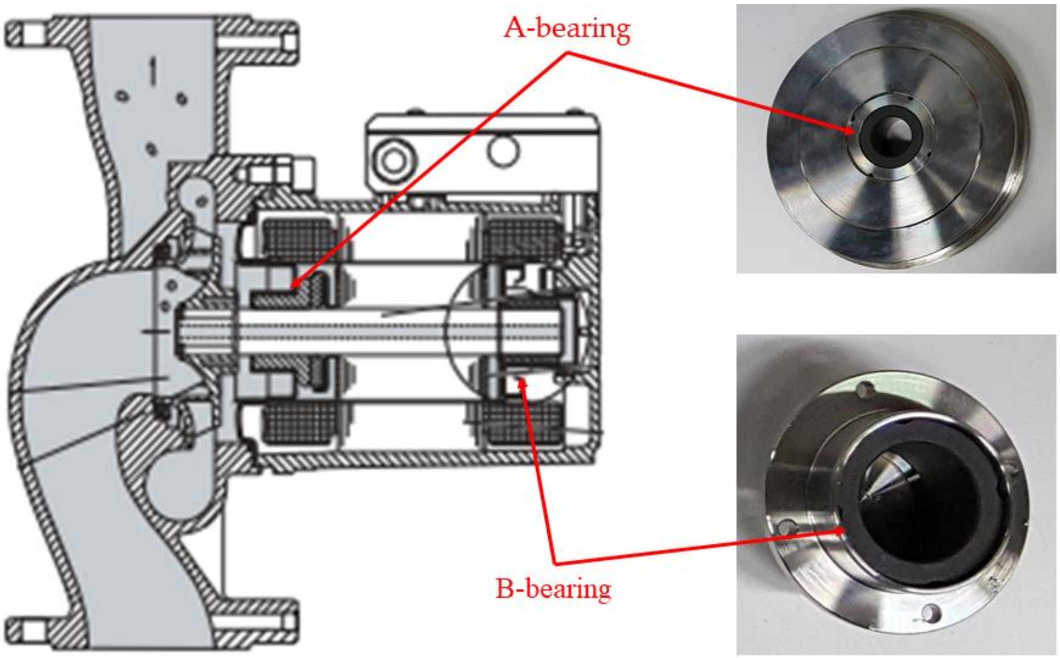

Figure 4.7: Location and picture of the journal bearings used

After grinding down the diameter of the bushing, a special measurement device was used to check the measure. After assembling the individual components and measuring, the measurement was taken again to validate whether the diameter had changed. However, no change in diameter was detected during the measurement in any case.

Figure 4.8: Measurement device for measuring the bushing diameter

4.2.5 Dry-Running Rotor

The rotor of this type of wet-rotor pumps is normally surrounded by water. The water is mainly needed to lubricate the journal bearings. Without water, no lubricating film can form between the shaft and the bearing. This can lead to increased heat development and wear of the journal bearings. The water enters the inside of the can via small holes and is pumped through the shaft, which is designed as a hollow shaft. If the water supply is stopped due to contamination, for example, the rotor can run dry. This *dry-running rotor* fault was provoked with the help of foam material and armor tape at the boreholes. The impeller of the pump was still surrounded by the fluid so that the pump was able to produce hydraulic power. Consequently, this fault differs from the fault *dry running*, where the impeller is running dry.

4.2.6 Dry Running

To implement the fault *dry running*, the entire test bench as well as the pump unit was cleared of water. This left only air under atmospheric pressure in the piping system. Due to the lack of water, the pump was no longer able to build up water pressure. Thus, the pressure signals of the test bench were used to verify that there was no water in the system.

4.3 Test Benches and Measurement Setup

A total of three test benches with different characteristics were used to measure the pumps. In the following, the multi-pump test bench will be described first, which allowed several pumps to be measured simultaneously. This is followed by a description of the pump test rig, which allowed measuring inline centrifugal pumps up to 2 kW. Finally, the wastewater test bench will be described, which was specially constructed for the measurement of wastewater pumps.

In all measurements in the pump test benches, attention was paid to ensuring that the inlet pressure at the suction nozzle of the pump was sufficiently high (NPSHa>NPSHr) in order to prevent cavitation in the pumps. Before the data acquisition was started, the pumps and the pressure sensors were vented at the intended nozzle.

4.3.1 Multi-Pump Test Bench

In the multi-pump test bench (see Figure 4.9), three pumps can be operated in parallel. The test bench consisted of five parallel vertical pipes. All pipes had a nominal diameter of DN100. In the three middle pipes, the pumps were installed ①. The water flowed through the outer pipes back to the suction ports of the pumps. A radiator was installed in the back of the test bench ②. It could be switched on in order to cool the water of the test bench. In each of the middle pipes, shut-off valves were installed on the suction and pressure sides of the pump ③. On the one hand, they were used to separate single strands from the test bench. On the other hand, they could be used to set the flow of a single strand and thus vary the pump load. Above the lower shut-off valve, expansion joints were installed to minimize the vibration level of the test bench ④. Pressure sensors (IFM PU5415) were installed on the pressure side and the suction side of the pumps ⑤. They were connected via 0-10 V signal to the data acquisition system of the test bench (NI USB-6363) ⑥. An ultrasonic flow meter could be used to measure the flow in the right pipe (Omega FDT-25) ⑦. This is especially interesting when measuring a single pump. Here, the left pipe was shut off. To guarantee safe pump operation, proper safety technology was applied. Both an electronic pressure switch (WIKA PSD-30) ⑧ and an electronic temperature switch (WIKA TSD-30) ⑨ were installed in the hydraulic circuit. Both were integrated into the enabling logic of the energy supply of the pumps. The pressure switch only allowed the absolute pressure of the test bench to be over 1 bar and lower than 5.5 bar. The lower threshold was applied to prevent damage to the test bench and measuring devices due to leakage. Additional mechanical protection was provided by a pressure relief valve, which was triggered at a pressure of 6 bar ⑩. The electronic temperature switch ensured that the temperature was below 50 °C. Both electronic switches were connected to a safety switchgear (Siemens 3TK2825-1BB40). An electronic time relay (3RP1555-1AP3O) was used to switch the pump supply on and off for certain periods of time. Additional components were two thermal expansion tanks, an inlet nozzle, and vent valves. With the help of the power analyzer Yokogawa PX8000 ⑪, the input values (U, I, power factor) of the pump were measured. The measurement devices ⑫ to ⑭ were used for high-precision measurement of the electric signals; for more details, see section 4.3.3.

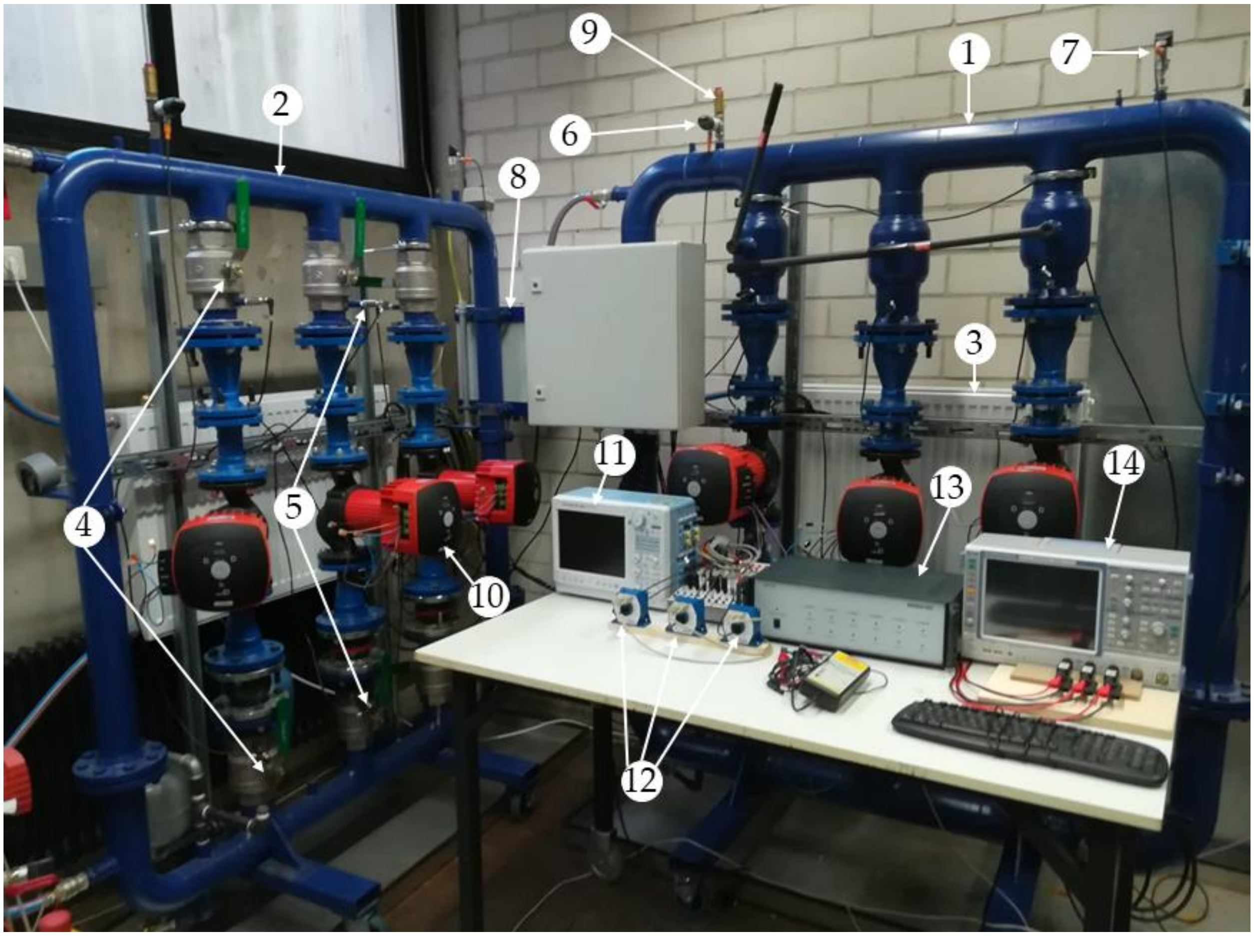

Figure 4.9: Test bench for condition monitoring and life-accelerated pump tests

4.3.2 Single-Pump Test Bench

The test bench for inline centrifugal pumps up to 2 kW consisted of a pressure vessel and pipelines in which the fluid was circulated by the pump unit through the closed hydraulic circuit. The test bench was constructed according to the German standard DIN EN ISO 9906. Two control valves connected in parallel ensured the throttling of the hydraulic system and thus a variation of the system characteristic curve. To enable measurement of the pump characteristics, both a differential pressure (WIKA DPT-10) and a flow sensor (ABB Watermaster FER100) were installed. Further measuring sensors included a fluid temperature sensor and an absolute pressure sensor. For the replacement of the pump unit, two ball valves blocked the circuit, so that only the water in the intermediate pipe had to be drained and thus it was not necessary to completely drain the water in the entire test bench. Control and acquisition of the measuring data was done by a data acquisition module (NI USB 6363), which was operated via a user interface on a PC. The program used for this purpose was programmed using the LabVIEW software, which enables automated test execution and evaluation.

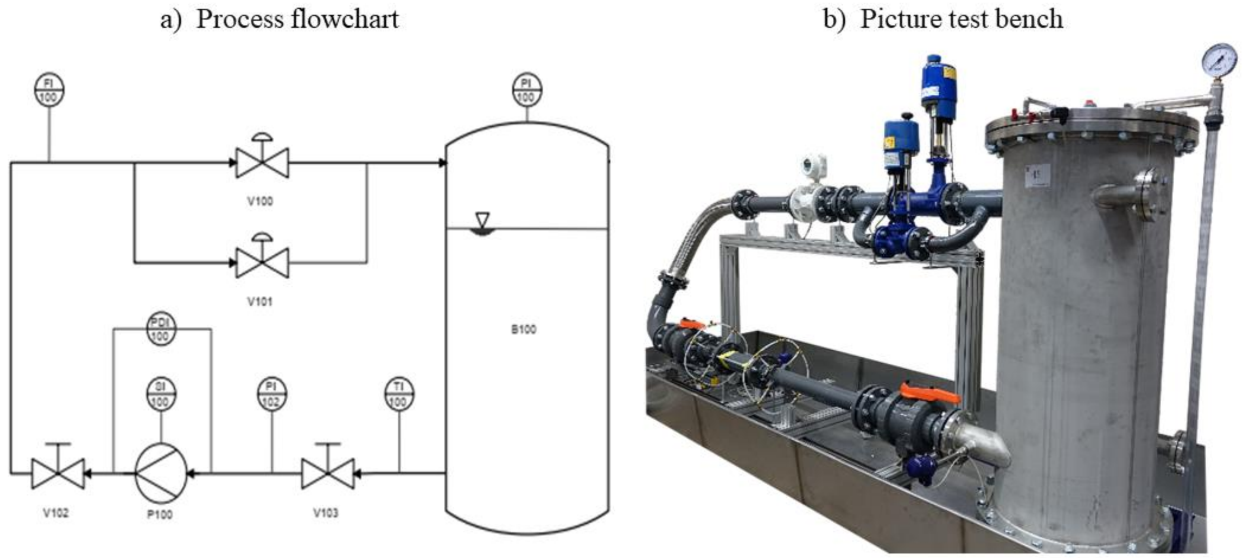
a) Process flowchart

b) Picture test bench

Figure 4.10: Single-pump test bench

4.3.3 Current Measuring Setup

The measurement setup illustrated in Figure 4.11 ensured high-precision recording of the current signature. The three-phase current coming from the VSD or, in the case of line-fed motors, from the grid, induced an equivalent voltage signal in the zero flow current transducers (LEM IT 200-S; see ⑫ in Figure 4.9), which were galvanically isolated from the power circuit. With the help of the Multichannel Current Transducer System (Signaltec MCTS, ⑬), the supply of the current transducers was provided and their voltage signal was captured. The three galvanically isolated current channels and the separate internal power supplies of the MCTS reduced both external and internal interference. The outgoing measuring signal was tapped via shunts (Yokogawa 19/SH5/BNC/0,05) and transmitted to the oscilloscope (Rohde & Schwarz RTE 1034, ⑭). For each measurement, a sampling rate of 10 kHz with a running time of 60 s was set.

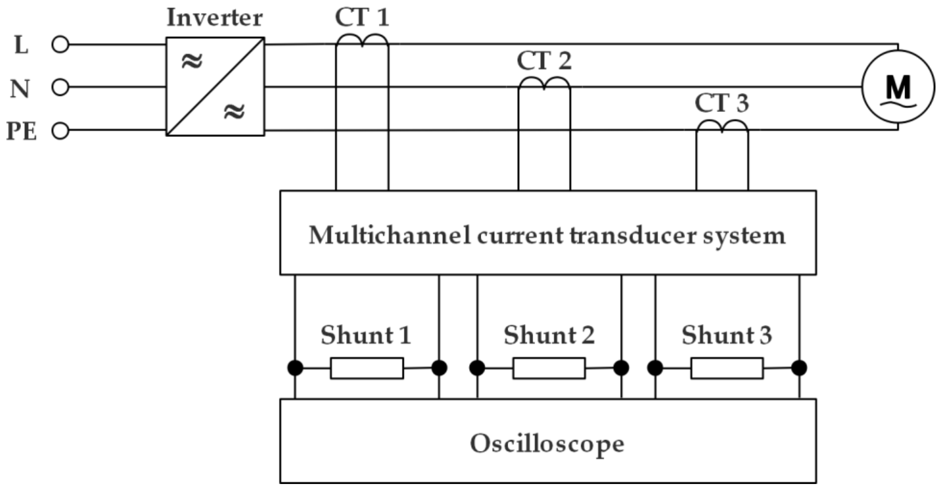

Figure 4.11: Setup for precision measurement of the motor current

4.3.4 Wastewater Test Bench

The test stand was designed as an open circuit according to the standard DIN EN ISO 9906. The most important components of the test bench for this measurement are depicted in Figure 4.12. The liquid was pumped from the inlet tank (see number 1 in Figure 4.12) via a measuring section and a filter system to a second tank (2) on the pressure side. The desired flow was set by means of two valves (3) in the measuring section. The ESP (4) was submerged in the inlet tank on the supply side. A DN100 measuring section was installed above the tanks for measuring the flow with a magnetic inductive flow meter (5). The head of the ESP was measured by means of a membrane pressure sensor (6) in a pressure-measuring line with four measuring holes. Both flow and pressure sensors provided analogue signals, which were collected by the data acquisition system. The electrical values were measured with a power meter (7). To capture the current, a high-precision current transducer (8, LEM IT 200-S) with a sample rate of 2 kHz was used. To implement the fault *clogging*, rags were pushed in front of the suction mouth of the pump via a filling device.

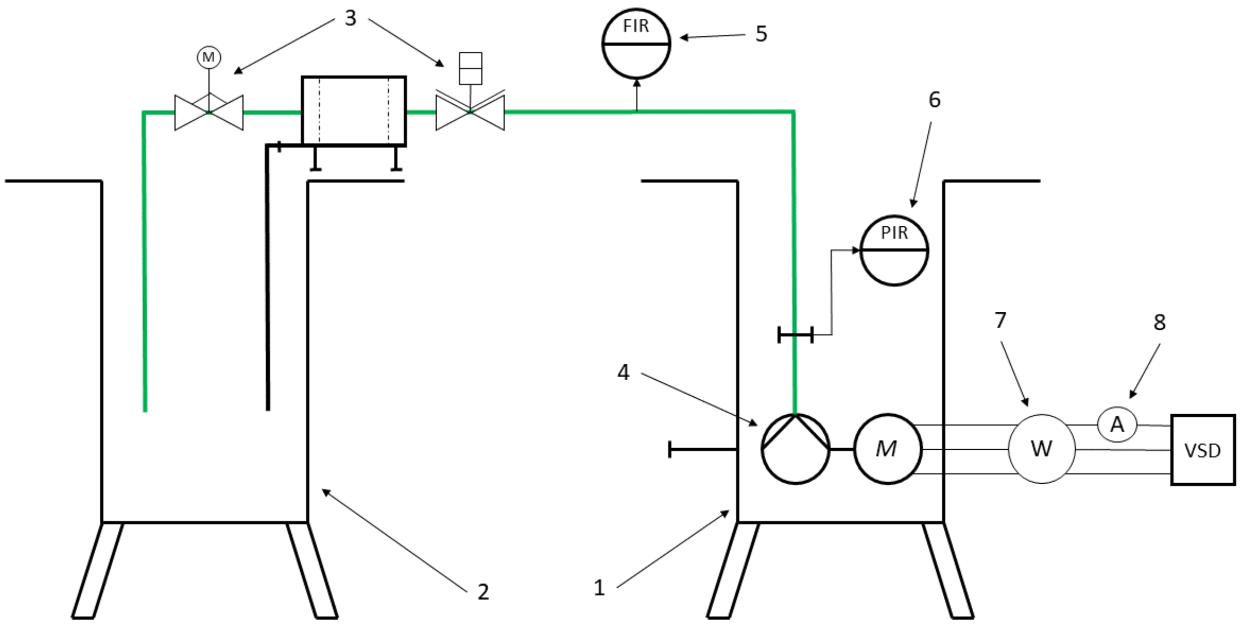

Figure 4.12: Sketch of the wastewater test stand used for the measurements

A special test sequence was performed for the experiment. The test sequence included an initial normal operation, after which a rag was pushed into the impeller of the ESP. After clogging, a manual deragging procedure (i.e., a repeated reversal of the rotation direction of the motor) was initiated until the clogging was cleared. The single steps are listed in detail below:

1. Start (0 s): Normal pump operation at 40 Hz supply frequency.
2. 10 s: Insertion of a rag via the filling device. After 10 s, the rag was sucked into the impeller. The pump was driven in this condition for 5 s.
3. 15 s:. Switching off of the pump for 5 s.
4. 20 s: Operation of the motor in the opposite direction for 5 s at 50 Hz.
5. 25 s: Switching off of the pump for 5 s.
6. 30 s: Operation of the motor in the normal direction for 5 s at 50 Hz.
7. 35 s: Switching off of the pump for 5 s.
8. 40 s: Operation of the motor in the opposite direction for 5 s at 50 Hz.
9. 45 s: Switching off of the pump for 5 s.
10. 50 s: Operation of the motor in the normal direction at 50 Hz. After 1 to 2 s, the pump was cleared.
11. 55 s: Switching off of the pump for 5 s.

12. 60 s: Normal operation, first at 50 Hz and after 2 s at 40 Hz.

4.4 Analysis Methods

This section presents the analysis methods used in this thesis. First, the MCSA will be presented, which is based on the evaluation of the current spectrum of a motor in stationary condition. Then the LoPoFIA method will be presented, which is based on the MCSA but includes the current load point of the pump in the analysis. Following this, reference will be made to ARFT, which is a particularly resource-efficient method for investigating the current spectrum. Thereafter, a method will be proposed for monitoring pumps where ARFT is implemented for feature extraction based on a cloud. Finally, ATCSA will be presented, which was used to investigate the current signal in the time-frequency domain.

4.4.1 Motor Current Signature Analysis, MCSA

MCSA was used based on a self-built Matlab program. As a first step, the captured current signal was normalized. This was done by dividing the data vector (single-column current signal) by its maximum value. The maximum value was found by using the Matlab command *max()*. After normalization, the signal was windowed with the help of the Hamming window. This window was calculated with the help of the command *hamming()*, based on the length of the data vector. Afterwards, the data vector was multiplied with the window. The windowed data vector was then transformed into the frequency domain by applying the Matlab command *fft()*. Since only the amplitude spectrum is of interest in MCSA, the absolute value of the complex data vector was calculated with the Matlab command *abs()*. After this, the amplitude spectrum had to be scaled, which was implemented by means of division by the vector length and multiplication with 2. After another normalization, the signal was converted into the dB scale. As a result, the amplitude spectrum of the current signal was obtained up to half of the sampling frequency.

4.4.2 Load Point Depending Fault Indicator Analysis, LoPoFIA

Load Point Depending Fault Indicator Analysis (LoPoFIA) is a diagnostic method that is based on MCSA. It makes it possible to obtain the relation between amplitudes at certain frequencies that are influenced by faults in MCSA, and the hydraulic load point of the motor pump. LoPoFIA was especially developed for pumps that are fed by a VSD. Depending on the speed, VSD-fed pumps have a large operating range since their head depends on the flow through the process and the motor speed. The affinity laws give an overview of the relation between the hydraulic values and the speed of the motor. Consequently, the amplitude at a certain fault frequency depends on the mentioned values. The Q-H map was selected as the display format, as is common for pumps, with the addition that the amplitude at a frequency was displayed in color. Furthermore, this method is only suitable for faults that allow a flow in the process. This fact excludes, for example, the faults *hydraulic blockage*, *dry-running* or a *fully clogged pump*.

LoPoFIA is a diagnostic method derived from MCSA, so the first steps of both methods are the same. The first step was the normalization of the current signal to the maximum value. This ensures that the maximum amplitude of the frequency domain is 0 dB, which simplifies comparison of the results. After normalization, FFT was applied to obtain the frequency spectrum of the current signal. It was assumed that the captured current signal was stationary and that the valve position remained constant during current measurement. Figure 4.13.a illustrates the MCSA result of a single load point at a flow of 10 m^3/h and a head of 6 m. In comparison to MCSA, where the whole spectrum is considered, only two defined frequencies are considered in LoPoFIA, depending on the load point. This was done for the two frequencies calculated based on equation (2.14). The two amplitudes at the fault frequencies $f_{r,pump-}$ and $f_{r,pump+}$ are marked in Figure 4.13.a. For LoPoFIA, these amplitudes are extracted, and each amplitude is displayed depending on the measured flow and head. Consequently, each amplitude has its own plot. In this example, $f_{r,pump+}$ is located at the top of Figure 4.13.b and $f_{r,pump-}$ at the bottom of Figure 4.13.b.

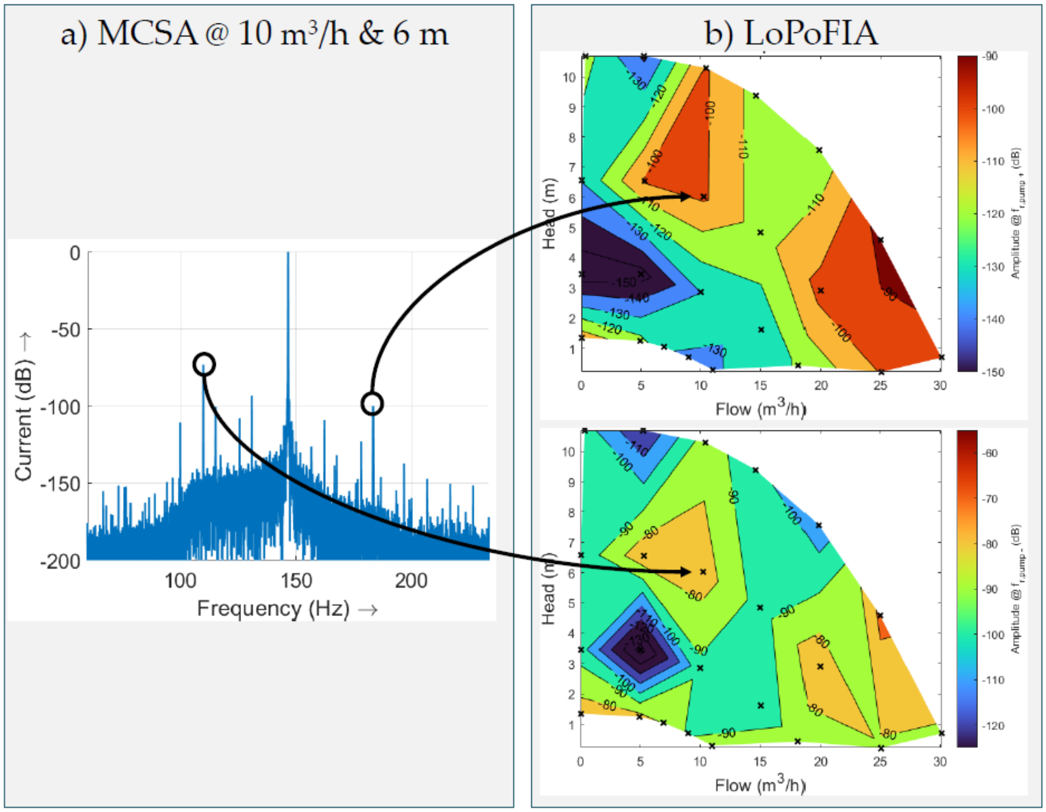

Figure 4.13: Methodology of feature extraction from (a) MCSA to (b) LoPoFIA

MCSA was applied to each load point in order to extract the load-dependent information of the two fault indicators. The analysis was done with the help of a self-built tool that performs MCSA and calculates the fundamental frequency and the two fault frequencies automatically. To find the maxima at each fault frequency, the tool searches for the maximum value around the calculated frequency within a range of 0.3 Hz. The flow chart of the tool is presented in Figure 4.14.

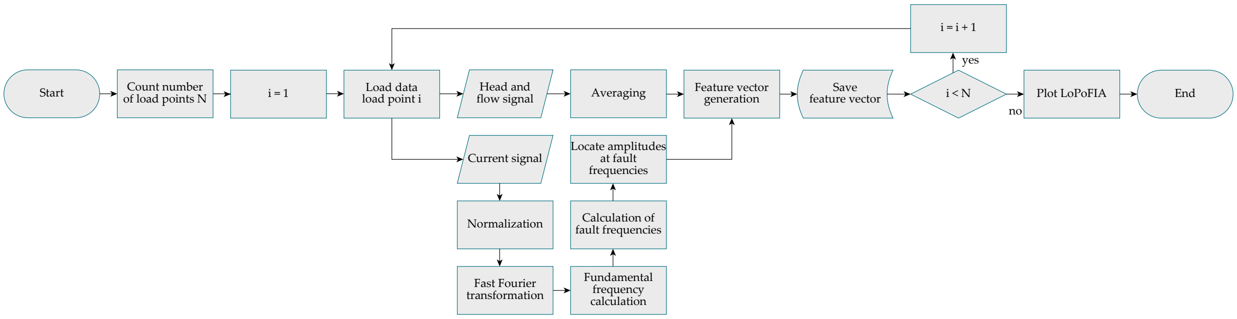

Figure 4.14: Flow chart of the implementation of LoPoFIA

4.4.3 Advanced Reference Frame Theory, ARFT

The theoretical background of the ARFT method was already illustrated in section 3.3. In this section, we will present how the algorithm was implemented and how its function was verified in a laboratory test and a field test. The goal of ARFT in general is the calculation of the amplitude at given frequencies. In the context of this work, especially the two frequencies $f_{r,pump-}$ and $f_{r,pump+}$ were investigated, since they contain information about the condition of the pumps. Section 3.3 discussed two approaches to implementing ARFT. Due to the advantages (see Table 3.2) and the fact that in the application as a circulating pump, no fast load changes were to be expected (see (Eckl, 2019b)), approach A was implemented.

4.4.3.1 Algorithm Implementation

The method for investigating the amplitudes at $f_{r,pump}$ was implemented in Matlab/Simulink, which allowed implementation in the laboratory test with dSpace hardware, as well as implementation in the firmware of the MPU of the wet-rotor pump. Figure 4.15 depicts an overview of the subsystems of the algorithm. As input values, the α- and β-current was used as one vector ("inputValueClarkeTransformationAlphaBeta") and the speed in rpm ("PLLestimatedSpeed") as the other. One parameter that is important in different subsystems was the sample time of the processor ("motorControlStepTime"). While the individual sub-blocks will be explained individually in the following, we obtained the two amplitudes at the points $f_{r,pump-}$ ("I_fault_minus") and $f_{r,pump+}$ ("I_fault_plus") as output variables.

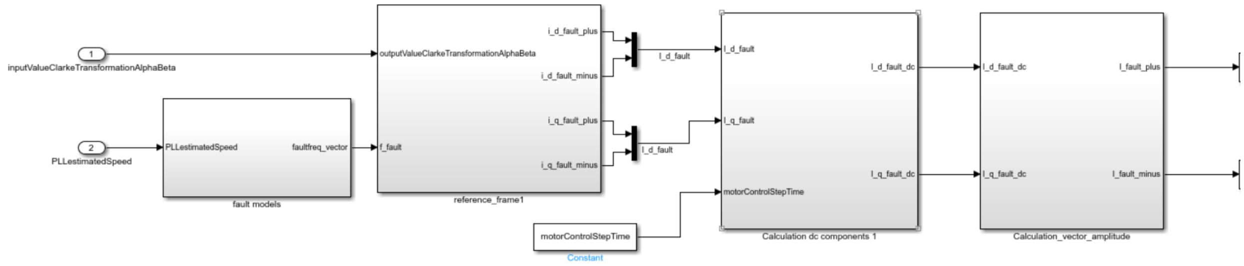

Figure 4.15: Overview of the algorithm based on ARFT

The two fault frequencies $f_{r,pump-}$ and $f_{r,pump+}$, which were combined into one vector "faultfreq_vector", were calculated in the subsystem "fault models"; see Figure 4.16. The only parameter needed in this subsystem was the number of pole pairs of the motor “numberOfPolePairs”. In summary, this subsystem only included the calculation of the fault frequencies according to equations (2.14) or (2.17) if $v = 1$ and $n_d = 1$ (in both cases $s = 0$, since it was implemented in the MPU of a PMSM).

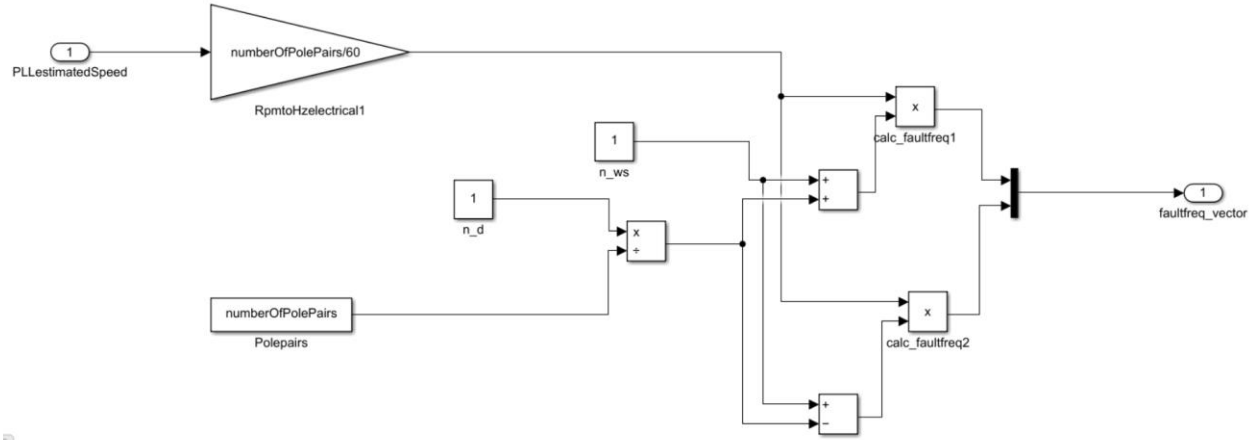

Figure 4.16: Block “fault models”

Figure 4.17 depicts the core of the algorithm, the Park transform of the current signals. As a first step, the two frequencies that were the input signals were converted from Hz to rad^{-1}. After conversion, the angle was calculated from the frequency signals by integrating the frequency signals. The integrators were implemented in another subsystem, which will be considered in the next paragraph. After integration, both angles were multiplied with a cosine and a sine function. Both trigonometric functions were implemented as look-up tables with a variable number of data points. The following multiplication and sum blocks were used to implement equation (3.62).

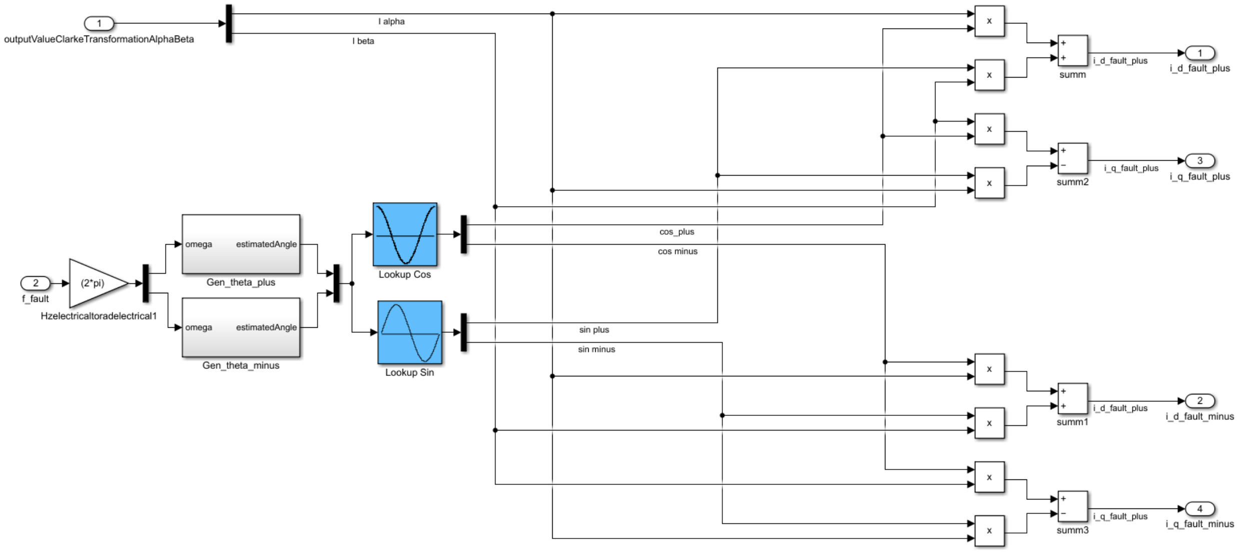

Figure 4.17: Block “reference frame1”

In order to implement a time-discrete integrator, a self-built function block was built, which was optimized for the data type *single*. In addition to the angular velocity “omega”, the “motorControlStepTime” was also used as an input value for the integrator. As an output signal, the angle “estimatedAngle” in a range from 0 to 2π was outputted.

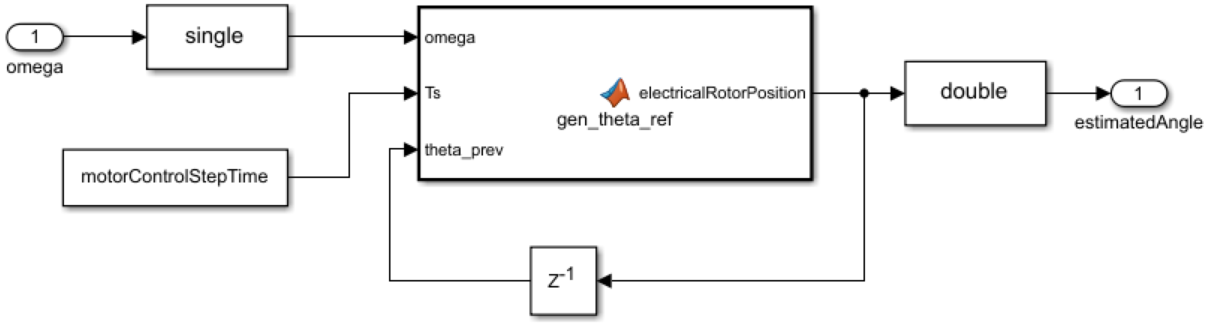

Figure 4.18: Block “Gen_theta_minus”

Figure 4.19 a) shows the sub-model of the block “calculation dc components 1”, which contains a first-order filter in a second subsystem. As a time constant of the filter (“time constant filter”), a value of 10 s was used in all measurements. The filter outputs the dc parts of the d and the q-parts of the oscillations. The filter itself was built as a first-order Butterworth filter, based on equation (3.73).

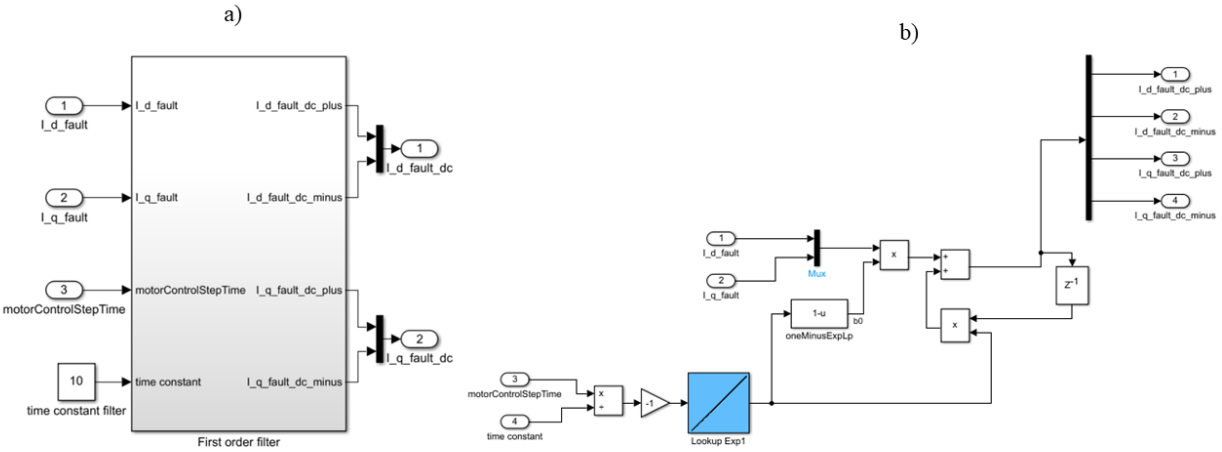

Figure 4.19: a) Block "calculation dc components 1"; b) Block "First order filter"

Figure 4.20 reveals the individual steps taken to calculate the amplitudes "I_fault_minus" at $f_{r,pump-}$ and "I_fault_plus" at $f_{r,pump+}$. This is the implementation of equation (3.67), where the geometric sums are calculated from the d and q-parts of the currents.

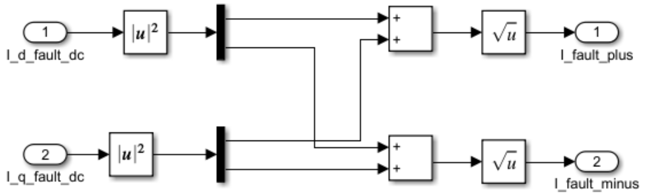

Figure 4.20: Block "Calculation_vector_amplitude"

4.4.3.2 Validation Approach

The goal of the research regarding ARFT is to verify that a spectral analysis of the current signal can be applied in a real environment, in our case in the application of a wet-rotor pump. In general, the validation procedure involves two steps, a laboratory test and a field test of the algorithm, as illustrated in Figure 4.21. In order to perform the laboratory test, the algorithm was implemented on a MicroLabBox from the manufacturer dSpace. In the field test, the algorithm was implemented in the firmware of the MCU of the pump. In this step, the manufacturer of the pump had to be involved, as they were the only ones with access to firmware changes. In every test procedure, the algorithm was optimized by adapting the parameters.

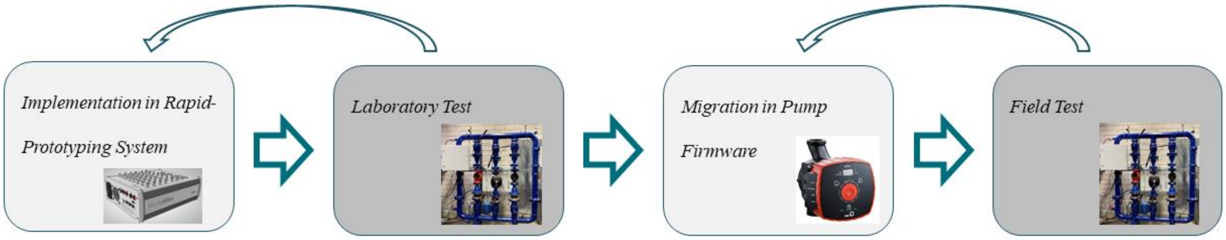

Figure 4.21: Steps in the development of the health-monitoring algorithm for circulation pumps

In the following two sections, the two validation steps will be described in more detail.

4.4.3.2.1 Laboratory Test

To perform the laboratory test, the ARFT algorithm (see section 4.4.3.1) was implemented in the rapid-prototyping system dSpace MicroLabBox. This system allowed direct implementation of the algorithm based on Matlab/Simulink. The sampling frequency of the MicroLabBox was set to 8.3 kHz. The test object (DUT1) was installed in the middle strand of the right test bench, as shown in Figure 4.9 b). The speed was set to 2800 rpm and the flow was set to 11 m^3/h, resulting in a pump head of 11 m (healthy condition). To test the function of the algorithm, one impeller channel of the pump was clogged in a second experiment.

As a basis for the ARFT algorithm, additional current sensors (LEM LTS 15-NP) were installed between the VSD and the motor; see Figure 4.22. The signals of the sensors were inputted into the analog input channel of the dSpace MicroLabBox. The left-hand current sensor system was used for verification of the results; compare section 4.3.3.

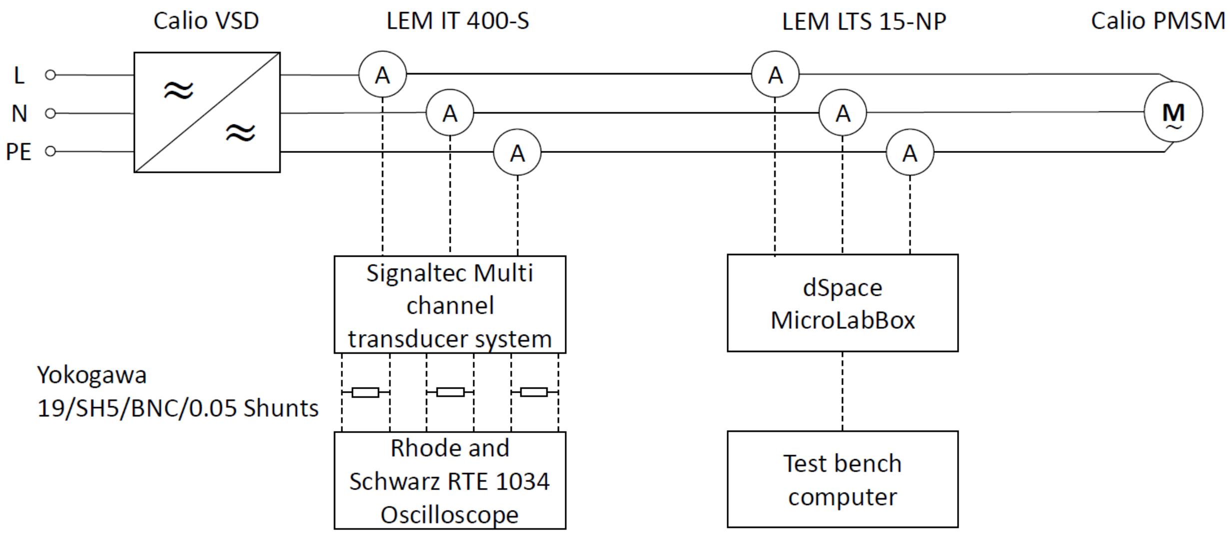

Figure 4.22: Measuring concept of the laboratory test for ARFT validation

The drawback of this setup was that there was no access to the real-time signal of the speed of the motor, as it was calculated in the motor control MCU of the pump. The first option was to read the signal that the pump provided via Modbus interface. However, this signal was too slow for the algorithm. As a result, there was large variation in the results of the algorithm. Better results were obtained using an additional subsystem to estimate the speed based on counting the zero crossings of a single-phase current signal, as described below:

Each time the sign changed from negative to positive, a counter variable (counter) was incremented by the value one. This created a staircase-shaped signal. The width of the steps corresponded to the reciprocal of the frequency. From the measured current curve, an estimate of the instantaneous fundamental frequency was derived by measuring the zero crossings. The reciprocal value of the time interval between two zero crossings represented the estimated frequency. Therefore, to improve the accuracy of the estimator, an additional linear interpolation was introduced. This allowed intermediate temporal values of the zero crossing to be calculated between the discrete sampling times (see Figure 4.23).

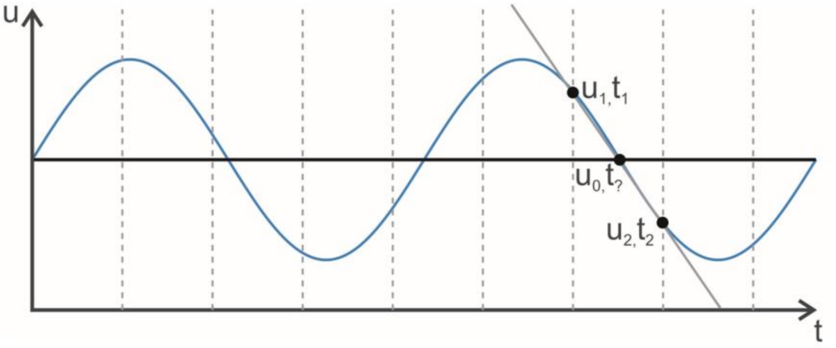

Figure 4.23: Interpolation to optimize the accuracy of the frequency estimator

4.4.3.2.2 Field Test

The goal of the field test was to verify whether the ARFT can run in a real environment, in this case on the MPU of a state of the art circulation pump. In the research laboratory, there was no possibility to create firmware for the pump. Therefore, the manufacturer was involved in the verification. The methodology can be seen in Figure 4.24. In the first step, the manufacturer was provided with a Simulink model, which was then migrated into the firmware of the pump and made available again to the research laboratory. Using the software *Pactware*, this firmware was installed on the pump electronics. The next step was to verify the results. Here, the results of the ARFT from the control board MCU were passed on to the laboratory computer via Modbus. In addition to the results coming from the pump's MCU, the measuring setup based on Figure 4.11 was used to capture the current signals of the pump. After this, an adjustment of the parameters took place. In particular, the number of support values of the trigonometric functions (see Figure 4.17) and the exponential function in the filter had to be optimized. The required trigonometric functions for the application of the Park transform were implemented by means of look-up tables with 360 value pairs to minimize the memory requirements of the MPU. This process went through several loops until the pump ran in a state without overloading any of the MPUs.

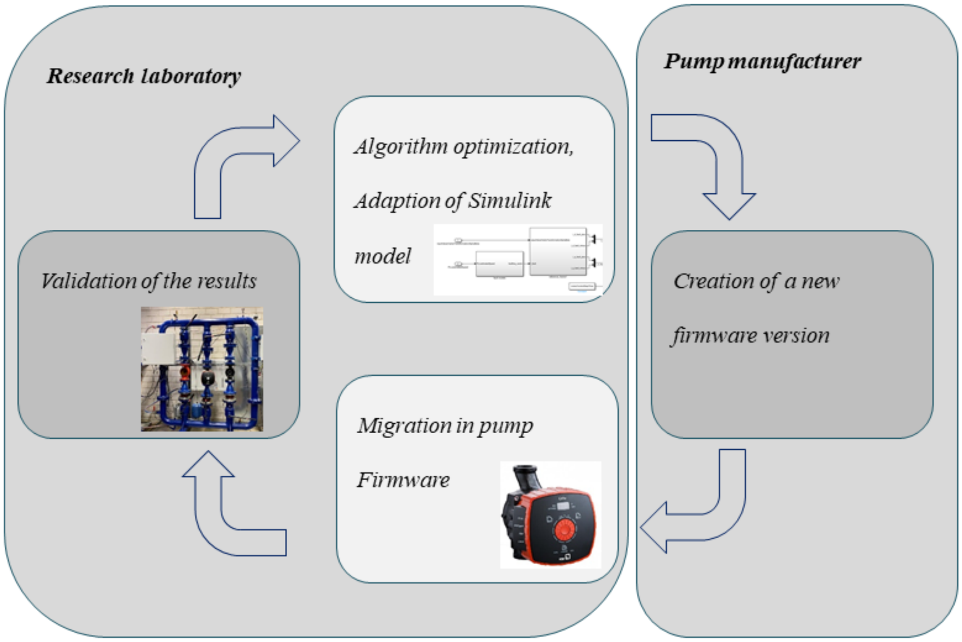

Figure 4.24: Methodology for verifying the function of the ARFT method in a field test

4.4.4 Cloud-based Condition Monitoring

An example of such a system is depicted in Figure 4.25. The pump, in this case a heating circulating pump, calculates the damage factor SF using the method described above and transmits this via a gateway to an external evaluation unit, which is implemented as a cloud-based evaluation unit. In the cloud, the transmitted data, in particular the damage factor and other operating parameters (e.g., operating point, speed, temperatures, service life) of the pump, are combined with corresponding data of other pumps from the same fleet.

Due to the large database of a complete pump fleet, a comparison of the damage factors under similar boundary conditions (operating point, speed, temperatures, service life) can then be carried out. This serves to filter out defective pumps, as well as to detect the imminent failure of pumps. A large deviation of the damage factor of a pump from the respective values of the other pumps or an average value of the other pumps can be interpreted as degeneration or clogging of the impeller. In this case, the pump owner or operator can be informed directly and, if necessary, a service employee can be dispatched. Notification of the pump owner or operator and/or placement of the service order can preferably be done and generated automatically by the system.

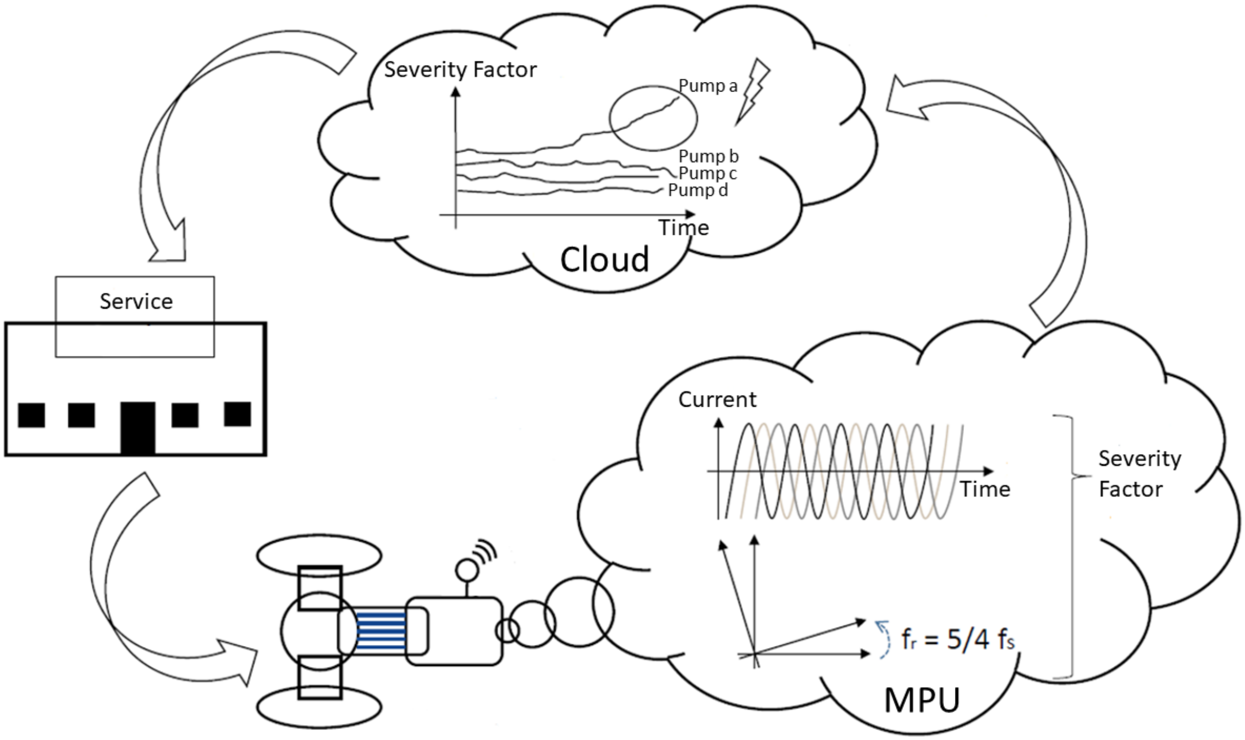

Figure 4.25: Proposal for cloud-based monitoring of a pump fleet based on feature extraction using ARFT

4.4.4.1 Laboratory Test

For the validation of the cloud approach, three pumps were simultaneously operated in the right part of the multi-pump test bench (see Figure 4.9). One of the three pumps was operated in healthy condition, one with three clogged impeller channels, and one with a two-sided bearing damage of +0.1 mm. For feature extraction, the ARFT method was implemented on the pumps' MPU; see section 4.4.3.2.2. The three pumps were connected via Modbus interface to the test bench computer. In addition to the two severity factors SF1 and SF2 calculated by ARFT, the values speed, flow, and head were captured with the same interface. The software tool LabVIEW was utilized as a local cloud where the data was collected.

During the measurement, the three pumps were controlled via proportional pressure control, which is the most common control type for circulation pumps. This control mode was set via the control panel of the pump. The pumps were operated in different load conditions, at 0%, 25%, 50%, 75%, and 100% of the rated flow. The flow of each pump was set manually using the pressure side shut-off valve on the basis of the estimated flow of the pump. In each load point, the pumps were operated for 90 minutes, starting with 0% flow and ending with 100% flow.

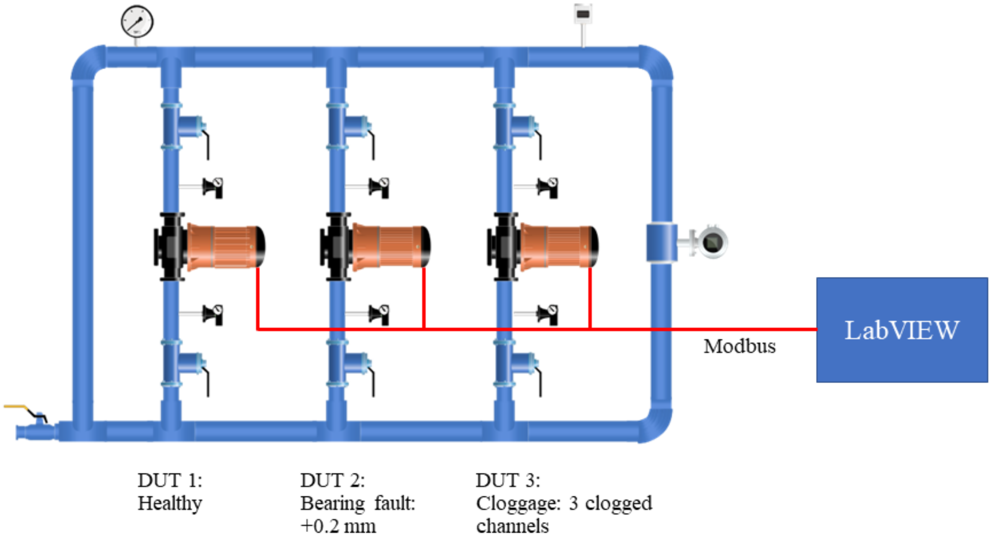

Figure 4.26: Measurement setup for the laboratory test of the cloud-based monitoring approach

4.4.5 Advanced Transient Current Signature Analysis, ATCSA

For the analysis of the transient current regimes of a motor pump, ATCSA was implemented in a self-built Matlab program. As input of the program, the current signal in one of the motor supply phases is needed. As a first step in the program, this current signal is normalized to the maximum value of the current vector by dividing the current vector by the maximum value of the current vector. The maximum value is found by using the Matlab command *max()*. After this, some important parameters are defined, including the length of the time window, the slope of the atom, and the number of DFT calculation points. As a time window, values between 0.8 and 1 s were used for the analyses. For the number of DFT calculation points, a value of 10000 was selected. Based on equation (3.80), the Gaussian function was calculated for the selected time window. On the basis of equation (3.54), the DFT was calculated for the same time window. During the subsequent loop, the same was done for the next time window.

5 Experiment Results: Stationary Analysis

In this section, the experiment results concerning the stationary analysis of the pumps will be discussed. First, the RMS value of the current and other stationary values will be analyzed. This is followed by the investigation of the results when MCSA is used. Next, the influence of the load point of the pump on the fault indicators in the current spectrum will be analyzed with help of the LoPoFIA method. This is followed by the validation of the DTFA, which is used to understand the transfer behavior of a motor as a sensor for pump faults with the help of the measurement results. Next, the results of the laboratory and field testing of the ARFT method will be presented. Finally, a validation of the approach to cloud-based monitoring of pumps will take place.

5.1 RMS Current and Other Stationary Values

The focus of this section is on stationary values, especially the RMS value of the current, as the main topic of this work is related to current-based fault detection. However, other stationary values, such as efficiency, will also be evaluated in order to understand the influence of a hydraulic fault on the operation of a pump. Additionally, for the wet-rotor pump, we will analyze whether faults can have an influence on their parameter estimation. The faults considered in this section are *clogging, hydraulic blockage*, and *dry running*.

5.1.1 Clogging

If an impeller of a motor pump is clogged, the pump head is decreased and consequently, the flow through the process is also decreased. How a system reacts to a decreasing flow, or in some cases to the decreasing head, depends on the system design. If a valve is used for flow regulation, an opening valve could compensate for the decreasing flow. However, the decision to open the valve has to be based on a measured signal, coming, for example, from a flow sensor. In a water heating system, for example, decreasing flow leads to decreasing heat transfer of the radiator, and thus to decreasing room temperature. In most cases, thermostatic valves are installed, which react to the decreased room temperature by opening the valve. In the following sections, the influence of clogging on the RMS current and other parameters will be investigated for a wet-rotor pump and a wastewater pump.

5.1.1.1 *Wet-Rotor Pump (800 W)*

In this section, the influence of the fault *clogging* on the stationary values of the 800 W wet-rotor pump will be investigated. First, we will focus on the steady-state variables, and then analyze the influence of the error on the parameter estimation in the next section.

5.1.1.1.1 Stationary Values

Two measurement runs were performed to evaluate the influence of clogging on the wet-rotor pump. In the first measurement run, the valve position was kept in constant position. After the measurement of the healthy variant at a speed of 2500 rpm, the impeller channels were successively clogged one by one (only adjacent channels), up to five clogged channels. Then, in the second measurement run, further reference points were recorded in the healthy state. The electrically supplied power was used as a reference.

Table 5.1 indicates the values *Proportion of Active Channels, Flow, Head, Electric/Hydraulic Power, RMS Current*, and *Efficiency* for different configurations. All variables are mean values of the measured values. The value *Proportion of Active Channels* is calculated by dividing the number of healthy channels of the impeller by the total number of impeller channels. Since the hydraulic power was decreased in the case of faulty operation, the load of the motor also decreased, resulting in an efficiency decrease of the motor. In order to make a statement about the influence of the clogging on efficiency, a healthy variant with the same power consumption is indicated for each fault variant.

Table 5.1: Values of healthy and faulty wet-rotor pump (2500 rpm) for measurement at constant valve position

	Proportion of Active Channels (%)	**Flow (m^3/h)**	**Head (m)**	**Electric/Hydraulic Power (W)**	**RMS Current (A)**	**Efficiency (%)**
Healthy	100	17.9	6.6	580/321	2.8	55
Healthy 1	100	16.4	6.9	558/308	2.6	55
1 clogged channel	86	16.6	5.7	556/257	2.6	46
Healthy 2	100	12.3	8.0	493/265	2.4	54
2 clogged channels	71	15.7	5.2	494/222	2.4	45
Healthy 3	100	10.1	8.4	450/230	2.2	51
3 clogged channels	57	14.5	4.6	454/181	2.2	40
Healthy 4	100	7.6	8.8	393/180	1.9	46
4 clogged channels	43	12.6	3.6	396/123	1.9	31
Healthy 5	100	5.1	8.9	335/124	1.6	37
5 clogged channels	29	11.0	2.7	343/81	1.7	24

In healthy condition, the pump consumed 580 W of power and produced 321 W of hydraulic power, resulting in an overall efficiency of 55%. In faulty condition, both electric and hydraulic power decreased. However, the efficiency of the pump also decreased. The hydraulic power decreased in a similar ratio as the proportion of active channels. For example, in the case of three clogged channels (four of seven active channels), the hydraulic power decreased by 44% and the proportion of active channels was reduced by 43%. Compared to the reference points with the same power input, it can be concluded that the efficiency was 9 to 15% lower than in healthy condition.

There are two possibilities that explain why the efficiency of the pump decreased: either due to a decrease in the efficiency of the conversion from electrical to mechanical energy (motor) or of the conversion from mechanical to hydraulic energy (impeller/pump). In all variants, the power consumption of the motor decreased due to clogging, which led to a change in the operating point of the motor. In all cases, the operating point moved away from the nominal point, which could increase losses in the motor. In addition, it is possible that clogging results in higher velocities in the impeller passages that are still operating, which could increase hydraulic friction losses.

Compared to the healthy condition, the RMS current also decreased in faulty condition. The reason is the mentioned decreasing hydraulic load. The authors of (Jahangiri, 2018) showed the same behavior for a pump with one clogged impeller channel. However, the healthy variants with the same power consumption also consumed the same RMS current. Consequently, in terms of fault detection, the RMS current is not suitable for detection of the fault *clogging*. If head and flow sensors are applied in the hydraulic system, the efficiency could be used for the detection of the fault. However, in most cases, such sensors are not installed.

5.1.1.1.2 Parameter Estimation

In this section, the influence of the fault *clogging* on the parameter estimation of a wet-rotor pump, especially that of the two hydraulic parameters flow and head, will be investigated. Figure 5.1 depicts the measured and estimated flow-head curves at a constant speed of 1870 rpm in healthy condition and with 2 adjacent clogged impeller channels. In the figure, the same marker is used for each associated point of the measured and estimated variable.

It was observed that due to clogging, the measured head in each operation point decreased (green curve) compared to the healthy variant (red curve). In other words, the pump curve was shifted downwards, which is a known behavior if the speed of a pump is lowered. As already verified in section 5.1.1.1.1, the efficiency and the input power also decreased in the case of clogging, which had an effect on the parameter estimation of the pump. At first glance, it looks as if both estimation curves are one pump curve. This was also interpreted by the pump in the same way, since the pump remained with its stored curve in its MPU for the speed of 1870 rpm. Because of the decreasing current due to the lower power supply, the pump assumed a larger pump head, since the head increases with decreasing flow and the same speed (see also Figure 2.2). This moved the estimated operating point away from the true operating point, resulting in a large error in flow and pressure variables. Especially the estimation of the head was worse in all cases compared to the estimation in healthy condition. The flow estimation was especially influenced by high flow. The estimation error in the highest flow condition (see “x” in Figure 5.1) equaled 35% for the flow and 53% for the head, compared to 8% for the flow and 25% for the head in healthy condition (see “□” in Figure 5.1). In lower flows, the flow was even more accurate than in healthy condition.

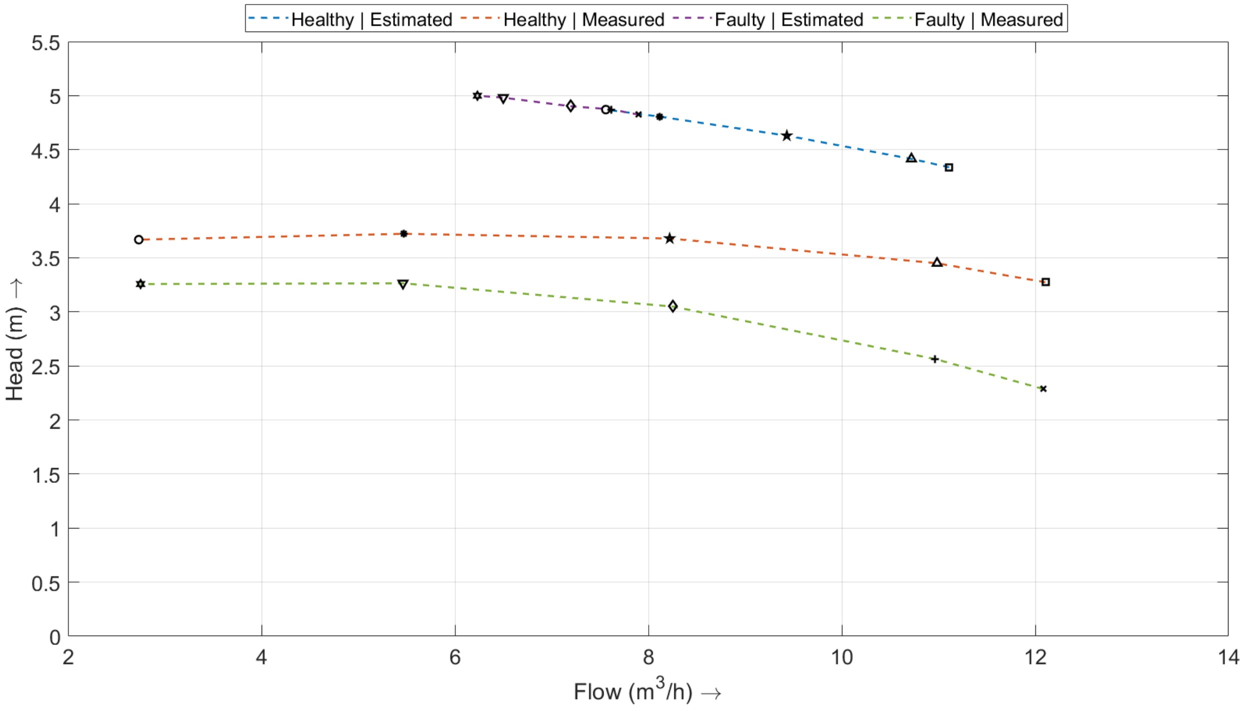

Figure 5.1: Influence of a fault on the parameter estimation of a pump, in the example of a circulation pump (800 W) running at 1870 rpm in healthy condition and with 2 clogged channels

If, for example, the estimated flow decreases in the field because of increasing clogging or impeller wear, the plant operator only observes a trend of decreasing flow and increasing head of the pump, which can be a process over several years. The seemingly low flow could lead to the conclusion that the pump being used is oversized for the process.

5.1.1.2 Submersible Pump (7.7 kW)

Figure 5.2 depicts the curves of flow, head, and RMS value of the current and the efficiency of the ESP during a defined test procedure; see section 4.3.4. At a time of 10 s, a decreasing flow and head indicated the clogging of the ESP. After the clogging, the hydraulic power decreased by 60%, while the efficiency decreased from 60 to 22%. Consequently, flow could still be generated despite the cloth being sucked in. The current exhibited a small peak at 10 s, but remained at the same level. In the second period of running the motor in the normal direction (from 30 s), flow and head were slightly higher in comparison with the normal condition, which was due to the increased supply frequency (50 Hz instead of 40 Hz). Compared to the condition after the ESP was cleared (from 52 s to 55 s), the hydraulic power decreased by 27%, which meant a lower decrease compared to the first period of clogging. After clearing, the efficiency of the normal condition was reached again. Other than small spikes during sucking in of the rag and startup, the RMS value of the current stayed at the same level. Consequently, as proven by the results, the RMS current value was not a good indicator for diagnosing the clogging. The function of the method presented by the authors in (Fullemann, 2013), which detected clogging by an increase in current, cannot be confirmed from this measurement data. If flow and head sensors are available in the process, the hydraulic power or the efficiency could be used for diagnosis. However, in most cases, such sensors are not available.

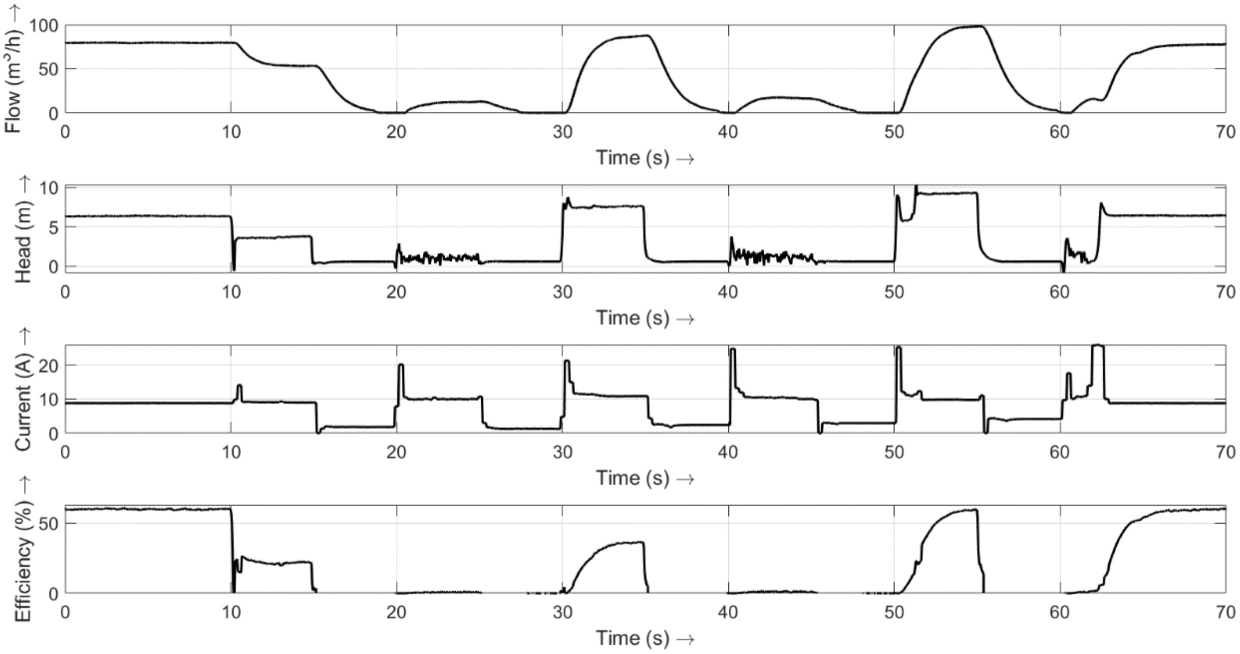

Figure 5.2: Curves of flow, head, current in one phase, and efficiency of the wastewater pump during the test sequence

5.1.2 Hydraulic Blockage, Dry Running, and Fully Blocked Impeller

In this section, the influence of the faults *hydraulic blockage*, *dry running*, and *fully blocked impeller* on the stationary values will be investigated. All three faults have in common that the flow through the piping system equals zero. Consequently, both the hydraulic power (see equation (2.2)) and the system efficiency (see equation (2.4)) equal zero, which makes the consideration of these quantities redundant. It is obvious that the use of a flow sensor can detect when there is no flow through the system. Thus, it could be inferred that one of these three faults is present.

First, the effect of a partial and a full hydraulic blockage on the RMS current was investigated. For this, the dependence of the RMS current on the flow was considered. Figure 5.3 depicts the current-flow curves for a wet-rotor pump and a dry-runner pump. In all cases, the supply frequency remained constant, resulting in constant speed if the slip of the dry-runner pump is neglected. The wet-rotor pump ran at a speed of 1870 rpm.

In all cases, the current decreased constantly if the flow became smaller. In the case of hydraulic blockage (0 m^3/h), in a), the current decreased by 14%, compared to the rated value, and in b) by 10%. This is a known behavior of pumps, which was also described in (Gülich, 2014). The results indicate that the monitoring of the RMS current can be a good tool for detecting a full or partial hydraulic blockage.

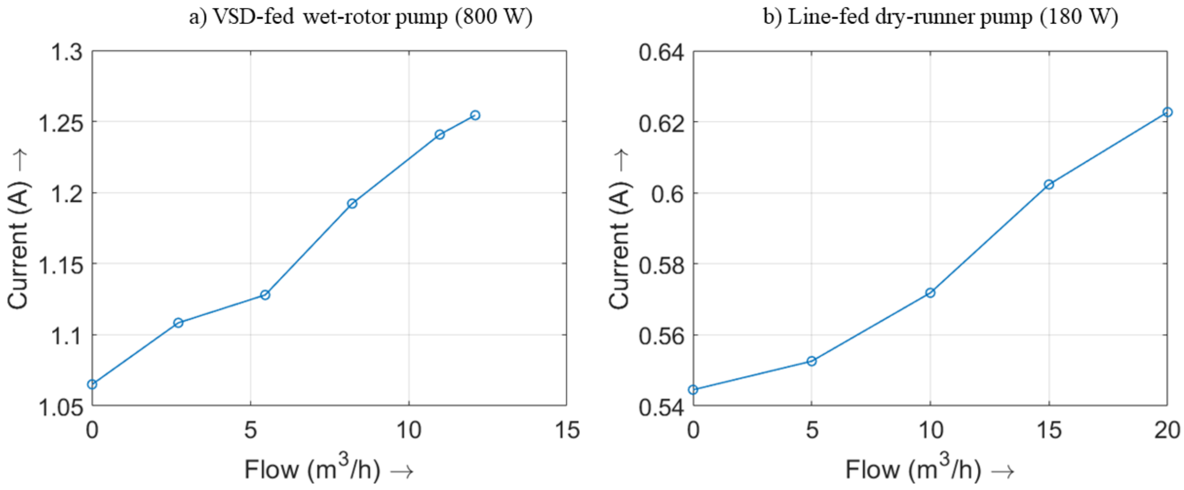

Figure 5.3: RMS current in dependence of the flow; a) VSD-fed wet-rotor pump (800 W); b) line-fed dry-runner pump (180 W)

Second, the three faults *hydraulic blockage, dry running,* and *clogged impeller* were compared with each other for a wet-rotor pump. Figure 5.4 depicts the electric power consumption in dependence of the speed for the three mentioned faults. In the cases of a hydraulic blockage and a clogged impeller, the power was almost equal in all measurement points, with the power increasing non-linearly with increasing speed. However, for the fault *dry running*, the power was lower at the two speeds 1800 and 2500 rpm. With increasing speed, the difference became more obvious. In the case of dry running, the power-speed relation was linear.

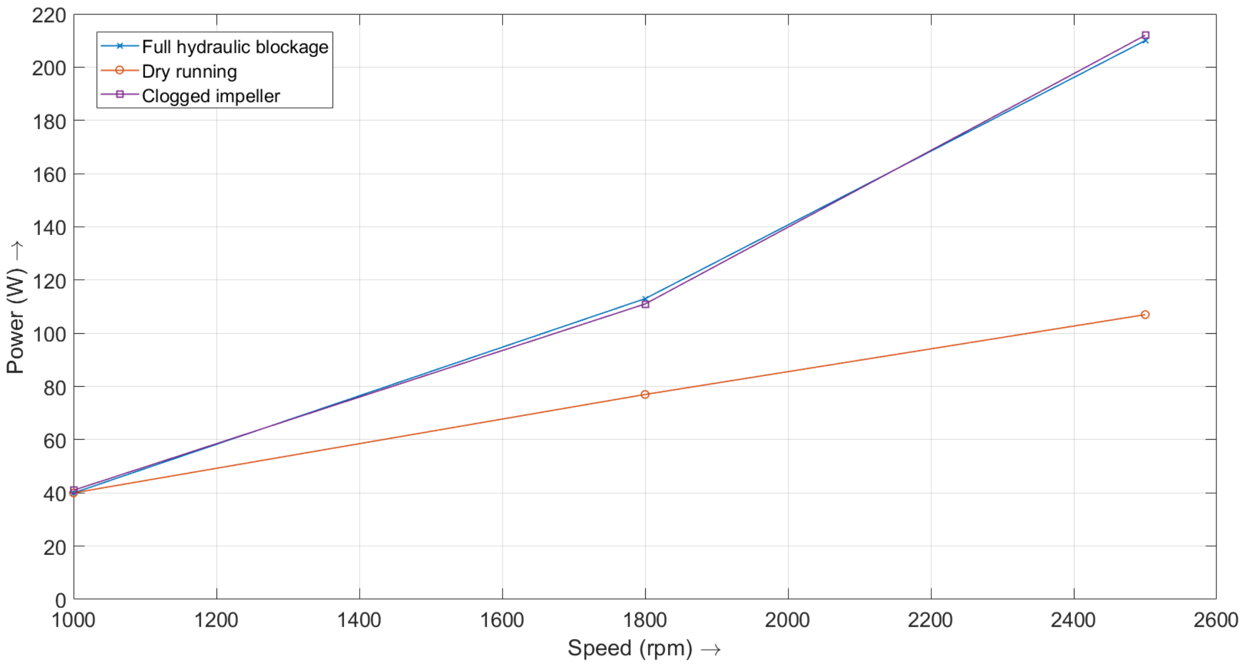

Figure 5.4: Electric power consumption of an 800 W wet-rotor pump with different faults

Two things could be deduced from the observations. First, the fault *dry running* meant lower power consumption for the operator than the other two faults, especially at higher speeds. Second, the observation of the power allows a conclusion to be drawn about the state of health of the pump, since in the case of the fault *dry running*, the power consumption is clearly lower than in the case of other faults or operating points. This result confirms the result of (KSB, n.d.), where a procedure for the detection of dry running was presented.

5.1.3 Conclusion

In this section, we demonstrated that typical pump faults have an influence on the stationary parameters of a pump. Furthermore, pump faults can decrease the efficiency of a pump, which was shown for two different pumps for the fault *clogging*. The faults *dry running* and *hydraulic blockage* led to a flow of zero, which resulted in zero efficiency. In these conditions, the pump consumes energy that cannot be used in the process, which means that all input energy is transformed into heat. In the case of dry running, the power consumption was lower than in the case of the other faults and lower compared to normal operation. Consequently, this fault can be detected by evaluating the power consumption or the RMS current of the pump. For the submersible pump, it was illustrated that due to the clogged impeller, the efficiency dropped from

60% to 22%. In this condition, however, the RMS current remained on a constant level. In all cases, the RMS current did not increase due to the fault *clogging*. For the wet-rotor pump, the RMS current even decreased. Consequently, the faults *hydraulic blockage* and *clogging* cannot be separated by monitoring only the power consumption or the RMS current. It was also demonstrated that the fault *clogging* can disturb the implemented parameter estimation of a wet-rotor pump.

5.2 Motor Current Signature Analysis, MCSA

In this section, the results of using MCSA to investigate the current spectrum of different pump types and faults will be presented. The section starts with the consideration of the healthy variants. These results are used in the following sections as a reference in order to obtain the influence of the fault on MCSA. After investigation of the faults *clogging*, *cracked impeller*, *bearing damage*, *dry-running rotor*, *dry-running*, and *hydraulic blockage*, the section finishes with the conclusion.

5.2.1 Healthy Condition

In this section, the current spectrum of four different pumps in healthy condition will be investigated, with special focus on the typical frequencies investigated in MCSA.

5.2.1.1 Wet-Rotor Pump (800 W)

Figure 5.5 depicts the MCSA of a wet-rotor pump (800 W) at a speed of 2500 rpm in healthy condition. In the analyzed load point, the current consumption equaled 2.9 A, resulting in a power consumption of 580 W, a flow of 17.9 m^3/h, and a head of 6.6 m.

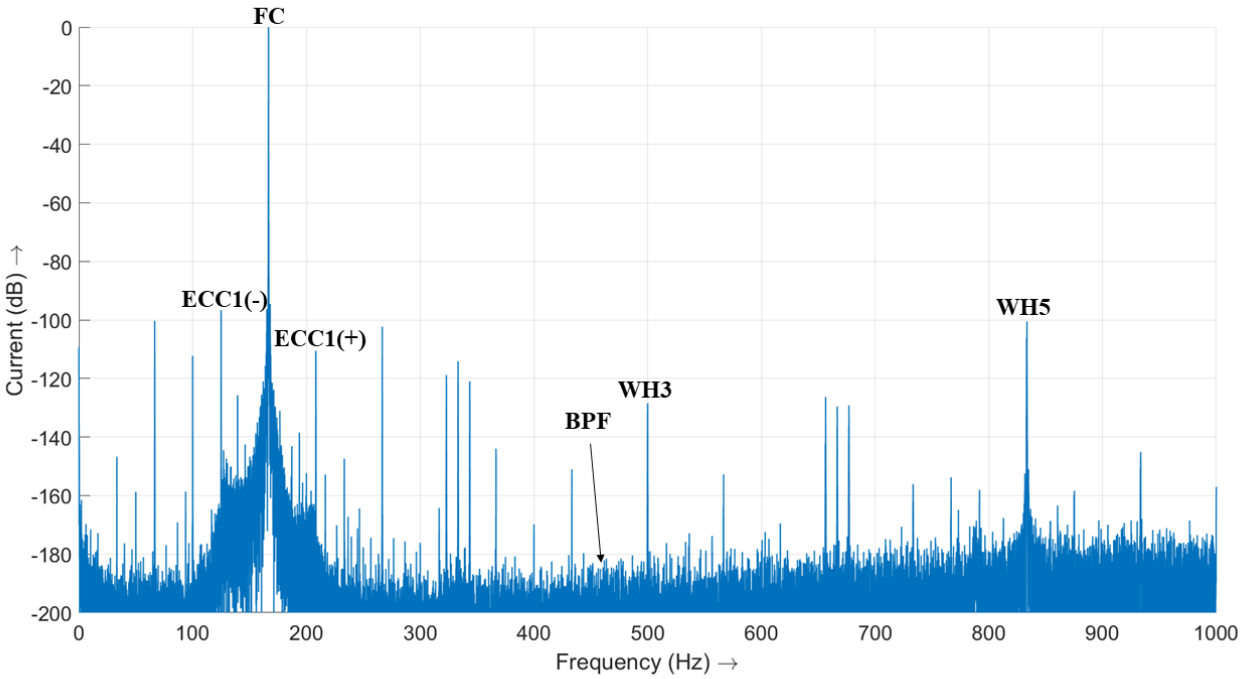

Figure 5.5: MCSA of a wet-rotor pump (800 W) at a speed of 2500 rpm in healthy condition

Since the rotor rotated with a speed of 2500 rpm and the motor had four pole pairs, the FC was at a frequency of 166.7 Hz. At this point was the highest peak in the frequency spectrum, normalized to a value of 0 dB. Additional peaks were detected at every integer multiple of the supply frequency and at several other locations. The odd multiples could be attributed to the WHs of the stator. The BPF component, which was located at 458.4 Hz, is also indicated in Figure 5.5. However, the amplitude was not significant compared to the noise level in the current signal. This was also proved for other different load conditions. At 10 Hz, 100 Hz, and 200 Hz, peaks were located; these were independent of the speed. Additionally, peaks were found at 66.7 and 266.7 Hz (±100 Hz around the FC). Both were caused by the VSD operation, which will be verified in ATCSA; see section 6.1.1. The eccentricity components at 125.0 Hz and 208.4 Hz are visible in the spectrum of the healthy variant. At 125.0 Hz, a slightly higher peak (−98.5 dB) was observed than at 208.4 Hz (−109.9 dB). The amplitudes of the eccentricity peaks have a strong dependence on the current load point, which will be analyzed in section 5.3.1.

5.2.1.2 Wet-Rotor Pump (150 W)

Figure 5.6 depicts the MCSA of a wet-rotor pump with 150 W at a speed of 2740 rpm in healthy condition at a load point with a flow of 8.1 m^3/h and a head of 1.7 m.

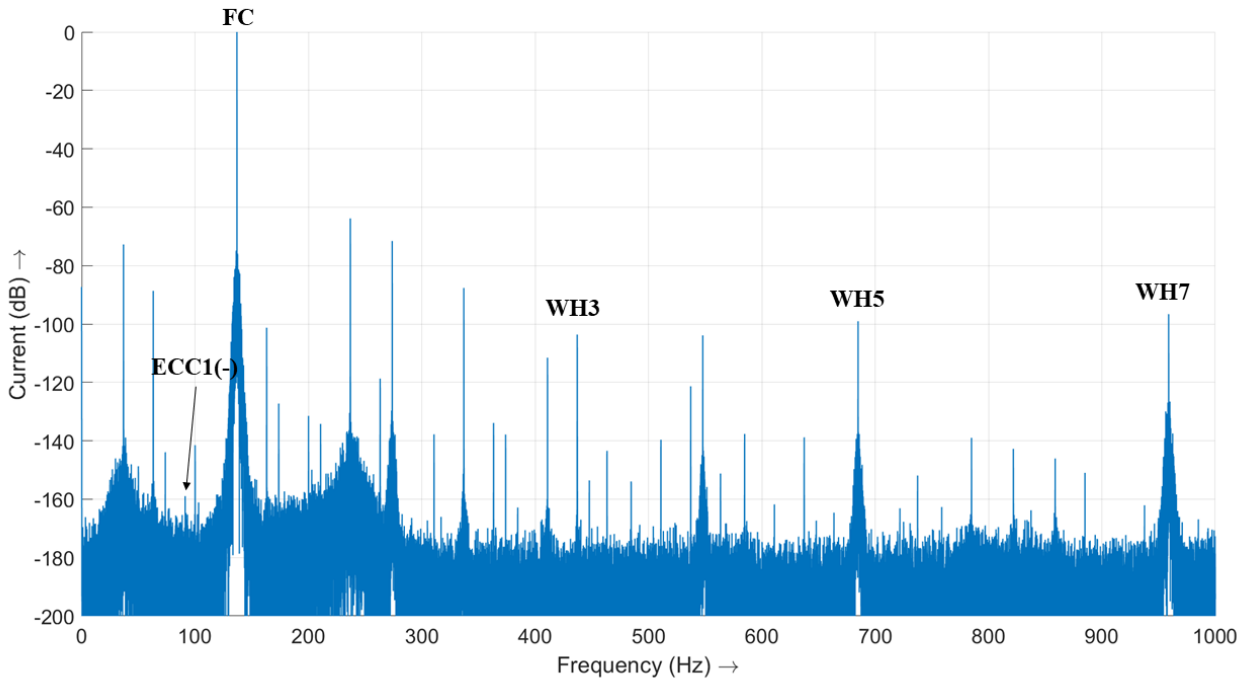

Figure 5.6: MCSA of a wet-rotor pump (150 W) at a speed of 2740 rpm in healthy condition

Since there were three pole pairs of this pump type and the rotor was rotating with a speed of 2740 rpm, the frequency of the FC equaled 137 Hz. At the every multiple of the FC, amplitudes are visible. The highest amplitudes are visible at WH5 and WH7. Additionally, at ±100 Hz of the FC and in 100 Hz steps with decreasing amplitude up to a frequency of 937 Hz, peaks are visible that were caused by the operation with a VSD. The BPF was located at a frequency of 376.8 Hz. However, no frequency spike is visible at the location of the BPF. With very slight visibility (−159.0 dB), the ECC1(−) component can be seen at a frequency of 91.3 Hz.

5.2.1.3 Dry-Runner Pump (180 W)

Figure 5.7 depicts the MCSA of a dry-runner pump in healthy condition at a flow of 15 m^3/h at a head of 3.4 m for the frequency range of 0 to 1000 Hz. The slip of the motor at this load point equaled 7.5%. The WH are present in the current spectrum, with WH7 at 350 Hz having the highest amplitude (−85.2 dB), followed by WH5 at 250 Hz (−91.9 dB) and WH3 at 150 Hz (−94.9 dB). Further WHs are also visible in the spectrum. However, their amplitude is lower than that of WH3, WH5, and WH7. The PSH, especially PSH1(+) at 790.1 Hz with −128.5 dB and PSH3(−) at 590.0 Hz with −153.1 dB, are also visible in the current spectrum. Additionally, the BPF is visible in the current spectrum at a frequency of 235.1 Hz and an amplitude of −166.9 dB. Higher-order

BPF components ($k_1 > 1$) did not appear in the current spectrum. However, the amplitude of this component is small compared to other components. In the lower frequency range of 0 to 100 Hz, there were also noticeable components, which are depicted in Figure 5.8.

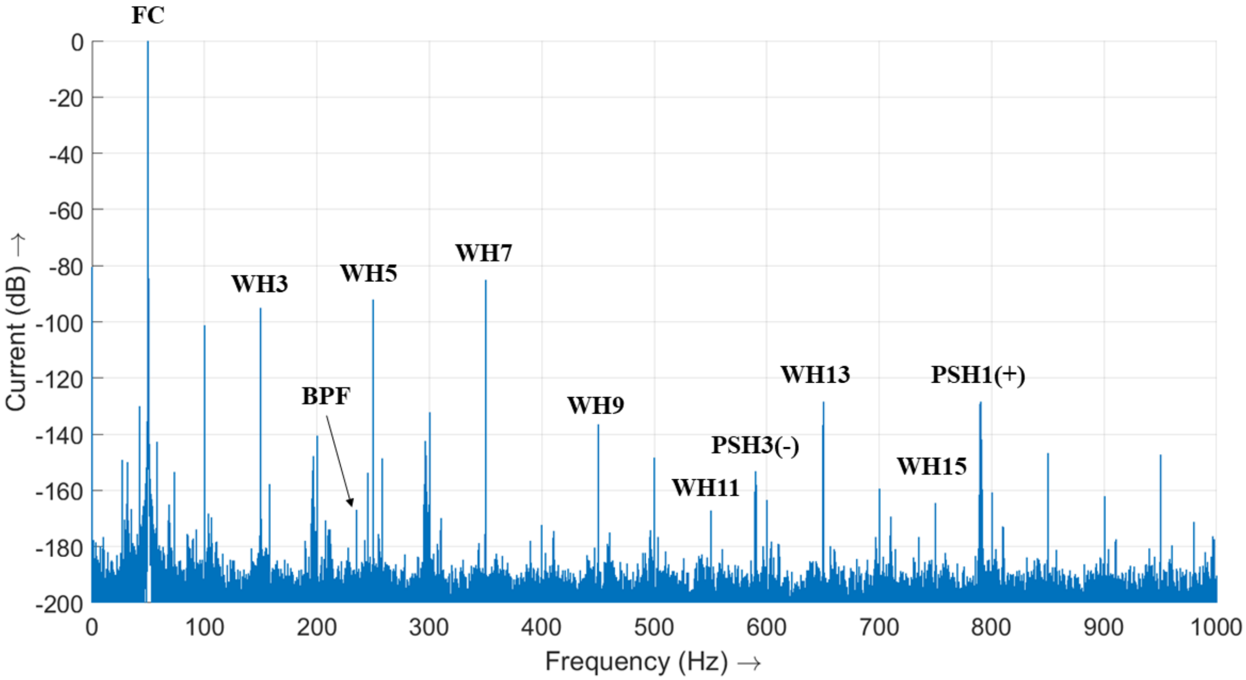

Figure 5.7: MCSA of a dry-runner pump (180 W) in healthy condition at a flow of 15 m^3/h at a head of 3.4 m at 0-1000 Hz

Although the motor was in healthy condition, both ECC and BBH appeared in the current spectrum. However, both components have small amplitudes and will not lead to alarms of a potential monitoring system. Regarding dynamic eccentricity, the most common components ECC1 around the FC appeared at 26.9 Hz (−149.2 dB) and 73.2 Hz (−153.5 dB). Also, the BB was visible in the most common frequency band BB1 at 42.5 Hz (−129.9 dB) and 57.5 Hz (−142.7 dB). However, since the amplitudes of BB1 were below −60 dB, the condition of the rotor bars could be labeled as *excellent* (Thomsen, 2017). Between ECC and BBH, two additional components appeared, which could not be attributed to a common component in the state of the art.

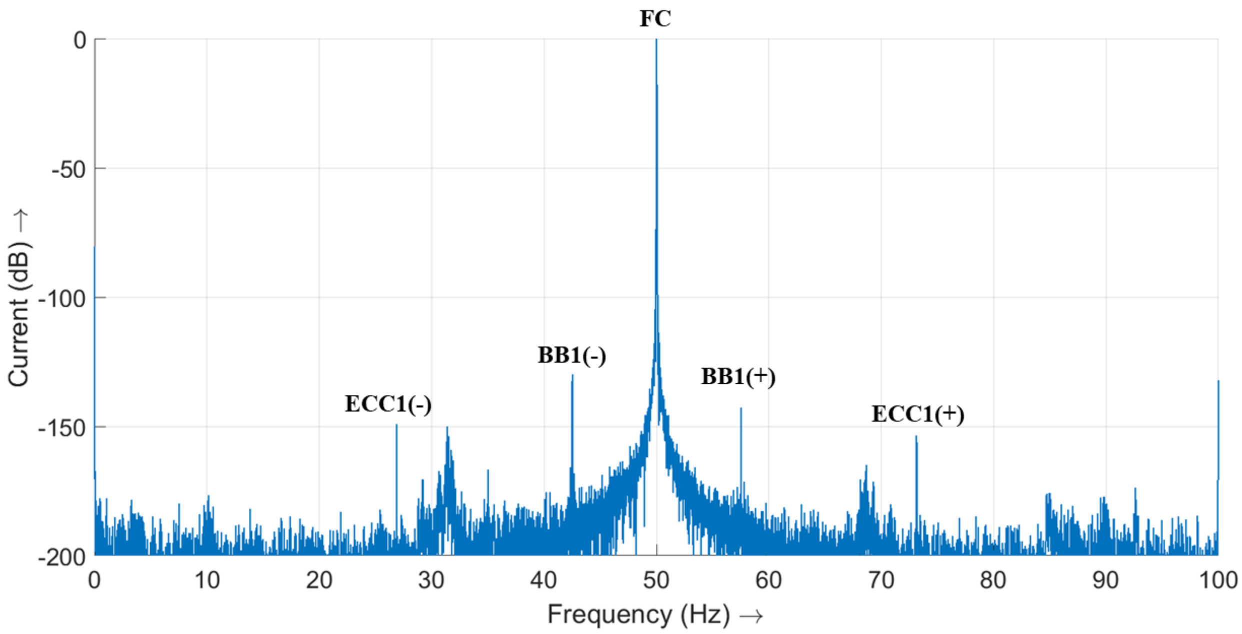

Figure 5.8: MCSA of a dry-runner pump (180 W) in healthy condition at a flow of 15 m^3/h at a head of 3.4 m at 0-100 Hz.

In order to evaluate how the operation with a VSD influences MCSA results in the low-frequency range, the dry-runner pump was also measured with a VSD at the same load point. In the first configuration, U/f control was used and in the second configuration, vector control was used to operate the pump. Figure 5.9 depicts the MCSA results of these configurations in the frequency range of 0-200 Hz.

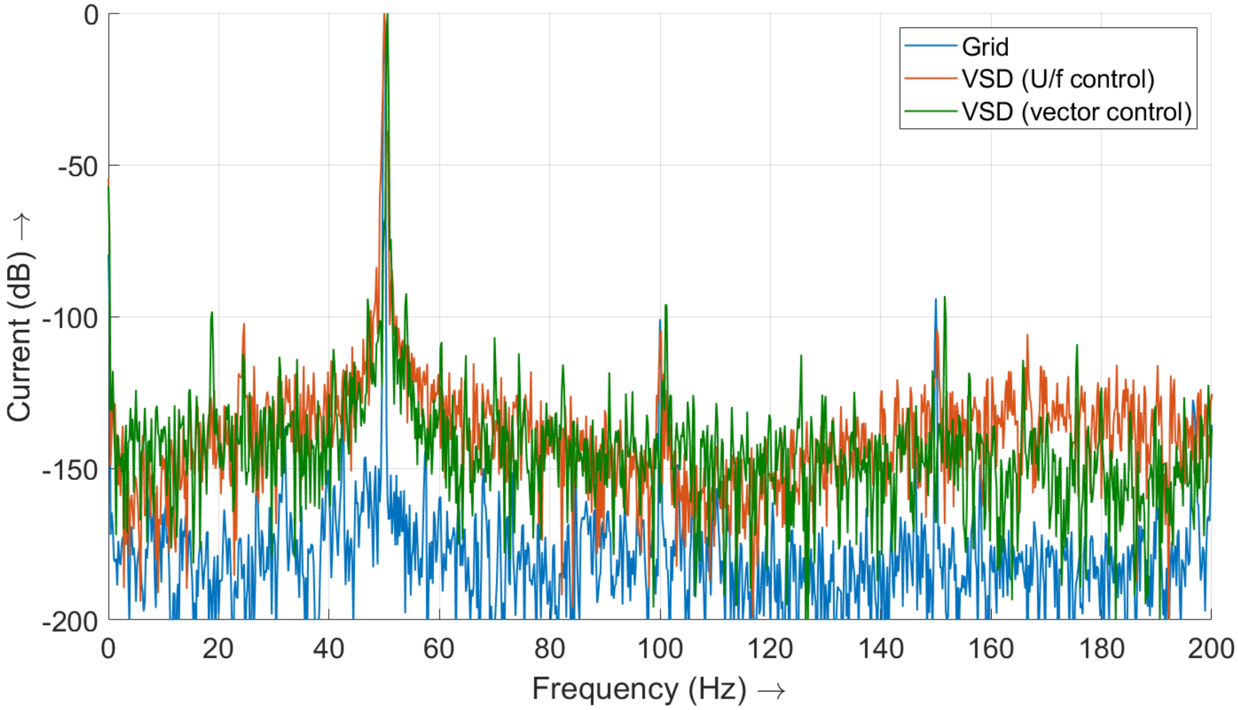

Figure 5.9: MCSA of a dry-runner pump (180 W) in healthy condition at a flow of 15 m^3/h at a head of 3.4 m at 0-200 Hz in different control modes: grid (blue curve), VSD (U/f control) (red), VSD (vector control) (green).

Compared to the operation at the grid, both VSD-driven configurations indicated an increased level of noise in the range of 0-200 Hz. What was noticeable was that in the VSD-operated variants, the peaks at the FC were not as defined in the mains-powered variant. Additionally, peaks appeared that were not visible in the MCSA of the grid-driven pump. For example, in U/f control operation, a peak of −102.2 dB appeared at 24.6 Hz, and in vector control operation, a peak of −98.4 dB appeared at 18.8 Hz. Finally, the eccentricity components, which were clearly visible in the grid-powered variant, were no longer visible in the VSD-operated variants.

5.2.1.4 Submersible Pump (7.7 kW)

Figure 5.10 depicts the MCSA of a submersible pump in healthy condition in a frequency range from 0-1000 Hz. As a load point, the flow was set to a value of 79.5 m^3/h, resulting in a head of 6.3 m. The FC of this VSD-driven motor is at 40 Hz. The slip at this load point equaled 1.8%. Both the visible peaks of the WH and the PSH are marked in Figure 5.10. At the odd multiples of the FC, all WH from WH3 to WH13 are clearly visible in the current spectrum. With an amplitude of −77.6 dB, WH5 had the highest WH and WH9 had the lowest with −174.7 dB. In total, four PSH had visible amplitudes in the spectrum. In this motor, the highest PSH is PSH1(−) with an amplitude of −107.6 dB, followed by PSH1(+) with −120.5 dB. Next to the WH and the PSH, many peaks are visible in the MCSA, which could be due to the VSD operation of the motor. With two exceptions, the amplitudes of these peaks are below −150 dB. The exception is located to the left of WH7 at a frequency of 260.0 Hz (−102.3 dB) and to the right of WH7 at 340.0 Hz (−107.3 dB).

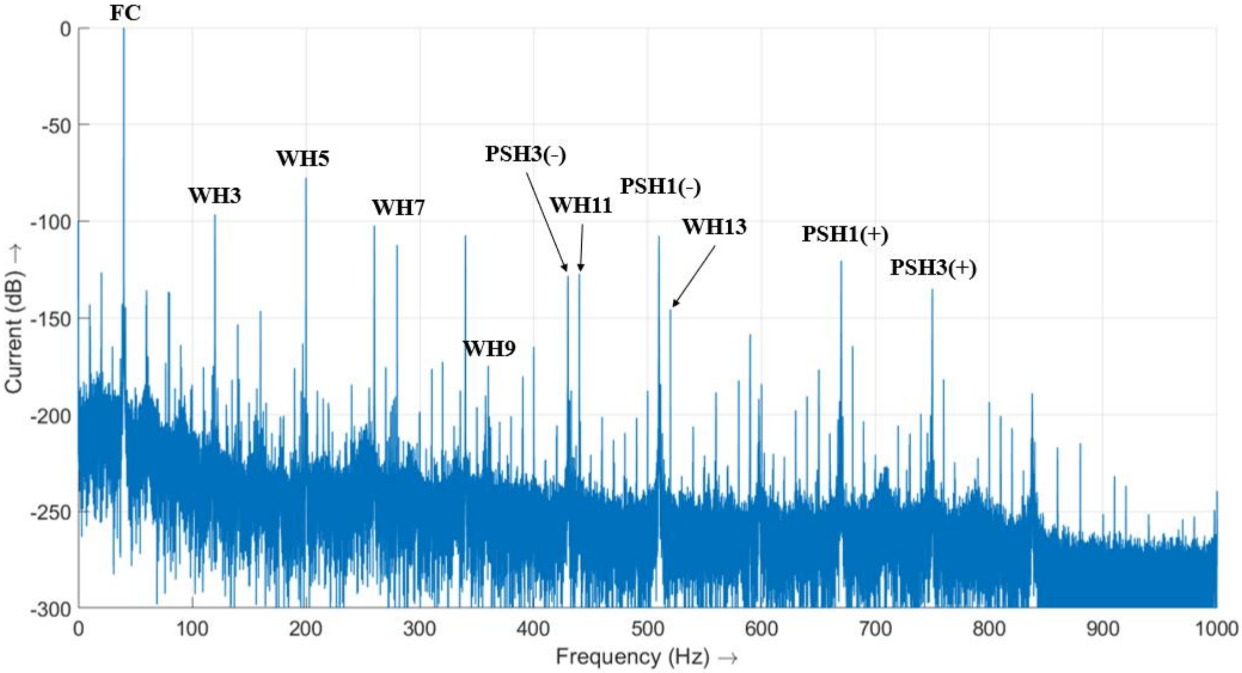

Figure 5.10: MCSA of a dry-runner pump (7.7 kW) in healthy condition at 0-1000 Hz.

In the frequency range from 0-100 Hz, several peaks are also visible; see Figure 5.11. The BBH are noticeable around the FC, with BB1(−) having the highest amplitude (−142.8 dB). Also, both eccentricity components, ECC1(−) with −126.5 dB and ECC1(+) with −143.3 dB, are visible in the MCSA, indicating a slight eccentricity of the motor. At 79.3 Hz, a peak of the height −136.4 dB is visible. As marked in Figure 5.11, this frequency band is equal to the BPF. However, BPF1(−), which should be at 0.7 Hz, did not differ from the noise level. Additionally, the PSH13 component can be detected in this low-frequency range with an amplitude of −164.7 dB. Additional peaks that could not be explained on the basis of the state of the art are visible at 10 Hz, 60 Hz, 80 Hz, and 100 Hz.

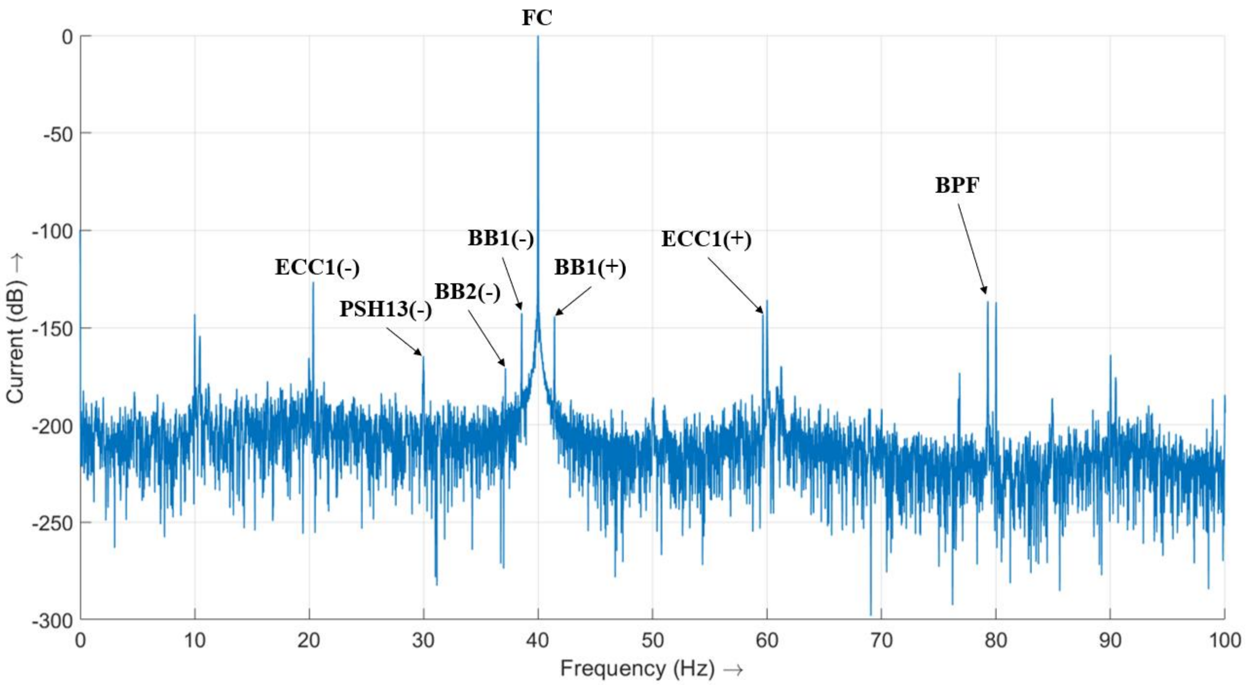

Figure 5.11: MCSA of a dry-runner pump (7.7 kW) in healthy condition at 0-100 Hz.

5.2.1.5 Discussion

The current amplitude of an oscillation is determined by the transfer behavior of the electric motor, which was demonstrated in section 3.1. The two analyzed wet-rotor pumps indicated that the BPF component is not visible in the current spectrum. There can be two reasons why no peaks were visible on the BPF: (1) No vibrations were generated by the design of the radial impeller, or (2) the amplitudes were so small that they were completely damped by the transfer behavior of the motor. The analyzed current spectra of the dry-runner pump and the submersible pump indicated small spikes (<−100 dB) at the points of the BPF. However, for the submersible pump, only BPF(+) had a pronounced amplitude, whereas BPF(−) was not visible. In the literature, the BPF has been demonstrated to be visible in the current spectrum with higher amplitudes, compared to the findings of this work. The authors of (Park, 2017) measured an amplitude of −52.2 dB at the BPF of a 2.2 kW motor with a 2-blade impeller. (Tian, 2014) revealed that the amplitude of a pump with a 5-blade impeller was in the range of −50 dB to −55 dB, depending on the flow. These high values for the BPF could not be confirmed in this work.

All analyzed pump variants indicated an amplitude at the dynamic eccentricity component ECC1 around FC. However, in all cases the amplitude was small in relation to FC. The wet-rotor pump with 800 W had the highest amplitude, followed by the submersible pump. The wet-rotor pump with 150 W had the lowest amplitude, which means that the higher amplitudes of the 800 W variant at ECC1 were not due to the pump design. Since in all variants the amplitude differed from the noise level, a slight eccentric run of the rotor could be concluded. A slight eccentric run can be caused by the journal bearing, in the case of the wet-rotor pump or, in all cases, by the uneven run of the rotor due to manufacturing tolerances.

In all variants, the WH were clearly visible. As also described in the literature, WH3, WH5, and WH7 were the WH with the highest amplitude (Antonino-Daviu, 2019). In all cases, the amplitudes of the WH were below −70 dB. In addition to the uneven multiples of FC, in every variant amplitudes at even multiples of FC appeared as well. For the two analyzed wet-rotor pumps, these amplitudes were higher than the respective WH3, which could be due to the operation with a PMSM with tooth coil windings.

Both IM-driven pumps (dry-runner pump and submersible pump) additionally indicated the typical amplitudes of BBH and PSH. Since in both cases, the amplitudes of BBH were below −60 dB, the condition of the bars could be labeled as *excellent* (Antonino-Daviu, 2019). In the current spectrum of the dry-runner pump, two PSH were visible with PSH1(+) and PSH3(−). For the submersible pump, both PSH1 and PSH3 were visible, and additionally PSH13(−) in the low-frequency range. The visible PSH of both variants could be used for slip approximation if the pump was driven without a speed sensor.

The influence of the VSD on the frequency range from 0-1000 Hz was also visible in all variants. Three of the four variants were operated with VSD, while the last variant, the dry-runner pump, was measured with VSD operation and in line-fed operation. Compared to line-fed operation, around FC the noise level increased under both U/f control and vector control. An increased noise level around FC was also observed in the conditions of *cavitation* and *hydraulic blockage* (Perovic, 2000). Accordingly, when operating with a VSD, care must be taken to avoid false alarms.

5.2.2 Clogging

Each pump examined was also measured in the clogged state. The results of the MCSA of each pump will be analyzed in the following sections.

5.2.2.1 Wet-Rotor Pump (800 W)

In this section, the results of the MCSA for the wet-rotor pump with 800 W will be analyzed, with special focus on the fault frequencies $f_{r,pump}$ and f_{BPF}. Figure 6.3 depicts the MCSA around these fault frequencies in a waterfall diagram. All MCSA results from healthy to seven clogged channels are illustrated. In addition, the MCSA around the frequencies 791.9 Hz and 875.3 Hz are depicted. These frequencies are the sideband frequencies of the 5th harmonic. During the measurements of the evaluated current curves, the position of the shut-off valve remained constant, resulting in different power inputs for all variants.

As the results of Figure 6.3 have already shown, reveals that at the frequencies 125.0 Hz (a), 208.4 Hz (b), 791.9 Hz (c), and 875.3 Hz (d), the amplitude increased when the number of clogged channels increased. A maximum was reached at three or four clogged channels. From then on, the amplitudes decreased when the number of clogged channels kept increasing. At the frequency 125.0 Hz, the amplitude of −98.5 dB in healthy condition increased to −59.6 dB (+38.9 dB) for three clogged channels and −61.3 dB for four clogged channels. With complete clogging, the amplitude dropped to −90.6 dB (+7.9 dB). The variant with one clogged channel (−81.6 dB) behaved similarly to the variant with six clogged channels (−90.7 dB), and the variant with two clogged channels (−75.1 dB) behaved like the variant with five clogged channels (−69.2 dB). Considering the frequency 208.4 Hz, the amplitude increased from −109.9 dB to −79.6 dB (+30.3 dB) for three clogged channels and to −84.0 dB for four clogged channels, and decreased to −120.4 dB (+10.5 dB) for complete clogging. At the frequency 791.9 Hz, the amplitude increased from −157.9 dB to −117.8 dB (+40.1 dB) for three clogged channels, which was the biggest increase. At the frequency 875.3 Hz, the amplitude increased from −157.7 dB to −118.8 dB (+38.9 dB). If we look at the BPF component, we can see that there was an increase of the peak only in the case of three clogged channels. The absolute value for the peak for three clogged channels was −155.2 dB, which was thus lower than the peaks of the other fault frequencies.

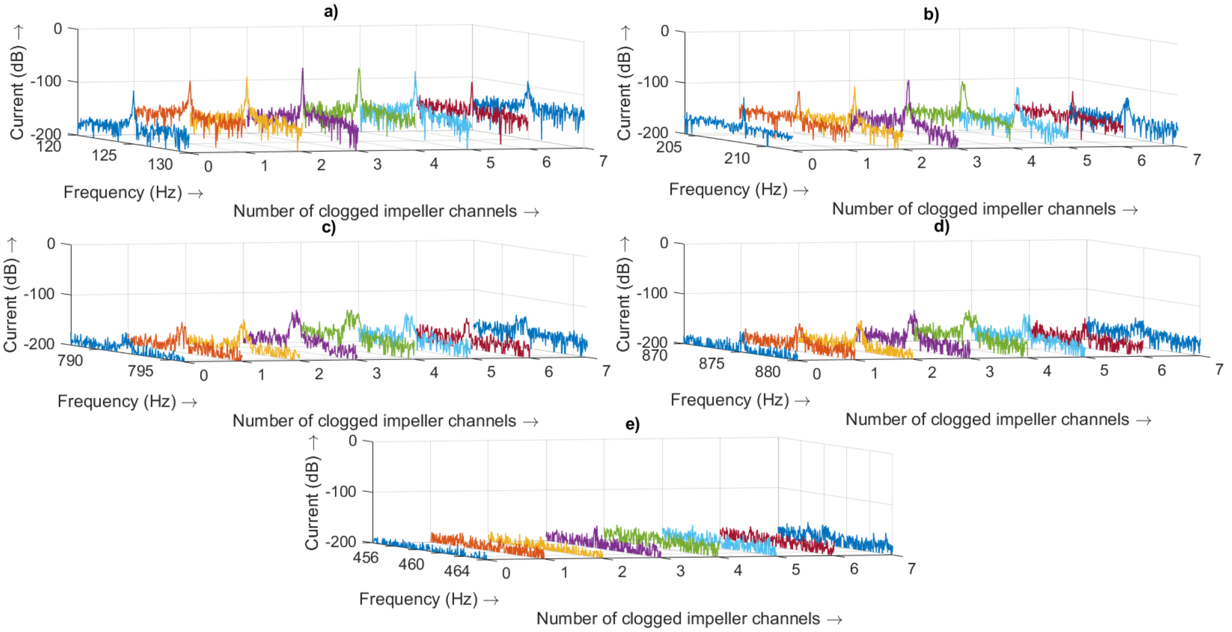

Figure 5.12: MCSA of a pump with different numbers of clogged impeller channels at a speed of 2500 rpm: (a) around $\boldsymbol{f_{r,pump-}} = \mathbf{125.0\ Hz}$; (b) around $\boldsymbol{f_{r,pump+}} = \mathbf{208.4\ Hz}$; (c) around 791.9 Hz; (d) around 875.3 Hz; (e) around $\boldsymbol{f_{BPF}} = \mathbf{458.4\ Hz}$

As can be seen in Table 5.1, the power consumption of the pump decreased with increasing clogging. For this reason, from here on, the faulty variants will be compared to the healthy variants with the same power consumption. The power was adjusted by adjusting the shut-off valve to match the power input of the faulty cases. This procedure ensured that the results analyzed were not obtained by decreasing the power consumption. In addition, the results allow better comparison of the faulty and healthy variants. For better visualization, the current signal was cut to a length of 1 s and for windowing, the hamming window was used. The focus was put on the two fault frequencies $f_{r,pump}$, as they were the frequencies mainly influenced in the MCSA. In Figure 5.13, the MCSA for the faulty variants and the corresponding healthy variant with the same power consumption of the pump are illustrated.

As the results of Figure 6.3 have already shown, the faults with three and four clogged channels showed the most obvious characteristics. In any case, the amplitude at $f_{r,pump}$ was greater than that of the corresponding healthy variant. Table 5.2 gives an overview of how much the amplitude increased in comparison to the healthy variant. Additionally, the results for the speed 1800 rpm and 1000 rpm are listed. At a speed of 2500 rpm, the increase was the highest in the case of three clogged channels, followed by four and two clogged channels. The remaining fault variants were more difficult to detect due to the lower increase. This trend could also be seen at a speed of 1800 rpm. Here, the increase of the amplitudes was about the same in the case of three and four clogged channels. At a speed of 1000 rpm, the results were no longer clear. With four clogged channels, an amplitude decrease of −27.9 dB could even be observed.

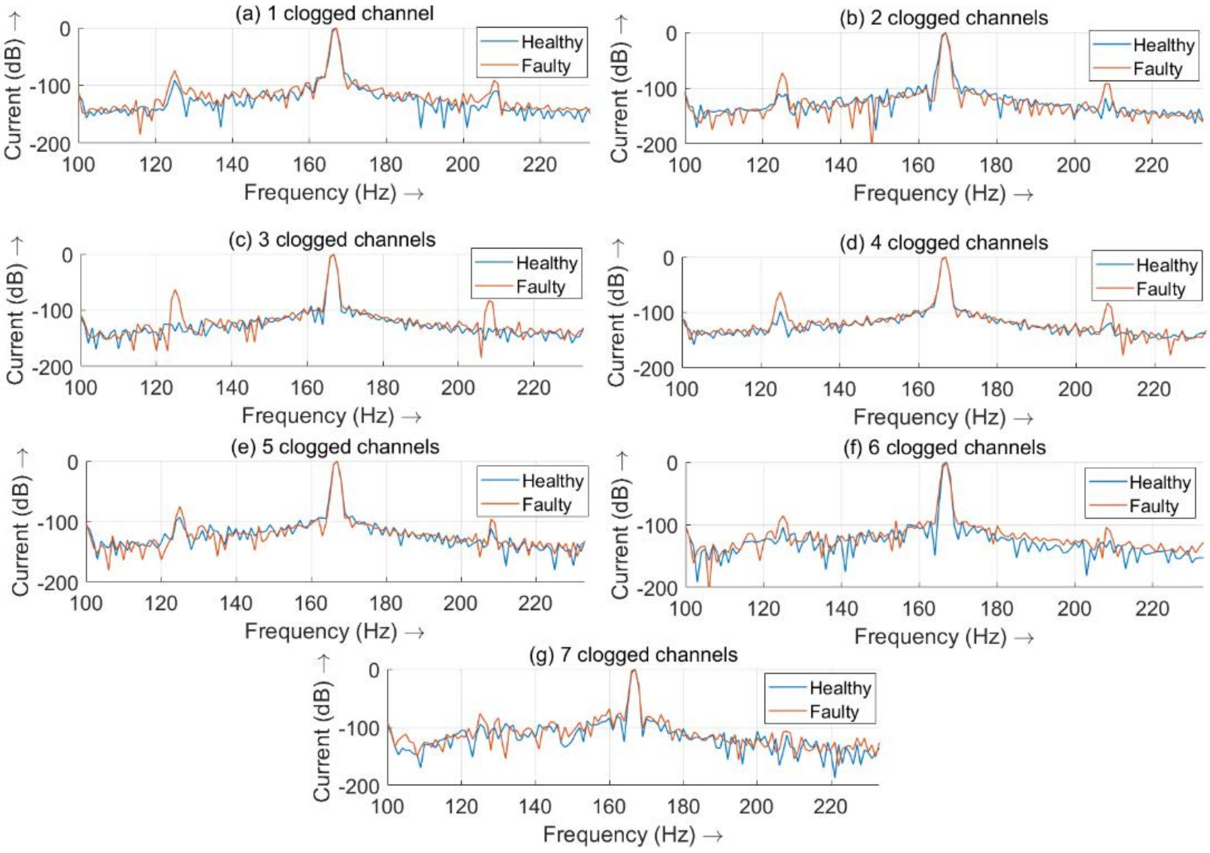

Figure 5.13: MCSA of a pump with different numbers of clogged impeller channels at a speed of 2500 rpm and the corresponding healthy variant with the same power consumption: (a)-(g) 1-7 clogged channels

Table 5.2: Increase of amplitudes in dB in the case of *impeller clogging* for different speeds and numbers of clogged channels

	1 clogged channel	**2 clogged channels**	**3 clogged channels**	**4 clogged channels**	**5 clogged channels**	**6 clogged channels**	**7 clogged channels**
n=2500 rpm							
$f_{r,pump-} = 125.0Hz$	+17.0	+36.8	+47.1	+35.0	+18.2	+18.3	+18.6
$f_{r,pump+} = 208.4Hz$	+18.7	+29.0	+48.7	+35.1	+15.2	+20.8	+5.8
n=1800 rpm							
$f_{r,pump-} = 90.0Hz$	+8.1	+30.5	+39.2	+42.2	+24.0	+7.1	+16.9
$f_{r,pump+} = 150Hz$	+14.0	+29.1	+46.9	+36.6	+18.4	−26.1	+8.9
n=1000 rpm							
$f_{r,pump-} = 50.3Hz$	−20.8	−1.3	+7.0	−27.9	−17.5	+18.4	+7.8
$f_{r,pump+} = 83.8Hz$	+5.1	+9.0	+12.9	+6.2	+0.5	+20.6	+4.0

5.2.2.2 Wet-Rotor Pump (150 W)

In this section, the influence of a clogged impeller channel on a wet-rotor pump with a power of 150 W will be investigated. In the investigated load point, the speed was set to 2740 rpm and the flow to 8 m^3/h. In the current spectrum, only the frequencies at $f_{r,pump-}$ and $f_{r,pump+}$ were slightly influenced by the clogged impeller channel. The BPF component was also checked and no change was noticed compared to the healthy variant. Figure 5.14 depicts the current spectrum around the two frequencies $f_{r,pump-}$ and $f_{r,pump+}$.

At $f_{r,pump-}$, the amplitudes increased from −161.6 dB in healthy condition to −147.9 dB in faulty condition, which resulted in an increase of 13.7 dB, whereas at $f_{r,pump+}$, the amplitude remained almost at the same value, i.e., at −163.2 dB in healthy condition and at −161.3 dB in faulty condition (+1.9 dB).

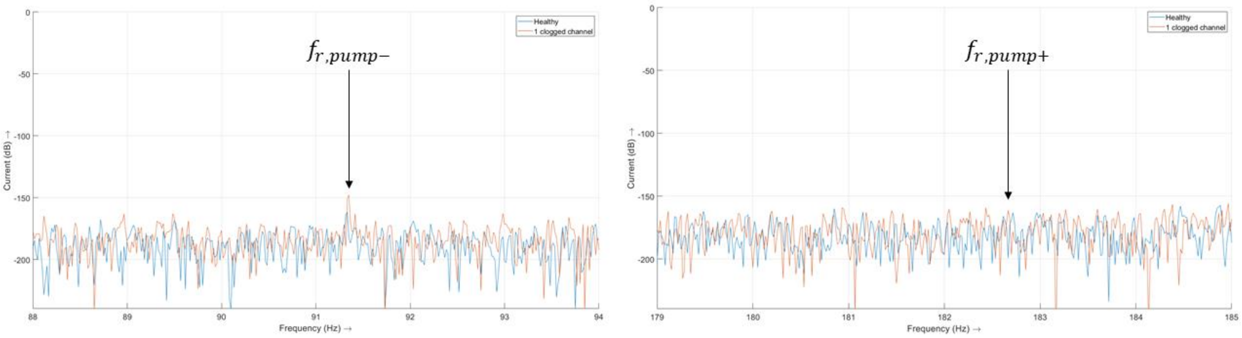

Figure 5.14: MCSA of the wet-rotor pump (150 W) around $\boldsymbol{f_{r,pump-}}$ and $\boldsymbol{f_{r,pump+}}$

Compared to the same pump with higher power (800 W vs. 150 W), the increase was lower; see section 5.2.2.1. One reason could be the transfer behavior of the electric motor. This effect will be reviewed in more detail in section 5.4. With regards to the detection of such faults, this means that it is more difficult to use the MCSA for the variant with 150 W.

5.2.2.3 Dry-Runner Pump (180 W)

The fault components related to the line-fed (50 Hz) dry-runner pump faults in the current spectrum are illustrated for three different load points, where the flow was adjusted from 10 m^3/h (Figure 5.15) to 15 m^3/h (Figure 5.16) to 20 m^3/h (Figure 5.17), with the amplitude spectrum depicted in the frequency ranges from 23 Hz to 30 Hz and 70 to 77 Hz. As demonstrated in equation (2.14), the fault components $f_{r,pump}$ depend on the slip of the motor. Because of that, the frequencies $f_{r,pump}$ changed depending on the condition and the load of the pump. It is visible in Figure 5.15 to Figure 5.17 that $f_{r,pump-}$ became smaller and $f_{r,pump+}$ became greater with increasing number of clogged channels, indicating that the slip became smaller with higher fault severity. The BPF will not be considered, as neither an increase nor a decrease of this amplitude was caused by the faults.

Figure 5.15 depicts the amplitudes at the two fault frequencies at a flow of 10 m^3/h. At $f_{r,pump-}$, the amplitude first decreased from −148.4 dB (healthy) to −153.7 dB (1 clogged channel) and then increased to −146.2 dB (3 clogged channels), which corresponds approximately to the amplitude of the healthy variant. For the variant with five clogged channels, the amplitude increased to −132.8 dB, resulting in an increase of +15.6 dB. At $f_{r,pump+}$, the amplitude decreased from −150.0 dB (healthy) to −155.8 dB (1 clogged channel) to −158.0 dB (3 clogged channels). For the variant with five clogged channels, the amplitude increased by 6.3 dB compared to the healthy variant, to a value of −143.7 dB.

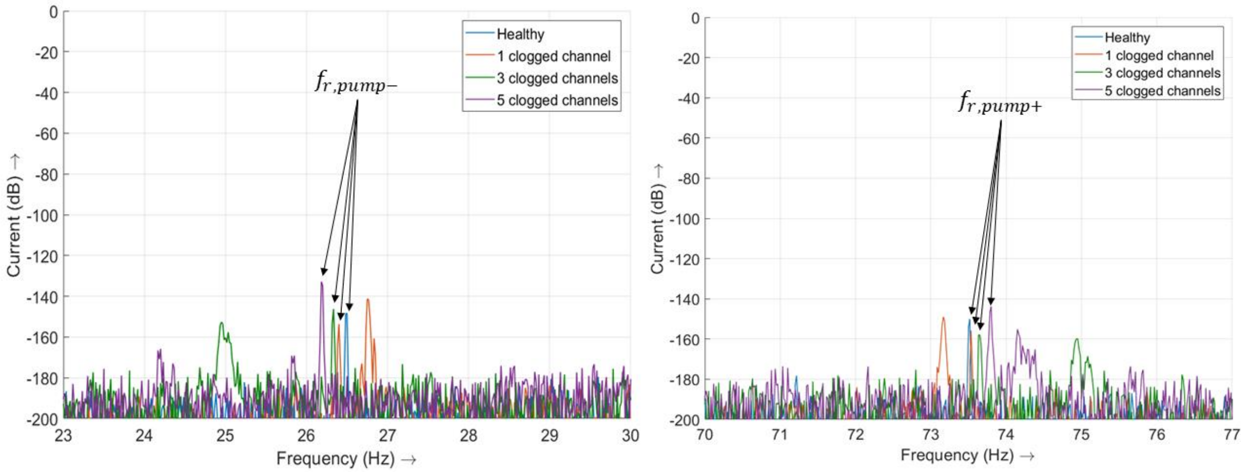

Figure 5.15: MCSA of a clogged line-fed dry-runner pump around the fault frequencies $\boldsymbol{f_{r,pump-}}$ and $\boldsymbol{f_{r,pump+}}$ at a flow of 10 m^3/h

The fault components $f_{r,pump-}$ and $f_{r,pump+}$ at a flow of 15 m^3/h are illustrated in Figure 5.16. At this load point, both amplitudes at $f_{r,pump-}$ and $f_{r,pump+}$ became larger with increasing number of clogged channels. At $f_{r,pump-}$, the amplitude increased from −149.2 dB (healthy) to −143.0 dB (1 clogged channel) to −139.1 dB (3 clogged channels) and finally to −126.6 dB (5 clogged channels). Compared to the healthy variant, the clogged pump with the highest fault severity increased its amplitude by 22.6 dB at $f_{r,pump-}$. At $f_{r,pump+}$, the amplitude increased from −153.5 dB (healthy) to −148.6 dB (1 clogged channel) to −140.4 dB (3 clogged channels) and finally to −135.8 dB (5 clogged channels), resulting in an amplitude increase of 17.7 dB. Consequently, the amplitude increase at $f_{r,pump+}$ is smaller compared to the one at $f_{r,pump-}$.

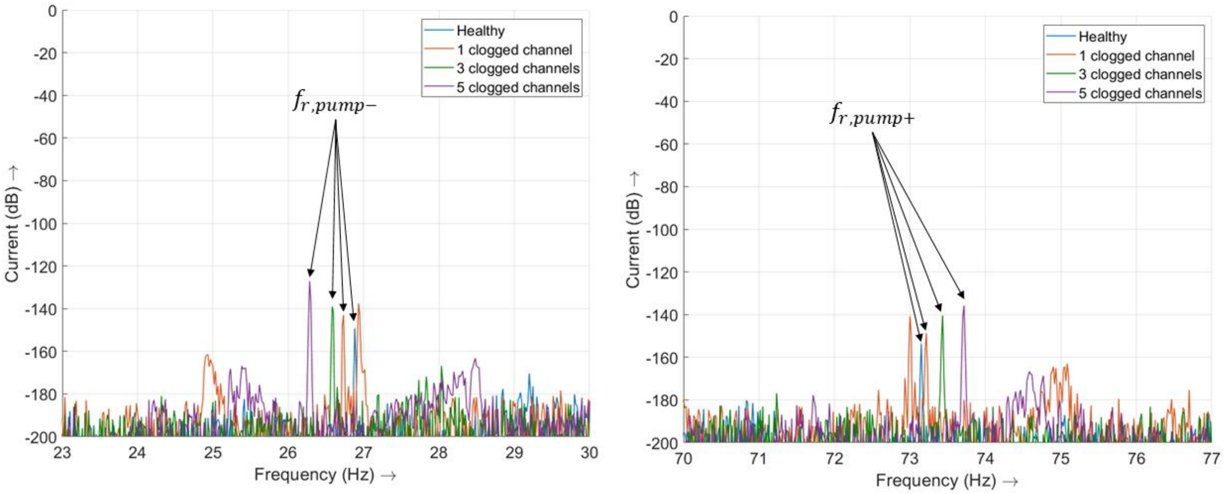

Figure 5.16: MCSA of a clogged line-fed dry-runner pump around the fault frequencies $\boldsymbol{f_{r,pump-}}$ and $\boldsymbol{f_{r,pump+}}$ at a flow of 15 m^3/h

Figure 5.17 depicts the amplitudes at the two fault frequencies $f_{r,pump-}$ and $f_{r,pump+}$ at a flow of 20 m^3/h. As already demonstrated with a flow of 15 m^3/h, the amplitudes increased with increasing number of clogged channels. At $f_{r,pump-}$, the amplitude increased from −151.1 dB (healthy) to −150.5 dB (1 clogged channel) to −123.3 dB (3 clogged channels) and finally to −118.5 dB (5 clogged channels). At $f_{r,pump+}$, the amplitude increased from −159.2 dB (healthy) to −149.0 dB (1 clogged channel) to −129.7 dB (3 clogged channels) and finally to −127.3 dB (5 clogged channels). The values prove that especially the variants with three and five clogged channels have a strong influence on the two amplitudes. For the variant with five clogged channels, the amplitude increased by 32.6 dB at $f_{r,pump-}$ and by 31.9 dB at $f_{r,pump+}$ compared to the healthy variant. This constitutes the highest increase in amplitude of all investigated load points.

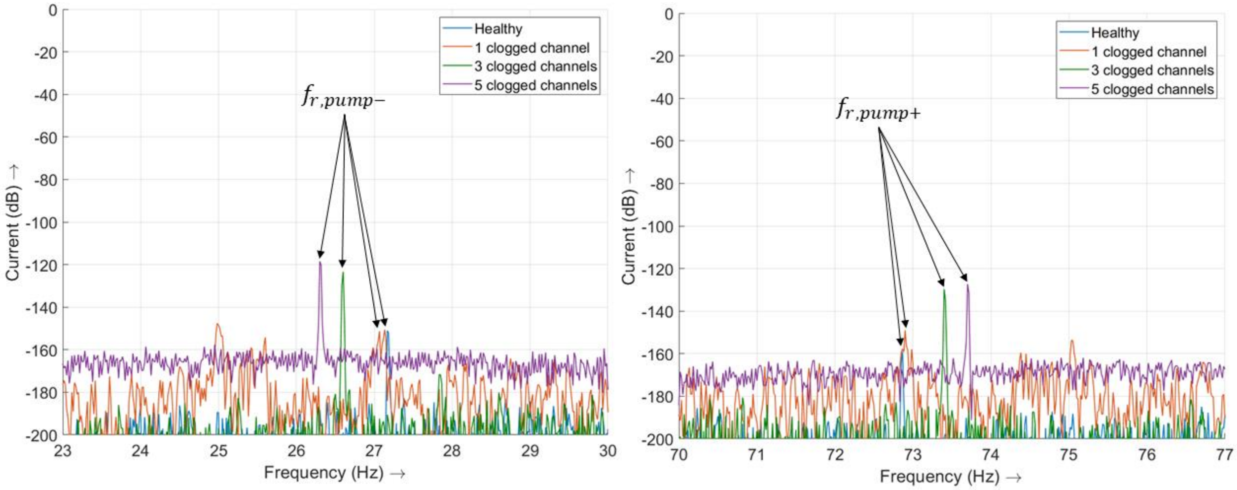

Figure 5.17: MCSA of a clogged line-fed dry-runner pump around the fault frequencies $\boldsymbol{f_{r,pump-}}$ and $\boldsymbol{f_{r,pump+}}$ at a flow of 20 m^3/h

5.2.2.4 Submersible Pump (7.7 kW)

In this section, MCSA will be used to analyze the current signal of the ESP. Since the time intervals in which the pump was operated in a steady state condition were short in the measurement, the frequency resolution was poor in the current spectrum. For both signals, the healthy and the clogged variants, signals with a length of 3599 samples were used, resulting in a frequency resolution of 0.56 Hz. Figure 5.18 depicts the MCSA of the submersible pump in healthy condition and in clogged condition in the frequency range from 0 to 100 Hz.

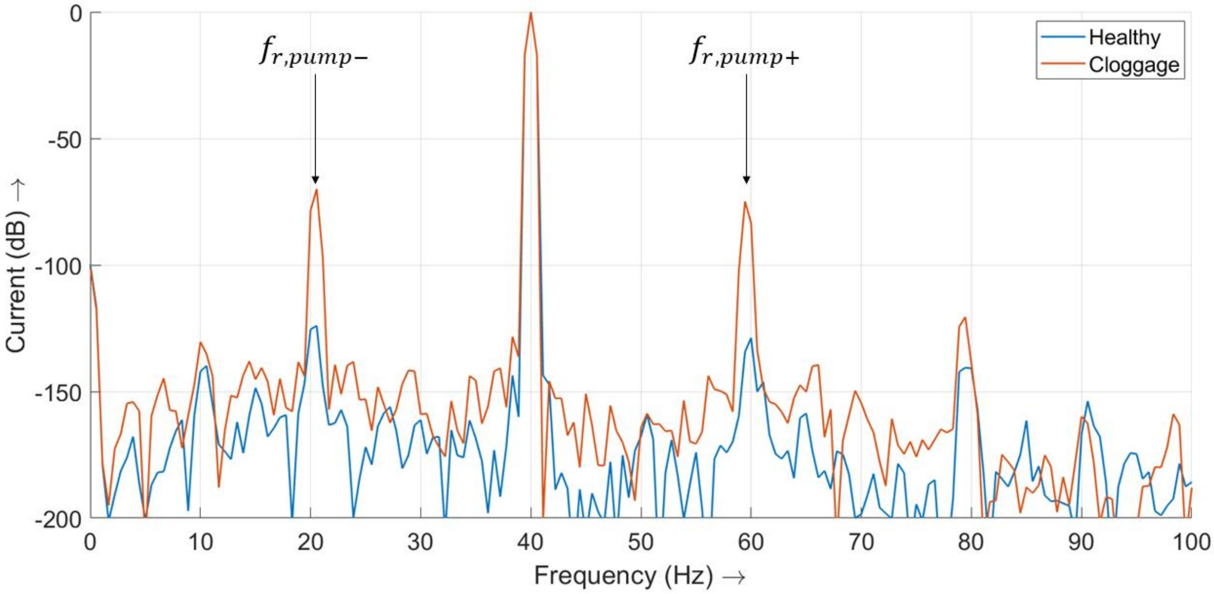

Figure 5.18: MCSA of the ESP in healthy and clogged condition in the frequency range from 0 to 100 Hz

Note that the fundamental component f_s in the current signal was at 40 Hz with the normalized amplitude of 0 dB. At the frequency points $f_{r,pump-}$ and $f_{r,pump+}$, the amplitudes increased from −124.0 dB to −70.0 dB (+54.0 dB) and from −128.8 dB to −74.9 dB (+53.9 dB) when we compare the healthy and the clogged cases.

On the other hand, in the higher-frequency range, the current spectrum was also influenced by the clogging. Figure 5.19 depicts the MCSA in the frequency range from 90 to 310 Hz.

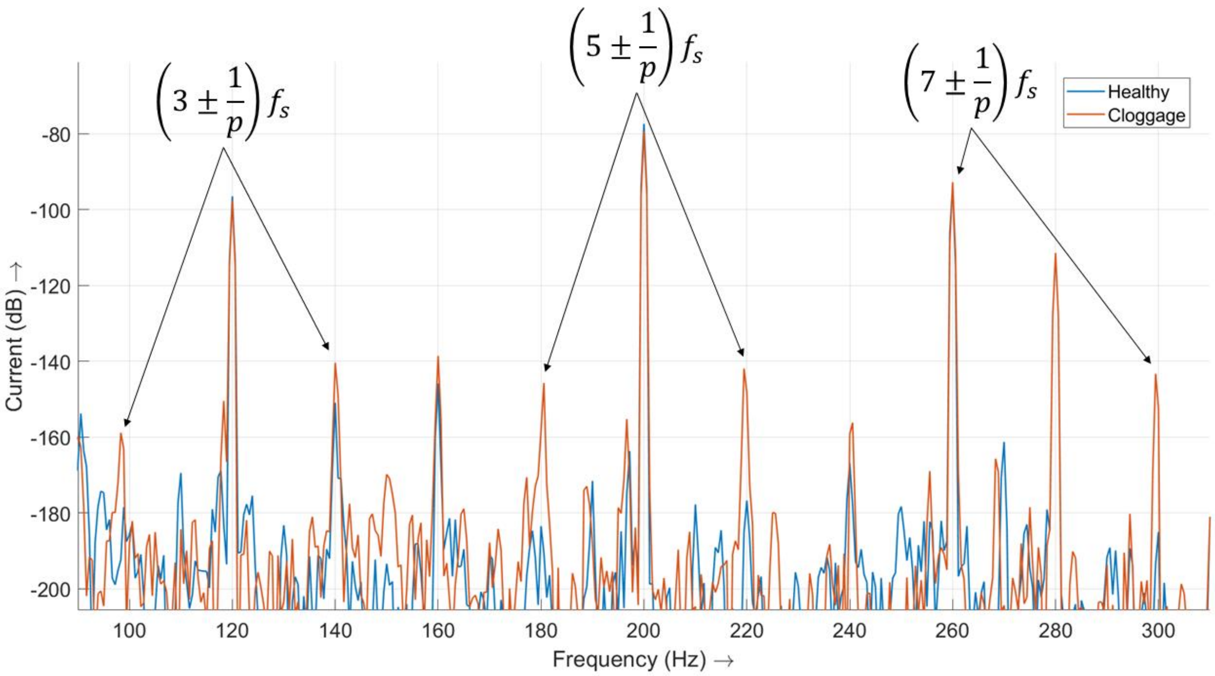

Figure 5.19: MCSA of the ESP in healthy and clogged condition in the frequency range from 90 to 310 Hz

As Figure 5.19 illustrates, in the range from 90 to 310 Hz, the 3rd (120 Hz), 5th (200 Hz), and 7th (280 Hz) WH are found, with the 5th having the highest amplitude. Around the WHs, at a distance of $\frac{1-s}{p}$, there were sideband components whose amplitudes increased due to the clogging. This became clearer at the harmonics around the 5th WH. The left sideband increased from −183.5 dB to −145.7 dB (+37.8 dB) and the right sideband from −176.8 dB to −141.9 dB (+34.9 dB). Around the 3rd and the 7th WH, there was also at least one sideband whose amplitude increased. However, at the frequencies 140 Hz and 260 Hz, amplitudes were visible even in the healthy variant, which could be caused by the VSD.

Therefore, MCSA demonstrated that the frequencies predicted by equation (2.14) are influenced by the clogging of the ESP. Compared to the state of the art, this is a new finding for a fully clogged ESP (not tested in previous papers). Additionally, the sidebands around the pronounced WH are influenced by the clogging, which was not predicted by equation (2.14). Even though the differences between healthy condition and clogged condition are clear in the MCSA, the resolution is relatively small due to the short recording times (presence of frequent transients and short stationary intervals). This highlights the disadvantage of applying MCSA in this use case.

5.2.2.5 Discussion

In all tested variants, an influence on the BPF due to the fault *clogging* was analyzed, but neither a decrease nor an increase of the BPF was found in all variants. Consequently, the BPF is not suitable for detecting the fault *impeller clogging* of the investigated variants. The same result was obtained with a similar application in (Jahangiri, 2018). A decrease of the BPF caused by *impeller clogging*, as described in (Tian, 2014), cannot be confirmed here.

Based on (Bonaldi, 2012), the hypothesis is that $f_{r,pump}$ can be influenced by the fault *impeller clogging*, although in (Bonaldi, 2012), only the faults *misalignment* and *unbalance* are mentioned. The hypothesis that $f_{r,pump}$ can also be influenced by the fault *clogging* was confirmed by the results. All measured variants indicated an increase of the amplitudes at $f_{r,pump}$ in faulty condition. For the three variants with a radial impeller, the amplitude increased with increasing number of adjacent clogged impeller channels. Especially with half-sided clogging of the wet-rotor pump (800 W), with three and four (of seven) clogged channels, there was a high increase in amplitudes at the frequency $f_{r,pump}$. However, smaller faults also showed differences to the healthy variant. This was especially true for higher speeds, in this case greater or equal 1800 rpm. That the fault of clogging of the impeller was found to cause an increase in the component $f_{r,pump}$ is new compared to the state of the art. In the literature, only (Perovic, 2000) showed that a damaged impeller increases the amplitude at $f_{r,pump+}$.

However, not only the two frequencies $f_{r,pump}$ were influenced by the faults, but also the sidebands of WH of the variants. In the presence of the *clogging* fault of the wet-rotor pump (800 W), the sidebands at $\left(5 \pm \frac{1-s}{p}\right) \cdot f_s$, in particular, increased. When the submersible pump had clogged impeller channels, the two frequencies $\left(3 - \frac{1-s}{p}\right) \cdot f_s$ and $\left(5 + \frac{1-s}{p}\right) \cdot f_s$ were influenced. These increases cannot be explained by equation (2.14) and argue for an adaptation of equation (2.14) for the fault *clogging*. Equation (5.1) represents the adapted form of equation (2.14), also capturing the influence of the fault *clogging* on the higher frequencies. It equals the equation for the calculation of dynamic eccentricities, see equation (2.16), if $n_d = 1$. It gives a more general explanation of equation (2.14), which is also true for all the findings described in this section. Like for the dynamic eccentricities, the largest values are expected for $v = 1$, which is also confirmed by the results in this section.

$$f_{r,pump} = \left(n_{ws} \pm \frac{(1-s)}{p} \right) \cdot f_s \tag{5.1}$$

Whether this is the same for other types of pump units is part of future work. In particular, it should be examined whether the components of the wet-rotor pump, particularly the journal bearings used, have an influence on this result.

5.2.3 Cracked Impeller

How the fault *cracked impeller* influences the current spectrum of an 800 W wet-rotor pump will be analyzed in this section. The fault was implemented on the basis of the explanations in section 4.2.2. As a load point, a speed of 2800 rpm and a flow of 20 m^3/h was set. The current spectrum of both the healthy variant and the variant with a cracked impeller is depicted in Figure 5.20.

At the frequency $f_{r,pump-}$, the amplitude increased from −114.6 dB in healthy condition to −103.3 dB in faulty condition (+11.3 dB), and at $f_{r,pump+}$, the amplitude increased from −131.8 dB in healthy condition to −118.1 dB in faulty condition (+13.7 dB). Other frequencies in the current spectrum were not influenced by the fault.

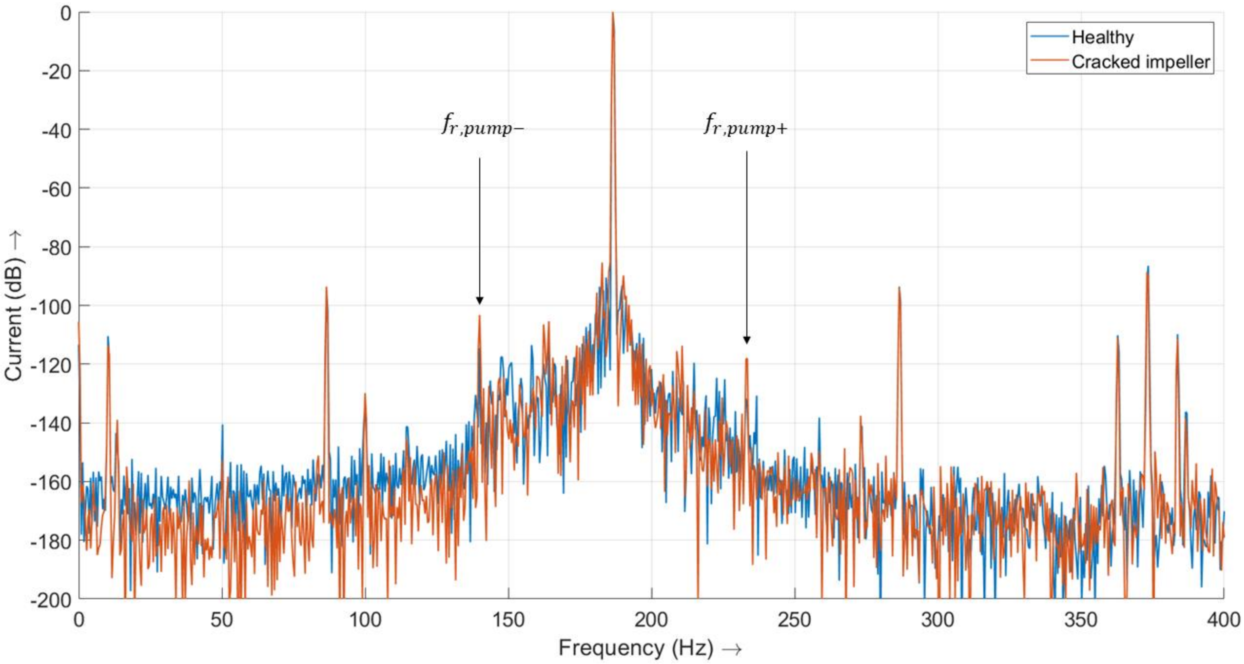

Figure 5.20: MCSA of the wet-rotor pump (800 W) with a cracked impeller from 0–400 Hz.

The findings of this section confirm the finding of (Perovic, 2000), which demonstrated an influence at the frequency $f_{r,pump+}$. Compared to (Perovic, 2000), in the pump investigated here, the frequency $f_{r,pump-}$ also increased. A decreased amplitude at the BPF component due to impeller damage, as shown in (Tian, 2014), was not confirmed by our results.

5.2.4 Bearing Damage

In this section, the influence of a damaged journal bearing on the MCSA will be evaluated. A wet-rotor pump with a power of 800 W was measured at a load point with a flow of 10.0 m^3/h and a head of 11.1 m at the speed of 2800 rpm, while the diameter of the bearing shell and the position of the damaged bearing was varied. The current spectrum of the healthy and the faulty variant differed at four frequencies. All frequencies were related to the eccentricity frequencies, which are calculated based on equation (2.16). The first frequency bands could be attributed to a dynamic eccentricity since $v = 1$ and $n_d = 1$. In the following, these two frequency bands will be denoted as f_{ecc1}. The third and fourth frequency bands influenced were located in the sidebands at the 5th harmonic ($v = 5$), at 4.75 times f_s (886.8 Hz), and at 5.25 times f_s (980.2 Hz), resulting in an eccentricity order of $n_d = 1$. These two frequency bands will be denoted as f_{ecc5}. Since $n_d = 1$, the results indicated a dynamic eccentricity of the motor due to the bearing defect. Figure 5.21 depicts the frequency range from 0-373 Hz, and Figure 5.22 the range 850-1000 Hz.

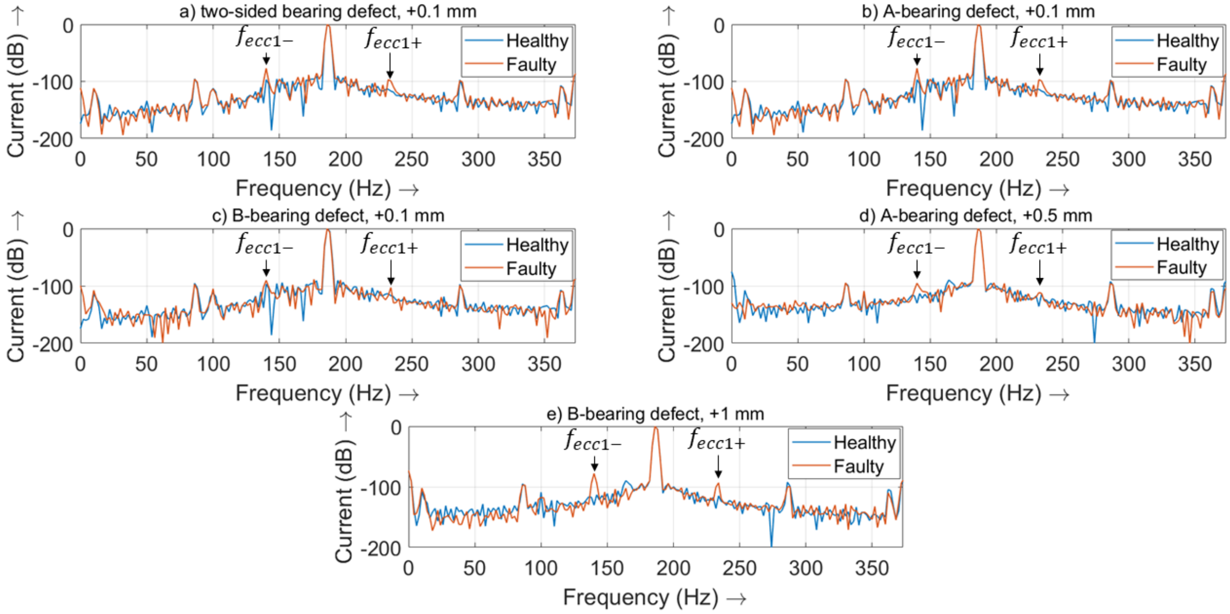

Figure 5.21: MCSA of the wet-rotor pump (800 W) with varying severity of bearing damage from 0–373 Hz; (a) two-sided bearing defect, +0.1 mm; (b) A-bearing defect, +0.1 mm; (c) B-bearing defect, +0.1 mm; (d) A-bearing defect, +0.5 mm; (e) B-bearing defect, +1 mm.

For variant a), the amplitude of the frequency component f_{ecc1-} equaled –81.6 dB, for b) –78.9 dB, for c) –90.8 dB, for d) –97.0 dB, and for e) –78.9 dB. The amplitude at f_{ecc1+} equaled–97.0 dB for a),–99.3 dB for b), –109.4 dB for c), –115.2 dB for d), and–97.5 dB for e). For both components, f_{ecc1-} and f_{ecc1+} increased compared to the corresponding healthy components. The highest amplitudes were reached at the B-bearing defect of +1 mm, followed by the two-sided bearing defect of +0.1 mm.

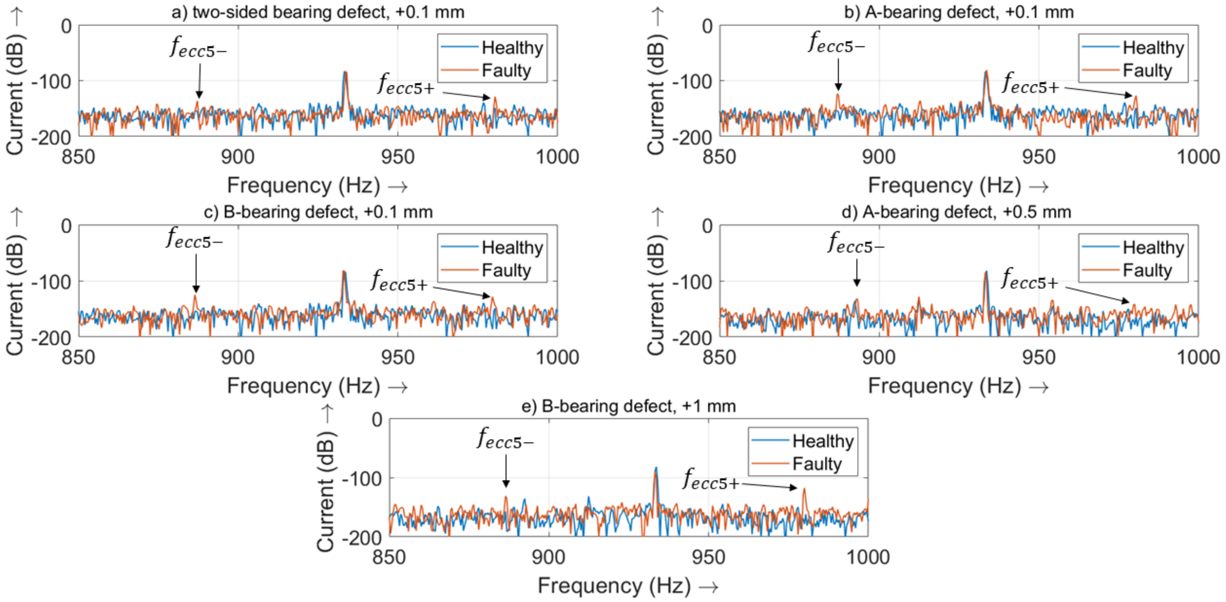

Figure 5.22: MCSA of the wet-rotor pump (800 W) with varying severity of bearing damage from 850–1000 Hz; (a) two-sided bearing defect, +0.1 mm; (b) A-bearing defect, +0.1 mm; (c) B-bearing defect, +0.1 mm; (d) A-bearing defect, +0.5 mm; (e) B-bearing defect, +1 mm.

For variant a), the amplitude of the frequency component f_{ecc5-} equaled–139.7 dB, for b) –135.6 dB, for c) –145.1 dB, for d) –144.1 dB, and for e) –133.9 dB. At f_{ecc5+}, the amplitude equaled for –137.4 dB variant a), –135.4 dB for b),–147.2 dB for c),–154.8 dB for d), and –129.4 dB for e). The amplitudes at f_{ecc5} had the same behavior as the amplitudes of f_{ecc1}, with the variant of the B-bearing defect of +1 mm having the highest amplitudes, followed by the two-sided bearing defect of +0.1 mm.

These results are an indication that due to the worn journal bearing, the rotor no longer has any guidance and thus runs dynamically eccentrically. Thus, in the case of journal bearings, it is not the typical frequencies of bearings (see section 2.4.4.7) that are affected in the MCSA. Rather, wear on plain bearings causes the rotor to run eccentrically, which can be seen in the eccentricity frequencies.

5.2.5 Dry-Running Rotor

To evaluate whether the fault *dry-running rotor* influences the MCSA, a wet-rotor pump was measured. The load point was set to a flow of 10.0 m^3/h and a head of 11.1 m at a pump speed of

2800 rpm. Figure 5.23 illustrates the current spectrum of the pump in the frequency range from 0-400 Hz.

Like the fault *bearing damage*, the fault *dry-running rotor* influenced the dynamic eccentricity component f_{ecc1}, according to equation (2.16). The amplitude of the frequency component f_{ecc1-} equaled –109.2 dB for the faulty variant, which meant an increase in amplitude of +32.4 dB, while the frequency component f_{ecc1+} equaled –125.7 dB, resulting in an increase of +31.6 dB compared to the healthy condition of the motor.

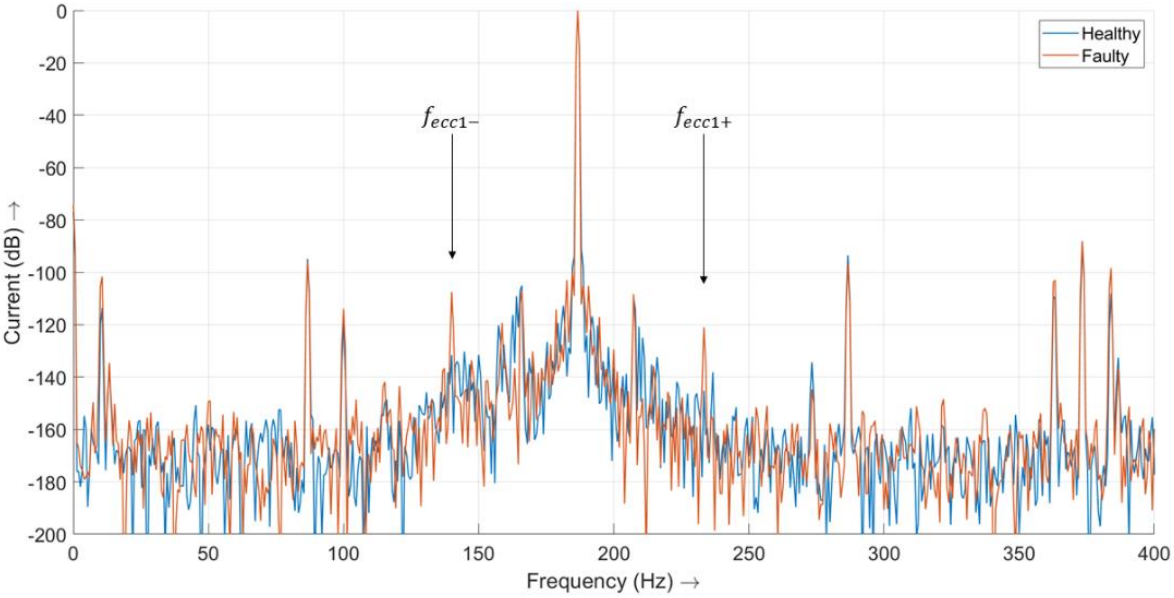

Figure 5.23: MCSA of the wet-rotor pump (800 W) with a dry-running rotor from 0–400 Hz.

The results indicate that a slight dynamic eccentricity was caused by the dry-running rotor. This behavior can be explained by the fact that no lubricating film could form between the bearing and the shaft because there was no water in the rotor space. The gap between shaft and bearing was sufficient to cause a slight eccentricity.

5.2.6 Dry Running

Compared to the fault *dry-running rotor*, the fault *dry running* can occur for different pump types, including dry-runner pumps and wet-rotor pumps. However, for wet-rotor pumps, dry running can provoke a quick breakdown since the journal bearings are no longer lubricated.

In this section, the influence of *dry running* on the MCSA of a wet-rotor pump will be investigated. Figure 5.24 and Figure 5.25 depict the MCSA for the fault *dry running* at the two speeds 1800 and 2500 rpm. At a speed of 1800 rpm, the amplitude at f_{ecc1-} increased from –90.7 dB to –51.1 dB (+39.6 dB) and at f_{ecc1+} from –113.1 dB to –80.0 dB (+33.1 dB), compared to the healthy variant. At a speed of 2500 rpm, the amplitude at f_{ecc1-} increased from –94.7 dB to –49.6 dB (+45.1 dB) and at f_{ecc1+} from –109.0 dB to –75.6 dB (+33.4 dB). However, not only these two frequencies were influenced. The noise band and other peaks were also higher in the case of the dry-running pump.

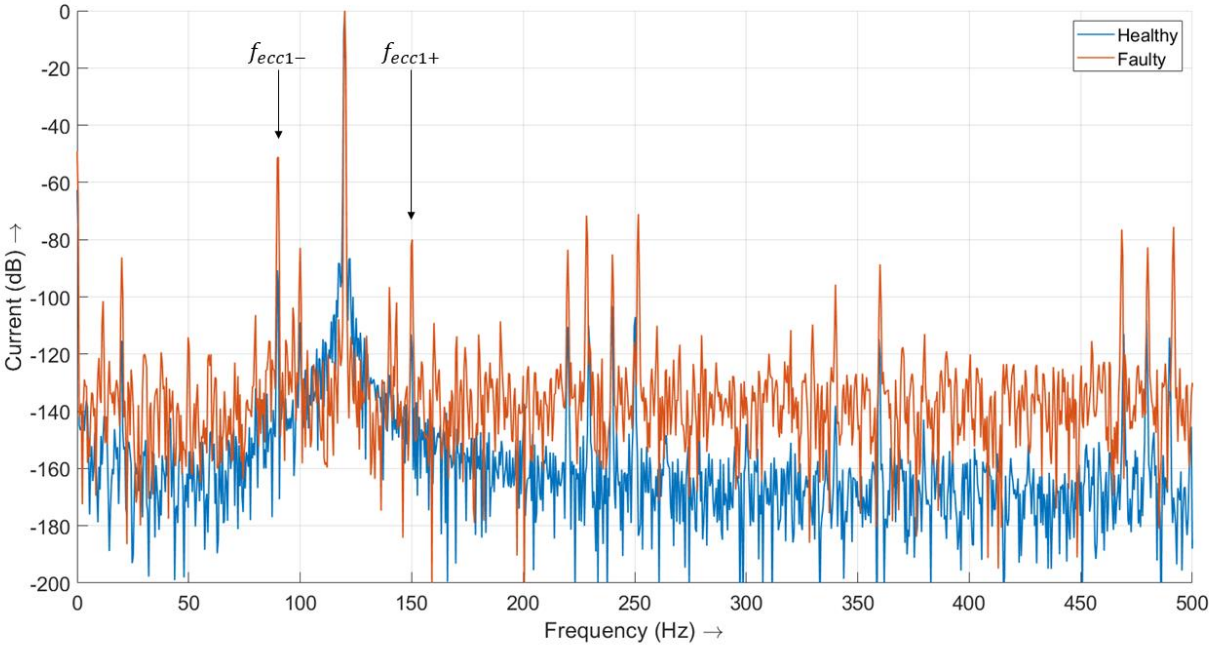

Figure 5.24: MCSA of dry-running wet-rotor pump (800 W) at a speed of 1800 rpm from 0–500 Hz

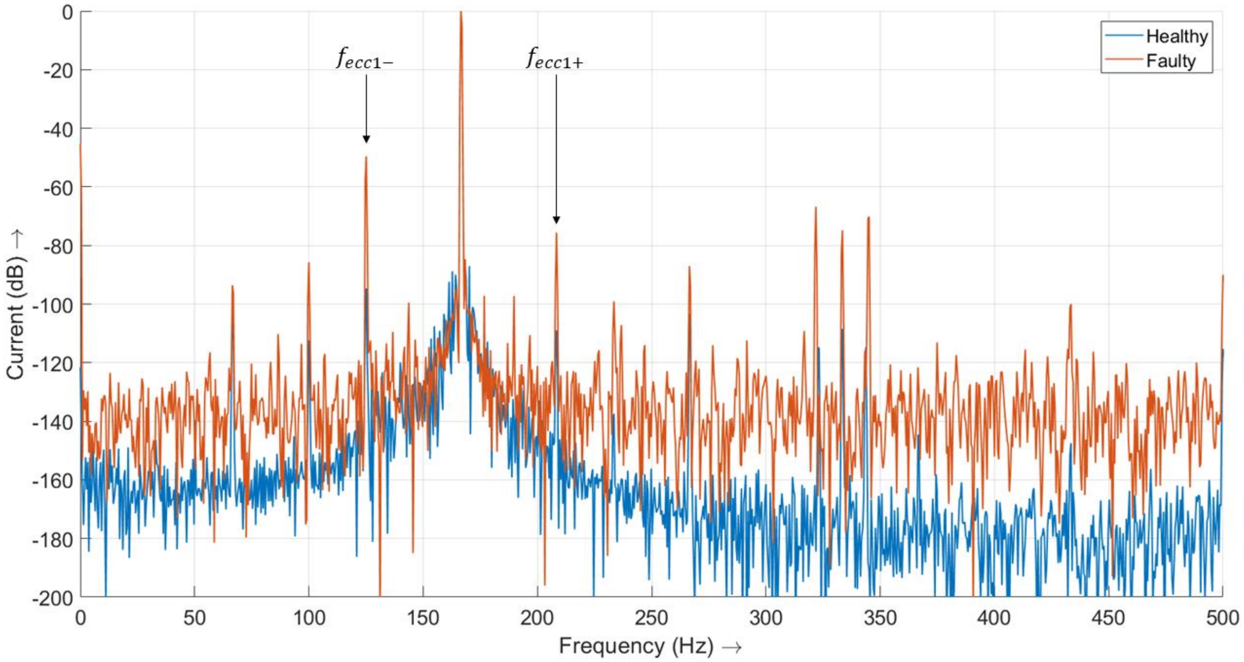

Figure 5.25: MCSA of dry-running wet-rotor pump (800 W) at a speed of 2500 rpm from 0–500 Hz

Not only the faults *bearing damage* and *dry-running rotor* can lead to increased ECC1 components, but also the fault *dry running*. Compared to the dry-running rotor, the amplitudes at f_{ecc1} even increased in the case of dry running, which speaks for an increased eccentric run and increased fault severity.

5.2.7 Hydraulic Blockage

In this section, it will be evaluated whether a hydraulic blockage was detected in the current spectrum of the dry-runner pump. The noise band around the FC will be analyzed first and foremost. Especially in the ±25 Hz range, (Perovic, 2000) found an increase in the amplitude response due to the fault *hydraulic blockage*.

5.2.7.1 Wet-Rotor pump (800 W)

The influence of a hydraulic blockage on the wet-rotor pump running at a speed of 2200 rpm is depicted in Figure 5.26, while Figure 5.27 shows the pump at a speed of 2800 rpm. In both cases, a pump running in healthy condition at a flow of 15 m^3/h at the same speed is illustrated as a reference.

At a speed of 2200 rpm, the curves were exactly on top of each other, so no difference could be detected between the two variants. The exception is the noise band from about 100 to 120 Hz, where a slight increase due to the fault could be observed.

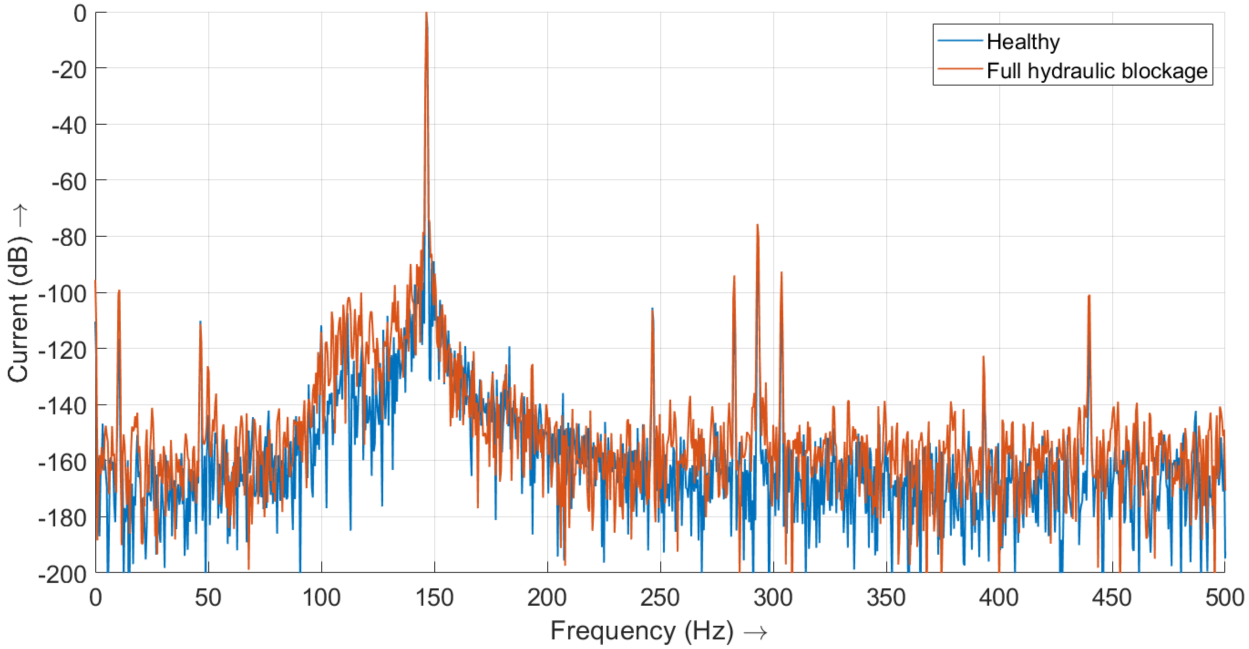

Figure 5.26: MCSA of the wet-rotor pump (800 W) with a hydraulic blockage from 0–500 Hz at a speed of 2200 rpm

At a speed of 2800 rpm, a slight increase in the noise band was detected in the whole signal, but especially around the FC. However, the increase was quite small, which makes a clear separation difficult.

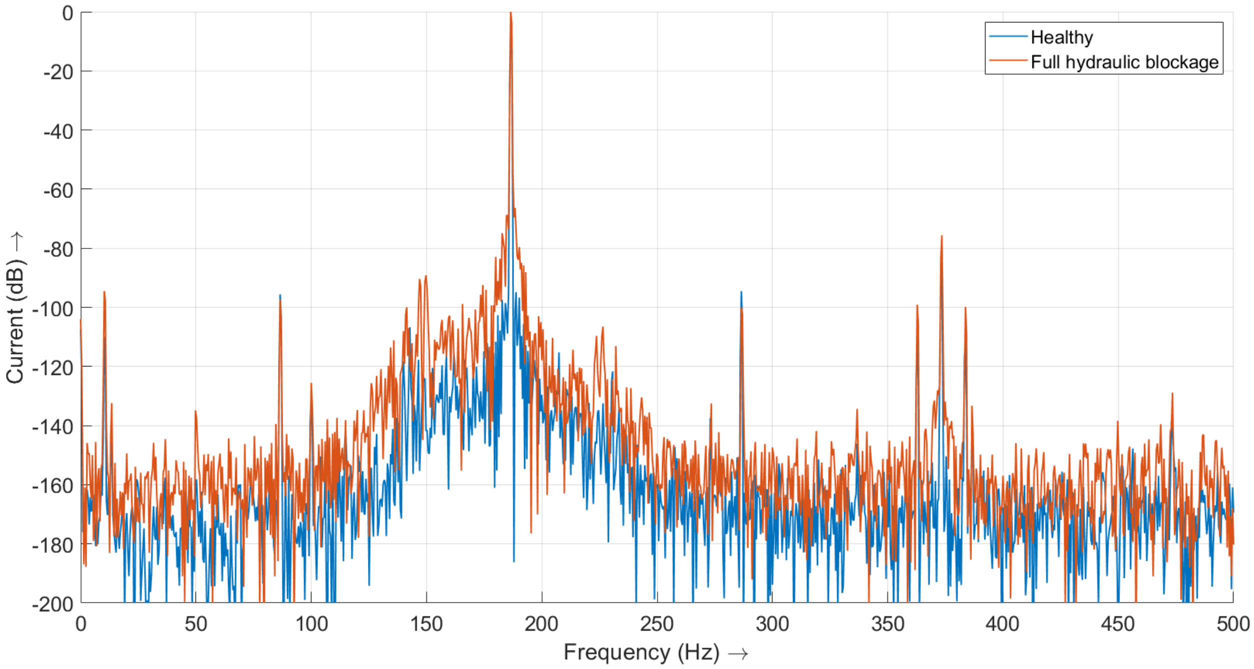

Figure 5.27: MCSA of the wet-rotor pump (800 W) with a hydraulic blockage from 0–500 Hz at a speed of 2800 rpm

In summary, the influence of the fault *hydraulic blockage* on the current spectrum was found to be relatively small, making it difficult to separate the faulty variant from the healthy variant.

5.2.7.2 Dry-Runner Pump (180 W)

Figure 5.28 depicts the MCSA in the range from 25 to 75 Hz in five different load conditions: 0, 5, 10, 15, 20, and 25 m^3/h. At 0 m^3/h, we speak of a hydraulic blockage, while the load points at flows of 5 and 10 m^3/h can be considered partial hydraulic blockages.

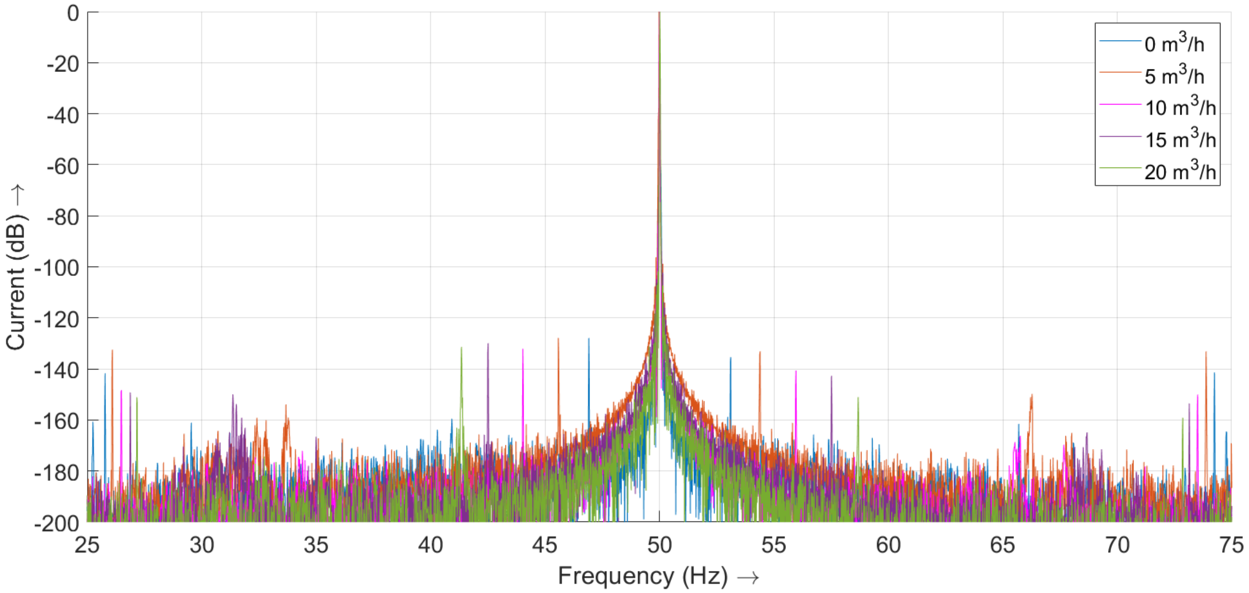

Figure 5.28: MCSA of the dry-runner pump in dependence of the flow in the range from 25 to 75 Hz

Due to the changed load condition depending on the load, some harmonics in the range also change their position. This is especially visible for BB1, which changes the frequency distance to FC from the single load points from 0 to 20 m^3/h, from 3.1, 4.4, 6.0, 7.5 to 8.7 Hz. The amplitudes of the broken bar harmonics remain in the same ranges. The same effect of a changing position is visible for the ECC components. However, the amplitudes also increased slightly with decreasing flow, with the highest amplitude at 5 m^3/h. Considering the noise bands, the highest noise band is visible for the flow of 5 m^3/h, followed by 15 m^3/h, 10 m^3/h, 20 m^3/h, and finally 0 m^3/h. Consequently, the noise band shows no trend in dependence of the flow.

5.2.7.3 Discussion

No strong influence on the noise band around the FC, as found in (Perovic, 2000), was observed in the two pumps we studied. Moreover, in the low-frequency range, no amplitude was found that was increased by the hydraulic blockage. A better indicator for a hydraulic blockage diagnosis is the evaluation of the RMS current, as demonstrated in section 5.1.2.

5.2.8 Conclusion

The state of the art of current-based pump fault detection revealed that different fault indicators exist in the current signal. In this section, the influence of different faults on the MCSA of three different pump types was investigated. It was demonstrated that two fault indicators, in particular, were influenced by the faults: the amplitude at the frequency $f_{r,pump}$, and the RMS value of the current signal; see Table 5.3. The two indicators amplitude at f_{BPF}, and noise band, however, were not influenced by the faults. For the pumps and faults studied, these two features are not suitable for detecting faults. The RMS value of the current, however, decreased in every fault. We should also remember that hydraulic blockage is not necessarily a fault for all pumps. The amplitude at $f_{r,pump}$ enables the detection of a problem at the pump impeller. This is true for the faults *impeller damage, clogging, dry-running rotor,* and *dry running*. However, the fault *bearing damage* also influenced the same frequencies. Therefore, it can be summarized that the amplitude at $f_{r,pump}$ makes a statement about the health condition of the rotating parts of the pump. A separation of the faults using MCSA was not possible.

Table 5.3: Fault indicators of the investigated pumps

Fault	**DUT**	$f_{r,pump}$	f_{BPF}	**Noise band**	**RMS value**
Impeller damage	Wet-rotor pump (800 W)	✓ | ↑	x	x	✓ | ↓
Clogging	Wet-rotor pump (800 W)	✓ | ↑	x	x	✓ | ↓
	Wet-rotor pump (800 W)	✓ | ↑	x	x	✓ | ↓
	Dry-runner pump (180 W)	✓ | ↑	x	x	✓ | ↓
	Submersible pump (7.7 kW)	✓ | ↑	x	x	x
Dry-running rotor	Wet-rotor pump (800 W)	✓ | ↑	x	x	✓ | ↓
Dry running	Wet-rotor pump (800 W)	✓ | ↑	x	x	✓ | ↓
Hydraulic blockage	Wet-rotor pump (800 W)	x	x	x	✓ | ↓
	Dry-runner pump (180 W)	x	x	x	✓ | ↓

5.3 Load Point Depending Fault Indicator Analysis, LoPoFIA

In this section, the results of the LoPoFIA, which was implemented according to section 4.4.2, will be presented. The wet-rotor pump with 800 W (see section 4.1.1) was used as a test item. The faults *clogging*, *cracked impeller*, and *bearing defect* were investigated.

5.3.1 Healthy Condition

In order to obtain a reference for the faulty variants, the LoPoFIA results of the healthy variant are considered first. Figure 5.29 depicts the LoPoFIA of the lower sideband (left) and the upper sideband (right). The measured load points are marked with a black x. The four pump curves for the four speeds are visible, starting with 0 m^3/h at 1.3 m, 3.6 m, 6.8 m, and 10.8 m. With increasing flow, the pump curves exhibit typical pump behavior with decreasing head.

It was remarkable that the lower sideband indicated a higher amplitude than the upper sideband. The highest amplitude of the lower sideband was 30 dB higher than that of the upper sideband. The lower sideband amplitude was mainly dependent on the pump flow. The lowest amplitudes were reached in the high flow range. The upper sideband had a dependence on head and flow. The highest amplitude took place in the medium flow range at higher speeds.

A hydraulic blockage that allowed no flow in the process was detected with the help of the lower sideband. At zero flow and low speed, the amplitude was the highest. Depending on the application, zero flow can be interpreted differently. When designating the normal operating range, care must be taken not to generate false alarms, as the amplitudes are increased compared to the nominal flow range. In the ranges marked in green, there is a possibility of false negative alarms if decision-making with constant thresholds is used.

To summarize the findings, both flow and head had a certain influence on the amplitude of both sidebands. This is an important fact, especially for decision-making design and for the definition of thresholds.

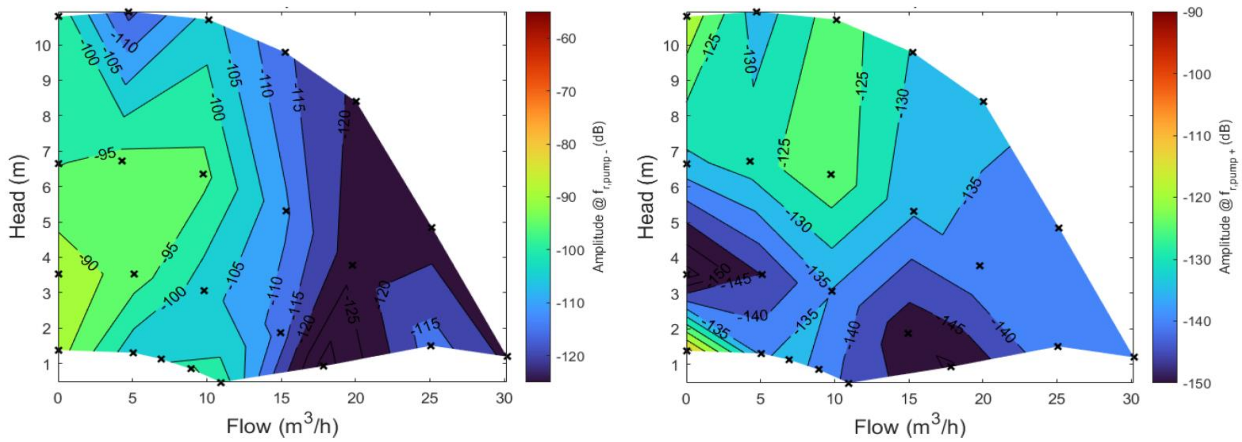

Figure 5.29: LoPoFIA for the fault indicators $\boldsymbol{f_{r,pump-}}$ and $\boldsymbol{f_{r,pump+}}$ in healthy condition.

5.3.2 Clogging

Figure 5.30 depicts the results for the impeller fault *clogging* (one clogged channel). Both sidebands indicate a pattern with three pronounced ranges. The first range is at 0 m^3/h and 1000 rpm. This load point, which can be seen as a combination of hydraulic blockage and clogging, was only slightly increased compared to the healthy variant. The second area is in the medium flow and higher speed range. Compared to the healthy variant, in this area the amplitudes increased by 20–25 dB. The third range, influenced by clogging, is in the high flow range. Compared to the healthy variant, the amplitudes increased by 40–50 dB. The highest amplitudes are at the lower sideband of −68 dB and the upper sideband of −84 dB at 25 m^3/h and 2800 rpm.

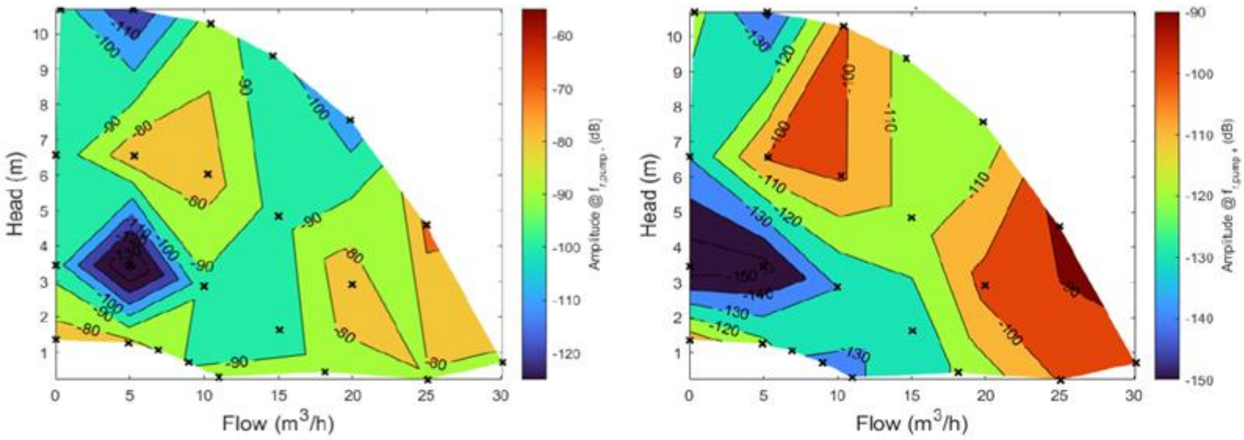

Figure 5.30: LoPoFIA for the fault indicators $\boldsymbol{f_{r,pump-}}$ and $\boldsymbol{f_{r,pump+}}$ for a pump with one clogged impeller channel

5.3.3 Cracked Impeller

Figure 5.31 depicts that a cracked blade also influenced the two frequencies in the LoPoFIA. This confirms the findings in (Pradhan, 2019), where it was demonstrated that a damaged pump impeller influences the speed and the motor current. The highest amplitudes of both sidebands were reached in the high flow range. At $f_{r,pump-}$ a maximum of -74 dB was reached, and at $f_{r,pump+}$ a maximum of -96 dB. The lower sideband had a quite constant amplitude from -80 dB to -90 dB, where the risk of false positive alarms is low. An exception to the risk of false positive alarms is the area marked in blue.

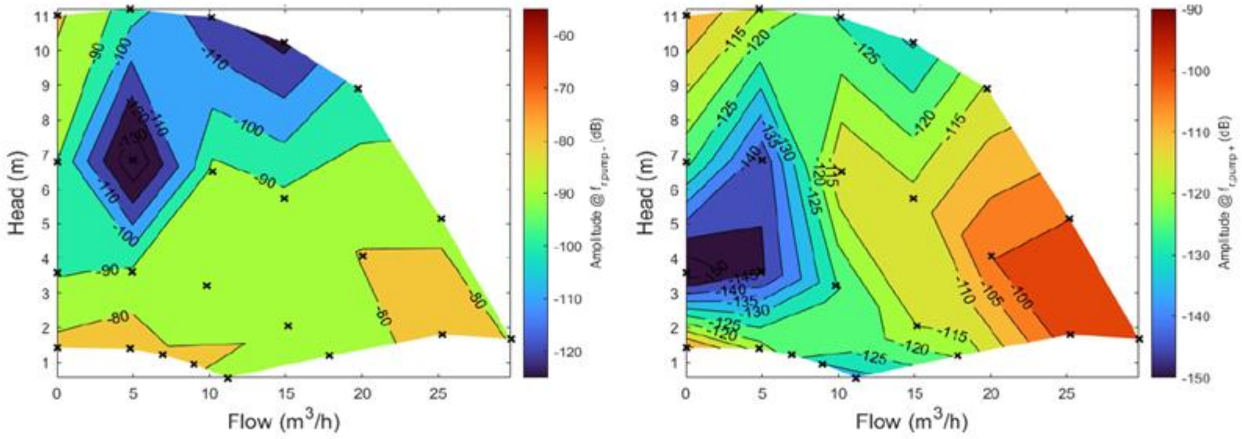

Figure 5.31: LoPoFIA for the fault indicators $f_{r,pump-}$ and $f_{r,pump+}$ for a pump with a cracked impeller blade

5.3.4 Bearing Defect

Finally, the influence of bearing defects was investigated. Figure 5.32 and Figure 5.33 illustrate the results for a one-sided bearing defect. Figure 5.34 depicts the results for a two-sided bearing defect. If the results of the A-bearing defect are compared with the healthy variant, a similar pattern can be observed. However, the amplitudes were more pronounced for the A-bearing defect. The highest amplitudes of the lower sideband are visible in the low flow range. The maximum (-75 dB) was reached in the low flow and head range. At the nominal point of the pump, the amplitudes reach their minima. Here the difference to the healthy variant becomes small. At the upper sideband, no clear pattern is visible. The highest amplitude was reached at 2800 rpm and 5 m^3/h. At this point, the amplitude increased by 35 dB compared to the healthy variant.

With the B-bearing defect, both sidebands indicate a remarkable pattern. The highest amplitudes were at 5 m^3/h and at speeds of 2200 and 2800 rpm. As for the A-bearing defect, the amplitudes became smaller in the nominal range. A B-bearing defect can be separated from an A-bearing defect in the higher flow range of the lower sideband since an A-bearing defect has higher amplitudes in this flow range.

For the AB-bearing defect, the amplitudes of both the lower and upper sidebands increased compared to a one-sided bearing defect and the healthy variant. Also, both sidebands had flow dependence here. At the lower sideband, the highest amplitudes are visible in the lower flow range. The maximum was reached at 0 m^3/h and 3.5 m. Amplitudes at 0 m^3/h were interpreted as a combination of a bearing defect and hydraulic blockage. This combination thus led to the highest amplitudes. As in the case of one-sided bearing defects, the amplitudes decreased at the nominal point. However, the AB-bearing defect had an increased amplitude compared to the one-sided bearing defects and the healthy variant at the nominal point.

All bearing defects indicated an obvious difference compared to the healthy variant. Furthermore, each bearing defect had its own pattern. The AB-bearing defect with the highest fault severity had the highest amplitudes. At the nominal point of the pump, the fault influence on the amplitudes was the smallest. In this area, the risk of false positive alarms increases. If MCSA is applied without including the load points, every load point in the blue areas has a risk of false positive alarms.

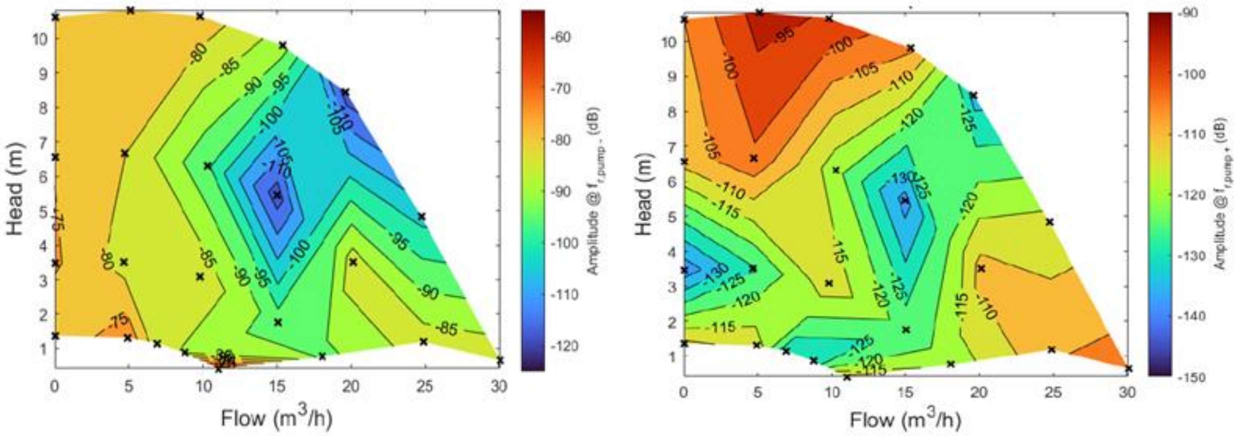

Figure 5.32: LoPoFIA for the fault indicators $f_{r,pump-}$ and $f_{r,pump+}$ for a pump with a one-sided bearing defect (A-bearing defect)

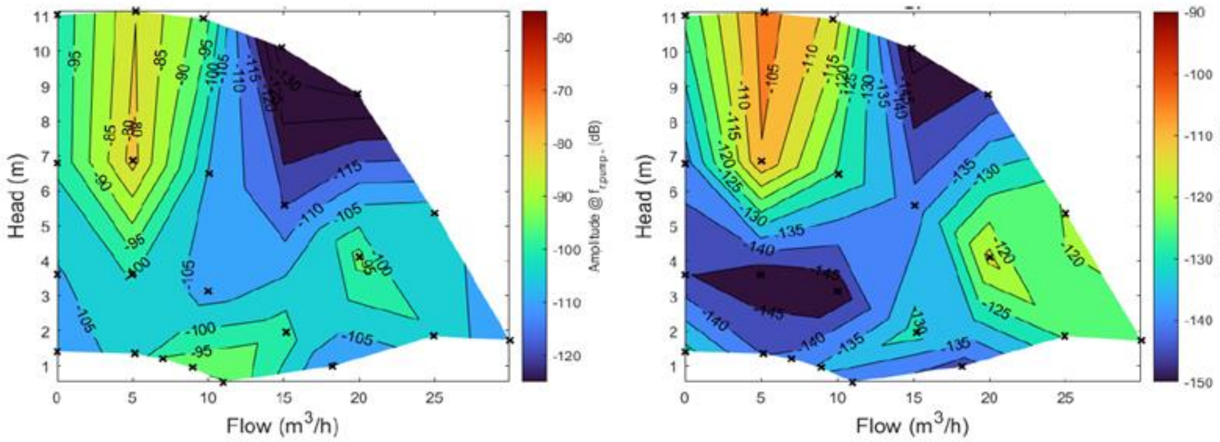

Figure 5.33: LoPoFIA for the fault indicators $\boldsymbol{f}_{\boldsymbol{r,pump-}}$ and $\boldsymbol{f}_{\boldsymbol{r,pump+}}$ for a pump with a one-sided bearing defect (B-bearing defect).

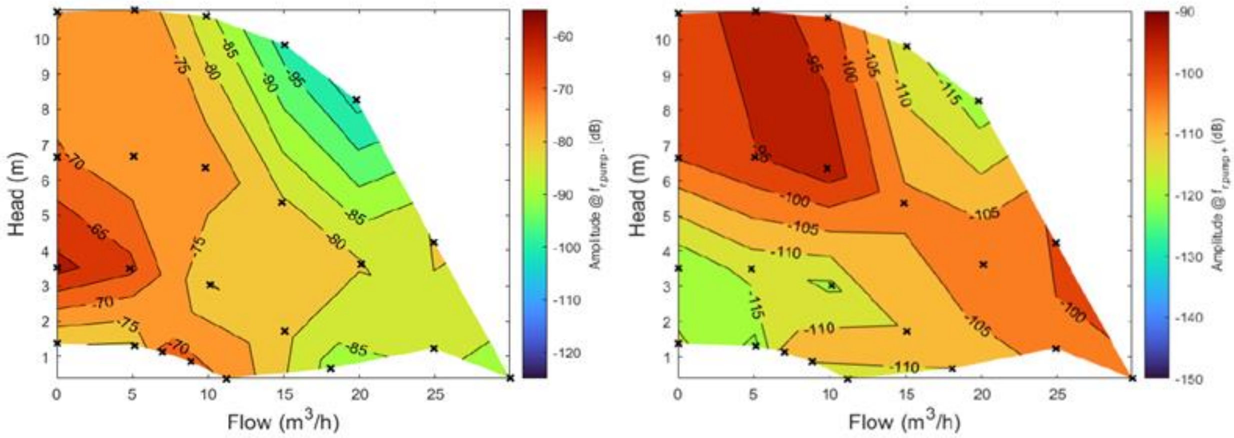

Figure 5.34: LoPoFIA for the fault indicators $\boldsymbol{f}_{\boldsymbol{r,pump-}}$ and $\boldsymbol{f}_{\boldsymbol{r,pump+}}$ for a pump with bearing defects on both sides (AB-bearing defect)

5.3.5 Conclusion

The LoPoFIA of the healthy variant showed that, at certain load points, the two fault indicators were increased compared to other load points. The amplitude at the lower sideband had an obvious dependence on the flow. When the flow equaled zero, which could be interpreted as the fault *hydraulic blockage*, this amplitude was the highest. Consequently, a hydraulic blockage could be detected by analyzing the lower sideband.

The LoPoFIA of every fault variant differed from the healthy variant, and each variant had its own pattern. *Clogging* and *cracked impeller* mainly influenced higher flow ranges, while *bearing* faults mainly influenced lower flow ranges. Consequently, LoPoFIA provides a way to separate impeller and bearing defects. Building on previous approaches, LoPoFIA is another method for the separation of defects affecting the same frequencies. In addition, we observed that the defects did not affect the fault frequencies at each load point. If MCSA is applied to these load points, this can lead to false positive alarms. This affects, in particular, the defects with a lower degree of severity, such as one-sided bearing defects.

5.4 Disturbance Transfer Function Approach, DTFA

The DTFA was validated by comparing the results of two different PMSM-fed wet-rotor pumps, one with 150 and one with 800 W, in healthy condition and with one clogged impeller channel. Since the number of impeller channels of both pumps equaled seven, it was assumed that the torque oscillation due to the fault *clogging* would be the same in relation to the brake torques of the pumps. However, with the existing experimental setup, it was not possible to verify that the assumption was correct. On the other hand, the results of section 5.3 revealed that in healthy and in faulty conditions, the load point had a strong influence on the two amplitudes at $f_{r,pump-}$ and $f_{r,pump+}$, which has no pattern that could be predicted by any analytical equation.

For a qualitative validation of DTFA, the amplitude at the rotational speed f_R in the d-q frame of the current is shown depending on the load point of the pumps. Figure 5.35 depicts this for the two investigated pumps with 150 and 800 W in healthy condition and in faulty condition with one clogged impeller channel.

The patterns were similar to those observed in LoPoFIA. However, with regard to the transfer behavior in the Bode plot (see Figure 3.3), another observation could be made for the 800 W pump in the faulty state: At a speed of 2200 rpm (load points "x" in the area marked red in Figure 5.35), three points where very high amplitudes occurred can be observed. We know that in the range around 2300 rpm, an amplitude increase is to be expected due to the transfer behavior of the motor as a sensor. Basically, a stronger influence of the fault can be observed in the entire load range for the 800 W variant compared to the 150 W variant. This indicates that the motor of the 800 W variant had a consistently better transmission behavior, i.e., a higher gain, than the 150 W variant.

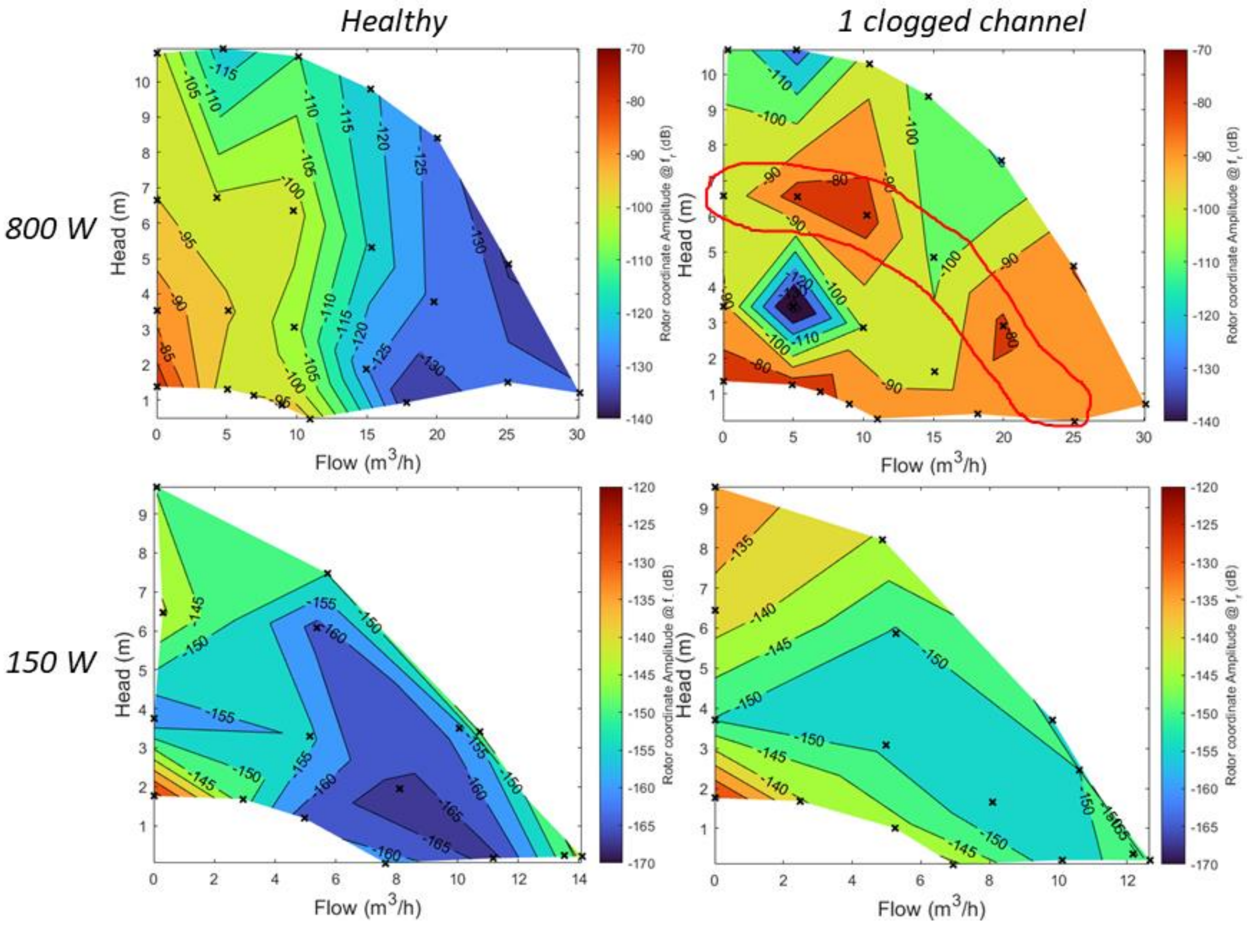

Figure 5.35: Amplitude of $\boldsymbol{I_q}$ at $\boldsymbol{f_R}$ of two circulation pumps with different power (150 and 800 W) in healthy condition and with one clogged channel

The results of this section demonstrate that DTFA can give an indication of the quality of a motor when acting as a sensor to detect faults in the load. However, the verification of the transfer functions by measurement is still pending. It has been proven that for this type of pump, the load point has a particular influence on the fault characteristics that is difficult to interpret analytically. There are many influences here which are very complex to understand, such as turbulence on the impeller and in the can, influence of the journal bearing, resonances, etc. In addition, it is not clear for this type of pump how the hydraulics affect the moment of inertia of the motor. A dependence of the moment of inertia on process variables such as flow, fluid volume, or piping properties cannot be ruled out.

5.5 Adapted Reference Frame Theory, ARFT

In this section, the results of the ARFT will be discussed. The method was subjected to various tests, the results of which are presented here. The methods and the experimental setup were illustrated in section 4.4. First, the results of the laboratory test will be analyzed, followed by the consideration of the field test. In the conclusion, the main findings will be summarized.

5.5.1 Laboratory Test

The procedure for implementing the laboratory test, the implemented method, and the parameters used were already illustrated in section 4.4.3.2.1. Since it was not possible to use a real-time speed or FC signal of the motor, which is needed for ARFT, the current signal was used to estimate its fundamental frequency. Figure 5.36 depicts the estimated FC during the laboratory test, where the speed of the motor was set to 2800 rpm, resulting in a fundamental frequency of 186.7 Hz (8-pole motor).

The estimated frequency varied in the range from 183.5 to 188.5 Hz, resulting in a deviation from the set value of 186.7 Hz of between –3.2 and +1.8 Hz. Consequently, the maximum error of the frequency estimator was at 1.7%. However, it was not possible to make a statement about the actual value of the frequency, since the PMSM was controlled via FOC and thus was under the influence of small speed variations. Frequency estimation errors also influence the results of ARFT. However, since the goal of the laboratory test was to validate the functionality of ARFT, no further improvement on the estimator was undertaken.

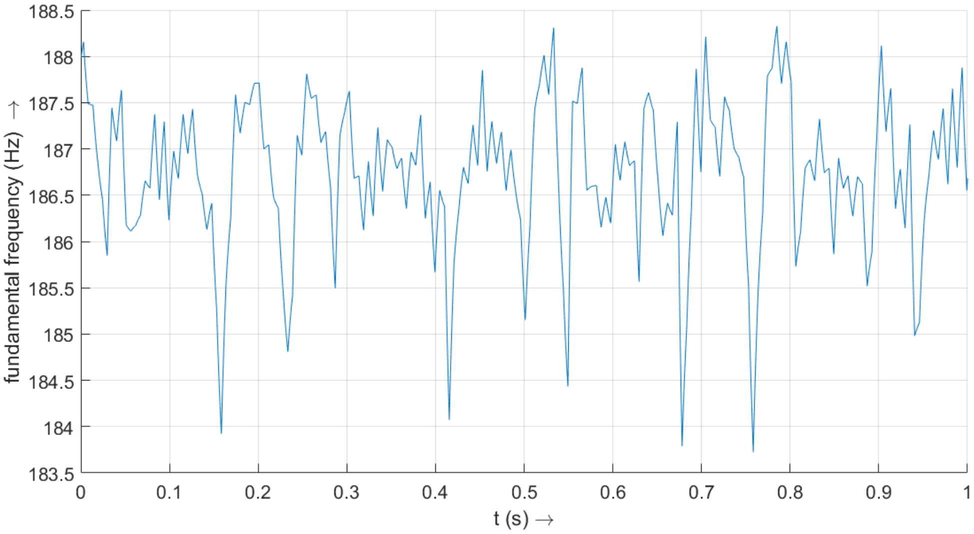

Figure 5.36: Fundamental frequency estimation based on periodic counter

Figure 5.37 and Figure 5.38 depict the results of the ARFT for the calculation of $\hat{\imath}_f$ at the two frequencies $f_{r,pump+}$ ("right-side band") and $f_{r,pump-}$ ("left-side band") with varying time constants of 1 and 10 s. It can be seen that the results of the use of a time constant of 1 s oscillate more than the results of a time constant of 10 s. Additionally, if the mean values are considered, for the variant with a time constant of 10 s, lower values are noticed. The reason is that the two control values showed a low frequency fluctuation (~0.1 Hz) due to erroneous speed estimation. However, it was noticeable that the values for $\hat{\imath}_f$ of the faulty variant were higher than the respective values of the faulty variant. The left-side band increased from 0.02 A to 0.08 A and the right-side band increased from 0.01 A to 0.05 A with the time constant of 1 s.

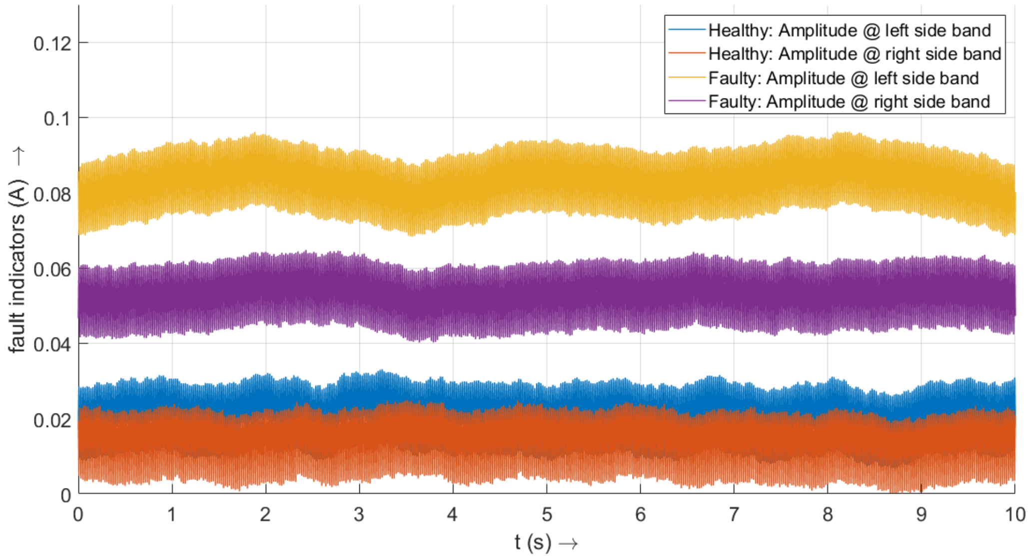

Figure 5.37: Curves of the fault indicators in the laboratory test with a time constant of 1 s

In the case of a time constant of 10 s, the left-side band increased from 0.014 A to 0.052 A and the right-side band increased from 0.007 A to 0.025 A.

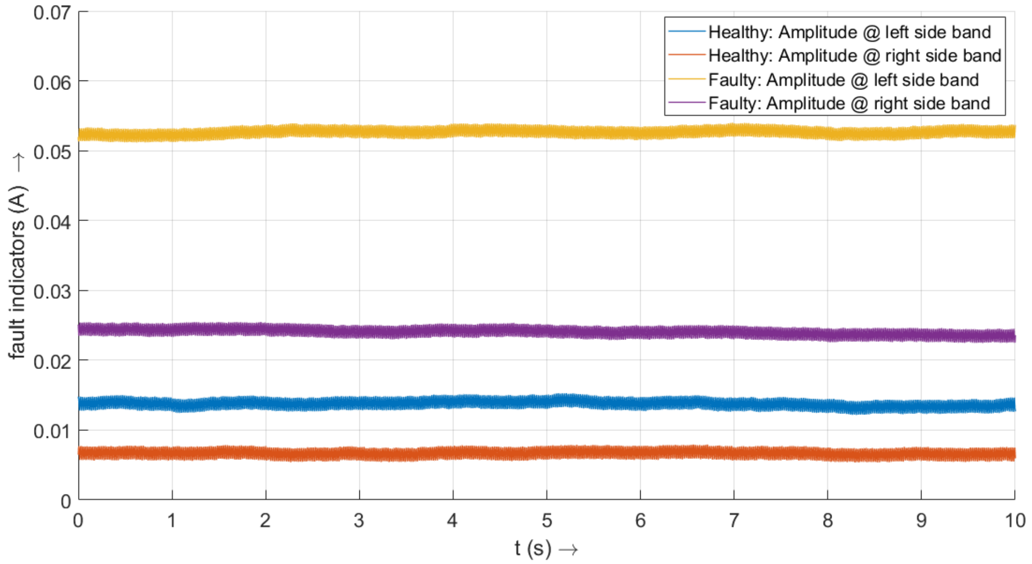

Figure 5.38: Curves of the fault indicators in the laboratory test with a time constant of 10 s

The results confirmed the findings of MCSA, where an increase in the amplitudes of the frequencies at $f_{r,pump+}$ and $f_{r,pump-}$ was also found. Additionally, in MCSA, higher values for $f_{r,pump-}$ compared to $f_{r,pump+}$ were also detected.

5.5.2 Field Test

Since the results of the laboratory test looked promising, the next step of the validation was the field test of the algorithm. The ARFT method was implemented according to section 4.4.3.2.2. The time constant of the low pass filter was set to 10 s in order to fully filter the oscillations in the current signals. In comparison to MCSA, where the components are given in dB, the amplitudes were calculated in %. Figure 5.39 shows the results of the severity factors (SFs) calculated on the basis of ARFT for the three different load points, where the speed (1600, 2200, and 2800 rpm) was varied. For both the upper and the lower sideband, the SFs were calculated.

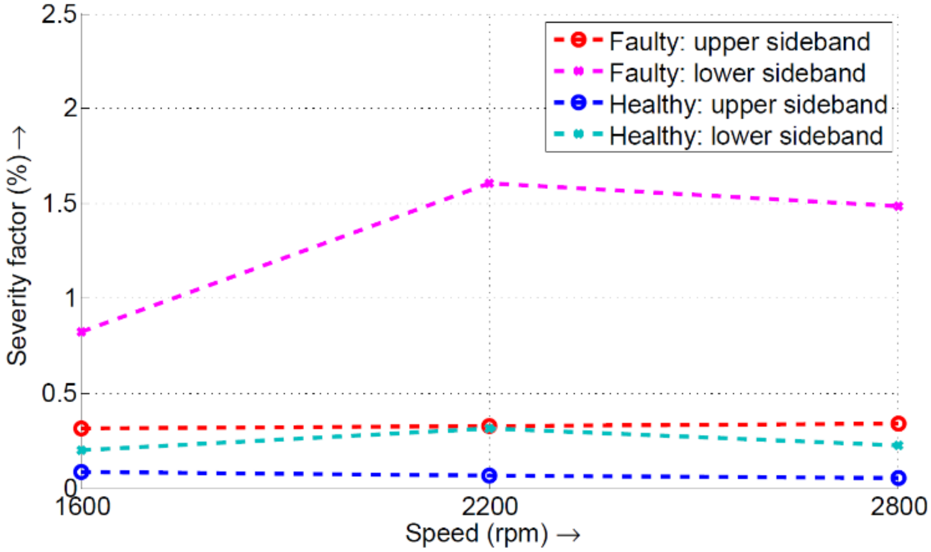

Figure 5.39: Calculated fault severity factors on the basis of ARFT of the lower and upper sidebands at different speeds for the healthy configuration and for the configuration with one clogged impeller channel (faulty)

At every speed, both the upper and the lower sideband SFs were higher for the faulty variant than the respective SFs in healthy condition. This is clearly visible when we look at the lower sideband curves. At the speed of 2800 rpm, the fault SF of the faulty variant was 1.5%. Compared to the healthy variant at the same speed (0.2%), the value was eight times as high. Only at a speed of 1600 rpm did the lower sideband SF decrease. However, it was still four times as high as the respective healthy variant. As already seen in the MCSA, the upper sideband was not so pronounced. However, the results were constant over the entire speed range, with those of the faulty variant (0.3%) being three times higher than those of the respective healthy variant (0.1%).

It was demonstrated that ARFT is useful for the online detection of the fault *impeller clogging* in wet-rotor pumps. For the final implementation, thresholds had to be set – one for the upper and one for the lower sideband.

5.5.2.1 MCSA versus ARFT

In order to verify the SFs calculated on the pump's MPU, we will now compare the results with the results obtained with MCSA. Table 5.4 lists the results for the SFs of the two methods MCSA and ARFT for the speeds 1600 rpm, 2200 rpm, and 2800 rpm.

Table 5.4: Severity factors of MCSA and ARFT for the healthy configuration and for the configuration with one clogged impeller channel at 1600, 2200, and 2800 rpm

	Healthy		**1 Clogged Channel**	
Method	**MCSA**	**ARFT**	**MCSA**	**ARFT**
		1600 rpm		
SF@$f_{r,pump}+$	0.15%	0.08%	0.16%	0.31%
SF@$f_{r,pump}-$	0.56%	0.20%	1.10%	0.83%
		2200 rpm		
SF@$f_{r,pump}+$	0.13%	0.07%	0.71%	0.33%
SF@$f_{r,pump}-$	0.52%	0.31%	2.29%	1.61%
		2800 rpm		
SF@$f_{r,pump}+$	0.18%	0.05%	0.99%	0.34%
SF@$f_{r,pump}-$	0.31%	0.22%	2.23%	1.49%

Although the ARFT values differ from the MCSA results, the overall trends are the same. In general, except for one case, the values of the ARFT are smaller than the values of the MCSA, with the values for the upper sidebands indicating a larger deviation than those of the lower sidebands. These two results could be related to the fact that the estimated rotational speed, which was an input parameter, is subject to fluctuation and thus influences the results of the ARFT. For the upper sideband, the multiplication of the FC by 1.25 is amplified, which could have caused the larger deviation compared to the lower sideband. In addition, it must be taken into account that, unlike in line-fed motors, the FC of the current also varies, which may have affected the results of the MCSA. In addition, another factor is that, unlike measurement with an oscilloscope, no equally precise measurement of the current of the pump's MPU can be assumed. Considering that these were low-cost components, ARFT provided relatively stable and accurate results.

LoPoFIA was used to validate the dependence of the amplitudes at $f_{r,pump}$ on the hydraulic load point. The hydraulic load point itself depends on the head, flow, and speed of a pump. As illustrated in Table 5.4, there are differences in the amplitudes at $f_{r,pump}$ calculated with the implemented ARFT and MCSA. In this section, we will evaluate whether the differences depend on the hydraulic load point for the three variants *healthy*, *1 clogged channel*, and *two-sided bearing damage*. Figure 5.40, Figure 5.41, and Figure 5.42 depict the deviation of the amplitudes at $f_{r,pump-}$ and $f_{r,pump+}$ using MCSA and ARFT for these three variants.

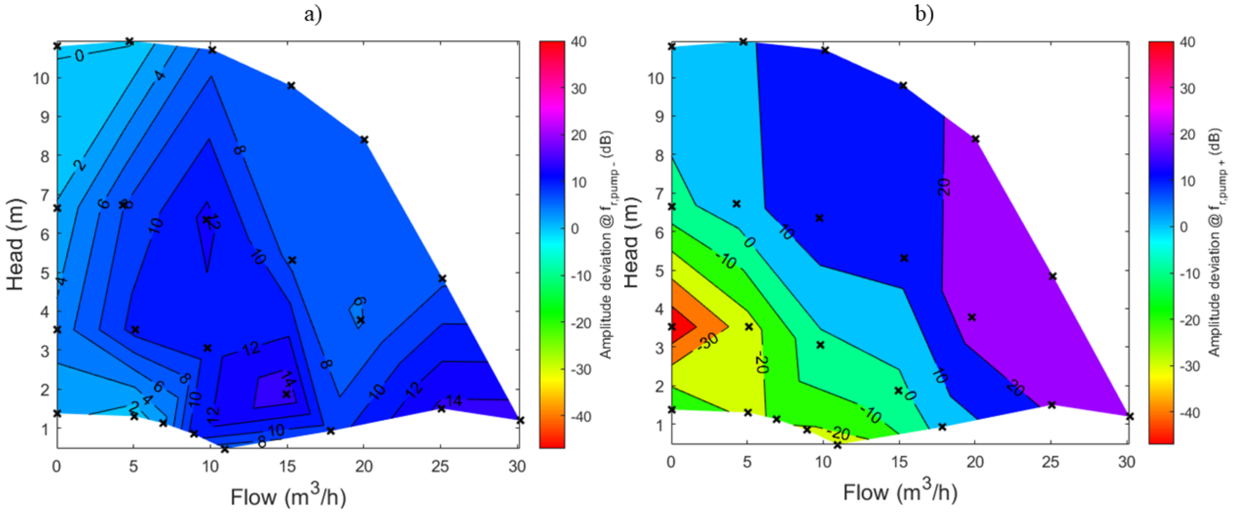

Figure 5.40: Deviation of the fault indicators calculated with MCSA and ARFT in healthy condition; amplitude deviation at a) $\boldsymbol{f_{r,pump-}}$ and b) $\boldsymbol{f_{r,pump+}}$

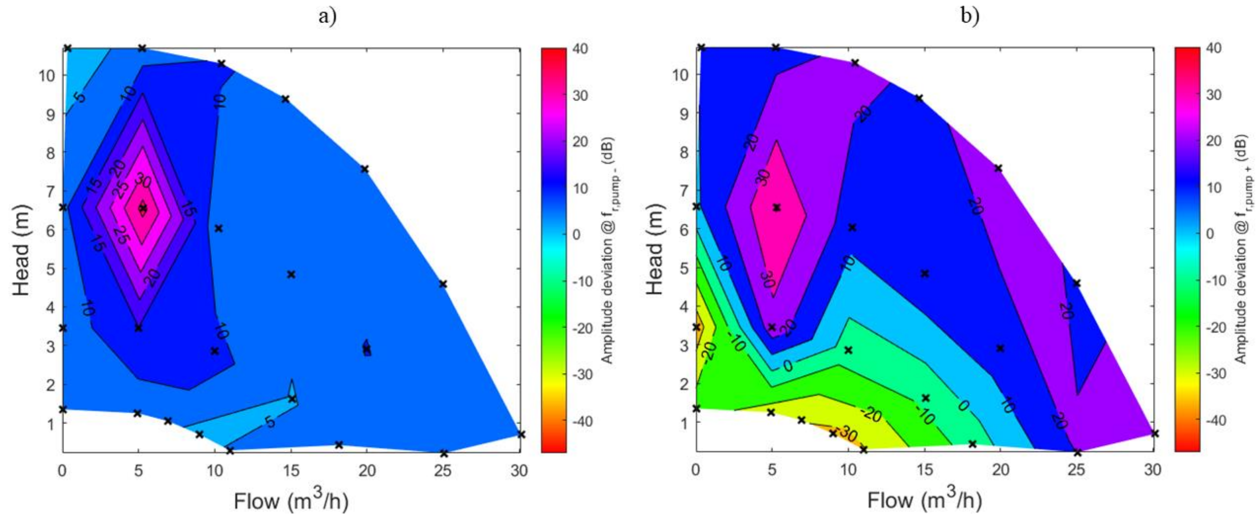

Figure 5.41: Deviation of the fault indicators calculated with MCSA and ARFT in clogging condition; amplitude deviation at a) $\boldsymbol{f_{r,pump-}}$ and b) $\boldsymbol{f_{r,pump+}}$

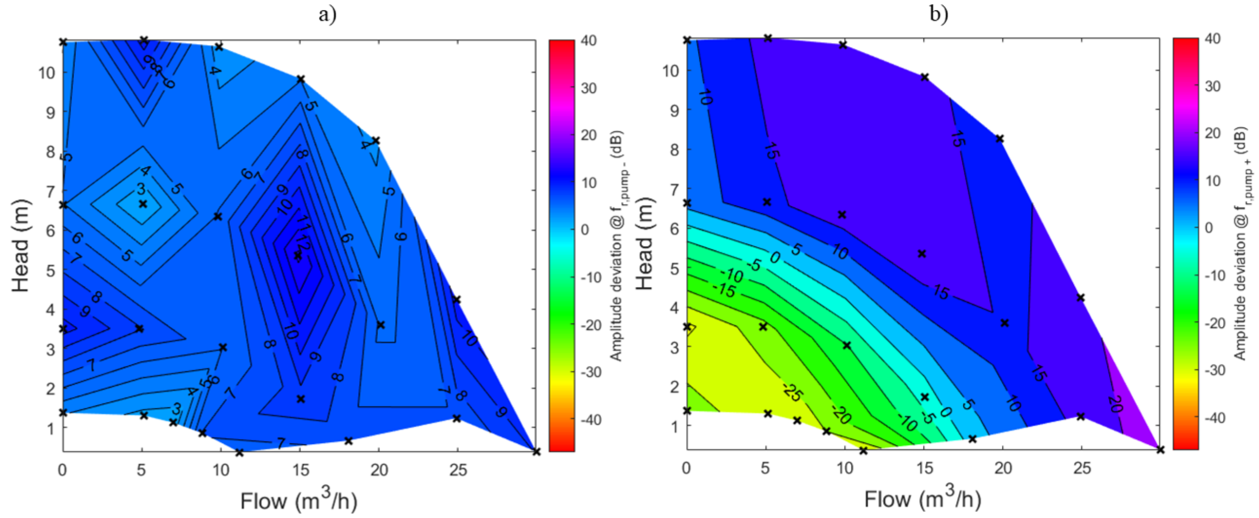

Figure 5.42: Deviation of the fault indicators calculated with MCSA and ARFT with AB-bearing fault; amplitude deviation at a) $\boldsymbol{f_{r,pump-}}$ and b) $\boldsymbol{f_{r,pump+}}$

The analysis indicates that, in general, the amplitudes at $f_{r,pump-}$ calculated with ARFT and MCSA are closer together than the amplitudes at $f_{r,pump+}$. With one exception in the clogging condition (load point at 5 m^3/h and 6.8 m), the amplitude deviation is below 14 dB. No dependence of the hydraulic load point is visible for $f_{r,pump-}$. The picture is different for $f_{r,pump+}$, where larger deviations can be seen. Deviations of −40 to +40 dB are observed. In addition, a pattern can be detected depending on the hydraulic load point. Negative deviations are seen more at low speeds and positive deviations more at higher speeds. A small deviation is seen mainly at medium speed.

5.5.3 Conclusion

In this section, a method for online condition monitoring of wet-rotor pumps was presented. The method is based on ARFT and is used to analyze amplitudes at defined frequencies of the current spectrum. ARFT was implemented on the MPU of a wet-rotor pump. The functionality was proved with an investigation of the fault *impeller clogging*. To verify the ARFT, it was tested in a laboratory test and a field test. While a qualitative evaluation of the results was carried out in the laboratory test, justified by the absence of a speed sensor, in the field test, a comparison was made with the results of the MCSA.

MCSA indicated that the fault *clogged impeller channel* affected the upper and lower sidebands of the FC. Especially at higher speeds (2200 rpm and 2800 rpm), these two frequency bands contain information about the pump condition. The results of the ARFT proved that the method is suitable for online monitoring of pumps. The investigated upper and lower sidebands both exhibited a significant increase when the fault was present. Finally, we compared the results of MCSA and ARFT and showed that the calculated SF of ARFT was generally smaller than that of MCSA. Considering the fact that only low-cost hardware was used in the case of ARFT, the results are sufficient to be used for fault detection. However, future work should focus on increasing the accuracy of ARFT. Since faults such as *dry running* and *bearing damage* affect the same frequency, part of our future work will be to find a way to distinguish the faults based on the proposed approach.

ARFT can be used fully automatically and without human intervention to detect a fault in a pump. It is a purely software-based method, so no additional sensor is required. The implementation of ARFT is based on simple trigonometric functions and therefore requires only a relatively small amount of memory and computational effort. ARFT can also be used to investigate other faults that affect the current spectrum of a motor. Furthermore, the method is also suitable for implementation in rotating machine applications, for example in variable speed drives (as depicted, for example, in Figure 4.3 b)).

5.6 Cloud-based Condition Monitoring

To validate the cloud-based condition monitoring approach, three pumps, one in healthy condition, one with three clogged impeller channels, and one with bearing damage, were measured simultaneously in a test bench, and the data calculated on the basis of ARFT in the pumps' MPU was collected via Modbus interface; see section 4.4.4.1.

The first thing that could be noticed is that the temperature of the healthy variant was the highest of all three variants, especially at the end of the measurement, followed by that of the variant with bearing damage. One possible reason for this is that the estimated flow was calculated incorrectly for the two faulty variants and is lower than the real value. As a result, the brake torque and thus the current consumption and the heat generation would be lower. Another possibility is that with the *bearing* fault, the cooling of the motor was even favored by the fault. Considering the flow, it was notable that for three hours, the flow remained constant for the fault *clogging*. The reason was that due to the clogging, the pump was unable to provide more flow. This is also the reason why the temperature of this variant remained the lowest of the three variants. If the severity factors are considered, both were one a constantly low level for the healthy variant. The severity factors of the fault *bearing damage* indicate a dependence on the load point. Throughout the entire measurement, they were higher than those of the healthy variant, but the difference was not large in some load points. However, the severity factors of the variant with three clogged channels had high values during the entire time of measurement. It was confirmed by the results that in higher flow ranges, the faults *clogging* and *bearing damage* could be separated from each other. In lower flow ranges, the fault *bearing damage* could be separated from the healthy variant. It was also demonstrated that the consideration of the data in comparison to each other could be helpful for the decision-making process.

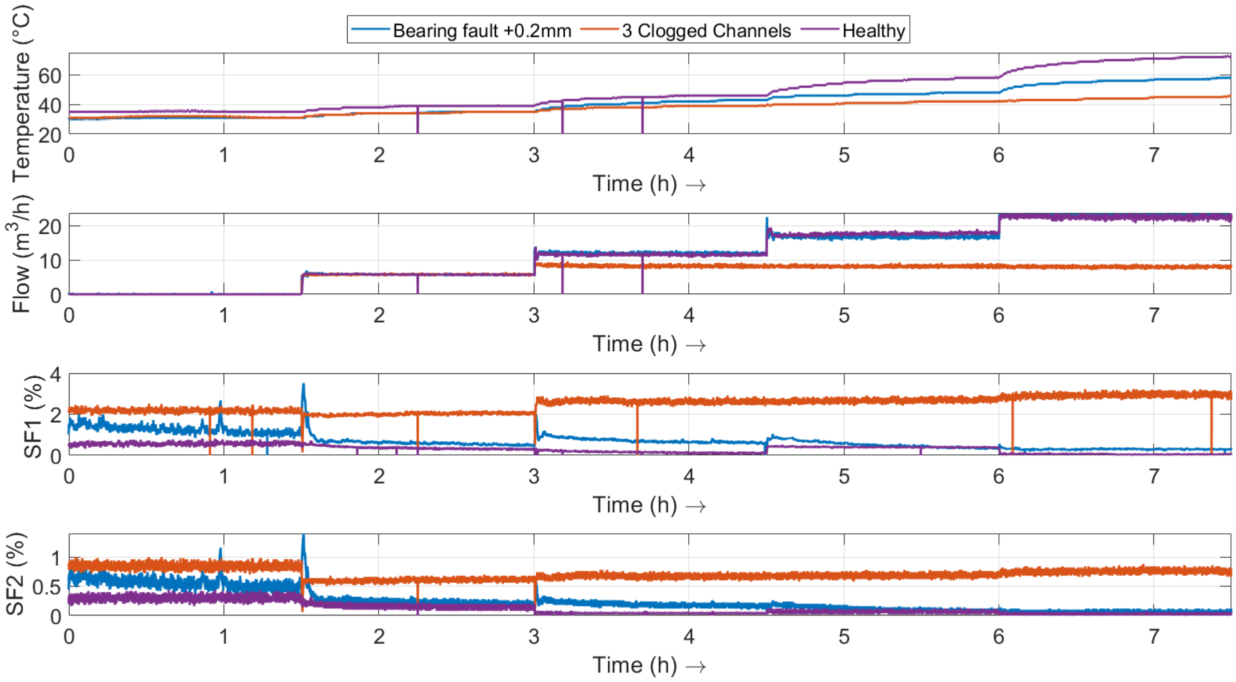

Figure 5.43: Curves of temperature, flow, and the severity factors SF1 and SF2 during the laboratory test

6 Experiment Results: Transient Analysis

In this section, the results of a transient analysis of the current signal will be presented. As in section 5, different pumps and different faults will be investigated. As there are no known implementations of transient analysis available in the state of the art, no comparison of the pump faults with other pump faults in the literature was possible. The method that was implemented was ATCSA (see section 4.4.5). We start with the analysis of the healthy variant, followed by the faults *clogging*, *cracked impeller*, *bearing damage*, *dry-running rotor*, *dry running*, and *hydraulic blockage*. At the end of this section, the results are summarized in the conclusion.

6.1 Healthy Condition

In this section, a transient analysis of the current signal of the healthy variants is presented. This is important in order to understand the evolutions of different harmonics in the time-frequency map that are visible even in healthy condition, and to have a reference for the results of the faulty variants.

6.1.1 Wet-Rotor Pump (800 W)

The ATCSA of a wet-rotor pump with 800 W in healthy condition for a startup from 1000 to 3000 rpm is depicted in Figure 6.1. Since the speed was ramped up from 1000 to 2800 rpm and the motor had four pole pairs, the fundamental component f_s of the stator current started at a frequency of 66.7 Hz and ended at 186.7 Hz. With the exception of the 6th-order harmonic, an increased amplitude was visible at every integer multiple of the stator frequency. Especially the 2nd, 5th, and 7th harmonics had high amplitudes. A closer look at Figure 6.1b) reveals a component that started at about 170 Hz and ended at 295 Hz, meaning it had a lower slope than all the other components. In the same distance to the fundamental, a second component was visible, which started at 5 s from 0 Hz and ended at 95 Hz; see Figure 6.1a). In both figures, these two components are marked with f_{slope}. Additionally, in Figure 6.1a) are three constant frequency components f_{const}, at 200, 100, and 10 Hz. Due to the non-linear dependence of f_{slope} and f_{const} on f_s, these two components could be attributed to the VSD operation.

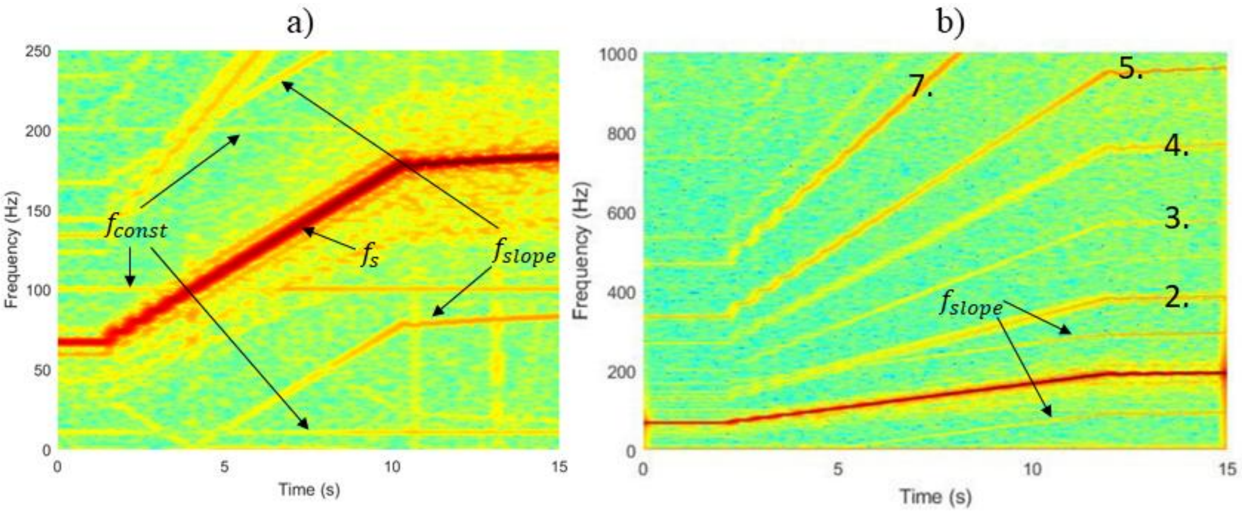

Figure 6.1: ATCSA of the wet-rotor pump (800 W) in healthy condition for a startup from 1000 to 2800 rpm at (a) 0–250 Hz; (b) 0–1000 Hz

The analysis of the healthy variant already shows an advantage of ATCSA. A correlation between different frequency components could be identified. In this case, the VSD generated different frequencies that were not known before the analysis. In ATCSA, these components could easily be differentiated from other frequency components. However, if only one operation condition at one motor speed is considered, as for example in MCSA, f_{slope} or f_{const} can equal a frequency component related to a fault, which can, depending on the thresholds, lead to false negative alarms.

6.1.2 Wet-Rotor Pump (150 W)

Figure 6.2 depicts the ATCSA for the wet-rotor pump with a power of 150 W for the startup from 1000 to 3520 rpm. As a six-pole motor was used to drive the pump, the FC was visible starting at a frequency of 50 Hz and ending at a frequency of 176 Hz. Additionally, the patterns of the stator harmonics were visible, with exception of the 6th harmonic, but they were not as pronounced as in the 800 W motor. In this motor pump, the 2nd-order harmonic had the strongest pattern. Furthermore, several other harmonics produced by the operation with VSD were visible in the analysis. The ones with a constant distance (same slope as FC) from the FC are marked in Figure 6.2 with f_{slope}. Additionally, there were two components with a negative slope (f_{neg}); the first one ended at 25 Hz and the second one ended at 125 Hz.

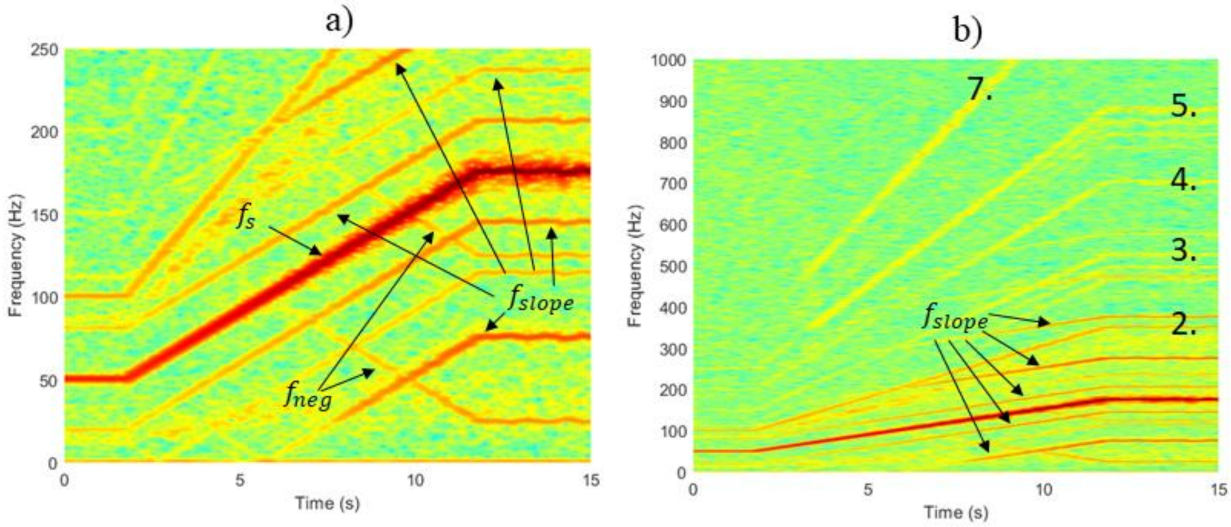

Figure 6.2: ATCSA of the wet-rotor pump (150 W) in healthy condition for a startup from 1000 to 3520 rpm at a) 0–250 Hz b) 0–1000 Hz

As for the 800 W variant, ATCSA can be a useful tool for understanding frequency components and their relation to the FC. For the interpretation of the MCSA, see, for example, Figure 5.5.

6.2 Clogging

In this section, the influence of the fault *clogging* on ATCSA will be investigated. This fault was analyzed for the two pump types wet-rotor pump and submersible pump. For the wet-rotor pump, two different variants, one with a power of 800 W and one with 150 W, were investigated. For the variant with 800 W, different severities of clogging were investigated.

6.2.1 Wet-Rotor Pump (800 W)

For the wet-rotor pump with 800 W, different severities of clogging were investigated. In total, seven fault variants were measured, from one clogged impeller channel to a fully clogged impeller, but also two, three, four, five, and six adjacent clogged impeller channels. Figure 6.4 depicts these variants from a) healthy to h) fully clogged impeller.

All clogging variants could be separated from the healthy variant at the fault frequency $f_{r,pump}$. The frequency components showed the typical trajectory for this type of fault, as predicted by Figure 3.11. However, the result for the healthy variant revealed that the motor had a slight eccentric running, even in healthy condition. The most significant pattern at $f_{r,pump}$ showed the variants with two to five adjacent clogged channels. This confirms the findings of MCSA, where the highest amplitudes at $f_{r,pump}$ were detected for this number of adjacent clogged channels. Both fault variants with one and six clogged channels differed from the healthy variant; however, the differences were not so significant.

Once again, the advantage of ATCSA should be mentioned. In the time frequency maps, it could be seen that the component $f_{r,pump-}$ crossed the constant component at $f_{const} = 100$ Hz. Since different speeds are considered in ATCSA, confusing the two components is impossible. For example, if an MCSA were performed for a speed (in this example $n = 2000\,rpm$) where $f_{r,pump-} = 100$ Hz, and there was no fault on the pump, the peak at 100 Hz could cause a false alarm. This is ruled out by evaluating the startup.

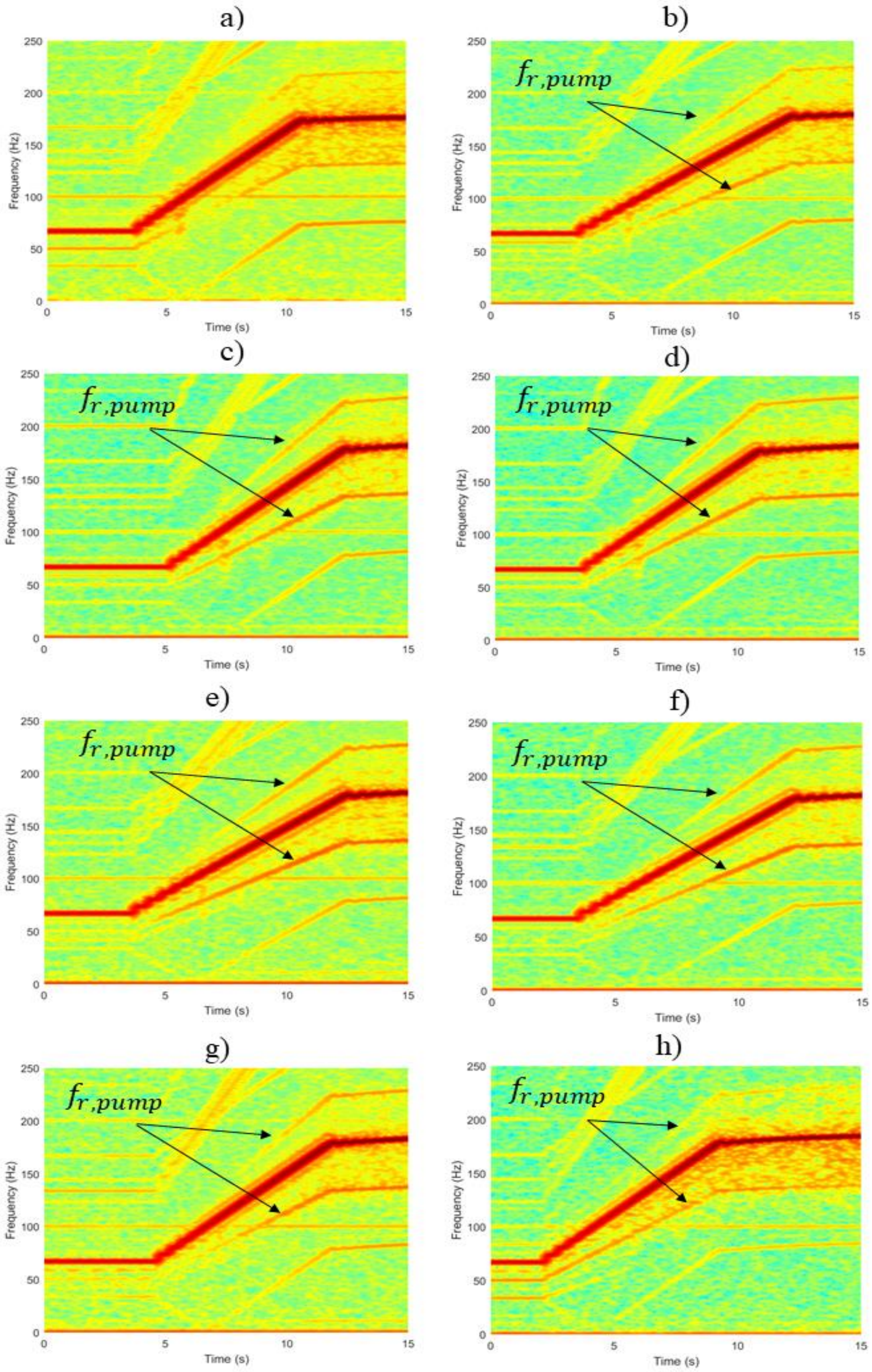

Figure 6.3: ATCSA of the wet-rotor pump (800 W) with varying degrees of clogged impeller channels for a startup from 1000 to 2800 rpm at 0–250 Hz; (a) healthy; (b) – (g) 1 to 6 adjacent blocked channels; (h) fully clogged

As in MCSA, there were two additional components in the higher-frequency range that were influenced by the fault *clogging*. These components around the 5th WH of the FC were only slightly visible in the ATCSA since they had only a small amplitude in comparison to other harmonics. This is verified in Figure 6.4, where the patterns at $\left(5+\frac{1}{p}\right)\cdot f_s$ and $\left(5-\frac{1}{p}\right)\cdot f_s$ are slightly visible at the end of the startup (b)), although the two patterns are not visible in the healthy condition (a)).

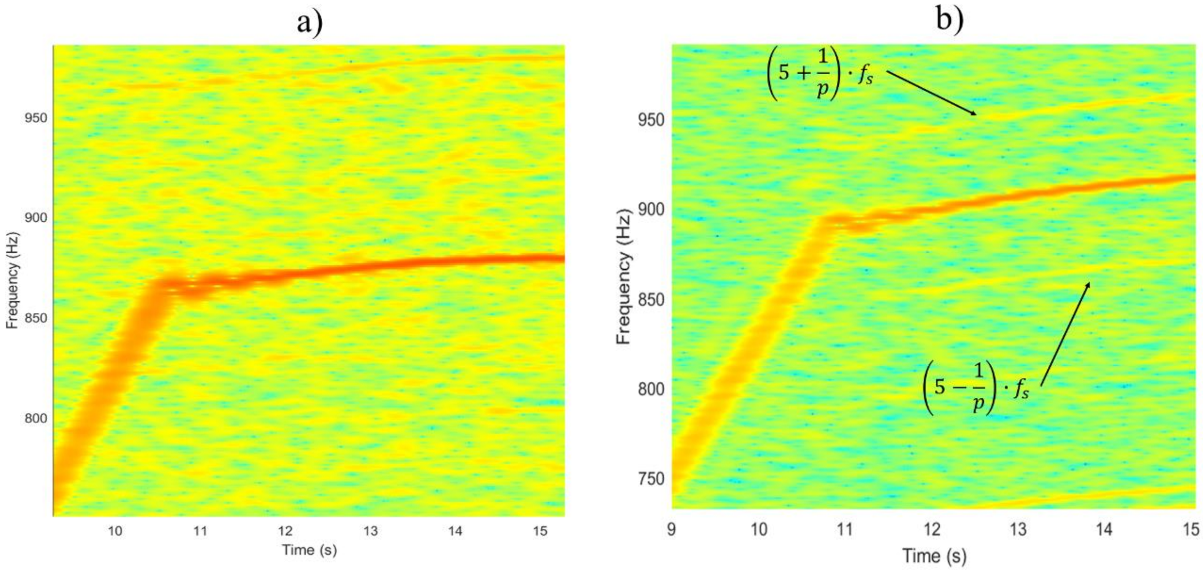

Figure 6.4: ATCSA of the wet-rotor pump (800 W) with 3 adjacent blocked channels for a startup from 1000 to 2800 rpm at 730–980 Hz; (a) Healthy; (b) 3 adjacent blocked channels

6.2.2 Wet-Rotor Pump (150 W)

Figure 6.5 depicts the ATCSA of a 150 W wet-rotor pump in healthy condition (a) and with one clogged impeller channel (b). The analysis revealed that no typical pattern appeared at the expected frequencies $f_{r,pump-}$ and $f_{r,pump+}$. The ATCSA of both the healthy and the faulty variant looked similar, and thus this approach is not suitable for the detection of this fault in this pump. The reason is that the components only slightly increased in the faulty condition because of the higher damping of this motor.

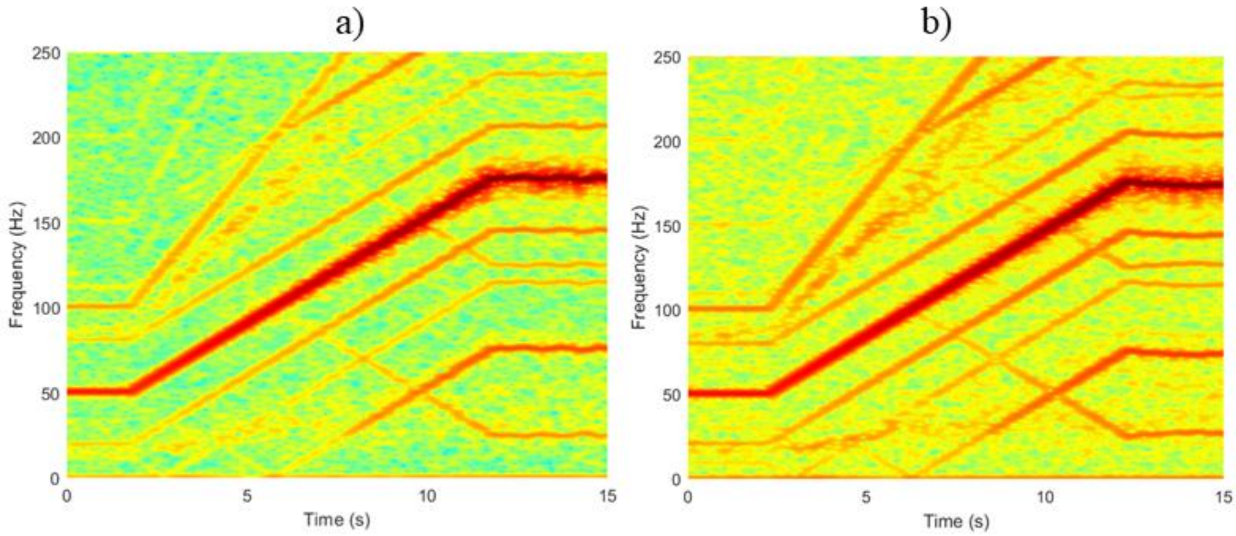

Figure 6.5: ATCSA of the wet-rotor pump (150 W) with one clogged impeller for a startup from 1000 to 3520 rpm at 0–250 Hz; (a) healthy condition; (b) 1 clogged impeller channel.

6.2.3 Submersible Pump (7.7 kW)

In this section, the use of ATCSA to analyze the process of clogging and clearing of a submersible pump with a power of 7.7 kW will be described. The measurement procedure was described in section 4.3.4. Figure 6.6 depicts the ATCSA considering the frequency range from 0−100 Hz. Note that, at the beginning, the ESP was in healthy condition, with f_s being equal to 40 Hz. Also note that at 20 Hz and 60 Hz, a pattern was visible, indicating a slight dynamic eccentricity in the ESP. After 10 s, the rag was sucked into the impeller and, from then on, the ESP was clogged. A strong pattern was visible at 20 Hz and 60 Hz. After clogging, the deragging procedure was started. In the condition of running in the opposite direction (20−25 s and 35−40 s), no pattern of $f_{r,pump}$ was visible. The pattern was only visible while running the ESP in the normal direction (10−15 s and 30−35 s). It is also clearly visible in the figure when the pump was cleared. This happened at 52 s, when it was observed that the pattern at $f_{r,pump}$ disappeared.

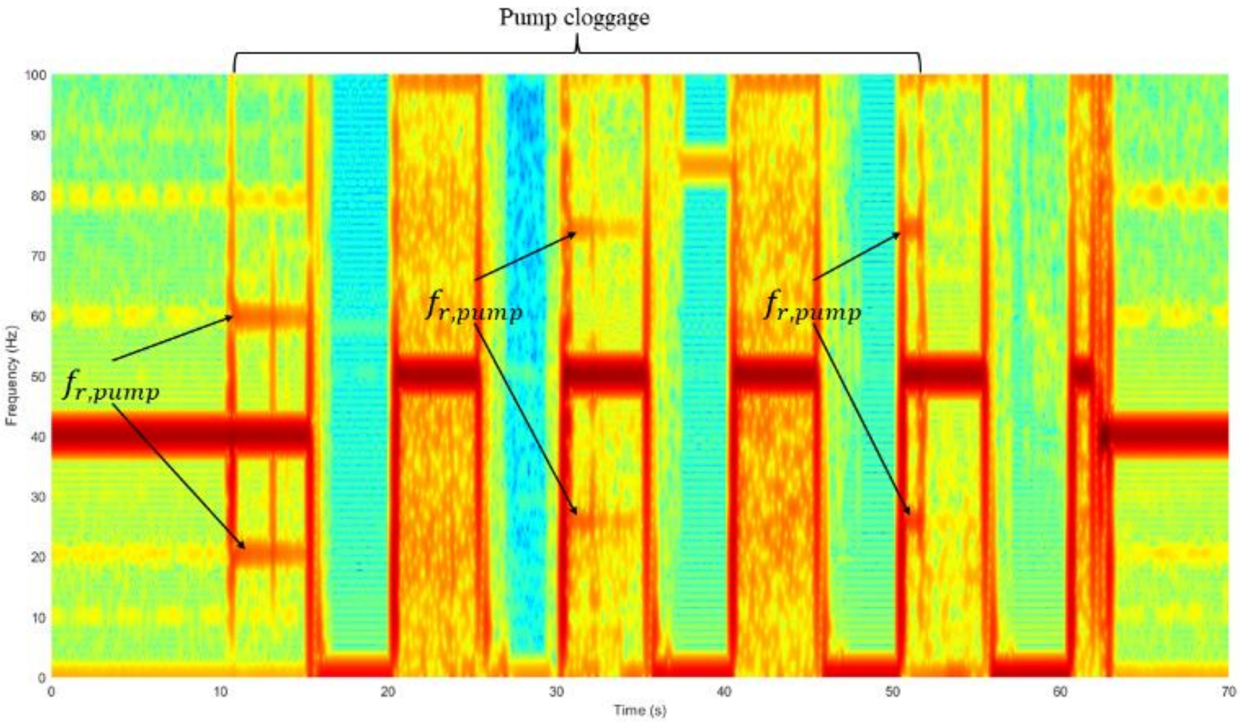

Figure 6.6: ATCSA of the submersible pump in the frequency range of 0-100 Hz

In section 5.2.2.4, it was demonstrated that the amplitudes of higher frequencies were also influenced by the fault *clogging*. Therefore, in ATCSA the same frequency range from 90 to 400 Hz was also considered (see Figure 6.7).

Note that especially at the moment when, at 10 s, the rag was sucked into the impeller, patterns became visible in the higher frequency range. The result was equal to that of MCSA, with the frequencies appearing at 100, 180, 220, and 300 Hz. However, in other periods, the patterns were not visible anymore, indicating that the severity of the fault decreased.

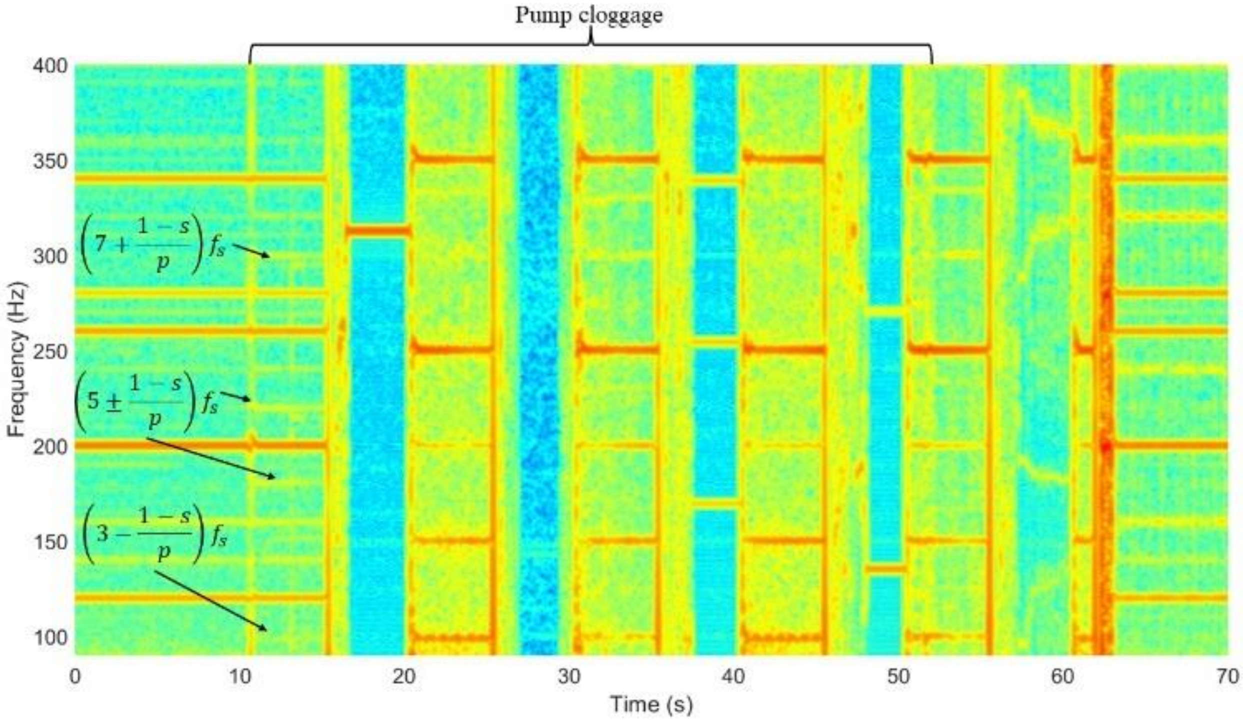

Figure 6.7: ATCSA of the submersible pump in the frequency range of 90-400 Hz

In conclusion, it is confirmed that ATCSA is a very useful tool for detecting the clogging of an ESP as well as to detect the clearing of the pump. Compared to MCSA, ATCSA has the advantage that transients due to changed fault severities do not influence the results or lead to wrong decisions in the decision-making process, yielding higher reliability in the diagnosis process.

6.3 Cracked Impeller

Figure 6.8 depicts the ATCSA of an 800 W wet-rotor pump with a cracked impeller. As in the case of the fault *clogging*, the fault *cracked impeller* also showed the typical fault trajectory at the two frequencies $f_{r,pump-}$ and $f_{r,pump+}$, where especially the amplitude of $f_{r,pump-}$ was visible. The results confirm the results of MCSA, where an increase of the two frequencies was also detected. Other frequencies, like the BPF, were not influenced in ATCSA.

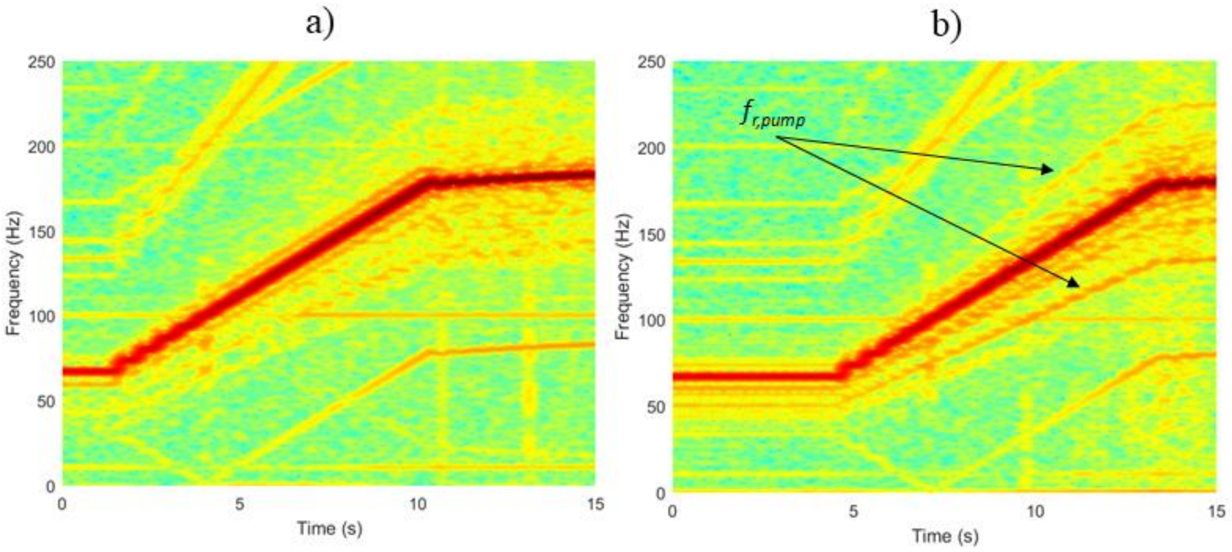

Figure 6.8: ATCSA of the wet-rotor pump (800 W) for the fault *cracked impeller* from 1000 to 2800 rpm at 0–250 Hz; (a) healthy; (b) cracked impeller

6.4 Bearing Damage

Figure 6.9 depicts the ATCSA of an 800 W wet-rotor pump with varying fault severity of a bearing defect. On the one hand, the diameter increase of the bearing shell was varied, and on the other hand, the place of the bearing defect. In (b) – (d), the diameter of the bearing shell was increased by 0.1 mm, while (b) illustrates the results for the two-sided bearing defect, (c) and (d) the results for a one-sided bearing defect. (e) depicts the ATCSA for a one-sided bearing defect on the impeller side (A-bearing defect) with an increase of the bearing shell diameter of 0.5 mm and (f) shows the results for a bearing defect on the electronic side (B-bearing defect) of the pump.

All variants indicated the typical patterns of an eccentricity problem in a PMSM with the ECC1 amplitudes around the FC. With increased fault severity ((e) and (f)), the patterns became more pronounced compared to the lighter faults ((c) and (d)). Consequently, higher bearing wear led to a more eccentric running of the rotor of the motor. Furthermore, the two-sided bearing fault (b) indicated a more pronounced pattern compared to the one-sided bearing fault with the same fault severity ((c) and (d)). This suggests that in the case of a one-sided bearing failure, one bearing could still support the shaft. It was also possible to differentiate between the two one-sided bearing faults. For the defect on the electronic side ((d) and (f)) , f_{ecc-} and f_{ecc+} started to be visible at higher speeds compared to the defect on the impeller side ((c) and (e)). Consequently, the location of the bearing defect also had an influence on the degree of eccentricity in the motor. With the help of ATCSA, the location of the bearing defect could be determined. On the other hand, for the one-sided bearing defect, an additional amplitude was visible between the ECC1 component and the FC.

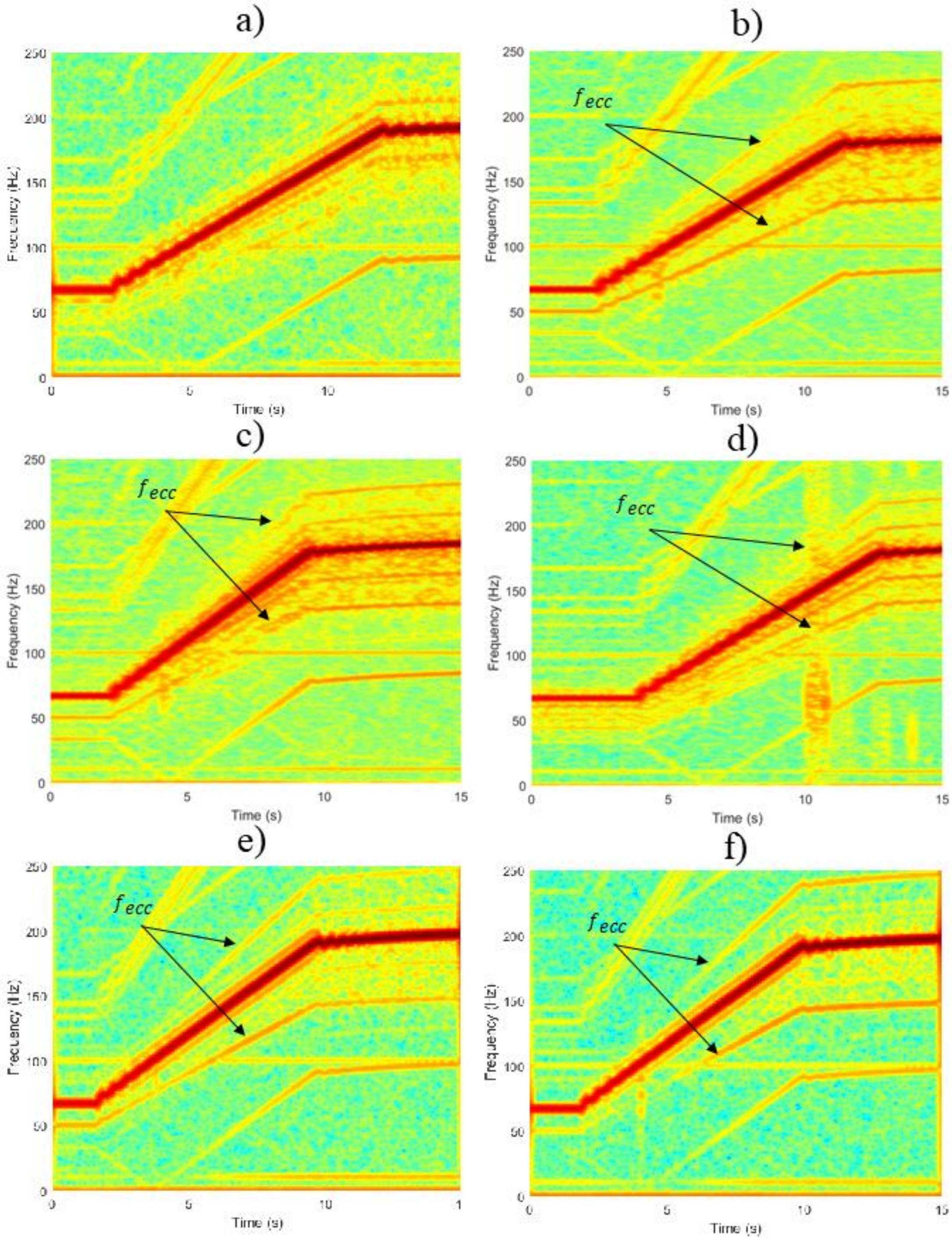

Figure 6.9: ATCSA of the wet-rotor pump (800 W) with varying severity of bearing wear from 1000 to 2800/3000 rpm at 0–250 Hz; (a) healthy; (b) two-sided bearing defect, +0.1 mm; (c) A-bearing defect, +0.1 mm; (d) B-bearing defect, +0.1 mm; (e) A-bearing defect, +0.5 mm; (f) B-bearing defect, +1 mm

6.5 Dry-Running Rotor

Figure 6.10 depicts the ATCSA for an 800 W wet-rotor pump with a dry-running rotor for the startup from 1000 to 3000 rpm. In the analysis, a very slight pattern was noticeable, which indicated the predicted pattern for dynamic eccentricity. Particularly notable is the frequency f_{ecc-}, which was visible over the entire time history.

The results prove that a slight dynamic eccentricity was caused by the dry-running rotor. This behavior could be explained by the fact that no lubricating film could form between the bearing and the shaft because there was no water in the rotor space. The gap between the shaft and the bearing was sufficient to cause a slight eccentricity.

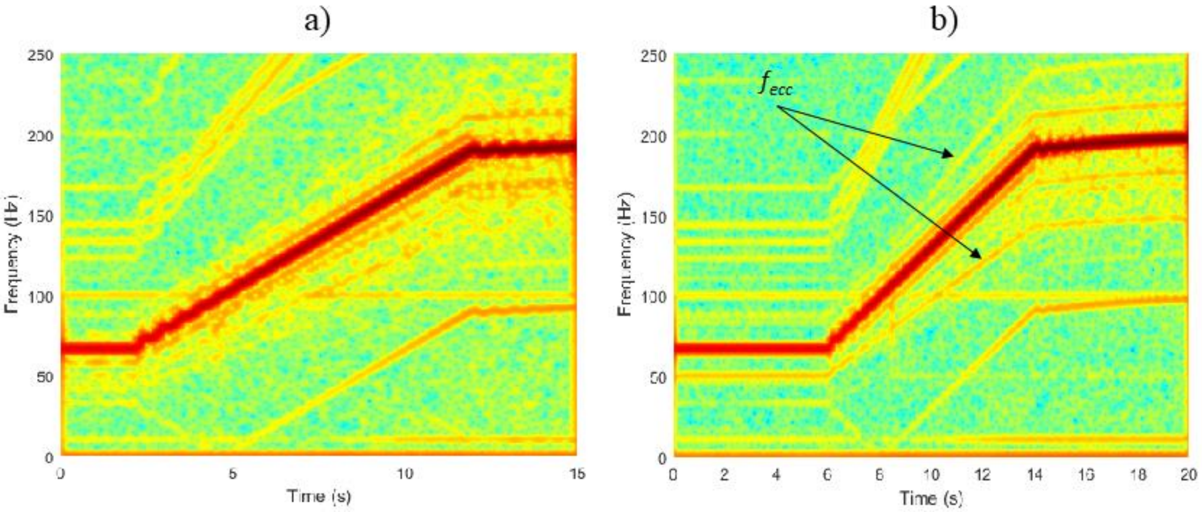

Figure 6.10: ATCSA of the wet-rotor pump (800 W) for a dry running rotor from 1000 to 3000 rpm at 0–250 Hz; (a) healthy; (b) dry-running rotor

6.6 Dry Running

In this section, the influence of the fault *dry running* on the ATCSA for the startup from 1000 to 2800 rpm will be investigated. Figure 6.11 depicts the transient analysis of both the faulty and the healthy condition of the 800 W wet-rotor pump. There was a clear difference between the two variants, which was visible at the two frequencies f_{ecc-} and f_{ecc+}. Both amplitudes were clearly visible from the beginning of the startup at a speed of 1000 rpm, during the startup, and at the end, which indicates the severity of this fault. The basic color of the pattern generally tends to yellowish in the fault case, compared to the healthy state, which suggests an increased noise level. The results confirm the MCSA results, where high increases of the ECC1 component and of the noise level were found.

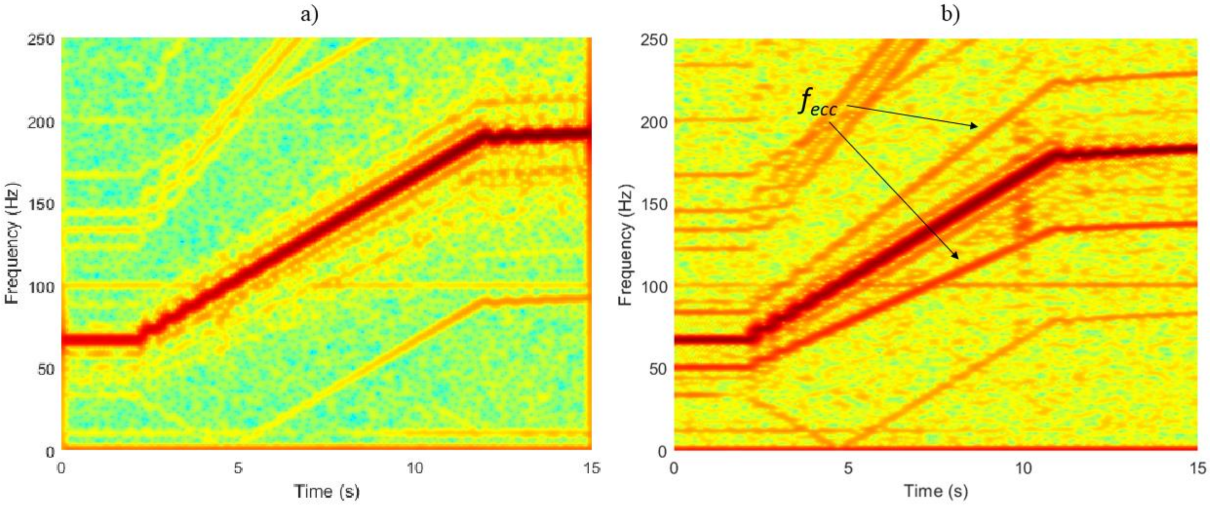

Figure 6.11: ATCSA of the wet-rotor pump (800 W) for a dry running rotor from 1000 to 2800 rpm at 0–250 Hz; (a) healthy; (b) dry-running

6.7 Hydraulic Blockage

Finally, the ATCSA of a hydraulic blockage is depicted in Figure 6.12, compared with a healthy startup of the 800 W wet-rotor pump. The difference between the two patterns is mainly seen in the noise band around the FC. This effect became clearer as the speed of the motor increased. These results confirm the findings from the MCSA, where a slight increase of the noise band was detected in stationary operation of the same pump.

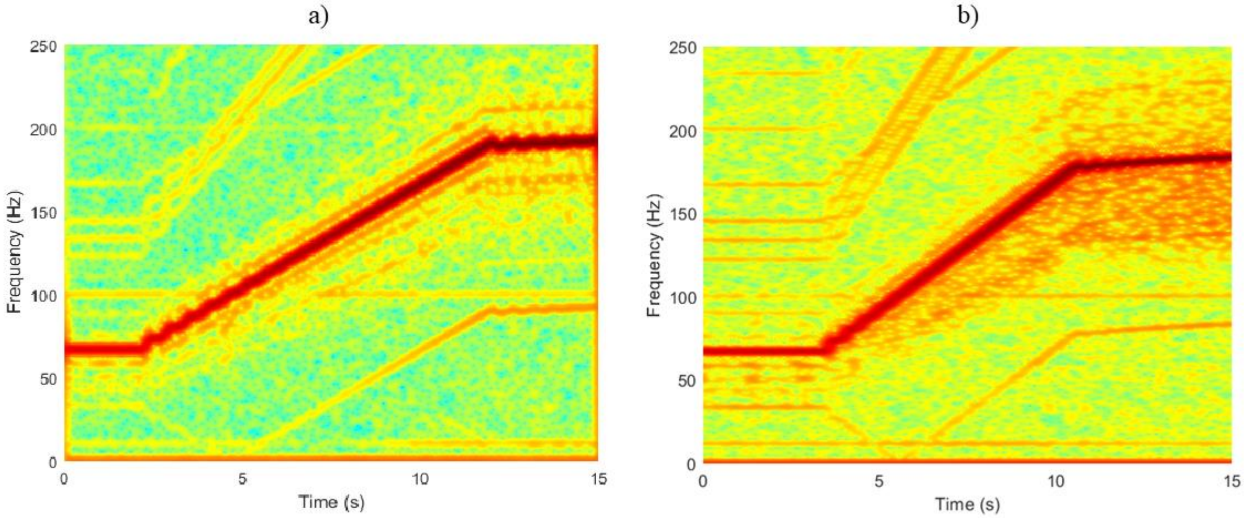

Figure 6.12: ATCSA of the wet-rotor pump (800 W) for a hydraulic blockage from 1000 to 2800 rpm at 0–250 Hz; (a) healthy; (b) hydraulic blockage

6.8 Conclusion

In this section, the results of using ATCSA for the evaluation of current signals during startup were discussed. First, the healthy variants of the two wet-rotor pumps identical in design were investigated. Additionally, in every integer multiple of the FC, typical patterns were detected. Furthermore, frequency components were detected that did not linearly increase with the FC. Some of them were constantly independent of the FC, some even had a negative slope during startup, and some had a constant distance from the FC. These components were caused by the VSD operation of the motor. This inference was only possible by applying ATCSA. After consideration of the healthy variant, various faults were investigated. It was demonstrated that one typical pattern, in particular, was visible for the wet-rotor pump with 800 W for the faults *clogging*, *cracked impeller*, *bearing damage*, dry-running rotor, and *dry running*. The strongest patterns were noted for half-sided clogging, severe bearing damage, and dry running. However, in the 150 W wet-rotor pump, this pattern was not visible for the fault *clogging*. Furthermore, no separation between the faults was possible with ATCSA. ATCSA demonstrated its advantage over MCSA in the minimization of false alarms. If MCSA is applied, there is always the risk that frequencies produced by the VSD are confused with the fault frequencies. For the detection of the fault *clogging* in the submersible pump, ATCSA showed great performance, as the fault provoked frequencies that were clearly visible in the analysis. This was true for the process of sucking in the rag (clogging) and for cleaning. In general, the results of MCSA were confirmed by the results of ATCSA.

7 Conclusions and Future Work

In the final section of this work, the findings will be summarized and an outlook on future work will be given.

7.1 Conclusion

In this thesis, different techniques based on the analysis of motor currents were used to diagnose typical faults in pumps driven by the motor. In total, three different pump types – a wet-rotor pump, a dry-runner pump, and a submersible pump – were measured in different test benches. The main focus has been put on the fault detection of the wet-rotor pump. The faults that were investigated were: a *bearing defect* (wet-rotor pump), *impeller clogging* (all pumps), *cracked impeller* (wet-rotor pump), *dry-running rotor* (wet-rotor pump), *dry running* (wet-rotor pump and dry-runner pump), and *hydraulic blockage* (wet-rotor pump and dry-runner pump). To analyze the faults, different techniques were implemented.

As a first step, the stationary values were considered. Considering the rms value of the current (with the exception of the cloggage of the submersible pump, where it remained constant), the analyzed faults led to a decrease of the rms current in all cases. Consequently, a decreasing rms current can be one symptom of a faulty pump operation. However, no differentiation between the single faults and a partial load condition is possible by simply evaluating the rms current. The only fault that can be separated from other faults was found to be *dry running*. In this case, the current consumption becomes smaller than it would be possible in the case of any other fault or operating condition. It was also found that especially the fault *clogging* can lead to a dramatic decrease of efficiency in both wet-rotor and submersible pumps. Finally, the influence of the fault *clogging* on the parameter estimation of a wet-rotor pump was analyzed. It turned out that both flow and head estimation worsened in the faulty condition.

After consideration of the stationary values, the current signal in stationary condition of the pumps was investigated. First, MCSA was used for this. For all investigated pumps, one frequency family, in particular, was found to be influenced by the implemented faults. These frequency bands are located on the left and right of the FC at the distance of the rotational frequency. This observation was made for all pumps in the case of the fault *clogging;* for wet-rotor pumps, it was also observed for the faults *impeller crack*, *bearing damage*, *dry-running rotor*, and *dry running*. The fault *hydraulic blockage* did not influence these frequency bands. As stated in some references, it was not the BPF that was affected by the faults in the pumps we studied. By evaluating the amplitude at these frequencies, a statement about the severity can be made. In the case of *clogging*, the highest amplitudes were reached when three or four adjacent impeller channels were clogged. Furthermore, severe faults also influenced bands in the higher-frequency range around the 3rd and 5th harmonic.

Next, the two fault frequencies for the wet-rotor pump were analyzed in more detail. We investigated whether the hydraulic load point has an influence on the amplitudes at the frequency bands. To evaluate this, the LoPoFIA methodology was proposed, which indicates the relation between the amplitudes and the hydraulic load point in a flow-head map. It was demonstrated that the load point has a strong influence on amplitudes in both healthy and faulty condition. Each fault – *impeller clogging*, *bearing damage*, and *cracked impeller* – had its own characteristic pattern in the flow-head map. In addition, the LoPoFIA revealed a weakness of the MCSA in that a difference between healthy and defective is not evident at each load point. Additionally, LoPoFIA makes it possible to differentiate between bearing and impeller faults (*clogging* and *cracked impeller*), since the impeller faults especially influence the amplitudes in higher flow ranges. Bearing faults are more visible in the case of lower flows.

To facilitate understanding of the behavior of the motor as a sensor for diagnosing pump faults, DTFA was presented in the theoretical background section. In order to validate DTFA, the oscillation of the q-current at the rotational frequency of the rotor was analyzed depending on the load point of the pump. This was done for two pumps that were identical in construction, but which had different sizes (150 W and 800 W). We compared two variants, one in healthy condition and one with seven clogged impeller channels. The fault was especially visible for the 800 W pump, which indicates that the function of the motor as a sensor was better. Especially around a speed of 2200 rpm, high amplitudes were detected, which was explained by the amplitude increase due to the low damping degree of the motor.

Since the two frequency bands deliver information about the pump in healthy condition, the next step was to develop an algorithm that can calculate these two amplitudes in real time. As a test object, we used a wet-rotor pump that already had an MPU for the implementation of such an algorithm. Additionally, it already had built-in current sensors, which were used as input for the method. However, as the first step, the method was verified using a laboratory test. During the laboratory test, the method was implemented on a MicroLabBox (dSpace) and external current sensors were used. The results demonstrated that this method was capable of calculating the amplitudes at the mentioned frequencies. In a field test, the method was implemented in the firmware of an MCU of a circulation pump. It was observed that the results were almost equal to the results of MCSA. Consequently, the method was capable of diagnosing the implemented pump faults.

As the last part of this work, a transient current analysis was performed for the wet-rotor pump and the submersible pump. The results of the stationary analysis were confirmed, as the same frequency bands were influenced as in the stationary analysis. With the exception of the fault *hydraulic blockade*, all faults indicated time-frequency evolutions at the frequencies. Additionally, for the submersible pump, it was clearly visible in the ATCSA when the rag was sucked in (clogging) and when the deragging was successful. The method also proved its main advantage, i.e., its reliability in preventing false indications.

7.2 Main Contributions

- Pump-related faults, especially the clogging fault, lead to a decrease of efficiency of the measured pumps. The clogging fault leads in case of the 800 W wet-rotor pump to an efficiency reduction of 9 to 15% and with the 7.7 kW submersible pump of maximum 38%. Additionally, the parameter estimation of a wet-rotor pump is worsened in faulty condition.
- The rms value of the current decreases or remains constantly. Consequently it can be one symptom that indicates a faulty operation of a pump. However, an increase of the rms current, which is partly used in literature for clogging detection, was not detected in the measured variants.
- In MCSA one frequency family, on the left and right of the FC at the distance of the rotational frequency, was found to be influenced by the implemented faults. All investigated faults with exception of the fault hydraulic blockage influenced these frequency bands. The amplitudes at the BPF component, however, were not influenced by the faults. The amplitude increase in

faulty condition depends on the fault type and the pump used. The maximum increase due to a clogged impeller was found to be +54.0 dB, compared to the healthy variant.

- A novel methodology was proposed in which the influenced fault components were related to the hydraulic load point. For this purpose, the amplitude at a certain frequency is displayed in color in the flow-head map usual for pumps. It was demonstrated that the load point has a strong influence on amplitudes in both healthy and faulty condition with each fault having its own characteristic pattern. It is one possibility to differentiate between faults are caused by load oscillations (in our case the clogging and impeller crack faults) and faults that cause eccentric rotation of the rotor (in our case bearing damage).
- A novel method to analyze the transfer behavior of load oscillations of controlled PMSM was presented and qualitatively validated with two pumps identical in construction. The method helps to predict whether a PMSM can successfully be used as a sensor to detect pump-related faults.
- A novel algorithm was presented, that makes it possible to calculate the fault components in the current signal in real-time on a memory-friendly way. The proposed algorithm, which is based on ARFT was tested in a laboratory and a field test with a real circulation pump and showed similar results like MCSA.
- On the basis of ARFT a method for cloud-based monitoring of a pump fleet was proposed in the thesis. While the ARFT runs on the MPU of a single pump, the decision making process is outsourced to a central data acquisition system (“cloud”). In this cloud the fault indicators of many pumps of different sizes can be compared.
- ATCSA was used in order to analyze whether the investigated faults are visible in the time-frequency maps. It was shown that the ATCSA is a useful tool in order to have a more reliable decision making compared to MCSA. Especially in submersible pumps ATCSA showed its performance in order to detect the clogging fault and a cleaning of the pump.

7.3 Future Work

- The methods in this work were used to investigate three different pump types. Despite many tests have been developed for each pump type and fault condition, it remains to be investigated whether the methods also work for other pump powers and pumps with other characteristics, especially in higher power ranges.

- Different pump faults were investigated in this work. However, other typical pump faults must also be investigated in more detail. One of these faults is *cavitation*, which is a known problem in pumping systems. Cavitation can also lead to damage of the impeller. Consequently, if cavitation would be detected, wear at the impeller could be prevented. Furthermore, other faults like *seal damage* or *water hammering* should be investigated in future work.
- The data that was analyzed was acquired in the framework of laboratory tests. Whether the same results can be obtained for pumps in the field is part of future work.
- It was demonstrated that MCSA can be implemented in real time by using ARFT, even in systems with low memory and computing power. However, it has to be considered how transient analysis can be implemented in real applications. Especially in the application of wastewater pumps, transient analysis could help to obtain a reliable detection of clogging.
- Most of the faults influenced two sidebands in the current spectrum. Consequently, other features had to be included in the analysis in order to enable separation of the faults. With the methods we used, no other frequencies were observed that could simplify this separation. Part of future work will be to validate whether other procedures, e.g., based on Artificial Intelligence, make it possible to differentiate the faults. Note that the features should be selected well in order be able to make a statement about the severity of a fault, which can be difficult, e.g., in the case of some statistical features in the time domain.
- In order to assess the transfer behavior of a motor for the detection of pump faults, DTFA was proposed in this work. However, the measurement data only enabled qualitative validation of the approach. For further validation, we propose measuring a motor on a test bench that allows generating torque oscillations in variable frequencies. This would allow quantitative validation of DTFA.
- In this work, a methodology for the cloud-based monitoring of a pump fleet was proposed and validated in a laboratory test. However, the concept has to be validated for more than three pumps and also for other faults. Implementing ARFT in the pumps' MPU, will enable pump manufacturers to acquire and evaluate big data sets.

Literature

Abitha, M.W., & Rajini, V. (2013). Park's vector approach for online fault diagnosis of induction motor. *2013 International Conference on Information Communication and Embedded Systems (ICICES)*, 1123-1129.

Ahmad, Z., Prosvirin, A.E., Kim, J., & Kim, J. (2020). Multistage Centrifugal Pump Fault Diagnosis by Selecting Fault Characteristic Modes of Vibration and Using Pearson Linear Discriminant Analysis. *IEEE Access, 8*, 223030-223040.

Albers, A., Burger, W., Scovino, R., & Dickerhof, M. (2006). Monitoring Lubrication Regimes in Sliding Bearings Using Acoustic Emission Analysis. *Technology*, 1–4.

de Almeida A. T., Fonseca P., Falkner H. & Bertoldi P. (2003). Market transformation of energy-efficient motor technologies in the EU. *Energy Policy, 31*(6), 563-575. https://doi.org/10.1016/S0301-4215(02)00100-3.

Antonino-Daviu, J.A., Riera, M., Roger-Folch, J., & Molina, M.J. (2005). Validation of a new method for the diagnosis of rotor bar failures via wavelet transformation in industrial induction machines. *2005 5th IEEE International Symposium on Diagnostics for Electric Machines, Power Electronics and Drives*, 1-6.

Antonino-Daviu, J.A., Riera-Guasp, M., Folch, J.R., & Palomares, M. (2006). Validation of a new method for the diagnosis of rotor bar failures via wavelet transform in industrial induction machines. *IEEE Transactions on Industry Applications*, 42, 990-996.

Antonino-Daviu, J.A., Jover, P., Riera, M., Arkkio, A., & Roger-Folch, J. (2007). DWT analysis of numerical and experimental data for the diagnosis of dynamic eccentricities in induction motors. *Mechanical Systems and Signal Processing*, 21, 2575-2589.

Antonino-Daviu, J.A., Riera-Guasp, M., Pons-Llinares, J., Park, J., Lee, S.B., Yoo, J., & Kral, C. (2012). Detection of Broken Outer-Cage Bars for Double-Cage Induction Motors Under the Startup Transient. *IEEE Transactions on Industry Applications*, 48, 1539-1548.

Antonino-Daviu, J.A., Lee, S.B., & Wiedenbrug, E.J. (2014a). Reliable detection of rotor bar failures in induction motors operating in petrochemical plants. *2014 Petroleum and Chemical Industry Conference Europe*, 1-9.

Antonino-Daviu, J.A., Climente-Alarcón, V., Pons-Llinares, J., & Wiedenbrug, E.J. (2014b). Advanced rotor assessment of motors operating under variable load conditions in mining facilities. *2014 IEEE Energy Conversion Congress and Exposition (ECCE),* 617-621.

Antonino-Daviu, J.A., Pons-Llinares, J., Shin, S., Lee, K.W., & Lee, S.B. (2015). Reliable detection of induction motor rotor faults under the influence of rotor core magnetic anisotropy. 2015 *IEEE 10th International Symposium on Diagnostics for Electrical Machines, Power Electronics and Drives (SDEMPED)*, 14-21.

Antonino-Daviu, J.A., & Popaleny, P. (2018). Detection of Induction Motor Coupling Unbalanced and Misalignment via Advanced Transient Current Signature Analysis. *2018 XIII International Conference on Electrical Machines (ICEM)*, 2359-2364.

Antonino-Daviu, J.A (2019, February 25-26). *Advanced electric motor predictive maintenance techniques*. Seminar at the Department Electrical Engineering of Institute of Energy Technology of Universitat Politècnica de València.

Antonino-Daviu, J.A. (2020). Electrical Monitoring under Transient Conditions: A New Paradigm in Electric Motors Predictive Maintenance. *Applied Sciences, 10*, 6137.

Arkan, M., Çaliş, H. & Tağluk, M.E. (2005). Bearing and misalignment fault detection in induction motors by using the space vector angular fluctuation signal. *Electr Eng*, *87*, 197–206. https://doi.org/10.1007/s00202-004-0242-6

Bachus, L., Custodio, Á., & Custodio, Á. (2003). Know and understand centrifugal pumps. Elsevier Advanced Technology, New York, USA.

Barthel, C., & Thomas, S. (2006). Energy+ pumps: technology procurement for very energy efficient circulation pumps. Intelligent Energy Europe.

Barringer, H. (2003). A Life Cycle Cost Summary. *ICOMS 2003 International Conference of Maintenance Societies*, Perth (Australia). Paper 3

Beebe, R. (2004). *Predictive Maintenance of Pumps Using Condition Monitoring*. Elsevier Science & Technology Books. ISBN: 1856174085

Benbouzid M. E. H. (2000). A review of induction motors signature analysis as a medium for faults detection. *IEEE Transactions on Industrial Electronics, 47*(5), 984-993. doi: 10.1109/41.873206.

Bidstrup, N., van Elburg, M. and Lane, K. (2001). *Promotion of Energy Efficiency in Circulation Pumps especially in Domestic Heating Systems* (Contract No 4.1031/-Z/99-256). The Environmental Change Institute. https://www.eci.ox.ac.uk/research/energy/archive-eusave-pumps.html

Bidstrup, N., A New Generation of Intelligent Electronically Controlled Circulator Pumps. *2nd International Conference on Improving Electricity Efficiency in Commercial Buildings, IEECB 2002*, Nice, France.

Bonet-Jara, J., Quijano-López, A., Morinigo-Sotelo, D., & Pons-Llinares, J. (2021). Sensorless Speed Estimation for the Diagnosis of Induction Motors via MCSA. Review and Commercial Devices Analysis. *Sensors (Basel, Switzerland)*, 21

Bold, S., & Urschel, S. (2020). Assessment of approaches for technical diagnostic of pump faults with induction motor as transducer. *2020 23rd International Conference on Electrical Machines and Systems (ICEMS)*, 810-815. doi: 10.23919/ICEMS50442.2020.9291035

Bonaldi, E.L., Oliveira, L.E., Silva, J.G., Lambert-Torresm, G., & Silva, L.E. (2012). Predictive Maintenance by Electrical Signature Analysis to Induction Motors. *Induction Motors—Modelling and Control*, Rui Araujo, Eds., Rijeka, Croatia: InTech, 2012, 487–520, ISBN 978–953-51-0843-6, doi: 10.5772/48045

Blodt, M., Chabert, M., Régnier, J., Faucher, J., & Dagues, B. (2005). Detection of mechanical load faults in induction motors at variable speed using stator current time-frequency analysis. *2005 5th IEEE International Symposium on Diagnostics for Electric Machines, Power Electronics and Drives*, 1-6., doi: 10.1109/DEMPED.2005.4662496

Blodt, M. (2006). *Condition Monitoring of Mechanical Faults in Variable Speed Induction Motor Drives. Application of Stator Current Time-Frequency Analysis and Parameter Estimation*. (Doctoral dissertation). https://oatao.univ-toulouse.fr/.

Cameron, J., Thomson, W.T., & Dow, A.B. (1986). Vibration and current monitoring for detecting airgap eccentricity in large induction motors. *Proceedings IEEE, 133*(3), 155-163.

Cappelli, L., Coia, Y., Marignetti, F., & Zhu, Z.Q. (2014). Analysis of Eccentricity in Permanent-Magnet Tubular Machines. *IEEE Transactions on Industrial Electronics, 61*(5), 2208-2216. doi: 10.1109/TIE.2013.2271598

Cardoso, A.J., Cruz, S.M., & Fonseca, D.S. (1997). Inter-turn stator winding fault diagnosis in three-phase induction motors, by Park's Vector approach. *IEEE Transactions on Energy Conversion, 14*(3), 595-598. doi: 10.1109/60.790920.

Casada, D. (1994). Detection of pump degradation. *22nd Water Reactor Safety Information Meeting*. Bethesda, Maryland

Casada, D., & Bunch, S. (1995). The use of the motor as a transducer to monitor pump conditions. *Proceedings of the P/PM Technology Conference*, Indianapolis.

Čdina, M. (2003). Detection of cavitation phenomenon in a centrifugal pump using audible sound. *Mechanical Systems and Signal Processing, 17*, 1335-1347.

Cruz, S.M., & Cardoso, A.J. (2005). Multiple reference frames theory: a new method for the diagnosis of stator faults in three-phase induction motors. *IEEE Transactions on Energy Conversion*, 20, 611-619.

Deckers, J. (2001). *Development of a low-cost structure-borne sound sensor system for monitoring the wear behavior of low-power centrifugal pumps with roller bearings or journal bearings* (Translated Title). (Doctoral dissertation). Gerhard-Mercator-Universität Duisburg

Dergreg (2004). *Tauchpumpe für den Abwasserbereich*. https://commons.wikimedia.org/wiki/File:Tauchpumpe_Abwasser.jpg?uselang=de

Dias, A.L., da Silva, J.T., Turcato, A.C., & Sestito, G.S. (2021). An intelligent fault diagnosis for centrifugal pumps based on electric current information available in industrial communication networks. *2021 14th IEEE International Conference on Industry Applications (INDUSCON)*, 102-109.

Dister, C.J. (2003). On-line health assessment of integrated pumps. 2003 *IEEE Aerospace Conference Proceedings (Cat. No.03TH8652), 7*, 3289-3294.

Dutta, N., Umashankar, S., Shankar, V.K., Padmanaban, S., Leonowicz, Z., & Wheeler, P. (2018). Centrifugal Pump Cavitation Detection Using Machine Learning Algorithm Technique. *2018 IEEE International Conference on Environment and Electrical Engineering and 2018 IEEE Industrial and Commercial Power Systems Europe (EEEIC / I&CPS Europe)*, 1-6. doi: 10.1109/EEEIC.2018.8494594.

Dutta, N., Subramaniam, U., Sanjeevikumar, P., Bharadwaj, S.C., Leonowicz, Z., & Holm-Nielsen, J.B. (2020). Comparative Study of Cavitation Problem Detection in Pumping System Using SVM and K-Nearest Neighbour Method. *2020 IEEE International Conference on Environment and Electrical Engineering and 2020 IEEE Industrial and Commercial Power Systems Europe (EEEIC / I&CPS Europe)*, 1-6. doi: 10.1109/EEEIC/ICPSEurope49358.2020.9160689.

Ebrahimi, E.H., & Javidan, M. (2017). Vibration-based classification of centrifugal pumps using support vector machine and discrete wavelet transform. *Journal of Vibroengineering*, 19, 2586-2597.

Eckl M., Wurm F.-H., Liu S.; Urschel S., Schullerer, J., Schaab, J.,& Kowalski K. (2019a). New control mode to decrease energy consumption of circulator pumps. *4th International Rotating Equipment Conference*, Wiesbaden (Germany).

Eckl M. & Schullerer J. (2019b). *Method for the self-diagnosis of the mechanical and/or hydraulic state of a centrifugal pump,* (Patent No. WO2019141658A1). https://patents.google.com/patent/WO2019141658A1/en (Accessed on: Jan. 6, 2019).

Eser, M., Kasnakoğlu, C., & Benli, B.B. (2019). Vector Control of PMSM in Circulation Pump Application and an Adaptive Approach for EEI Optimization. *2019 11th International Conference on Electrical and Electronics Engineering (ELECO)*, Bursa, Turkey, 749-753. doi: 10.23919/ELECO47770.2019.8990438.

European Commission (2012). *Energy roadmap 2050.* Luxembourg: Publications Office of the European Union. ISBN 978-92-79-21798-2. doi:10.2833/10759

European Parliament. (2009) Directive 2009/125/EC. European Parliament and of the Council of 21 October 2009 establishing a Framework for the Setting of Ecodesign Requirements for Energy-related Products. *Official Journal of the European Union.* European Parliament, Council of the European Union. http://data.europa.eu/eli/dir/2009/125/oj

Fernandez-Cavero, V., García-Escudero, L.A., Pons-Llinares, J., Fernández-Temprano, M.A., Duque-Perez, O., & Morinigo-Sotelo, D. (2021). Diagnosis of Broken Rotor Bars during the Startup of Inverter-Fed Induction Motors Using the Dragon Transform and Functional ANOVA. *Applied Sciences, 11*, 3769.

Flygt. (2015). *Life Cycle Costs (LCC) for wastewater pumping systems*. [White paper]. https://www.xylem.com/siteassets/support/tekniska-rapporter/white-papers-pdf/life-cycle-costs-lcc-for-wastewater-pumping-systems.pdf

Flygt. (2017). *Adaptive N-Impeller Solves Clogging Issues For Small-Range Wastewater Pumps* [White paper]. https://www.xylem.com/siteassets/support/white-papers/white-paper-resources/adaptive-n_white_paper2553_en-us.pdf

Fullemann, A., Soderlund, F. ,& Karlen M. (2013). Pump control including cleaning procedure or stopping depending on motor load (Patent No. *WO2013/096726A1*). https://patents.google.com/patent/WO2013096726A1/fi (Accessed on: Nov. 24, 2021).

Directive 2009/125/EC. Directive 2009/125/ec of the European Parliament and of the Council of 21 October 2009 establishing a Framework for the Setting of Ecodesign Requirements for Energy-related Products. *Official Journal of the European Union*. European Parliament, Council of the European Union. http://data.europa.eu/eli/dir/2009/125/oj

Gevorkov, L., & Vodovozov, V. (2016). Study of the centrifugal pump efficiency at throttling and speed control. *2016 15th Biennial Baltic Electronics Conference (BEC),* 199-202.

Glover, A. and Lukaszczyk, M. (2005). Oversizing pump motors – the problems. *World Pumps, 466*, 36–38.

Grattan-Guinness, I. (2005). *Joseph Fourier*, Théorie analytique de la chaleur (1822).

Gülich, J. F. (2014). *Centrifugal Pumps* (3rd ed.). Springer Heidelberg Dordrecht London New York. ISBN 978-3-642-40113-8.

Haddad, R.Z., Lopez, C.A., Pons-Llinares, J., Antonino-Daviu, J.A., & Strangas, E.G. (2015). Outer race bearing fault detection in induction machines using stator current signals. *2015 IEEE 13th International Conference on Industrial Informatics (INDIN),* 801-808.

Haddad, R. Z. S. (2016). *Fault Detection and Identification in Permanent Magnet Synchronous Machines*. (Doctoral dissertation). https://d.lib.msu.edu.

Hamomd, O., Tian, X., Chen, Z., Al-Braik, A., Gu, F., & Ball, A.D. (2014). A new method of vibration analysis for the diagnosis of impeller in a centrifugal pump. *21st International Congress on Sound and Vibration*, Beijing, China.

Harihara, P.P., Kim, K., & Parlos, A.G. (2003). Signal-based versus model-based fault diagnosis- a trade-off in complexity and performance. *4th IEEE International Symposium on Diagnostics for Electric Machines, Power Electronics and Drives*, 2003. SDEMPED 2003., 277-282.

Harihara, P.P., & Parlos, A.G. (2008). Sensorless detection of impeller cracks in motor driven centrifugal pumps. *Design, Analysis, Control and Diagnosis of Fluid Power Systems, 5*, 17-23.

Harihara, P.P., & Parlos, A.G. (2012). Fault Diagnosis of Centrifugal Pumps Using Motor Electrical Signals. *In Centrifugal Pumps*. Springer, Berlin/Heidelberg, Germany, pp. 15–32, ISBN 978-953-51-0051-5.

Hernández-Solís, A., & Carlsson, F. (2010). Diagnosis of Submersible Centrifugal Pumps: A Motor Current and Power Signature Approaches. *EPE Journal, 20,* 58 - 64.

Hess, M., & Pelz, P.F. (2009). Comparison of Measurements on Axial Fans and Performance Prediction Using Common Scale-Up Methods at Part- and Overload. *Proceedings of FEDSM2009 ASME Fluids Engineering Division Summer Meeting*.

Husna, A., Indriawati, K., & Widjiantoro, B.L. (2021). Discriminant Feature Extraction of Motor Current Signal Analysis and Vibration For Centrifugal Pump Fault Detection. *2021 International Conference on Instrumentation, Control, and Automation (ICA)*, 207-212.

Irfan, M. A. A., Glowacz A (2019). Design of a Novel Electric Diagnostic Technique for Fault Analysis of Centrifugal Pumps. *Applied Sciences*, *9*(23):5093. https://doi.org/10.3390/app9235093

Jahangiri, M., Seyed Roknizadeh, S. (2018). Clogged Impeller Diagnosis in the Centrifugal Pump Using the Vibration and Motor Current Analysis. *Journal of Applied and Computational Mechanics*, *4*(4), 310-317. doi: 10.22055/jacm.2018.24774.1211

Janlepkowski (2014). *Heating pump blocked by contaminants*. https://commons.wikimedia.org/wiki/File:Blocked_heating_pump.jpg

Joksimović, G., Riger, J., Wolbank, T.M., Peric, N., & Vašak, M. (2013). Stator-Current Spectrum Signature of Healthy Cage Rotor Induction Machines. *IEEE Transactions on Industrial Electronics*, 60, 4025-4033.

Jones, D.L., & Parks, T.W. (1990). A high resolution data-adaptive time-frequency representation. *IEEE Trans. Acoust. Speech Signal Process.*, *38*, 2127-2135.

Kallesøe, C. S., Bidstrup, N., & Bayer, M. (2009). *Adaptive Selection of Control-Curves for Domestic Circulators*. [White paper]. Grundfos Management A/S. https://www.grundfos.com

Kallesøe, C. S. (2014). *Method for detecting the flow rate of a centrifugal pump*, (Patent No. EP2696175A1). https://patents.google.com/patent/EP2696175A1/en (Accessed on: Jan. 14, 2021).

Kostic-Perovic, D., Arkan, M., & Unsworth, P.J. (2000). Induction motor fault detection by space vector angular fluctuation. *Conference Record of the 2000 IEEE Industry Applications Conference. Thirty-Fifth IAS Annual Meeting and World Conference on Industrial Applications of Electrical Energy (Cat. No.00CH37129), 1*, Rome, Italy, 388-394. doi: 10.1109/IAS.2000.881140

Kotb, A., & Abdulaziz, A.M. (2015). Cavitation Detection in Variable Speed Pump by Analyzing the Acoustic and Vibration Spectrums. *Engineering*, *07*, 706-716.

KSB. (2022a). *NPSH*. Centrifugal Pump Lexicon. https://www.ksb.com/centrifugal-pump-lexicon/npsh/191284/.

KSB. (2022b). *Submersible pump*. Centrifugal Pump Lexicon. https://www.ksb.com/centrifugal-pump-lexicon/submersible-pump/192396/.

KSB (n.d.). *PumpDrive Installation/Operating Manual*. https://shop.ksb.com/ims_docs/00/00215A9B05B61ED98FF1564DB9CE389A.pdf

Lee, S., Hong, J., Lee, S.B., Wiedenbrug, E.J., Teska, M., & Kim, H. (2013). Evaluation of the Influence of Rotor Axial Air Ducts on Condition Monitoring of Induction Motors. *IEEE Transactions on Industry Applications*, 49, 2024-2033.

Lee, S.B., Park, S., Kim, S., & Shim, S. (2022). The Commercialization of Medium-Voltage Induction Motor Rotor Diagnostics Equipment: Helping Prevent In-Service Failures of Induction Motors and Processes. *IEEE Industrial Electronics Magazine.*

Lo, N.G., Soualhi, A., Frinì, M., & Razik, H. (2018). Gear and bearings fault detection using motor current signature analysis. *2018 13th IEEE Conference on Industrial Electronics and Applications (ICIEA)*, 900-905.

Mabrouk, A.E., Zouzou, S.E., Sahraoui, M., & Khelif, S. (2013). Discriminating time-varying loads and rotor cage fault in induction motors. *2013 9th IEEE International Symposium on Diagnostics for Electric Machines, Power Electronics and Drives (SDEMPED)*, 309-316. doi: 10.1109/DEMPED.2013.6645733.

McInroy, J., & Legowski, S. (2001). Using power measurements to diagnose degradations in motor drivepower systems: a case study of oilfield pump jacks. *IEEE Transactions on Industry Applications*, 37, 1574-1581.

Milan J.-J. (2004). *Wreckage of a centrifugal pump impeller on account of cavitation*. https://commons.wikimedia.org/wiki/File:Usure_par_cavitation_d%27un_impulseur_de_pompe_centrifuge_01.jpg

Muralidharan, V., Sugumaran, V., & Indira, V. (2014). Fault diagnosis of monoblock centrifugal pump using SVM. Engineering Science and Technology, an International Journal, 17, 152-157.

Nasiri, M.R., Mahjoob, M.J., & Vahid-Alizadeh, H. (2011). Vibration signature analysis for detecting cavitation in centrifugal pumps using neural networks. *2011 IEEE International Conference on Mechatronics*, 632-635.

Nejjari, H., & Benbouzid, M.E. (2000). Monitoring and diagnosis of induction motors electrical faults using a current Park's vector pattern learning approach. *IEEE Transactions on Industry Applications, 36*, 730-735.

Odavic, M., Sumner, M., Wheeler, P.W., & Li, J. (2010). Real-time fault diagnostics for a permanent magnet synchronous motor drive for aerospace applications. *2010 IEEE Energy Conversion Congress and Exposition*, 3044-3049. doi: 10.1109/ECCE.2010.5618381.

Park, Y., Jeong, M., Lee, S.B., Antonino-Daviu, J.A., & Teska, M. (2017). Influence of Blade Pass Frequency Vibrations on MCSA-Based Rotor Fault Detection of Induction Motors. *IEEE Transactions on Industry Applications*, 53, 2049-2058.

Perovic S. (2000). *Diagnosis of pump faults and flow regimes*. (Doctoral dissertation). Brighton, University of Sussex.

Pons-Llinares, J. (2013). *Metodología para el diagnóstico de averías en motores de inducción mediante el análisis de corrientes estatóricas transitorias utilizando átomos tiempo-frecuencia* [Tesis doctoral no publicada]. Universitat Politècnica de València. https://doi.org/10.4995/Thesis/10251/27555

Pons-Llinares, J., Morinigo-Sotelo, D., Duque, O., Antonino-Daviu, J.A., & Perez-Alonso, M. (2014a). Transient detection of close components through the chirplet transform: Rotor faults in inverter-fed induction motors. *IECON 2014 - 40th Annual Conference of the IEEE Industrial Electronics Society*, 3386-3392.

Pons-Llinares, J., Antonino-Daviu, J.A., Roger-Folch, J., Morinigo-Sotelo, D., & Duque-Perez, O. (2014b). Mixed eccentricity diagnosis in Inverter-Fed Induction Motors via the Adaptive Slope Transform of transient stator currents. *Mechanical Systems and Signal Processing, 48*, 423-435.

Popaleny, P., Péton N. (2019). Submersible pumps condition monitoring, using motor current signature analysis and vibration analysis comparison. *48th Turbomachinery & 35th Pump Symposia, Houston, Texas.*

Pradhan, P.K., Mohanty, A.R., Mahalik, N.P., & Dastidar, S.G. (2012). Fault detection in a centrifugal pump using vibration and motor current signature analysis. *Int. J. Autom. Control., 6,* 261-276.

Pradhan, P.K., Roy, S.K., & Mohanty, A.R. (2019). Detection of Broken Impeller in Submersible Pump by Estimation of Rotational Frequency from Motor Current Signal. *Journal of Vibration Engineering & Technologies, 8,* 613-620.

Rajagopalan, S., Aller, J.M., Restrepo, J.A., Habetler, T.G., & Harley, R.G. (2006). Detection of Rotor Faults in Brushless DC Motors Operating Under Nonstationary Conditions. *IEEE Transactions on Industry Applications, 42*(6), 1464-1477.

Rajagopalan, S., Roux, W.L., Habetler, T.G., & Harley, R.G. (2007). Dynamic Eccentricity and Demagnetized Rotor Magnet Detection in Trapezoidal Flux (Brushless DC) Motors Operating Under Different Load Conditions. *IEEE Transactions on Power Electronics, 22*(5), 2061-2069.

Rasmussen, K.F.; Thorup, N. (2002). Permanent magnet motors find their way to circulator pumps. *Proceedings of the 3rd International Conference EEMODS'02 Energy Efficiency in Motor Driven Systems,* Treviso, Italy, 18–20 September 2002.

Riera-Guasp, M., Antonino, J.A., Roger-Folch, J., & Molina, M.J. (2005). The use of the wavelet approximation signal as a tool for the diagnosis of rotor bar failures. *2005 5th IEEE International Symposium on Diagnostics for Electric Machines, Power Electronics and Drives*, 1-6.

Riera-Guasp, M., Cabanas, M.F., Antonino-Daviu, J.A., Pineda-Sánchez, M., & Garcia, C. (2010). Influence of Nonconsecutive Bar Breakages in Motor Current Signature Analysis for the Diagnosis of Rotor Faults in Induction Motors. *IEEE Transactions on Energy Conversion,* 25, 80-89.

Riera-Guasp, M., Pineda-Sánchez, M., Pérez-Cruz, J., Puche-Panadero, R., Roger-Folch, J., & Antonino-Daviu, J.A. (2012). Diagnosis of Induction Motor Faults via Gabor Analysis of the Current in Transient Regime. *IEEE Transactions on Instrumentation and Measurement*, 61, 1583-1596.

Rosero, J., Ortega, J.A., Gacía, A.C., & Romeral, L. (2007). On-line condition monitoring technique for PMSM operated with eccentricity. *2007 IEEE International Symposium on Diagnostics for Electric Machines, Power Electronics and Drives*, 95-100.

le Roux, W.G., Harley, R.G., & Habetler, T.G. (2007). Detecting Rotor Faults in Low Power Permanent Magnet Synchronous Machines. *IEEE Transactions on Power Electronics, 22*(1), 322-328.

Sapena-Bano, A., Pineda-Sánchez, M., Puche-Panadero, R., Pérez-Cruz, J., Roger-Folch, J., Riera-Guasp, M., & Martínez-Román, J. (2015). Harmonic Order Tracking Analysis: A Novel Method for Fault Diagnosis in Induction Machines. *IEEE Transactions on Energy Conversion, 30*(3), 833-841. doi: 10.1109/TEC.2015.2416973.

Salles, G., Filippetti, F., Tassoni, C., Crellet, G., & Franceschini, G. (2000). Monitoring of induction motor load by neural network techniques. *IEEE Transactions on Power Electronics*, *15*(4), 762-768. doi: 10.1109/63.849047.

Serna, E., & Pacas, J. (2006). Detection of Rotor Faults in Field Oriented Controlled Induction Machines. *Conference Record of the 2006 IEEE Industry Applications Conference Forty-First IAS Annual Meeting, 5*, Tampa, FL, USA, 2006, 2326-2332. doi: 10.1109/IAS.2006.256866.

Siegler, J.A., Sarkady, A.A., & Nemarich, C.P. (1995). Motor Current Signal Analysis for Diagnosis of Fault Conditions in Shipboard Equipment. *Naval Engineers Journal*, *107*, 77-98.

Spyropoulos, D.V., Mitronikas, E.D., & Dermatas, E. (2018). Broken Rotor Bar Fault Diagnosis in Induction Motors Using a Goertzel Algorithm. *2018 XIII International Conference on Electrical Machines (ICEM)*, Alexandroupoli, Greece, 1782-1788. doi: 10.1109/ICELMACH.2018.8506726.

Staubli T., & Nipkow J. (1996). Improvement of efficiency of small circulating pumps. *Pump Congress*, Karlsruhe.

Stopa, M.M., Filho, B.J., & Lage, B.L. (2010). An evaluation of the MCSA method when applied to detect faults in motor driven loads. *IECON 2010 - 36th Annual Conference on IEEE Industrial Electronics Society*, 760-765. doi: 10.1109/IECON.2010.5675028.

Stopa, M.M., Cardoso Filho, B.D., & Martinez, C.B. (2014). Incipient Detection of Cavitation Phenomenon in Centrifugal Pumps. *IEEE Transactions on Industry Applications, 50*, 120-126.

Tamminen, J., Ahonen, T., Kosonen, A., Ahola, J., & Tolvanen, J. (2014). Variable speed drive-based pressure optimization of a pumping system comprising individual branch flow control elements. *2014 16th European Conference on Power Electronics and Applications*, Lappeenranta, 1-11. doi: 10.1109/EPE.2014.6910988.

Thomson, W.T. (1994). On-line current monitoring to detect electrical and mechanical faults in three-phase induction motor drives. *International Conference on Life Management of Power Plants 1994,* Edinburgh, UK, 66-73, doi: 10.1049/cp:19941096.

Thomson, W.T., & Fenger, M. (2000). Industrial application of current signature analysis to diagnose faults in 3-phase squirrel cage induction motors. *Conference Record of 2000 Annual Pulp and Paper Industry Technical Conference (Cat. No.00CH37111)*, 205-211.

Thomson, W.T., & Culbert, I. (2017). *Current Signature Analysis for Condition Monitoring of Cage Induction Motors: Industrial Application and Case Histories*. John Wiley & Sons, Inc., Hoboken, New Jersey. ISBN: 978-1-119-02959-5.

Tian, X., Feng, G., Chen, Z., Al-Braik, A., Gu, F., & Ball, A.D. (2014). The investigation of motor current signals from a centrifugal pump for fault diagnosis. *27th International Congress of Condition Monitoring and Diagnostic Engineering*, Brisbane, Australia.

Tiwari, R., Bordoloi, D.J., & Dewangan, A. (2020). Blockage and cavitation detection in centrifugal pumps from dynamic pressure signal using deep learning algorithm. *Measurement 173*, 108676. https://doi.org/10.1016/j.measurement.2020.108676

Trajin, B., Régnier, J., & Faucher, J. (2010). Comparison between vibration and stator current analysis for the detection of bearing faults in asynchronous drives. *IET Electric Power Applications, 4*(2), 90-100.

Urschel, S., & Dolgirev, J. (2017). Energy- and resource saving synchronous reluctance machine for the use in circulation pumps. *2017 IEEE 3rd International Future Energy Electronics Conference and ECCE Asia (IFEEC 2017 - ECCE Asia)*, Kaohsiung 2139-2144. doi: 10.1109/IFEEC.2017.7992382.

Saidur, R., Mekhilef, S., Ali, M.B., Safari, A., & Mohammed, H.A. (2012). Applications of variable speed drive (VSD) in electrical motors energy savings. Renewable & Sustainable Energy Reviews, 16, 543-550.

Schaab, J. & Gontermann D. (2019). Improving the Efficiency of a Pump Fleet by Designing Pumps Specially for Individual Fixed Speed Drives. *4th International Rotating Equipment Conference.* Paper No. 55, Wiesbaden, Germany

Schmalz, S. C. & Schuchmann, R. P. (2004). Method and Apparatus of Detecting Low Flow/Cavitation in a Centrifugal Pump, US Patent No: US 6,709,240 B1, Mar 2004.

Schoen, R.R., & Habetler, T.G. (1996). Evaluation and implementation of a system to eliminate arbitrary load effects in current-based monitoring of induction machines. *IAS '96. Conference Record of the 1996 IEEE Industry Applications Conference Thirty-First IAS Annual Meeting*, 1, 671-678 vol.1.

Schöb R. (2002). Centrifugal pump without bearings or seals. *World Pumps 2002*(430), 34-37, https://doi.org/10.1016/S0262-1762(02)80218-8.

Schröder, D. (2009). *Elektrische Antriebe–Regelung von Antriebssystemen* (3rd ed.). Springer-Verlag Berlin Heidelberg. ISBN 978-3-540-89612-8.

Shankar, V.K., Umashankar, S., Paramasivam, S., & Hanigovszki, N. (2016). A comprehensive review on energy efficiency enhancement initiatives in centrifugal pumping system. *Applied Energy, 181*, 495-513.

Song, S., Choi, J., & Sul, S. (1996). Current measurement of digital field oriented control. IAS '96. *Conference Record of the 1996 IEEE Industry Applications Conference Thirty-First IAS Annual Meeting, 1*, 334-338 vol.1.

Sperlich, A., Pfeiffer, D., Burgschweiger, J., Campbell, E., Beck, M., Gnirss, R., & Ernst, M. (2018). Energy Efficient Operation of Variable Speed Submersible Pumps: Simulation of a Ground Water Well Field. *Water, 10*(9):1255. https://doi.org/10.3390/w10091255

Sustainability Victoria. (2009). *Energy Efficiency Best Practice Guide Pumping Systems*. Melbourne, VIC, Australia,; p. 27.

Viholainen, J., Tamminen, J., Ahonen, T., Ahola, J., Vakkilainen, E., & Soukka, R. (2013). Energy-efficient control strategy for variable speed-driven parallel pumping systems. *Energy Efficiency*, 6, 495-509.

Vodovozov, V., & Bakman, I. (2013). Performance Improvement of Pumps Fed by the Variable Speed Drives. *Electrical, Control and Communication Engineering, 4*(1), 45–50. http://dx.doi.org/10.2478/ecce-2013-0021.

Waide, P.A., & Brunner, C.U. (2011). Energy-Efficiency Policy Opportunities for Electric Motor-Driven Systems. *IEA Energy Papers*. Paris (France)

Werner, R., & Werthschützky, R. (2009). Intensity determination of cavitation at rotating pumps by means of integrated miniaturised pressure transducers. *SENSOR+TEST Conference 2009 - SENSOR 2009,* Nürnberg, Germany,115-119.

Wikimedia. (2013). https://commons.wikimedia.org/wiki/File:Pump_diagram.PNG

Wilo. (2005). *Fundamental principles of pump technology*. https://www.majo.rs/page_files/page_97/Planning%20guide%20-%20Fundamental%20principles%20of%20pump%20technology%20-%202005.pdf

World pumps (2019). *Siemens SIMOCODE beats blockages*. Water & wastewater (622). [Online]. Available: https://www.worldpumps.com/waste-wastewater/features/siemens-simocode-beats-blockages-/

Wowk, V. (1991). *Machinery Vibration: Measurement and Analysis*. McGraw-Hill, Inc., United States of America,

Xu, W. (2012). Permanent Magnet Synchronous Motor with Linear Quadratic Speed Controller. *2nd International Conference on Advances in Energy Engineering (ICAEE 2011) Energy Procedia* 14. 364 – 369

List of Publications

Journals

1. Becker, V., Schwamm, T., Urschel, S., & Antonino-Daviu, J.A. (2020). Fault Investigation of Circulation Pumps to Detect Impeller Clogging. *Applied Sciences, 10*, 7550.
2. Becker, V., Schwamm, T., Urschel, S., & Antonino-Daviu, J.A. (2021). Fault Detection of Circulation Pumps on the Basis of Motor Current Evaluation. *IEEE Transactions on Industry Applications, 57*, 4617-4624.
3. Becker, V., Schwamm, T., Urschel, S., & Antonino-Daviu, J. A. (2021). Two Current-Based Methods for the Detection of Bearing and Impeller Faults in Variable Speed Pumps. *Energies, 14(15)*, 4514.

Conferences

1. Becker, V., Schwamm, T., Urschel, S., & Antonino-Daviu, J.A. (2020). Detection of Rotor and Impeller Faults in Wet-rotor Pumps. *2020 International Conference on Electrical Machines (ICEM)*, 1, 1308-1314.
2. Becker, V., Eckl, M., Mueller, B., Urschel, S., & Antonino-Daviu, J.A. (2021). Online Condition Monitoring of Pumps based on Adapted Reference Frame Theory. *2021 IEEE 13th International Symposium on Diagnostics for Electrical Machines, Power Electronics and Drives (SDEMPED), 1*, 153-159.
3. Bold, S., Becker, V., Urschel, S., & Antonino-Daviu, J.A. (2022). Influence of faults on the efficiency of centrifugal pumps. *International Conference on Energy Efficiency in Motor Driven Systems 2022 (EEMODS)*.
4. Becker, V., Schneider M., T., Antonino-Daviu, J.A. & Urschel, S. (2022). Cloggage detection of a wastewater pump based on motor current analysis. *2022 International Conference on Electrical Machines (ICEM)*.

Books

1. Bold, S., Becker, V., Urschel, S., & Schaab, J. (2021). Comparison of Fixed and Variable Speed Pumps Under Consideration of Manufacturer and Operator Aspects. *Springer Proceedings in Energy*.